UHH
Universität Hamburg
DER FORSCHUNG | DER LEHRE | DER BILDUNG

Structural and Electrical Properties of Molecule-Linked Gold Nanoparticle Assemblies – A Single Interface Model

Dissertation

with the aim of achieving a doctoral degree at the
Faculty of Mathematics, Informatics and Natural Sciences,
Department of Chemistry, University of Hamburg

submitted by

Karen Schaefer

Hamburg, November 2024

The present work was carried out in the period from November 2021 to November 2024 in the Institute of Inorganic and Applied Chemistry in the group of Prof. Dr. Carmen Herrmann, Faculty of Mathematics, Informatics and Natural Science, University of Hamburg and in the Graduate School 2536 “Nanohybrid” funded by the Deutsche Forschungsgemeinschaft (DFG).

Examiner: Prof. Dr. Carmen Herrmann
Co-Examiner: Prof. Dr. Gabriel Bester

Date of Submission: 15.11.2024
Date of Disputation: 17.01.2025

List of Publications

All peer-reviewed research articles that were published within the framework of this thesis are listed below in a chronological order. An equal contribution of authors is denoted by a dagger (†) symbol.

Published

1. K. Schaefer, C.-Y. Liu, A. Meyer, H. Schlicke, T. Vossmeyer, C. Herrmann, “Cross-Linked Gold Nanoparticle Assemblies: What Can We Learn from Single Flat Interfaces?”, *J. Phys. Chem. C*, **2024**, 128, 9, 3994–4008.
2. G. Mitra, J. Zheng, K. Schaefer, M. Deffner, J. Z. Low, L. M. Campos, C. Herrmann, T. A. Costi, E. Scheer, “Conventional versus Singlet-Triplet Kondo Effect in Blatter Radical Molecular Junctions: Zero-bias Anomalies and Magnetoresistance”, *Chem*, **2025**, 102500.

In Preparation

1. C.-Y. Liu†, K. Schaefer†, C. Herrmann, T. Vossmeyer, “Towards Understanding the Structure of Cross-Linked GNP Assemblies: Mixtures of Thiols and Dithiols”, in preparation.

Contents

List of Abbreviations

3MPA	3-Mercaptopropionic Acid
5DT	1,5-Pentanedithiol
6DT	1,6-Hexanedithiol
6T	1-Hexanethiol
7DT	1,7-Heptanedithiol
8DT	1,8-Octanedithiol
9T	1-Nonanethiol
10DT	1,6-Decanedithiol
11T	1-Undecanethiol
12T	1-Dodecanethiol
14T	1-Tetradecanethiol
ADT	Alkanedithiol
AFM	Atomic Force Microscopy
AMT	Alkanemonothiol
CC	Coupled Cluster
CI	Configuration Interaction
cs	closed-shell
D	Dimer
DFT	Density Functional Theory
DFTB	Density Theory Based Tight Binding
fcc	Face-Centered-Cubic
FDE	Frozen Density Embedding
GGA	Generalized Gradient Approximation
GISAXS	Grazing-Incidence Small-Angle Scattering
GNP	Gold Nanoparticle
hcp	Hexagonal Closed Packing
HF	Hartree–Fock
IoT	Internet of Things
KS-DFT	Kohn–Sham Density Functional Theory
LB	Landauer–Büttiker
LbL-SC	Layer-by-Layer Spin-Coating
LDA	Local Density Approximation
LDOS	Local Density of States
LSPR	Localized Surface Plasmon Resonance
M	Monomer
MD	Molecular Dynamics

MR	Magneto resistance
NND	Nearest Neighbor Distance
os	open-shell
PBC	Periodic Boundary Condition
QCM	Quartz Crystal Microbalance
QMC	Quantum Monte Carlo
QM/MM	Quantum Mechanics/Molecular Mechanics
ReaxFF	Reactive Force Field
REM	Rayleigh-Emden Model
SAM	Self-Assembled Monolayer
SAXRD	Small-Angle X-ray Diffraction
SCC	Self-Consistent Charge
SCF	Self-Consistent Field
SEM	Scanning Electron Microscopy
SOMO	Singly Occupied Molecular Orbital
SUMO	Singly Unoccupied Molecular Orbital
t	tiplet
TEM	Transmission Electron Microscopy
TGA	Thermogravimetric Analysis
VOC	Volatile Organic Compound
XPS	X-ray Photoelectron Spectroscopy

1 Abstract

Cross-linked gold nanoparticle (GNP) assemblies show promise for applications such as room-temperature sensors for mechanical strain and gases, offering a low-power alternative to conventional metal oxide sensors. Despite several decades of investigation into GNP-based sensors, the underlying sensing mechanisms remain only partially understood. This thesis explores an atomistic, single flat particle–particle interface model to gain insights into fundamental properties of GNP assemblies, such as the interparticle distance and zero-bias conductances, first in the absence and then in the presence of analyte gases.

Using reactive force field (ReaxFF) molecular dynamics (MD) simulations and a tight-binding density functional theory approach, the interparticle distances and conductances of alkanedithiol (ADT)- and alkanemonothiol (AMT)-stabilized GNP assemblies are investigated, achieving qualitative agreement with the experiment. In case of ADT ligands also quantitative agreement with the experiment was reached for sufficiently large nanoparticles (approximately 7 nm). On the other hand, limitations of ReaxFF, including its inability to simulate thiol physisorption and the occurrence of unreasonable reactions in some dithiolate simulations are discussed.

Additionally, ligand distributions in mixed-ligand assemblies consisting of 1,9-nonanedithiol (9DT) and AMT ligands of varying chain lengths through the single-interface model are investigated theoretically and compared with the experiment. MD simulations, combined with charge transport calculations, revealed that mixtures of 9DT and 1-hexanethiol are best described by a mixed-ligand model, where the 9DT ligands cross-link the surfaces. In contrast, for longer AMT ligands, results are contradictory: while experimental intersurface distances align with those from MD simulations with randomly distributed ligands and no cross-linking, charge transport calculations indicate that the ligands separate into distinct domains, complicating predictions regarding ligand distributions in these mixtures.

The model is further extended to analyze changes in interparticle distance and conductance upon alkane adsorption, highlighting the limitations of the single-interface model in accurately predicting distance changes and resistances compared to experimental observations in GNP assemblies. Although the analyte-to-ligand ratio used in the simulations aligned with typical experimental values, the changes in interparticle distance and the relative resistance upon analyte incorporation into the interfaces were significantly overestimated. Additionally, the calculated relative resistances were mostly negative, in contrast to experimental observations. This can be explained by a non-uniform analyte concentration within the GNP assembly, where only a limited number of analyte molecules diffuse into the dense ligand matrix at the interfaces of the GNP assemblies, while the majority of analytes occupy voids within the structure. These analyte molecules may be predominantly responsible for the observed changes in interparticle distances and resistances, however, they are not considered within the single-interface model investigated in this thesis.

In the future, stable organic radicals, such as Blatter radicals, could serve as promising alternatives to ADT and AMT ligands in sensing devices. Currently, these radicals are primarily studied in single-molecule junctions to explore their fundamental properties. In cooperation with low temperature experiments, Blatter radical junctions are investigated in this thesis to support the theory that certain junction properties arise from the formation of Blatter radical dimers. Structure optimizations using density functional theory (DFT) suggest strong non-covalent binding between the two radicals. Exchange spin coupling for both isolated dimers and dimers within a junction tend to be predominantly antiferromagnetic, consistent with experimental findings. Additionally, zero-bias conductances of dimer junctions, computed using a Green's function approach combined with DFT, align better with experimental conductances than for monomer junctions, further supporting the theory of dimer formation.

In summary, this thesis contributes to the development of structural models for GNP assemblies, addressing their capabilities and limitations in sensing applications, while emphasizing the need for more robust and variable force fields for broader applications and future ligand screening.

2 Zusammenfassung

Vernetzte Goldnanopartikel (GNP)–Assemblate sind vielversprechend für die Anwendung als Raumtemperatursensoren für mechanischen Druck oder Gase. Im Vergleich zu herkömmlichen Metalloxidsensoren, die bei erhöhten Temperaturen bedient werden, bieten GNP-Assemblate somit eine stromsparende Alternative. Trotz jahrzehntelanger Forschung an GNP-basierten Sensoren sind die zugrunde liegenden Sensormechanismen allerdings nur teilweise verstanden. Diese Doktorarbeit untersucht ein einzelnes flaches Partikel-Partikel-Schnittstellenmodell, um Einblicke in die grundlegenden Eigenschaften von GNP-Anordnungen zu gewinnen, wie z.B. den Abstand zwischen den Partikeln und die Leitfähigkeit bei Zero-Bias, zunächst in Abwesenheit und dann in Anwesenheit von Analytgasen.

Mithilfe von reaktiver Kraftfeld-Molekulardynamik (ReaxFF-MD) und einem Tight-Binding-Dichtefunktionaltheorie-Ansatz werden die Abstände zwischen den Partikeln und die Leitfähigkeit von GNP-Assemblaten mit Alkandithiol (ADT)– und Alkanmonothiol (AMT)–Liganden untersucht. Eine quantitative Übereinstimmung besonders im Vergleich zu Assemblaten mit ausreichend großen Nanopartikeln ($\sim$7 nm) konnte erreicht werden. Andererseits werden Einschränkungen des ReaxFF-Ansatzes diskutiert, darunter die Unfähigkeit, Thiolphysisorption zu simulieren, und das Auftreten von zweifelhaften Reaktionen in einigen Dithiolatsimulationen.

Darüber hinaus werden Ligandenverteilungen in gemischten Ligandenanordnungen aus 1,9-Nonanedithiol (9DT)– und AMT–Liganden unterschiedlicher Kettenlängen durch das Einzelschnittstellenmodell untersucht. MD-Simulationen in Kombination mit Ladungstransportberechnungen zeigen, dass Mischungen aus 9DT und 1-Hexanthiol am besten durch ein Ligandenmodell beschrieben werden können, bei dem die Liganden zufällig verteilt sind und die 9DT-Liganden die Goldoberflächen vernetzen. Im Gegensatz dazu sind die Ergebnisse für längere AMT-Liganden widersprüchlich: Während die experimentellen Abstände zwischen den Oberflächen mit denen aus MD-Simulationen mit zufällig verteilten Liganden ohne 9DT-Vernetzung übereinstimmen, deuten Ladungstransportberechnungen darauf hin, dass sich die Liganden in unterschiedliche Domänen aufteilen, was Vorhersagen bezüglich der Ligandenverteilungen in diesen Systemen erschwert.

Das Modell wurde erweitert, um Änderungen des Abstands und der Leitfähigkeit zwischen den Partikeln bei der Adsorption von Alkanen zu analysieren. Dabei wurden die Einschränkungen des Einzelschnittstellenmodells bei der genauen Vorhersage von Abstandsänderungen und Widerständen im Vergleich zu experimentellen Beobachtungen in GNP-Anordnungen betrachtet. In diesem Fall scheint die Betrachtung der Schnittstelle zwischen zwei Partikeln nicht ausreichen zu sein, um die Eigenschaften der Assemblate unter Gasadsorption zu beschreiben. Obwohl das Verhältnis von Analyt zu Liganden in den Simulationen mit dem aus Experimenten abgeschätzten Verhältnis übereinstimmt, wurden die Änderungen des Partikelabstands und des Widerstands in den Simulationen signifikant überschätzt. Zudem wurden überwiegend negative relative Widerstände berechnet, was nicht mit den experimentellen Beobachtungen übereinstimmt. Daher könnte es sein, dass die Analytkonzentration innerhalb der GNP-Assemblate nicht homogen verteilt ist. Während beispielsweise an den Schnittstellen zwischen zwei Partikeln nur wenig Analytgas vorhanden sein könnte, könnte die Konzentration in kleinen Hohlräumen innerhalb der Netzwerke höher sein. Wenn diese spezifischen Bereiche der GNP-Assemblate die Sensoreigenschaften dominieren, wäre das Einzelschnittstellenmodell unzureichend, da dieses lediglich die Schnittstellen zwischen zwei Partikeln betrachtet und nicht das gesamte Netzwerk.

In Zukunft könnten neben ADT- und AMT-Liganden auch stabile organische Radikale, wie Blatter-Radikale, als interessante Liganden für Sensoren in Betracht gezogen werden. Derzeit werden diese Radikale hauptsächlich in Einzelmolekül-Junctions untersucht, um ihre grundlegenden Eigenschaften zu erforschen. In Kooperation mit Tieftemperaturexperimenten wurden in dieser Arbeit Blatter-Radikal-Junctions untersucht, um die Theorie zu stützen, dass bestimmte Eigenschaften dieser Verbindungen auf die Bildung von Blatter-Radikaldimeren zurückzuführen sind. Strukturoptimierungen mithilfe der Dichtefunktionaltheorie (DFT) deuten auf eine starke nicht-kovalente Bindung zwischen den beiden Radikalen hin. Die Austauschkopplungskonstanten sowohl für isolierte Dimere als auch für Dimere innerhalb einer Junction sind überwiegend antiferromagnetisch, was mit experimentellen Ergebnissen übereinstimmt. Darüber wurden Zero-Bias-Leitfähigkeiten von Dimerverbindungen mithilfe eines Green'schen Funktionsansatzes in Kombination mit DFT berechnet. Diese stimmten besser mit den experimentellen Leitfähigkeiten überein als die für Monomerverbindungen ermittelten Leitfähigkeiten, was die Theorie der Dimerbildung weiter unterstützt.

Zusammenfassend trägt diese Doktorarbeit zur Entwicklung von Strukturmodellen für GNP-Assemblaten bei, wobei sie sich mit ihren Fähigkeiten und Grenzen zur Vorhersage von Strukturen und zur Auflösung des Sensormechanismus befasst. Gleichzeitig betont sie aber auch die Notwendigkeit robusterer und variablerer Kraftfelder für breitere Anwendungen und zukünftige Ligandenscreenings.

3 Introduction

> *"If we had computers that knew everything there was to know about things – using data they gathered without any help from us – we would be able to track and count everything, and greatly reduce waste, loss and cost. We would know when things needed replacing, repairing or recalling, and whether they were fresh or past their best."*
>
> – Kevin Ashton, That 'Internet of Things' thing, RFID Journal, 2009.

The vision of a "smart world" is increasingly evident in our daily lives, taking shape as smart homes, smartphones, smartwatches, smart refrigerators, and even smart cities. Cars that drive autonomously, handheld devices that diagnose illnesses simply by breathing into them, and devices that notify us when food is no longer good for consumption are not science fiction anymore. These visions are all part of the concept of the Internet of Things (IoT), a term first introduced by British pioneer Kevin Ashton in 1999.[1] Ashton envisioned a future in which data from the physical world would be transmitted to the internet, allowing computers to simplify and enhance our lives. A key component of the IoT ecosystem is the sensor, which serves as the interface between the physical world and digital intelligence.

For specific IoT sensing devices – such as smoke detectors, breath analysis systems, and monitors for pollutants, air quality, and food ripening – sensors that can detect and differentiate between various gases are particularly important. In addition to IoT devices, those gas sensors are also part of existing chemical technologies, such as in the automotive, industrial, or aerospace sector, where gas sensors detect gases like NO_x, NH_3, O_3, or CO_2 in exhaust gases for environmental protection, or in the security sector for detecting traces of explosives.[2] Currently, the majority of gas sensors under investigation are chemiresistors, which operate by detecting changes in electrical resistance when adsorbing analyte vapor. Commercially available chemiresistors typically consist of metal oxide semiconductors because they are fast-responding, cost-effective, highly sensitive and selective, and easy to fabricate.[2] However, a significant disadvantage of these sensors is their requirement for high operating temperatures, leading to increased energy consumption.[3] Consequently, researchers have explored alternative materials, including nanoparticles,[4] conductive polymer composites,[5] carbon nanotubes,[6–8] silicon nanowires,[9, 10] and MXenes.[11, 12]

Among these materials, gold nanoparticles (GNPs) stand out as promising candidates, due to their stability, and well-established synthesis procedures.[13] Films made from GNPs can operate effectively at room temperature, resulting in lower power consumption compared to metal oxide sensors.[2, 14] Additionally, their resistive properties can be tuned through control of the sensor's structural features, enhancing their versatility and sensitivity for various applications.[15–24] GNP films typically consist of GNPs with sizes between 3 and 7 nm, which are interconnected by organic ligands. The most commonly used ligands are thiols, known for their ability to covalently bond with gold. The ligands can be classified into two categories: those that interlink two particles, such as dithiols, and those that only connect to a single particle but create a network through intermolecular interactions, such as monothiols.

When connecting the films to electrodes, it is commonly believed that charge transport occurs through a series of tunneling events across the intercore dielectric medium, which consists of organic ligands. This idea was introduced by Terrill et al.[16], who investigated the temperature dependence of the conductivity in alkanedithiol (ADT) cross-linked GNP assemblies. They demonstrated an Arrhenius-type T^{-1} dependence of the logarithmic conductivity $ln\sigma$. Based on the understanding that the electron transfer rate decreases exponentially with the interparticle distance, Terrill et al. proposed a model equation that includes an exponential tunneling term, thereby relating conductivity to interparticle spacing:

$$\sigma(T, \delta) = \sigma_0 e^{-\delta\beta} e^{-E_A/\mathrm{R}T} \ , \tag{3.1}$$

where σ_0 is a preexponential tunneling factor, β is the tunneling decay constant, δ the distance between two GNPs, E_A the activation energy required for charging the gold cores, T the temperature, and R the gas constant. This model equation was successfully applied to both alkanemonothiol (AMT)-stabilized[16, 25] and ADT-cross-linked[21, 24, 26] GNP assemblies to describe their temperature dependence onto the conductivity.

The activation energy is often described by the granular metal theory[24, 27]

$$E_A = \frac{e^2}{8\pi\epsilon_r\epsilon_0} \left(\frac{1}{R_{\mathrm{GNP}}} - \frac{1}{R_{\mathrm{GNP}} + \delta} \right) \ , \tag{3.2}$$

where e is the elementary charge, ϵ_r and ϵ_0 are the relative permittivity of the matrix material and of the vacuum, respectively, R_{GNP} is the radius of the particles, and δ represents the interparticle distance. Comparing activation energies, theoretically calculated by Equation (3.2), with those determined experimentally, good agreement was observed.[28, 29]

The structure of the GNP films plays a crucial role in determining the film's baseline conductivity. For example, as the size of the GNP increases, the thermal activation energy decreases, resulting in an increase in baseline conductivity.[25] Furthermore, by changing the length of the ligands, the interparticle distance δ can be precisely tailored.[16–18] Additionally, the choice of ligand can influence the tunneling decay constant β. Ligands featuring aromatic rings, where charge delocalization occurs, for instance, are known to yield larger β values compared to those composed of simple alkane chains.[15, 23, 24] Additionally, the structural order of the films was shown to impact the electrical properties of thiol-ligated films. Local structural disorder, for example, was shown to produce variations in the tunneling distance, thus causing a wide distribution of the resistance in the film, which is estimated to effect the current pathway across the GNP assembly.[30]

In the presence of external stimuli, such as mechanical strain or sorption of analyte molecules, the interparticle distance can increase, also known as swelling, and/or the permittivity and thereby E_A (see Equation (3.2)) of the GNP matrix can change.[17, 18, 31–37] Both changes can impact the films' conductivity (see Equation (3.1)), making GNP films highly suitable for sensing applications.

For real-world applications, sensors must demonstrate high stability, high sensitivity, and, especially in the case of gas sensors, high selectivity. One approach to enhance the sensitivity is to increase the structural flexibility of the ligands, and thereby the swelling response towards analyte adsorption. For example, this can be done by increasing the length of the ligands.[20–22] However, this can drastically reduce the baseline conductivity of the film, potentially resulting in overall lower responses. For improving the selectivity towards specific vapors, functional groups can be incorporated into the ligands.

A relatively new approach involves mixing different types of ligands to enhance chemiresistive sensor responses to analyte vapors (see e.g. Ref.[33, 38, 39], or Ref.[40] for a recent review). Ketelsen et al.[33] demonstrated that using 1,9-nonanedithiol (9DT) with functionalized monothiols such as 1-thioglycerol (TG), 3-mercaptopropionic acid (3MPA), or 4-mercapto-1-butanol (4M1OH) significantly improves the relative response to polar solvents like water and ethanol, compared to non-functionalized films. By integrating films with various ligand mixtures into an array, they were able to distinguish between different analyte vapors such as octane, toluene, ethanol, or water. Liu et al.[39] built upon this method by introducing a layer-by-layer spin-coating technique, providing a straightforward approach to fabricate GNP chemiresistors that consist of mixtures of monothiols and 9DT.

In many instances, the simplified model equation for GNP films (Equation (3.1)) can qualitatively describe the film's sensing properties. However, quantitatively, deviations can arise. For example, Olichwer et al.[41] conducted an in-depth study of dithiol cross-linked films and their sensing characteristics. They demonstrated that the responses predicted by Equation (3.1), using interparticle distances measured by grazing-incidence small-angle scattering (GISAXS) and weighted averages of the permittivity, were three times higher for toluene compared to the responses measured experimentally. This discrepancy shows the complexity of the sensing mechanisms involved and highlights the need for further refinement of the model to accurately capture the behavior of GNP films in practical applications. In an attempt to do so, Steinecker et al.[42] extended the existing model calculating the relative resistance change caused by analyte vapors based on the analyte's partition coefficients. With their refined model, they could predict sensor responses with reasonable reliability, but they had to include an empirical weighting factor to address the overestimation of the swelling response to the vapor (e.g., 0.233 for aliphatics and alcohols and 0.319 for aromatics).

Even with the refinements made by Steinecker et al., the model does not include detailed information regarding the atomistic structure of GNP films. Research on single-molecule junctions, however, has shown that several factors, including the length of the ligand, but also the structure of the gold tip or surface, as well as the conformation of the ligand, and the binding configuration, significantly influence their charge transport properties.[43] However, these factors, along with others, are not directly included in the model description for charge transport in GNP films (Equation (3.1)). Additionally, studying these factors experimentally is challenging, as they often exceed the resolution limits of techniques like transmission electron microscopy (TEM). To investigate features of the films that go beyond these resolution limits, theoretical models can be employed.

Yeh et al.,[44] for example, used a united-atom approach, where CH_2 and SH unit were treated as united atoms, to simulate the elastic properties of ADT cross-linked GNP assemblies. They started by annealing spherical particles. During the annealing process, flat facets were formed at the surface of the GNP, dominated by Au(111) and Au(100) surfaces. Next, ADT ligands were assembled on the GNP, and several particles were combined to form a 3D network. To evaluate the model, the authors investigated the interparticle distance dependence on the ADT ligand length, showing good agreement with experimental data. With their model, they could investigate mechanical properties of the films, and showed that especially the all-trans bridge linkers dominated the Young's modulus of the film.[45]

The work by Yeh et al. is a nice example of how theoretical simulations can deepen our understanding of the properties of systems such as GNP films. However, exploring charge transport characteristics in such large simulation systems (consisting of up to 150,000 atoms) can be difficult, as the computational requirements can become unreasonably time-consuming. These large systems are also inadequate for studying the explicit movements and interactions of all atoms, as approximations are often required, such as treating methyl groups as united atoms. As a result, the interactions between analyte molecules and the ligand matrix, as well as any potential structural rearrangements, may not be accurately represented.

In this thesis, a model is proposed that simplifies the structure of GNP films to focus on the key element that likely influences their properties: the interface between neighboring particles (see Figure 3.1). This "single-interface model" consists of two flat Au(111) surfaces that are either cross-linked by ADT or capped with AMT molecules. Initially, we will evaluate how accurately this model captures fundamental characteristics of the films, such as the interparticle distance for various AMT and ADT ligands, as well as the conductance in the absence of external stimuli.

Once we confirm that the model accurately represents these basic features of GNP films, we will expand it to investigate the structure of mixed-ligand films composed of ADT and AMT ligands. Specifically, we aim to understand how well these ligands mix: whether they form

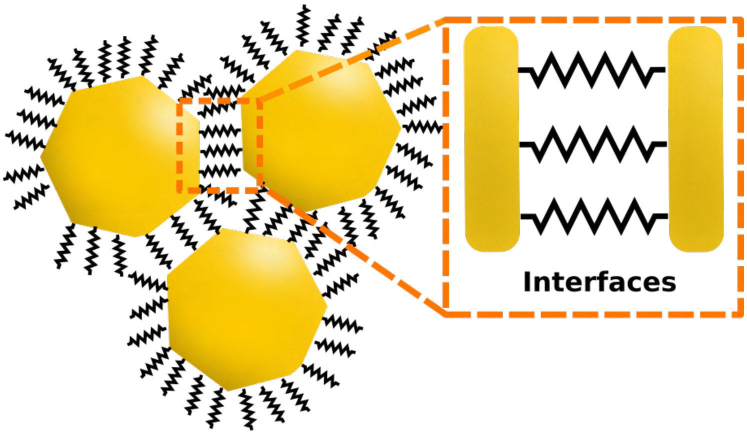

Figure 3.1: Illustration of the single-interface model as an approximation for cross-linked GNP assemblies.

homogeneous structures or separate into distinct domains. Then, we will introduce analyte molecules into the model and investigate whether the single-interface model adequately captures the chemiresistive properties of the GNP assemblies.

As an alternative to ADT and AMT ligands, radicals can present a stable alternative as linker molecules for future sensing applications. The Blatter radical, for example, was shown to have a good air and vacuum stability, with its radical character being preserved in films over a long period of time.[46] This radical has attracted considerable attention as conducting molecule in single-molecule junctions, due to its electrical and magnetic properties.[47] In contrast to ADT and AMT ligands, the properties of these molecules are far less understood. In a collaborative study with Elke Scheer's group at the University of Konstanz and Theo A. Costi from the Forschungszentrum Jülich, we aimed to fundamentally study the charge transport of Blatter radicals by investigating them in single-molecule junctions. We explored potential monomer and dimer structures of the Blatter radical and analyzed their charge transport and magnetoresistive properties, and especially their exchange spin-coupling constant. The goal of this project was to deepen our understanding of the potential applications of Blatter radicals in future devices.

4 Theory

To describe structures of systems such as GNP assemblies, single-molecule junctions, and charge transport phenomena within these systems, it is crucial to first select a theoretical model that accurately describes their structural and/or electronic properties. The choice of model depends on the system's size and the relevant time scales. Various approaches are available depending on different levels of approximations (see Figure 4.1).[48]

For small systems, such as individual molecules, *ab initio* methods such as Hartree–Fock (HF) theory or correlated wavefunction techniques (e.g., configuration interaction (CI) and coupled cluster (CC) methods) can be used.[49] When considering slightly larger systems such as single-molecule junctions, density functional theory (DFT) is often used due to its better scaling with system size compared to many-body wavefunction methods.[50]

To further enhance computational efficiency, DFT can be applied within a tight-binding framework, known as density functional based tight binding (DFTB), which allows the description of even larger systems while still explicitly considering the electronic structure. On the other hand, classical molecular dynamics (MD) simulations do not take electronic details into account; instead, they focus on atomic degrees of freedom, making them suitable for modeling larger systems and longer time scales. Furthermore, reactive force fields (ReaxFFs) have been developed to enable simulations of processes that involve reactions.[51–54] For systems that exceed feasible limits for MD simulations, coarse-grained models may be employed. In these models multiple atoms are grouped and represented as one particle or bead. Thereby, assemblies of several nanoparticles and thousands of ligands can be simulated.[55]

Additionally, there are several methods that combine different levels of theory or approximations. For instance, Born–Oppenheimer molecular dynamics incorporates electronic structure into molecular dynamics simulations [56]. Furthermore, techniques such as quantum mechanics/molecular mechanics (QM/MM)[57] and frozen density embedding (FDE)[58] separate the system into a region (or selection of atoms) that is treated quantum mechanically and a region that is treated using classical interactions. With the aid of machine learning, computational times can be improved significantly (see, for example, studies by Behler et al.[59, 60]).

In this thesis, structures with different system sizes were investigated. The methods that were used to model these structures (DFT, DFTB, and MD) will be introduced in the following sections, followed by an introduction to the theory of charge transport through small molecules.

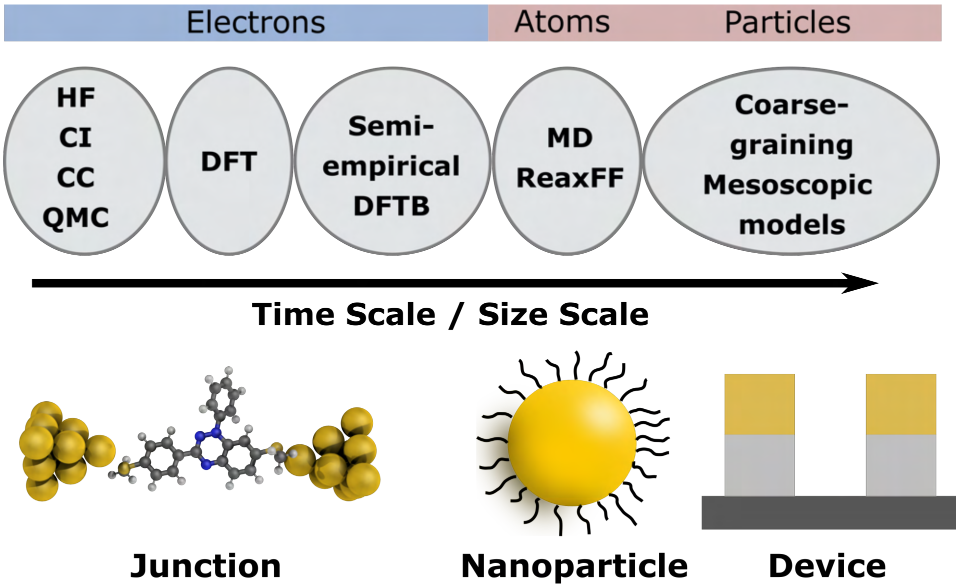

Figure 4.1: A hierarchy of different theoretical models and their dependence on system size and simulation time scale. The abbreviations stand for Hartree–Fock (HF), configuration interaction (CI), coupled-cluster (CC), quantum Monte Carlo (QMC), density functional theory (DFT), density functional tight-binding (DFTB), molecular dynamics (MD), and reactive force field (ReaxFF).

4.1 Density Functional Theory

In 1964, Hohenberg and Kohn[61] introduced two theorems, which build the basis for DFT. The first theorem states that for every ground state density, there is a uniquely determined external potential, which in turn leads to a uniquely defined ground state wave function:

$$\rho_0(\vec{r}) \leftrightarrow V_{\text{ext}}\left(\vec{r}\right) \tag{4.1}$$

$$\rho_0(\vec{r}) \leftrightarrow \Psi_0\left(\vec{r}_1, ..., \vec{r}_N\right) \ . \tag{4.2}$$

The second theorem states that the variation principle is applicable to the energy functional of the electron density. Hence, E_0 can be determined by minimizing the energy functional $E[\rho]$ with respect to ρ,

$$\tilde{E}[\tilde{\rho}] \leq E_0 \ . \tag{4.3}$$

Based on these two theorems, the ground state energy of a system can be determined from the electron density, without needing to know the wave function. In contrast, other electronic structure theories, such as HF, CI, or CC, require knowledge of the wave function Ψ to calculate the energy of a system. They use Slater determinants, which depend on all electron coordinates, and therefore require $3N$ coordinates (or $4N$ when also considering the spin). On the other hand, the electron density only relies on three coordinates.[50] This reduces the complexity of the problem compared to wave function-based methods significantly.

As a starting point, the (unknown) energy functional $E[\rho]$ can be written as the sum of the following contributions,

$$E[\rho] = T_n[\rho] + T_e[\rho] + V_{ee}[\rho] + V_{en}[\rho] + V_{nn}[\rho] \ , \tag{4.4}$$

where T_n and T_e are the kinetic energy of the nuclei n and the electrons e, while V_{ee}, V_{en}, and V_{nn} describe the electron-electron interaction, the electron-nuclei interaction, and the interactions between the nuclei, respectively, which are all of Coulomb type. The Born–Oppenheimer approximation[62] can be applied to simplify the expression for the energy functional. This approximation states that the movement of the electrons and the nuclei can be considered separately, as the nuclei move much slower than the electrons, due to their higher mass. Therefore, the nuclei can be treated as classical particles with fixed positions during the electronic optimization.

$V_{en}[\rho]$ and the Hartree energy $V_H[\rho]$, which represents the classical part of the electron-electron interaction V_{ee}, can be classically expressed as

$$V_H[\rho] = \frac{1}{2}\int\int \frac{\rho(\vec{r}_i)\rho(\vec{r}_j)}{r_{ij}} d^3\vec{r}_i d^3\vec{r}_j \text{ , and} \tag{4.5}$$

$$V_{en}[\rho] = -\sum_{a=1}^{K} Z_a e \int \frac{\rho(\vec{r})}{|\vec{R}_a - \vec{r}|} d\vec{r} \text{ ,} \tag{4.6}$$

where Z_a is the charge number, K represents the total number of nuclei in the molecular system, and R_a is the position of the core a, while $\rho(\vec{r})$ is the electron density at position $\vec{r}$, and r_{ij} is the distance between electrons i and j.

For the remaining terms, it is not feasible to express them using a classical formulation dependent on electron density. Therefore, Kohn and Sham[63] developed an approach where the kinetic energy is divided into a term that can be calculated exactly and an additional correction term. The resulting Hamilton operator can be describes as[50]

$$\hat{H}_\lambda = \hat{T} + V_{\text{ext}}(\lambda) + \lambda V_{ee} \text{ ,} \tag{4.7}$$

where $0 \leq \lambda \leq 1$. V_{ext} represents the external potential in which the electrons move. When $\lambda = 1$, it corresponds to the real physical system, where $V_{\text{ext}} = V_{en}$. The kinetic energy can be calculated exactly when the system is assumed to consist of non-interacting fermions, with $\lambda = 0$. The resulting missing part of the exact kinetic energy, along with non-classical contributions to the electron-electron interaction energy, the electron correlation energy E_C and the exchange energy E_X, are taken into account as an additional exchange correlation functional $E_{XC}[\rho]$ in the energy calculation

$$E_{\text{DFT}}[\rho] = T[\rho] + V_{en} + V_H[\rho] + E_{\text{XC}}[\rho] \text{ ,} \tag{4.8}$$

$$E_{\text{XC}}[\rho] = (T[\rho] - T^{\text{SD}}) + (V_{ee}[\rho] - V_H[\rho]) \text{ .} \tag{4.9}$$

This exchange–correlation functional $E_{XC}[\rho]$ cannot be calculated exactly except for very simple systems, and needs to be approximated. For this, various density functionals exist that can be assigned to one of the five categories: LDA, GGA, meta-GGA, hybrid or double-hybrid. An overview over the accuracy of these five categories can roughly be given by the *Jacob's ladder*[64] (see Figure 4.2). In general, a higher position on the ladder is expected to corresponds to a higher accuracy and a higher complexity of the functional. However, in an extensive assessment of 200 different density functionals Mardirossian and Head-Gordon have shown, among others, that this rule does not always apply.[65]

The LDA (local density approximation) functional is the simplest functional. It is based on the assumption that the local electron density can be described by a homogeneous electron gas. While for molecules, this approximation is insufficient, for metals the assumption of a homogeneous electron gas can be reasonably accurate.[50]

The GGA (generalized gradient approximation) functionals include the derivative of the density at a certain point in addition to the electron density. This increases the chemical

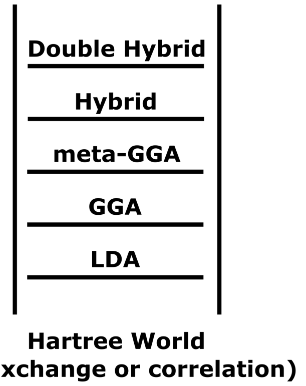

Figure 4.2: Jacob's ladder as described in Ref.[64]: Representation of the accuracy of the five categories of DFT functionals. Functionals positioned higher on the ladder are expected to demonstrate greater chemical accuracy, while simultaneously exhibiting increased complexity.

accuracy of these functionals compared to LDA functionals while they still require relatively low computational costs. For the calculation of the exchange and correlation energies, different approaches exist within the GGA framework (e.g. PBE,[66] BP86,[67, 68] and BLYP[67, 69]). When the second derivative of the density is additionally included, one speaks of meta-GGA functionals.
Next higher in the ladder are the hybrid functionals. In these functionals, only a part of the exchange–correlation energy is calculated with the help of LDA or (meta-)GGA functionals. For the remaining part, the exact exchange energy from HF theory is used. The optimal mixing ratio of exact exchange energy and exchange–correlation energy are unknown *a priori* and need to be determined through validation.

One of the most commonly used functionals among the hybrid functionals is the B3LYP (Becke, 3-parameter, Lee-Yang-Parr) functional. The exchange-correlation energy $E_{\mathrm{XC}}^{\mathrm{B3LYP}}$ in B3LYP is approximated as

$$E_{\mathrm{XC}}^{\mathrm{B3LYP}} = E_{\mathrm{XC}}^{\mathrm{LDA}} + \alpha_{\mathrm{HF}} \left(E_{\mathrm{X}}^{\mathrm{HF}} - E_{\mathrm{X}}^{\mathrm{LDA}} \right) + \alpha_{\mathrm{X}} \Delta E_{\mathrm{X}}^{\mathrm{B88}} + \alpha_{\mathrm{C}} \Delta E_{\mathrm{C}}^{\mathrm{LYP}} \ . \tag{4.10}$$

The LDA exchange-correlation functional $E_{\mathrm{XC}}^{\mathrm{LDA}}$ is being corrected by shares of the exact HF exchange $E_{\mathrm{X}}^{\mathrm{HF}}$, the Becke 88[67] exchange functional $E_{\mathrm{X}}^{\mathrm{B88}}$, and the correlation functional of Lee, Yang and Parr[69] $E_{\mathrm{C}}^{\mathrm{LYP}}$. The parameters α_{HF}, α_{X}, and α_{C} were determined empirically, with the optimum lying at $\alpha_{\mathrm{HF}} = 0.20$, $\alpha_{\mathrm{X}} = 0.72$, and $\alpha_{\mathrm{C}} = 0.81$.[70]

4.2 Density-Functional Tight-Binding Theory

While DFT usually offers good accuracy and efficiency for calculating a variety of structures, it cannot by applied universally. For large systems, for MD simulations with extended time scales, or when benchmarking large sets of structures, DFT may become too computationally expensive. In such scenarios, density functional tight-binding (DFTB) can be a valuable alternative. DFTB is directly parameterized from DFT and therefore treats the electrons using quantum mechanical principles.[71]

Starting from the Kohn–Sham DFT energy, several approximations are introduced in the DFTB formalism, as described in Ref. [71]. First, the electron density of the system is divided into atomic contributions, where the atoms in the system are assumed to be free and neutral, so that no charge transfer is allowed between the atoms. Therefore, the resulting density $\rho_0(r)$ no longer minimizes the energy functional $E[\rho(r)]$. However, it is assumed to be close to the true minimizing energy, allowing us to express it as $\rho_{\min}(r) = \rho_0(r) + \delta\rho_0(r)$. The basic idea of DFTB is to expand $E[\rho]$ at $\rho_0(r)$ to second order in fluctuation $\delta\rho(r)$ to yield

$$\begin{aligned} E[\delta\rho] \approx & \sum_a f_a \langle \Psi_a | -\frac{1}{2}\nabla^2 + V_{\text{ext}} + V_H[\rho_0] + V_{\text{XC}}[\rho_0] | \Psi_a \rangle \\ & + \frac{1}{2} \int \int' \left(\frac{\delta^2 E_{\text{XC}}[\rho_0]}{\delta\rho\delta\rho'} + \frac{1}{|r - r'|} \right) \delta\rho(r)\delta\rho'(r')\delta r \delta r' \\ & - \frac{1}{2} \int V_H[\rho_0](r)\rho_0(r) + E_{\text{XC}}[\rho_0] + E_{nn} \\ & - \int V_{\text{XC}}[\rho_0](r)[\rho_0](r) \ . \end{aligned} \tag{4.11}$$

The first line in Equation (4.11) is the band-structure energy

$$E_{\text{BS}}[\delta\rho] = \sum_a f_a \langle \Psi_a | H[\rho_0] | \Psi_a \rangle \ , \tag{4.12}$$

where f_a is the occupation of a single-particle state Ψ_a. The Hamiltonian $H[\rho_0]$ does not consider charge transfer. The second line in Equation (4.11) is the energy from charge fluctuations. It mainly consists of the Coulomb interaction but it also contains contributions of the exchange-correlation energy

$$E_{\text{coul}}[\delta\rho] = \frac{1}{2} \int \int' \left(\frac{\delta^2 E_{\text{XC}}[\rho_0]}{\delta\rho\delta\rho'} + \frac{1}{|r - r'|} \right) \delta\rho\delta\rho' \ . \tag{4.13}$$

The remaining terms are summarized in the repulsive energy

$$E_{\text{rep}} = -\frac{1}{2} \int V_H[\rho_0](r)\rho_0(r) + E_{\text{XC}}[\rho_0] + E_{nn} - \int V_{\text{XC}}[\rho_0](r)\rho_0(r) d^3r \ . \tag{4.14}$$

This repulsive energy can be seen as a practical equivalent to the exchange-correlation energy term from DFT, as it contains complex physics that are approximated by simple functions.[71]

The total energy functional can now be expressed as

$$E[\delta\rho] = E_{\text{BS}}[\delta\rho] + E_{\text{coul}}[\delta\rho] + E_{\text{rep}} \ . \tag{4.15}$$

In this functional, the repulsive energy term can be approximated as sum over pairs of atoms of a repulsive function $V_{\text{rep}}^{IJ}(R)$, which depends only on atomic numbers

$$E_{\text{rep}} = \sum_{I<J} V_{\text{rep}}^{IJ}(R_{IJ}) \ . \tag{4.16}$$

Similarly, the charge fluctuation term (Equation (4.13)) can also be converted into sums over atom pairs IJ and integrations over volumes $\nu_{I,J}$. The resulting terms with $I = J$

$$\frac{1}{2}\Delta q_I^2 \int_{\nu_I} \int_{\nu_I}' \left(\frac{\delta^2 E_{\text{XC}}[\rho_0]}{\delta\rho\delta\rho'} + \frac{1}{|r - r'|} \right) \delta\rho_I \delta\rho_I' \ , \tag{4.17}$$

can be approximated by the Hubbard U, which describes the curvature of the atom energy function upon extra charging $E(\Delta q)$ and which is approximated by $U = IE - EA$, where IE is the ionization energy and EA is the electron affinity. The terms 4.17 with $I = J$ become $\frac{1}{2}U_I \Delta q_I^2$. For the terms with $I \neq J$, the interaction is only electrostatic between the extra atomic populations $\Delta q_{I,J}$,

$$\frac{1}{2}\Delta q_I \Delta q_J \int_{\nu_I}\int_{\nu'_J} \frac{\delta\rho_I(r)\delta\rho'_J(r)}{|r-r'|} dr dr' \ . \tag{4.18}$$

The functions $\delta\rho_I(r)$ can be assumed by a Gaussian profile

$$\delta\rho_I(r) = \frac{1}{(2\pi\sigma_I^2)^{3/2}} \exp\left\{-\frac{r^2}{2\sigma_I^2}\right\} \ , \tag{4.19}$$

with

$$\sigma_I = \frac{\mathrm{FWHM}_I}{\sqrt{8\ln 2}} \ , \tag{4.20}$$

where FWHM_I is the full width at half maximum of the Gaussian profile. With this assumption, the electrostatic interaction term 4.18 becomes an expression that can be calculated analytically

$$\int_{\nu}\int_{\nu'} \frac{(\delta\rho_I)(\delta'\rho_J)}{|r-r'|} = \frac{\mathrm{erf}(C_{IJ}R_{IJ})}{R_{IJ}} \equiv \gamma_{IJ}(R_{IJ}) \ , \tag{4.21}$$

where

$$C_{IJ} = \sqrt{\frac{4\ln 2}{(\mathrm{FWHM}_I^2 + \mathrm{FWHM}_J^2)}} \ . \tag{4.22}$$

Overall, the charge fluctuation interaction can be written as

$$E_{coul} = \frac{1}{2}\sum_{IJ} \gamma_{IJ}(R_{IJ})\Delta q_I \Delta q_J \ , \tag{4.23}$$

where $\gamma_{IJ}(R_{IJ})$ adapts a form of

$$\gamma_{IJ}(R_{IJ}) = \begin{cases} U_I & \text{for } I = J \\ \frac{\mathrm{erf}(C_{IJ}R_{IJ})}{R_{IJ}} & \text{for } I \neq J \ . \end{cases} \tag{4.24}$$

Finally, the band structure energy is simplified by considering only valence electrons. A minimal local basis ϕ_μ can be used to express the molecular orbitals,

$$\Psi_a(r) = \sum_\mu c_\mu^a \phi_\mu(r) \ , \tag{4.25}$$

where minimal means that only one radial function for each angular momentum quantum number is used. With this, the band structure energy becomes

$$E_{BS} = \sum_a f_a \sum_{\mu\nu} c_\mu^{a*} c_\nu^a H_{\mu\nu}^0 \ , \tag{4.26}$$

where the matrix elements $H^0_{\mu\nu} = \langle\phi_\mu| H^0 |\phi_\nu\rangle$ are parameters of the DFTB method.

The final energy expression becomes

$$E_{\text{DFTB}} = \sum_a f_a \sum_{\mu\nu} c_\mu^{a*} c_\nu^a H^0_{\mu\nu} + \frac{1}{2}\sum_{IJ} \gamma_{IJ}(R_{IJ})\Delta q_I \Delta q_J + \sum_{I<J} V^{IJ}_{\text{rep}}(R_{IJ}) \ . \tag{4.27}$$

Parameters such as the repulsive functions $V^{IJ}_{\text{rep}}(R_{IJ})$ are derived by fitting to data obtained from theoretical calculations, in this case DFT. Specifically for the repulsive function, the derivative of the repulsion is optimized to ensure that it closely aligns with the forces calculated from DFT.

By fitting parameters to various sets of structural data, distinct parameter sets were generated. The main parameter sets that are currently available are the *mio* set[72] (for biological and organic molecules), the *matsci* set[73] (for various materials science problems), the *3ob* set[74] (improved set for DFTB3, an extension of the DFTB method that includes third-order terms in the expansion of the DFT total energy[75]), and the *pbc* set[76] (improved set for periodic boundary calculations, especially involving silicon clusters). In this thesis, we use the *Auorg* set[72, 77, 78], which was explicitly parameterized for gold-thiolate compounds, making it suitable for investigated properties of cross-linked GNP assemblies.

4.3 Molecular Dynamics Simulations

Molecular Dynamics (MD) simulations are a technique for studying time-dependent properties of interacting particles, such as atoms, molecules or larger coarse-grained particles, by solving classical equations of motion (even though variants that consider quantum effects, such as path integral MD,[79] are being developed). The field started in the 1950s with simulations of the motion of hard spherical particles within a periodic box.[80] Since then, the popularity of these methods has grown significantly, along with the complexity of the investigated systems.[81] Today, MD simulations provide insights into a wide range of research questions. In particular they are used in computational biology for studying protein folding and ligand binding, enhancing our understanding of processes in nature and within the human body.[81–84] Beyond biological studies, MD simulations are also applied to investigate chemical reactions,[85–88] single nanoparticles,[89–92] and the dynamics of nanoparticle assemblies,[93–98] among other fields.

In principle, MD simulations work by solving Newton's equations of motion for all particles by numerical integration

$$m_i \frac{\partial^2 \vec{r}_i}{\partial t^2} = \vec{F}_i \ , \tag{4.28}$$

where m_i is the mass of the particle i, r_i its current position, and F_i the force acting on the particle. The force can be derived from the gradient of the potential energy U

$$\vec{F}_i = -\frac{\partial U(\vec{r}_1, \vec{r}_2, ..., \vec{r}_N)}{\partial \vec{r}_i} \ . \tag{4.29}$$

A simplified overview of how MD simulations generally operate is shown in Figure 4.3. The process begins by defining the initial velocities, positions, and the timestep. Next, the forces acting on the particles are calculated, followed by the solution of the equations of motion for all particles. Subsequently, the desired physical quantities, such as temperature, pressure, and velocities, are computed. If the final timestep has not yet been reached, the algorithm repeats by recalculating the forces acting on the particles.

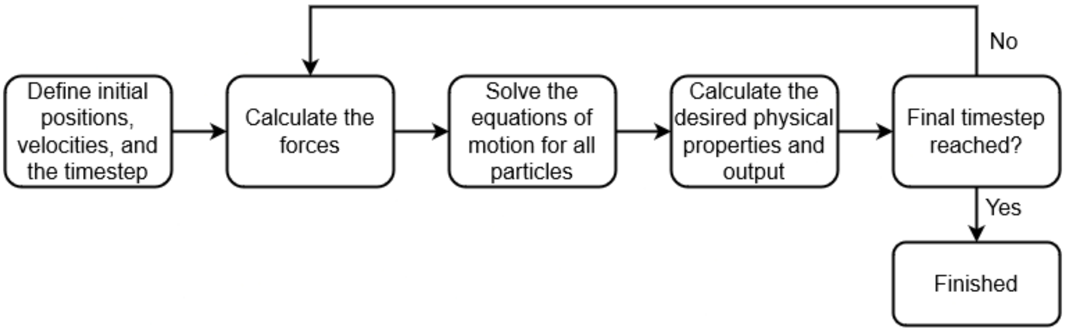

Figure 4.3: Simplified scheme of a standard MD simulation, as described in Ref.[99].

To calculate the forces acting on the particles, different methods have been developed. Besides classical force fields, there are methods that include quantum mechanical electronic structure calculations (e.g. Born–Oppenheimer MD[56] and related methods like Car–Parrinello MD[100]). Additionally, there are hybrid approaches that combine quantum mechanics and molecular mechanics, known as QM/MM MD, which were acknowledged with the Nobel Prize in Chemistry in 2013.[101]. Although, methods that include quantum mechanical approaches can be more accurate than classical force fields, they require higher computational costs compared to the classical approaches,[56] or methods that use the aid of machine learning (see studies by Behler et al.[59, 60]). High computational costs, or an unfeasible scaling with system size, is especially problematic when investigating large systems that consist of many atoms (e.g. ligand-stabilized GNPs or metal surfaces). As these are the systems of interest in this thesis, we will focus on classical force fields in the following section.

4.3.1 Classical Force Fields

Many commonly used force fields (such as UFF,[102] MM3,[103] CHARMM,[104] or AMBER[105]) sum contributions of forces related to the chemical bonds, bond angles, dihedral angles, non-bonded forces associated with van der Waals interactions, and electrostatic interactions. The resulting energy functionals typically have the form

$$E = E_{\text{nobond}} + E_{\text{bond}} + E_{\text{angle}} + E_{\text{dihedral}} + E_{\text{improper}} + E_{\text{elec}} \ . \tag{4.30}$$

Van der Waals interactions E_{nobond} are commonly modeled by a Lennard-Jones-6-12 potential[106]

$$E_{\text{LJ}} = 4\epsilon \left[\left(\frac{\sigma}{r}\right)^{12} - \left(\frac{\sigma}{r}\right)^{6} \right] \ , \tag{4.31}$$

where ϵ is the depth of the potential well, σ is the distance at which the interatom potential is zero, and r is the interatomic distance; or by a Morse potential[107]

$$E_{\text{M}} = D_M \left[1 - e^{-\alpha(r-R)}\right]^2 \ , \tag{4.32}$$

where D_M is the dissociation energy, R is the distance at which the potential energy curve has its minimum, and a is a constant that determines the curvature of the potential energy curve.

The simplest way to describe the interaction between two bonded atoms is by a parabola,

$$E_{\text{bond}} = k_b(r - r_0)^2 \ , \tag{4.33}$$

where k_b is the stiffness of a bond and r_0 is the equilibrium bond distance. The potential energy contribution from the angles in a molecules often has the form[99]

$$E_{\text{angle}} = k_a(\theta - \theta_0)^2 \ , \tag{4.34}$$

where k_a describes the stiffness of the bond angle, and θ and θ_0 are the bond angle and the equilibrium angle. The dihedral interaction, also known as torsion interaction, is described by a cosign function

$$E_{\text{dihedral}} = k_d[1 + cos(n\phi - \gamma)] \ , \tag{4.35}$$

where ϕ is the dihedral angle, γ represents the equilibrium angle, k_d is the force constant, and n gives the number of minima in the function as the bond is rotated by 360°. The improper torsion describes the torsion when the involved atoms are out-of-plane. It is commonly modeled by the function

$$E_{\text{improper}} = k_i(\psi - \psi_0)^2 \ , \tag{4.36}$$

where k_i is the improper torsion force constant, and ψ and ψ_0 are the improper torsion angle and its equilibrium value. Finally, the electrostatic interaction of an atom pair is usually given by a Coulomb interaction term

$$E_{\text{elec}} = \frac{Cq_iq_j}{r} \ , \tag{4.37}$$

where C is the Coulomb's constant and q_i and q_j are the charges of the two atoms. These Coulomb interactions are long-ranged which can cause artifacts in simulations with periodic boundary conditions (PBCs, see Section 4.3.4).[108]

4.3.2 Reactive Force Fields

While classical force fields perform well in scenarios where the binding situation within a structure is relatively well-defined and stable, they often struggle to accurately depict processes involving bond formations or dissociations, e.g. during chemical reactions. To address this limitation, reactive force fields (ReaxFFs) were developed. The foundation of ReaxFF was laid in the early 2000s by van Duin and his collaborators, who created a ReaxFF model for hydrocarbons. For describing chemical reactions, the bond order is included in the ReaxFF potential.[51] Consequently, ReaxFF incorporates additional energy contributions into the overall energy of the system, compared to classical force fields,

$$E = E_{\text{bond}} + E_{\text{over}} + E_{\text{under}} + E_{\text{val}} + E_{\text{pen}} + E_{\text{tors}} + E_{\text{conj}} + E_{\text{vdWaals}} + E_{\text{Coulomb}} \ . \tag{4.38}$$

Before examining the different energy contributions in Equation (4.38), we will look into how the bond order is represented in the ReaxFF framework. In ReaxFF, it is assumed that the bond order BO'_{ij} is directly related to the interatomic distance r_{ij} between two atoms. Thus, it can be expressed as

$$BO'_{ij} = \exp\left[p_{\text{bo},1} \cdot \left(\frac{r_{ij}}{r_0}\right)^{p_{\text{bo},2}}\right] + \exp\left[p_{\text{bo},3} \cdot \left(\frac{r^{\pi}_{ij}}{r_0}\right)^{p_{\text{bo},4}}\right] + \exp\left[p_{\text{bo},5} \cdot \left(\frac{r^{\pi\pi}_{ij}}{r_0}\right)^{p_{\text{bo},6}}\right] \ , \tag{4.39}$$

where r_0 is a parameter for the equilibrium bond radius of a certain atom. The parameters $p_{\mathrm{bo,x}}$ are specific to each atom type and are designed to accurately describe the relationship between bond order and interatomic distance r_{ij}. For example, in a C—C bond, the parameters for the first term, which represents a σ bond, are calibrated such that the term equals 1 when the interatomic distance is below approximately 1.5 Å, while it becomes negligible when r_{ij} exceeds 2.5 Å. The second term, which describes the first π bond, is parameterized to be 1 at distances below approximately 1.2 Å and to be negligible at approximately 1.75 Å. Finally, the third term, corresponding to the second π bond, is set to be 1 at a distance of about 1.0 Å and to be negligible when the distance exceeds approximately 1.4 Å for a C—C bond.[51] Thus, when the C—C distance is, for example, 1.0 Å, the bond order is approximately 3, indicating the presence of a triple bond.

For certain molecules, this description of the bond order can result in overcoordination, for example, when the C—C bond distance in an ethane molecule is reduced artificially from its equilibrium value of 1.53 Å to 1.0 Å, while keeping the rest of the geometry fixed. The resulting bond order exceeds the valence (4 for each carbon and 1 for each hydrogen atom). Therefore the bond order BO'_{ij} is corrected by taking into account the valence of each atom to give BO_{ij} (for a full description of the corrected bond order term see Ref.[51]).

Now that we have a general idea about the bond order in the ReaxFF, we can turn our attention back to the energy contributions in the ReaxFF overall energy description. The first term in Equation (4.38) is the bond energy E_{bond}, which also depends on the bond order

$$E_{\mathrm{bond}} = -D_e \cdot \mathrm{BO}_{ij} \cdot \exp\left[p_{be,1}(1 - \mathrm{BO}_{ij}^{p_{be,1}})\right] \ , \tag{4.40}$$

where D_e is the dissociation energy for a certain atom pair, and $p_{\mathrm{be},1}$ is an atom-specific parameter.

Even after the correction of the original bond order BO'_{ij}, some overcoordination or undercoordination can still exist in the molecule. To handle these cases, an energy term for overcoordinated systems E_{over} is added, which imposes an energy penalty on the system when an atom is overcoordinated, implying that the sum of bond orders is above the sum of valencies Val_i of a system

$$\Delta_i = \sum_{j=1}^{n_{\mathrm{bond}}} BO'_{ij} - \mathrm{Val}_i \ . \tag{4.41}$$

For undercoordinated atoms ($\mathrm{Val}_i < 0$), a correction term E_{under} is added, which takes into account the energy contribution that comes from the resonance of the π-electrons between two undercoordinated atoms.

The valence angle energy E_{val} is described through the deviation of the valence angle Θ_{ijk} from its equilibrium value Θ_0. Several additional terms $f_x(BO_{ij})$ are introduced to make sure that the valence angle energy goes to zero when the bond orders from the atoms in the valence angle go to zero. The $f_7(BO_{ij})$ term, for example, is responsible for the smooth disappearance of the valence energy contribution when a bond dissociates

$$E_{\mathrm{val}} = f_7(BO_{ij}) \cdot f_7(BO_{jk}) \cdot f_8(\Delta_j) \cdot (k_a - k_a \exp\left[-k_b(\Theta_0 - \Theta_{ijk})^2\right]) \tag{4.42}$$

Similarly, the torsion angle energy term E_{tors} is also chosen such that it depends on the bond order. For conjugated systems such as benzene or other aromatics, the developers of the ReaxFF for hydrocarbons introduced an additional term E_{conj}, which has its maximum contribution when successive bonds have a bond order of 1.5.

As non-bonded contributions, the energy from van der Waals interactions E_{vdWaals} and the Coulomb energy E_{Coulomb} are added. In the ReaxFF by van Duin et al., the van der Waals interactions are modeled by a distance-corrected Morse potential.

Compared to semiemperical PM3 electronic structure calculations, this ReaxFF reached similar accuracy for the description of stability and geometry of hydrocarbon structures, while requiring 100 times less calculation time.[51]

In the systems explored in this thesis, applying a ReaxFF offers significant advantages over a non-reactive one, particularly in accurately describing the association and dissociation of ligands, which directly relates to changes in bond order. However, the ReaxFF specifically designed for hydrocarbons cannot be applied to the systems of interest in this thesis, as the ReaxFF parameters are limited to structures that consist solely of carbon and hydrogen atoms. For simulating gold-alkanethiol systems, the same research group developed another force field parameterized based on B3LYP reference calculations.[52] This ReaxFF uses a somewhat simplified energy description compared to the ReaxFF developed for hydrocarbons (see Equation (4.38)). Notably, it does not include a term for conjugated bonds. The energy expression is given by

$$E = E_{\text{bond}} + E_{\text{over}} + E_{\text{under}} + E_{\text{val}} + E_{\text{tors}} E_{\text{vdWaals}} + E_{\text{Coulomb}} \ . \tag{4.43}$$

Bae and Aikens identified considerable shortcomings in this force field, such as its inability to accurately model linear or nearly linear S—Au—S "staple" motifs. This limitation motivated them to reparameterize the ReaxFF for gold-alkanethiolate systems using DFT calculations with a PBE functional.[109]

4.3.3 Velocity Verlet Algorithm

The next step after the calculation of the forces with the help of a force field is to solve the equations of motions for all particles. Due to the complexity of the equations of motion for any system of practical interest, they cannot be solved analytically. Instead, they are usually solved numerically using finite-difference methods, for example, the Verlet, Leapfrog, Velocity Verlet, Beeman, and predictor-corrector algorithms.[99] Among these algorithms, the Velocity Verlet algorithm is a computationally efficient and stable approach that simultaneously calculates atomic positions and velocities,[99] making it attractive for molecular dynamics simulators such as the Large-scale Atomic/Molecular Massively Parallel Simulator (LAMMPS). The velocity Verlet algorithm works as follows:[99]

1. The acceleration $a(t)$ is calculated at time t and position $R(t)$ of the atoms/particles:

$$a(t) = \frac{\partial^2 R(t)}{\partial t^2} \tag{4.44}$$

2. The particle position is calculated for the following time step $t + \delta t$:

$$R(t + \delta t) = R(t) + \delta t \cdot v(t) + \frac{1}{2} \delta t \cdot a(t) \tag{4.45}$$

3. The velocities v are calculated at mid-step $t + \frac{1}{2}\delta t$:

$$v(t + \frac{1}{2}\delta t) = v(t) + \frac{1}{2} \delta t \cdot a(t) \tag{4.46}$$

4. The acceleration at the following time step is calculated:

$$a(t + \delta t) = \frac{\partial^2 R(t + \delta t)}{\partial t^2} \tag{4.47}$$

5. The velocity move is completed:

$$v(t + \delta t) = v(t + \frac{1}{2}\delta t) + \frac{1}{2}\delta t \cdot a(t + \delta t) \tag{4.48}$$

4.3.4 Periodic Boundary Conditions

Before initiating a MD simulation, it is essential to define the boundary conditions of the system. There are two main types of boundary conditions: isolated boundary conditions and periodic boundary conditions (PBCs). The isolated boundary condition is commonly used for studying isolated molecules or small clusters, while PBCs are employed to approximate larger systems, such as bulk gold surfaces. Instead of simulating a large system, e.g. an extended surface, which would be computationally demanding, a smaller section of the system (unit cell) that is periodically replicated can be simulated. This approach allows the system to behave as though it is infinite in size, effectively eliminating edge effects.[99]

When PBCs are implemented, the particles (or atoms) within a unit cell are enclosed in a box that is translated in all Cartesian directions to create replicas. In a two-dimensional example, as shown in Figure 4.4, the unit cell is surrounded by eight identical replicas. These replicas copy the positions of the particles and their velocities and forces. When a particle leaves the simulation cell, it is replaced by a copy of itself with the same velocity, entering from the opposite side of the unit cell. This mechanism ensures that the total number of particles within the simulation remains constant.

To prevent interactions between a particle and its copy in an neighboring box, which can lead to non-physical dynamics, a cutoff radius R_{cut} is typically defined. Forces are then only computed between particles within this cutoff radius.

In certain scenarios, such as when simulating thin surfaces, the structural periodicity may only extend in two dimensions (i.e., along the surface). Then it can be better to apply periodic boundary conditions in only two dimensions (semi-periodic boundary conditions). As this option is not supported by all simulation programs, alternatively, one can apply full PBCs while including a sufficiently thick vacuum layer in the third dimension.

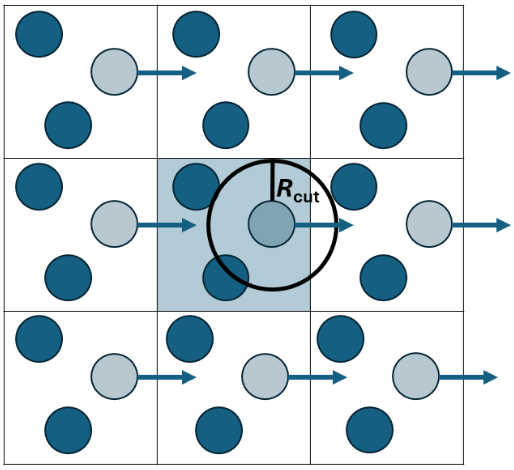

Figure 4.4: Illustration of periodic boundary conditions in two dimensions. The central box represents the simulation box or unit cell, which is surrounded by perfect replicas. When a particle leaves the unit cell (as indicated by the arrow), it is replaced by an identical particle from the replica cell from the opposite site. R_{cut} is the cutoff radius.

4.4 Charge Transport through Molecules

In macroscopic systems such as metallic wires, the charge transport can be accurately described by the well-known equation

$$\frac{dI}{dV} = \frac{1}{R} = G = \sigma \frac{S}{L} \,, \tag{4.49}$$

which represents Ohm's law. In this equation, the conductance G increases linearly with the transverse area S and decreases inversely with the length L of the sample. The conductivity σ is a material-specific property that characterizes how easily current can flow through the sample. However, as systems become smaller and approach the nanoscale, traditional concepts like Ohm's law cannot be applied anymore, as quantum effects start to dominate the behavior of these systems. This is especially the case when the system's width is comparable to or even smaller than the Fermi wavelength.[110]

In nanoscale systems, different types of charge transport can occur, depending on the scattering mechanism in the system. A very important distinction is between coherent and incoherent transport. Coherent transport retains the phase information of the electron wave function throughout the transport. On the other hand, this coherence can be lost by scattering processes, such as electron-electron or electron-phonon interactions, resulting in incoherent transport.

Coherent transport dominates when the time required for electrons to cross the device is shorter than the time needed for interactions with other electrons or for the excitation of vibrational modes.[111] As a result, longer molecular structures more frequently exhibit incoherent transport. In cases where the inelastic scattering time is much shorter than the time it takes for an electron to tunnel through the device, transport can be described as electrons hopping sequentially from one part of the molecule to the next via thermally activated tunneling events (see Figure 4.5). During this process, the quantum coherence is lost.[110] In addition to the length of the molecular structures, the temperature also has an influence on the type of transport dominant in a structure. High temperatures typically enhance the probability of hopping transport.[111]

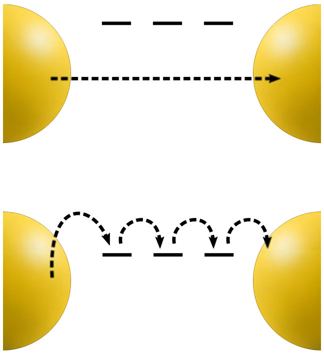

Figure 4.5: Coherent tunneling (top) and hopping (bottom) transport of electrons from the right electrode to the left electrode.

As described in the Introduction, the charge transport in assemblies of alkanethiol-stabilized GNPs is typically described by thermally activated tunneling through the alkanethiol ligands.[16] Research by Parthasarath et al.[112] has demonstrated that the height of the tunneling barrier, coming from the alkanethiol ligands, is too high for electrons to effectively hop across, and the ligands do not introduce any additional states into the barrier. This supports the tunneling picture at least for alkanethiol ligands with up to 12 carbon units, as investigated by the authors. Consequently, this section will concentrate on how coherent tunneling in nanoscale devices can be described.

4.4.1 Landauer–Büttiker Approach

Coherent tunneling in mesoscale systems can be described by the Landauer–Büttiker (LB) approach. This approach goes back to the 1950s, where Rolf Landauer[113] showed that the transport properties can be described by a scattering approach, thereby connecting the conductance G to the sum of all available transmission channels T_n of a system,

$$G = \frac{2e^2}{h} \sum_n T_n \left(E_F, V = 0\right) \ , \tag{4.50}$$

where e is the elementary charge and h is the Planck constant. The factor $\frac{2e^2}{h}$ in the so-called “Landauer formula” represents one quantum unit of conductance G_0. The factor of 2 accounts for spin degeneracy in the system. However, when the transmission channels for different spins are considered separately, as discussed in Section 6.4, this factor of 2 is removed and the sum over n runs over all channels of both spins.[110]

In typical transport experiments on nanoscale devices, the sample or molecule in the central or scattering region is connected to leads or electrodes (see Figure 4.6). In the LB picture, the electrodes act as ideal electron reservoirs in thermal equilibrium. Phase-coherence is preserved on the sample and inelastic scattering is only allowed on the electrodes.[110]

Following Ref. [110], for simplicity, a one-dimensional potential barrier is considered (see Figure 4.7), which represents the central part of the device. At this potential barrier, electrons are elastically scattered before reaching one of the electrodes. When a plane wave, $\left(1/\sqrt{L}\right) e^{ikx}$ (where L is the length of the system), arrives at the potential barrier from the left, it is partially reflected and partially transmitted with a probability $T = |t|^2$. The electrical current density J_k of an electron, represented by this wave, can be described by the quantum-mechanical expression

$$J_k = \frac{e\hbar}{2mi} \left[\Psi^*(x)\frac{d\Psi}{dx} - \Psi(x)\frac{d\Psi^*}{dx}\right] = \frac{e}{L} v(k) T(k) \ , \tag{4.51}$$

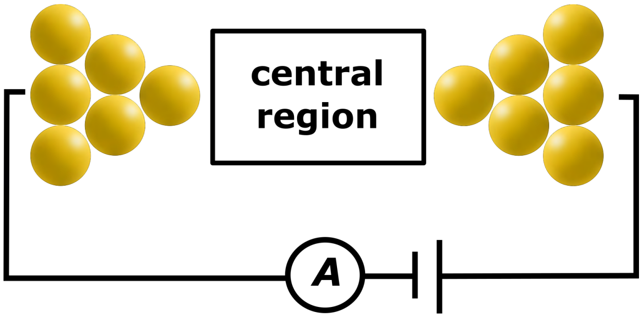

Figure 4.6: Illustration of a typical nanoscale device, consisting of two electrodes and a central/scattering region containing the sample (e.g., a single molecule and usually parts of the contact region).

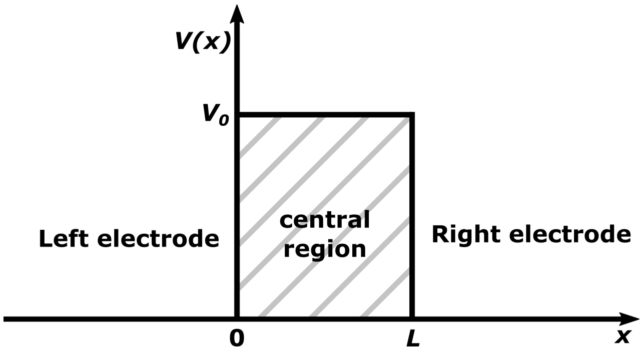

Figure 4.7: Simplified picture of a nanoscopic device. The central region is described as a single potential barrier with height V_0 and width L, where the electrons are elastically scattered before reaching one of the electrodes.

where $v(k) = \hbar k/m$ is the group velocity. In a real device, more than one electron is contributing to the current, therefore, a sum over k is introduced. Furthermore, the Pauli principle needs to be taken into account by introducing a factor $f_L(k)[1 - f_R(k)]$, where f_L and f_R are the Fermi functions of the left (L) and the right (R) electron reservoir. Hence, the current flowing from left to right $J_{L\to R}$ can be described as

$$\begin{aligned} J_{L\to R} &= \frac{e}{L}\sum_k v(k)T(k)f_L(k)[1 - f_R(k)] \\ &= \frac{e}{2\pi}\int dkv(k)T(k)f_L(k)[1 - f_R(k)] \;. \end{aligned} \tag{4.52}$$

The variable k can be replaced by the energy E by introducing the density of states, under the assumption that the conduction electrons can be described by a non-interacting electron gas, $dk/dE = (dE/dk)^{-1} = m/(\hbar^2 k)$ with $E = \hbar^2k^2/(2m)$. This way, the group velocity and the density of states cancel each other out, giving

$$J_{L\to R} = \frac{e}{h}\int dET(E)f_L(E)[1 - f_R(E)] \;, \tag{4.53}$$

and an analogous term for the current flow from the right to the left electrode $J_{R\to L}$. In the one-dimensional situation, the total current can then be calculated by

$$I(V) = J_{L\to R} - J_{R\to L} = \frac{2e}{h}\int_{-\infty}^{+\infty} dET(E,V)[f_L(E) - f_R(E)] \;. \tag{4.54}$$

The Fermi functions f_L and f_R are defined by

$$f_\alpha = \frac{1}{1 + e^{(E-\mu_\alpha)/k_B T}} \ , \tag{4.55}$$

where α is either L or R, and $\mu_{L,R} = \mu \pm eV/2$, with μ being the equilibrium chemical potential of the system.

At low temperatures, the Fermi functions are step functions, equal to 1 below $E_F + eV/2$ and $E_F - eV/2$, respectively, and equal to 0 above this energy.[110] At low voltages, inside the linear regime, $I = GV$ applies, giving the expression for the conductance

$$G = \frac{2e^2}{h} T(E_F, V = 0) \ , \tag{4.56}$$

where $T(E_F, V = 0)$ is the zero-bias transmission at the Fermi energy.

A slightly more accurate description of nanoscopic devices, compared to the simplified approximation shown in Figure 4.7, is a potential containing two barriers.[110] In Figure 4.6 each connection between one of the leads and the central region is then represented by a potential barrier. In a simple case, these barriers have the same height V_0 and the same width L. The total transmission of such a system can be calculated by

$$T_{12} = |t_{1,2}|^2 = \frac{T_1 T_2}{1 + R_1 R_2 - 2\sqrt{R_1 R_2} cos(2\Theta)} \ , \tag{4.57}$$

where $T_{1,2}$ are the transmission probabilities for the wave to be transmitted through the first or the second barrier, i.e. into or out of the sample region. $R_{1,2}$ are the respective reflection probabilities, and Θ denotes the phase shift, the wave gained by passing the sample region.

Transmission probabilities close to resonance ($\Theta \approx n\pi$ and $E \approx \epsilon_n = (hn\pi)^2/(2md^2)$) can be described by the Breit-Wigner formula[114]

$$T_{12} = \frac{\Gamma_1 \Gamma_2}{(E - \epsilon_0)^2 + (\Gamma_1 + \Gamma_2)^2/4} \ , \tag{4.58}$$

where ϵ_0 is the position of the energy of the resonance, and $\Gamma_i = T_B/2(d\Theta/dE)|_{E=\epsilon_0}$, with T_B being the transmission through one of the barriers at $E = \epsilon_0$. From Equation (4.58) we can learn that the transmission close to resonant conditions has a Lorentzian shape with its maximum lying at 1.[110]

4.4.2 Non-Equilibrium Green's Function Approach

Having outlined the fundamental concepts of coherent tunneling in simplified nanoscopic devices, we will now shift our focus to the description of elastic transmission in real systems. To derive an expression for coherent tunneling transmission using quantum mechanics, Green's functions can be used. This Green's function approach is fully equivalent to the Landauer scattering formalism discussed in the previous section; however, it offers the advantage of enabling the calculation of the transmission function through numerical techniques considering an explicit atomistic representation of the system.[115]

The time-independent retarded Green's function operator $\mathbf{G}^r(E)$ for a single-particle Hamiltonian $\mathbf{H}$ is given by

$$[(E + i\eta)\mathbf{I} - \mathbf{H}]\mathbf{G}^r(E) = \mathbf{1} \ , \tag{4.59}$$

or by

$$\mathbf{G}^r(E) = [(E \pm i\eta)\mathbf{1} - \mathbf{H}]^{-1} \ , \tag{4.60}$$

where η is an infinitesimally small number $\eta = 0^\dagger$.

The advanced operator $\mathbf{G}^a(E)$ is related the retarded operator through

$$\mathbf{G}^a(E) = \mathbf{G}^{r\dagger}(E) \ . \tag{4.61}$$

The retarded Green's function operator can also be rewritten such that it depends on the eigenfunctions Ψ_n and the eigenvalues ϵ_n of the single-particle Hamiltonian by using the completeness property $\sum_n |\Psi_n\rangle \langle\Psi_n| = 1$ and $\mathbf{H}|\Psi_n\rangle = \epsilon_n |\Psi_n\rangle$[110, 115]

$$\mathbf{G}^r(E) = \sum_n \frac{|\Psi_n\rangle \langle\Psi_n|}{E - \epsilon_n \pm i\eta} \ . \tag{4.62}$$

For electron transport calculations, the matrix Green's functions method is usually applied.[115] Here, the retarded single-particle Green's function matrix

$$\mathbf{G}^r(E) = \begin{pmatrix} G_{11} & G_{12} & \cdots & G_{1N} \\ G_{21} & G_{22} & \cdots & G_{2N} \\ \cdots & \cdots & \cdots & \cdots \\ G_{N1} & G_{N2} & \cdots & G_{NN} \end{pmatrix} \ , \tag{4.63}$$

can be calculated using Equations 4.59 and 4.60. Although these equations rely on the Green's functions operator, it was shown that they can also be applied using the matrix expression of the single-particle Green's function (see Ref. [110]).

Before looking into more complex systems, we will first consider a simple two-level system, such as a hydrogen molecule, in a tight-binding model, as described in Ref.[110]. In this model, the two hydrogen atoms are coupled to one another via a hopping matrix element t. For this system, the Hamiltonian takes the following form,

$$\mathbf{H} = \begin{pmatrix} \epsilon_0 & t \\ t & \epsilon_0 \end{pmatrix} \ , \tag{4.64}$$

where ϵ_0 are the on-site energies. The inverse of the Green's function matrix is given by

$$\mathbf{G}^{-1}(E) = \begin{pmatrix} E^{r,a} - \epsilon_0 & -t \\ -t & E^{r,a} - \epsilon_0 \end{pmatrix} \ , \tag{4.65}$$

and after inversion,

$$G^r(E) = \frac{1}{(E-\epsilon)^2 - (-t)^2} \begin{pmatrix} E^{r,a} - \epsilon_0 & t \\ t & E^{r,a} - \epsilon_0 \end{pmatrix} \ , \tag{4.66}$$

where $E^{r,a} = E \pm i\eta$, with η is again an infinitesimally small number $\eta = 0^\dagger$.

We will know consider the case where the system of interest is coupled between two electrodes, forming a single-molecule junction, following Ref.[115]. The full effective single-particle Hamiltonian matrix of such a system has the form

$$\mathbf{H} = \begin{pmatrix} \mathbf{H}_{\mathrm{L}} & \mathbf{V}_{\mathrm{LC}} & 0 \\ \mathbf{V}_{\mathrm{CL}} & \mathbf{H}_{\mathrm{C}} & \mathbf{V}_{\mathrm{CR}} \\ 0 & \mathbf{V}_{\mathrm{RC}} & \mathbf{H}_{\mathrm{R}} \end{pmatrix} , \tag{4.67}$$

where $\mathbf{H}_{\mathrm{L}}$, $\mathbf{H}_{\mathrm{C}}$, and $\mathbf{H}_{\mathrm{R}}$ are the Hamiltonian metrices of the left electrode (L), the central region (C), and the right electrode (R) respectively. The off-diagonal matrix elements describe the coupling of the molecules to the electrodes. Direct coupling between the electrodes is neglected. The Hamiltonian matrix is Hermitian, meaning that $\mathbf{V}_{\mathrm{CL}} = \mathbf{V}^{\dagger}_{\mathrm{LC}}$ and $\mathbf{V}_{\mathrm{CR}} = \mathbf{V}^{\dagger}_{\mathrm{RC}}$.

To calculate the current through a junction, we can write the Schrödinger equation $\mathbf{H}\Psi_n = E_n\Psi_n$ in the following form[115, 116]

$$\begin{pmatrix} \mathbf{H}^0_{\mathrm{L}} & \mathbf{V}_{\mathrm{LC}} & 0 \\ \mathbf{V}^{\dagger}_{\mathrm{LC}} & \mathbf{H}^0_{\mathrm{C}} & \mathbf{V}^{\dagger}_{\mathrm{RC}} \\ 0 & \mathbf{V}_{\mathrm{RC}} & \mathbf{H}^0_{\mathrm{R}} \end{pmatrix} \begin{pmatrix} \Psi_{\mathrm{L}} \\ \Psi_{\mathrm{C}} \\ \Psi_{\mathrm{R}} \end{pmatrix} = E \begin{pmatrix} \Psi_{\mathrm{L}} \\ \Psi_{\mathrm{C}} \\ \Psi_{\mathrm{R}} \end{pmatrix} , \tag{4.68}$$

where Ψ_{L}, Ψ_{C}, and Ψ_{R} are vector wave functions of the left electrode, the central region, and the right electrode, respectively. Now we consider that the initial wave that comes in from the left electrode Ψ^0_{L} is scattered, meaning that parts of it are reflected Ψ^1_{L}. Therefore, the left electrode can be described as a sum of the two parts $\Psi_{\mathrm{L}} = \Psi^0_{\mathrm{L}} + \Psi^1_{\mathrm{L}}$, while the right electrode is defined by the transmitted wave. Solving Equation (4.68) with these conditions, gives the *retarded* solutions

$$\Psi_{\mathrm{L}} = \left(1 + \mathbf{G}^{0r}_{\mathrm{L}}\mathbf{V}_{\mathrm{LC}}\mathbf{G}^{r}_{\mathrm{C}}\mathbf{V}^{\dagger}_{\mathrm{LC}}\right)\Psi^0_{\mathrm{L}} , \tag{4.69}$$

$$\Psi_{\mathrm{R}} = \mathbf{G}^{0r}_{\mathrm{R}}\mathbf{V}_{\mathrm{RC}}\mathbf{G}^{r}_{\mathrm{C}}\mathbf{V}^{\dagger}_{\mathrm{LC}}\Psi^0_{\mathrm{L}} , \tag{4.70}$$

$$\Psi_{\mathrm{C}} = \mathbf{G}^{R}_{\mathrm{C}}\mathbf{V}^{\dagger}_{\mathrm{LC}}\Psi^0_{\mathrm{L}} . \tag{4.71}$$

The partial current for a particular eigenstate $\Psi^0_{\mathrm{L}\lambda}$ from the left or right electrode to the system can be described as[115]

$$j_{\mathrm{s=L,R}} = \frac{ie}{\hbar}\left(\Psi^{\dagger}_{\mathrm{s}}\mathbf{V}_{\mathrm{sC}}\Psi_{\mathrm{C}} - \Psi^{\dagger}_{\mathrm{C}}\mathbf{H}^{\dagger}_{\mathrm{sC}}\Psi_{\mathrm{s}}\right) . \tag{4.72}$$

When the expressions for the wave functions are substituted and all partial contributions of the current are summarized, the total current can be calculated, which gives the same current as given by the Landauer formula (see Ref. [116])

$$I = \sum_{\lambda} \frac{e}{\hbar}\left(\Psi^{0\dagger}_{\mathrm{L}\lambda}\mathbf{V}_{\mathrm{LS}}\mathbf{G}^{a}_{\mathrm{C}}\Gamma_{\mathrm{R}}\mathbf{G}^{r}_{\mathrm{C}}\mathbf{H}^{\dagger}_{\mathrm{LS}}\Psi^0_{\mathrm{L}\lambda}\right) f_{\mathrm{L}}(E_\lambda) , \tag{4.73}$$

where the distribution function $f_L(E_\lambda$ describes the population of the left state, while the current flow from the right to the left state is not considered here. Γ_{R} is called the level-width function[115] of the right electrode given by $\Gamma_{\mathrm{R}} = i\left(\sum^r_{\mathrm{R}} - \sum^a_{\mathrm{R}}\right)$, where $\sum_{\mathrm{R}}$ is the self-energy of the right electrode. If one compares the expression in Equation (4.73) with the Landauer equation, when current flow is only allowed from the left to the right electrode, this gives[116]

$$I = \frac{e}{h}\int_{-\infty}^{+\infty} T(E) f_{\mathrm{L}}(E) dE , \tag{4.74}$$

and the transmission function depending on the energy is obtained as[115]

$$
\begin{aligned}
T(E) &= 2\pi \sum_{\lambda} \delta(E - E_{\lambda}) \left(\Psi^{0\dagger}_{\mathrm{L}\lambda} \mathbf{V}_{\mathrm{LC}} \mathbf{G}^{\mathrm{a}}_{\mathrm{C}} \Gamma_{\mathrm{R}} \mathbf{G}^{\mathrm{r}}_{\mathrm{C}} \mathbf{V}^{\dagger}_{\mathrm{LC}} \Psi^{0}_{\mathrm{L}\lambda} \right) \\
&= 2\pi \sum_{\lambda} \sum_{\delta} \delta(E - E_{\lambda}) \left(\Psi^{0\dagger}_{\mathrm{L}\lambda} \mathbf{V}_{\mathrm{LC}} \Psi_{\delta} \right) \left(\Psi^{\dagger}_{\delta} \mathbf{G}^{\mathrm{a}}_{\mathrm{C}} \Gamma_{\mathrm{R}} \mathbf{G}^{\mathrm{r}}_{\mathrm{C}} \mathbf{V}^{\dagger}_{\mathrm{LC}} \Psi^{0}_{\mathrm{L}\lambda} \right) \\
&= \sum_{\delta} \left(\Psi^{\dagger}_{\delta} \mathbf{G}^{\mathrm{a}}_{\mathrm{C}} \Gamma_{\mathrm{R}} \mathbf{G}^{\mathrm{r}}_{\mathrm{C}} \mathbf{V}^{\dagger}_{\mathrm{LC}} \left(2\pi \sum_{\delta} \delta(E - E_{\lambda}) \Psi^{0}_{\mathrm{L}\lambda} \Psi^{0\dagger}_{\mathrm{L}\lambda} \right) \mathbf{V}_{\mathrm{LC}} \Psi_{\delta} \right) \\
&= \mathrm{tr} \left(\Gamma_{\mathrm{L}} \mathbf{G}^{a}_{\mathrm{C}} \Gamma_{\mathrm{R}} \mathbf{G}^{r}_{\mathrm{C}} \right) \ .
\end{aligned}
\tag{4.75}
$$

5 Objectives

As described in the Introduction, a model for GNP assemblies is being developed that is fully atomistic and can be used to investigate the charge transport properties of these structures. In order to achieve this, the structural model must be sufficiently small, as excessive size would lead to prohibitively long computational times. Since the charge transport properties are likely dominated by interactions at the interfaces between neighboring particles, it is anticipated that basic features of the films can be accurately described by considering only the interface structures. The “single-interface model” consists of two Au(111) surfaces cross-linked by ADT ligands. Initially, MD simulations using a ReaxFF will be performed to identify the optimal ligand coverage and adsorption positions for ADTs on Au(111) monolayers. Based on these findings, an interface structure will be designed. The preferred surface-to-surface distance will be determined from the intersurface distance at the lowest potential energy of a simulation, where the intersurface distance is changed by pushing the surfaces together. The workflow is summarized in Figure 5.1.

To validate the model, interfaces of ADTs and AMTs with varying alkane chain lengths will be examined, and properties such as intersurface distance and tunneling decay constant will be compared to experimental values reported in the literature. Additionally, different structural features, including ligand coverage and ligand conformation, as summarized in Figure 5.2, will be analyzed to identify their potential influence on the characteristics of GNP film interfaces.

Once the potentials and limitations of the model for simulating pure ADT- or AMT-stabilized GNP assemblies have been investigated, the model will be extended to investigate more complex structures, particularly AMT/ADT mixed-ligand films. In a preliminary study, the energies of different potential configurations of AMT/ADT monolayers will be compared, including homogeneous ligand distributions, striped arrangements, and separations into differently large domains. Reasonable configurations identified in these monolayer simulations will be considered in the subsequent study of mixed-ligand interfaces. By comparing surface-to-surface distances and charge transport properties of potential mixture structures with experimental measurements from the literature and our collaborator Chih-Yin Liu, the most reasonable structures will be identified.

In the next section, analyte molecules will be introduced into the interface model. Initially, the feasibility of analyte molecules, such as alkanes, entering the dense ligand matrix at the interfaces will be examined. This includes the analysis of the diffusion of alkane molecules into self-assembled monolayers, followed by simulations of diffusion into interfaces. Once it has been demonstrated that such diffusion is feasible, analyte molecules will be positioned directly inside the ligand matrix of the interfaces. Changes in intersurface distance and zero-bias conductance upon analyte intercalation will be analyzed and compared to experimental results from the literature.

Finally, the characteristics of the Blatter radical in single-molecule junctions will be explored. Our experimental collaborators have suggested the formation of Blatter radical dimers in scanning tunneling microscope-based break-junction (STM-BJ) measurements, which may explain the magnetoresistive behavior observed in some of these measurements. To investigate this, the stability of such dimers will first be investigated through DFT calculations by analyzing the binding energy. Then, dimer junctions will be constructed, and their exchange-spin coupling constants as well as conductance values will be evaluated.

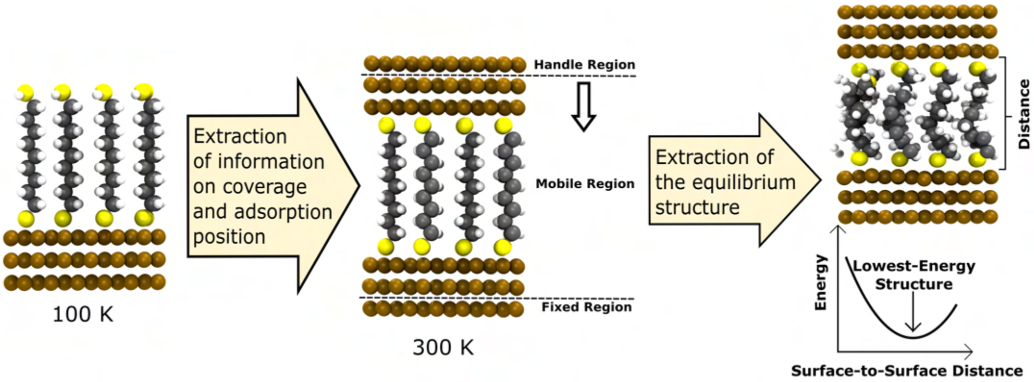

Figure 5.1: Workflow for constructing structures of ADT cross-linked gold surfaces. Hydrogen atoms are removed from the thiol groups of the ligands when positioning them on the gold surfaces. MD simulations are performed to investigate optimal occupation sites, coverages, and tilt angles of the singly deprotonated ADTs on a Au(111) surface. Monolayer simulations are performed at 100 K to prevent unwanted reactions between the ligands due to artifacts in the ReaxFF model (as further discussed in Section 6.1.4). Sandwich simulations are carried out at 300 K, closely resembling experimental conditions. Although the ligands slightly tilt during the SAM simulations, upright-standing ligands are used for constructing the sandwich structures, as cross-linkage with tilted SAM configurations is difficult to establish. The gold surfaces are pushed together, generating a potential energy versus surface-to-surface distance curve, from which the lowest-energy structure at the preferred surface-to-surface distance is extracted. Reprinted with permission from K. Schaefer et al. *J. Phys. Chem. C* 2024, 128, 9, 3994-4008 under an Open Access license.

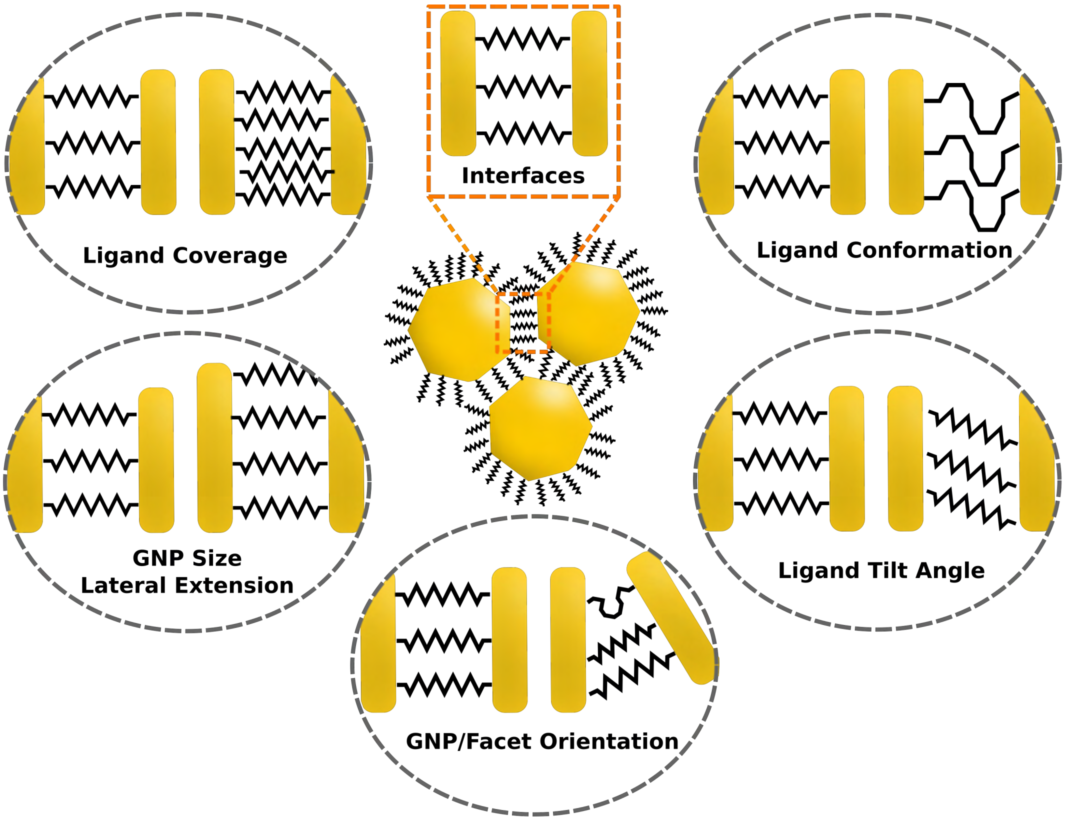

Figure 5.2: Illustration of single particle–particle interfaces of neighboring particles in a GNP film that are simulated as cross-linked flat surfaces (top orange square), together with structural features that can influence the characteristics of the GNP film interfaces (black dashed circles).

6 Results and Discussion

In the first part of this thesis, the particle–particle interface model will be described, beginning with an examination of the structure of self-assembled monolayers consisting of thiol ligands on Au(111) surfaces. This analysis will serve as the foundation for constructing the interfaces. The model will be validated through structural and charge transport properties observed for ADT and AMT ligands.

Next, the interface model will be expanded to include mixtures of ADT and AMT ligands to study the ligand distribution in these systems. Subsequently, analyte molecules will be introduced to the single-interface model to investigate their interactions with the ligand matrix, as well as how these interactions influence properties of the interfaces such as interparticle distance and zero-bias conductance. Finally, a more detailed examination of the transport properties of the Blatter radical within a single-molecule junction will be conducted.

6.1 A Single–Interface Model Validated through the Study of Mono- and Dithiols

The results presented in this Section have already been published in Ref.[117]. All simulations and calculations, data analysis and writing have been performed by the main author of this thesis.

Gaining insights into the atomistic structure of molecule-linked GNP assemblies through analytical methods can be difficult as the molecules themselves are usually not visible in TEM images. Atomic force microscopy (AFM) also provides only limited information, primarily regarding the overall structure of the film, such as its thickness, rather than details about the individual components. To investigate the atomistic features of GNP films that remain mostly inaccessible through experimental techniques, theoretical models can be used.

In this work, both the structural and the charge transport properties of GNP assemblies are investigated. Especially, we were interested also in the explicit interaction of analyte molecules with the ligand matrix. Therefore, a full atomistic description of the atoms was desired. In addition, the system needed to be small enough, such that charge transport calculations on DFTB level were not too computationally demanding. Still, the model should be able to describe basic properties of GNP assemblies, for example, the interparticle distance and the charge transport properties. The model, investigated in this thesis, simplifies the system to the component that is likely to dominate the sensing properties in the assemblies: the interface between the particles. This interface is modeled as two flat, cross-linked gold surfaces (as indicated in Figure 5.2).

But how valid is the approach of using cross-linked flat surfaces as an approximation for the interfaces, according to existing literature? In an early study, Ghorai and Glotzer[91] found that GNPs could exist as either perfect spheres or composed of flat facets, depending on the temperature. They simulated the self-assembly of AMTs on 3 to 11 nm large spherical GNPs, using a united-atom model. Their findings revealed that at higher temperatures (above 450 K), the particles remained in their spherical shape, with the ligands exhibiting a disordered arrangement. Conversely, at lower temperatures (below 450 K), the particles transitioned to structures featuring flat Au(100) and Au(111) facets, where the ligand arrangement resembled that of flat SAMs.

Further insights can be gained from the first conducted simulation of the self-assembly of AMT ligands on gold nanocrystals by Luedtke and Landman[89] in 1996. Their study examined the self-assembly of ligands on these nanocrystals, using united atom models, and compared the results to that on extended, flat gold surfaces. The crystals contained 140 to 568 Au atoms that were arranged in adjoining Au(111) and Au(100) facets. The authors found that ligands adsorbed on the gold surface, forming ordered bundles. However, they noted a distinct difference in ligand arrangement compared to extended, flat SAMs. Specifically, they found that the ligand packing density on the nanocrystals was 30 % higher than that in flat SAMs, with the sulfur-sulfur spacing of the AMT ligands varying from 3.9 to 4.5 Å, depending on the cluster size.

In a subsequent study, Luedtke and Landman[90] investigated larger cluster sizes of 1,289 Au atoms with larger Au(111) and Au(100) facets. For Au(100) facets they found that ligands arranged in a C(2 × 2) pattern, occupying the hollow sites. In contrast, on the Au(111) facets, the ligands formed hexagonal networks, covering both hollow and bridge sites.

Opposed to the simulations conducted by Luedtke and Landman, Djebaili et al.[118] reported less pronounced differences in ligand arrangement on GNPs compared to flat SAMs. In their study, the authors examined the surface area per adsorbed thiol molecule on differently sized icosahedral surfaces using a united atom model. They found that the area per molecule on the 20 Au(111) facets was only about 10 % smaller than that on bulk Au(111) surfaces. With increasing size of the gold cluster, the surface area per thiol molecule approached that of planar surfaces. The authors observed an area of 16 $Å^2$ per thiol on 2 nm large particles, compared to 18 $Å^2$ for 10 nm particles. In contrast, the surface area of flat Au(111) surfaces is around 21.5 $Å^2$ per thiol.

They also demonstrated that when focusing on the center of the facets, the difference in the occupied area was minimal compared to the bulk. The difference in occupied area compared to the bulk at the edges of the facets, on the other hand, were more significant. Here, the surface area per molecule was found to be 16 $Å^2$, compared to 19 $Å^2$ at the center of the facets. These findings suggest that approximating the interface between particles as flat facets is a reasonable approach, especially for larger particles.

6.1.1 Self-Assembly of Alkanedithiolates on Gold Surfaces

Now that literature studies indicate the reasonableness of our approach, we need to understand how thiol ligands assemble on flat gold surfaces. Our focus is on the structure of Au(111) surfaces, as they are the most commonly occurring facets in GNPs, according to Ref [44, 91] among other sources.

6.1.1.1 Ligand Adsorption as Thiol or Thiolate?

A fundamental question that often arises is: how are thiol ligands adsorbed on a gold surface? This topic has been broadly discussed within the scientific community. Currently, a widely accepted theory claims that thiol ligands are chemisorbed to the gold surface, forming a chemical bond between the ligand and the gold. During this bond formation, it is believed that the thiol ligand is converted to its thiolate form, resulting in the release of a hydrogen atom. In vacuum, it is assumed that these hydrogen atoms combine to form H_2,[119–122] while in the presence of oxygen, they may oxidatively convert into water.[123]

Conversely, the Venkataraman group[124] has proposed that thiol ligands may physisorb to the gold surface instead of undergoing chemisorption. Their conductance measurements during molecular break junction experiments in solution indicated that this physisorption occurs without the release of hydrogen. However, they also suggested that when there is an excess of ligand molecules combined with undercoordinated surface atoms, the S–H bond can be cleaved, leading to chemisorption of the ligands.[124] Although high-energy,

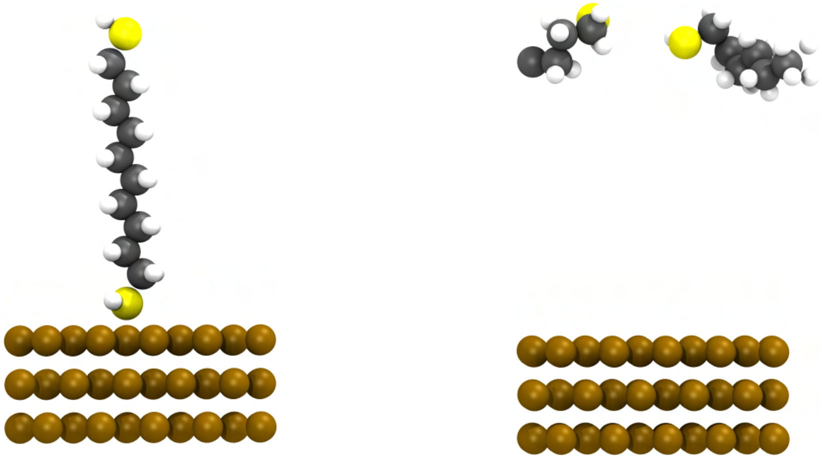

Figure 6.1: Snapshots from a MD simulation of a 10DT ligand adsorbed on an Au(111) surface without removing the hydrogen atom from the thiol group. Initially, the ligand adopts a straight, all-trans conformation (left), but it quickly dissociates from the surface (right). The unit cell is repeated periodically in x and y directions (parallel to the surfaces) under semi-periodic boundary conditions. As a result, the ligands depicted on the right are intact. Reprinted with permission from K. Schaefer et al. *J. Phys. Chem. C* 2024, 128, 9, 3994-4008 under an Open Access license.

undercoordinated gold atoms are rare in Au(111) SAMs,[125] the surface of GNPs may be less perfect, particularly at the edges of facets. Therefore, undercoordinated gold atoms could be present in GNPs, making the formation of thiolates feasible in GNP assemblies, especially when an excess of ligands was present during the formation of the assemblies.

To contribute to this ongoing discussion, MD simulations were performed using a ReaxFF. In these simulations, a single 1,10-decanedithiol (10DT) ligand was placed on a three-layered Au(111) surface consisting of 90 gold atoms. In the first simulation, the hydrogen atom was not removed from the adsorbed thiol group, while in the second simulation, it was removed prior to starting the simulation. The initial structures of both cases are shown below. In the first case, the 10DT ligand moved away from the surface after 5 ps, reaching a distance of over 100 Å after 50 ns (see Figure 6.1). Conversely, in the second case, where the ligand was singly-deprotonated, the ligand remained adsorbed (with an S–Au distance of less than 3 Å) for the majority of the simulation. Throughout the simulation, the ligand transitioned from an upright position to a laying-down position (see Figure 6.2). In the final stages of the simulation, the S–Au bond broke, but the ligand remained in close proximity to the surface.

The observed preference for the adsorption as thiolate rather than as thiol ligand aligns with the widely accepted theory of thiol ligand chemisorption. However, it is important to note that the simulations are based on a force field parameterized for thiolate SAMs, which may introduce bias into our results. Nonetheless, since the adsorption of thiolates was preferred over the thiol form, all following simulations were conducted with the ligands initially adsorbed as thiolates.

6.1.1.2 The Structure of Thiolate Self-Assembled-Monolayers

It has been shown that different arrangements of AMT ligands on Au(111) surfaces are possible, depending on the ligand coverage (see Figure 6.3). At low coverages, ligands tend to lie flat on the surface; however, as the coverage increases, the ligands increasingly adopt more upright conformations.[126] At the optimal coverage on an Au(111) surface (100 %, corresponding to a sulfur-sulfur spacing of ∼ 5.0 Å), the ligands occupy hollow sites in a

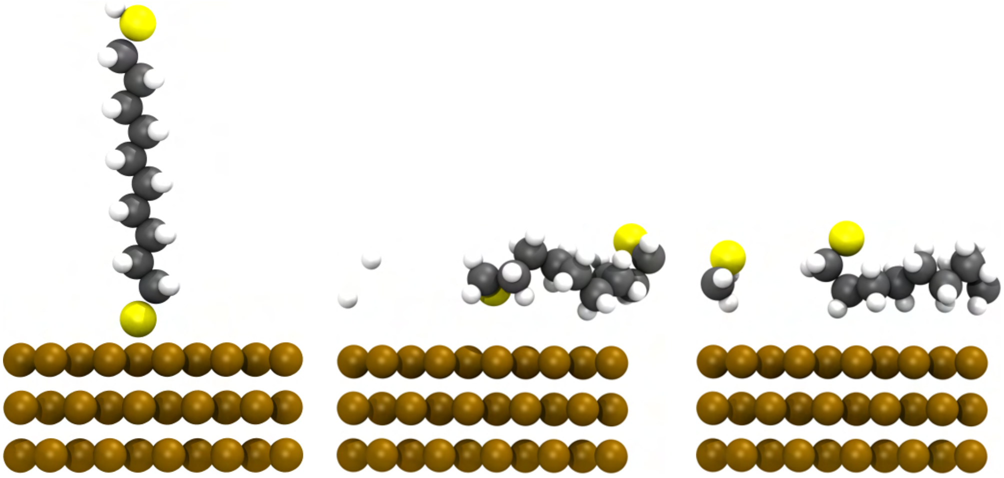

Figure 6.2: Snapshots from a MD simulation of a 10DT ligand adsorbed on an Au(111) surface as a thiolate ligand. Initially, the ligand is in a straight, all-trans conformation (left). As the simulation progresses, it gradually lays down onto the surface (center). In the final stages, the S–Au bond breaks, yet the ligand remains in close proximity to the surface (right). The unit cell is repeated periodically in x and y directions (parallel to the surfaces) under semi-periodic boundary conditions. Therefore, the ligands shown on the right are intact. Reprinted with permission from K. Schaefer et al. *J. Phys. Chem. C* 2024, 128, 9, 3994-4008 under an Open Access license.

$(\sqrt{3} \times \sqrt{3})$ R30° lattice structure (see Figure 6.4).[127] In this arrangement, the ligands tilt uniformly in one direction at an angle of around 30°, which may vary depending on the length of the alkane chain.

Furthermore, the incorporation of functional groups into the tails of alkanethiol ligands can significantly influence the tilt angle due to steric constraints and interactions between the tail groups. Spectroscopic measurements have shown that a hydroxyl tail group, for instance, reduces the tilt angle compared to a methyl tail group. In contrast, ligands with acid tail groups but identical chain lengths exhibited similar tilt angles to those with methyl tail groups (40° for $HS(CH_2)_{15}CH_3$, 38° for $HS(CH_2)_{15}CO_2H$, and 28° for $HS(CH_2)_{15}CH_2OH$).[129]

The tilt angles and overall structure of dithiol ligands on SAMs have been less extensively studied. Either upright alignments of the ligands, where one thiol group is bound to the gold surface while the other points upwards,[130–132] or a lying-down arrangement in which the

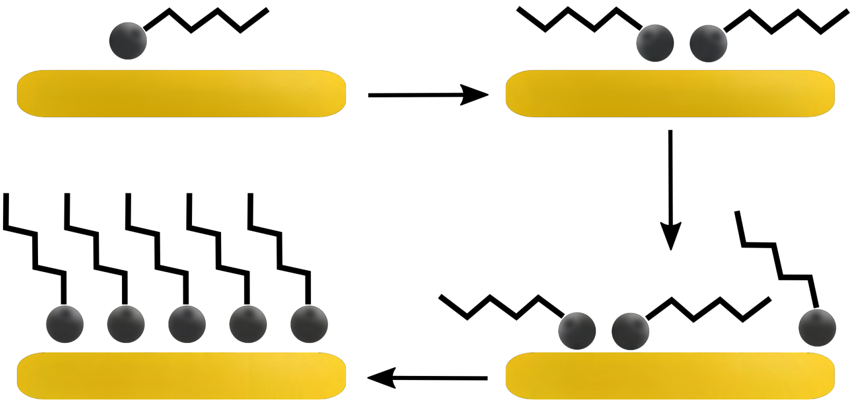

Figure 6.3: Different phases during SAM growth, as described by Poirer.[128]

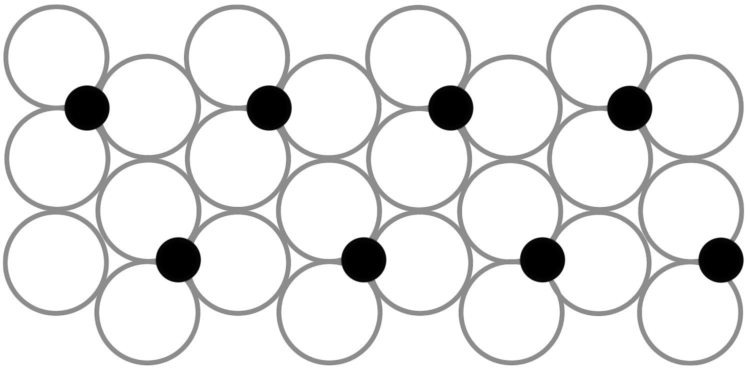

Figure 6.4: Ligand adsorption sites (black circles) on a flat Au(111) surface (gray circles) depicting the $(\sqrt{3} \times \sqrt{3})$ R30° structure, which is frequently observed for AMT ligands.

ligands are parallel to the gold surface have been reported.[133, 134] In addition, ligands may form loops where both thiol groups are attached to the surface. An upright arrangement, however, is expected to be energetically favored.[127] Consequently, the overall structure of ADTs is expected to resemble that of AMTs,[135] though with reduced ordering,[136] and potentially different tilt angles.

6.1.1.3 Ligand Coverages

Using a ReaxFF, we replicated the different arrangements reported for thiolate ligands on gold surfaces (shown in Figure 6.3) with singly-deprotonated ADT ligands. At low coverages (112 Å^2 per molecule, corresponding to 19 % coverage, as shown in Figure 6.5, left), the singly-deprotonated 10DT ligand was completely oriented flat on the surface. In contrast, at medium coverages (56 Å^2 per molecule, representing 39 % coverage, see Figure 6.5, center), an intermediate state was observed in which some ligands remained upright while others lay flat. In this mixed orientation, half of the ligands had dissociated from the surface. At high coverages (21.6 Å^2 per molecule, indicating 100 % coverage, see Figure 6.5, right), all ligands stood upright without any dissociation occurring. The coverage thresholds for these distinct phases align well with experimental observations.[127]

Loop formations, where both thiol groups of a single dithiol ligand attach to the same surface, were not observed in this study. This is in contrast to findings from experiments involving dithiol SAMs[137] and previously conducted MD simulations.[45]

The ligand arrangement at 100 % coverage closely resembled that of the $(\sqrt{3} \times \sqrt{3})$ R30° structure discussed earlier. The unit cell consisted of eight ligands, with an S–S spacing of 4.9 Å between neighboring ligands, consistent with the approximately 5 Å spacing reported in the literature. Furthermore, the S–Au bond distance in the simulations was 2.73 ± 0.02 Å, which aligns with findings from DFT calculations[138, 139] and MD simulations[44, 118] employing a united-atom approach together with Lennard-Jones potentials.

The only difference between the SAM structure occupied with ADT ligands, obtained by MD simulations with ReaxFF, and the reported structure for AMT-capped SAMs was the tilt angle. This will be discussed in the following paragraph.

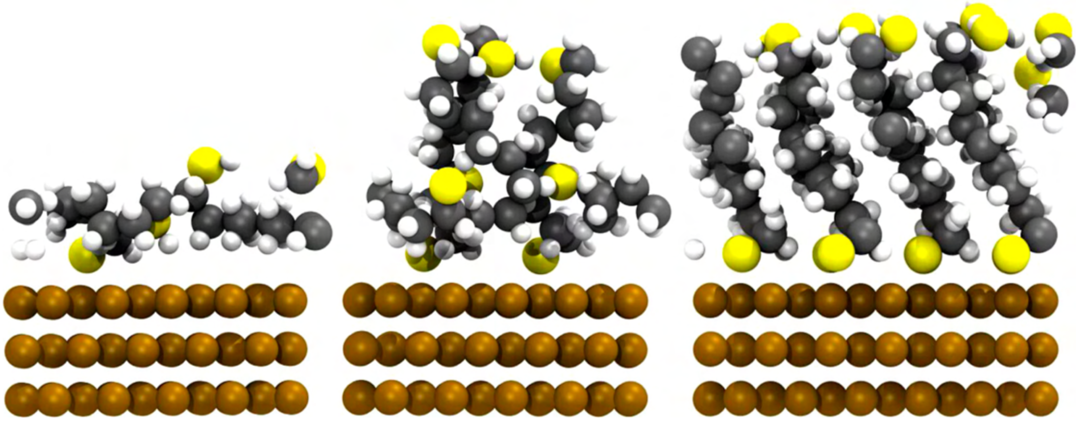

Figure 6.5: Representative structures from MD simulations showing singly-deprotonated 10DT ligands on Au(111) surfaces at low (left), medium (center), and full coverage (right). Specifically, 2, 4, and 8 ligands are adsorbed on the surface in each respective configuration. A clear transition from laying-down to standing-up orientations of the ligands is observed as the coverage increases. At medium coverage, half of the ligands dissociated from the surface, whereas at high coverage, all ligands remained adsorbed. Reprinted with permission from K. Schaefer et al. *J. Phys. Chem. C* 2024, 128, 9, 3994-4008 under an Open Access license.

6.1.1.4 Tilt Angle and Ligand Ordering

Initially, singly-deprotonated 1,9-nonanedithiol (9DT) ligands were positioned upright on the Au(111) surface. Throughout the MD simulation, the ligands tilted slightly. Ordering of the ligands was observed in only some simulations. Tilt angles were determined by measuring the angle between a line connecting the two sulfur atoms of a dithiol molecule and the surface normal (as shown in Figure 6.6). In the simulations involving 9DT ligands, tilt angles ranged from 5° to 24°. Simulations were the ligands were more ordered resulted in higher tilt angles than simulations were the ligands were less ordered. On average, the tilt angle was 16°, which is significantly lower than the approximately 30° tilt angles reported for monothiol SAMs. As noted earlier, the ligand tail group can influence the tilt angle. Functional groups such as hydroxyl groups are known to significantly reduce tilt angles.[129] The simulations suggest that the thiol tail group may have a similar effect.

Interestingly, by increasing the alkane chain length to 10DT, the ligands formed more ordered structures, with an increased frequency of tilting in the same direction. The tilt angles in this case varied from 17° to 26°, with an average of 23°. This finding aligns with the threshold for forming ordered structures reported by Ghorai and Glotzer for AMT ligands using non-ReaxFF models.[91] Furthermore, earlier experimental studies indicated a loss of film organization for shorter AMT monolayers, with the threshold for achieving ordered structures reported at 9 carbon units.[140]

Attempts to force the ligands into a higher tilt angle of 30° were unsuccessful. As shown in Figure 6.7, when beginning with a structure with ligands tilted by 30°, the ligands shifted to a less tilted configuration with an angle of approximately 20°. During this simulation, half of the ligands rapidly dissociated from the surface, demonstrating that the 30° tilted structure was unstable.

The reduced tilt angle observed in comparison to AMT monolayers may be attributed to the polar tail group of the ADT ligands, leading to intermolecular interactions that alter the monolayer structure, as reported before for hydroxy tail groups. Alternatively, this reduction could be an artifact of the applied force field. Since the force field was not explicitly

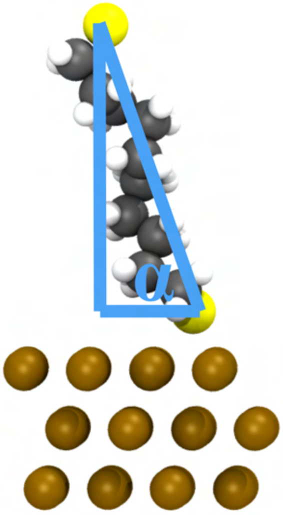

Figure 6.6: Simplified representation of a 10DT self-assembled monolayer unit cell, highlighting a single ligand (with the other seven ligands obscured). The tilt angle α is indicated by the blue lines and is defined as the angle formed between a line connecting the two sulfur atoms and the surface normal. Reprinted with permission from K. Schaefer et al. *J. Phys. Chem. C* 2024, 128, 9, 3994-4008 under an Open Access license.

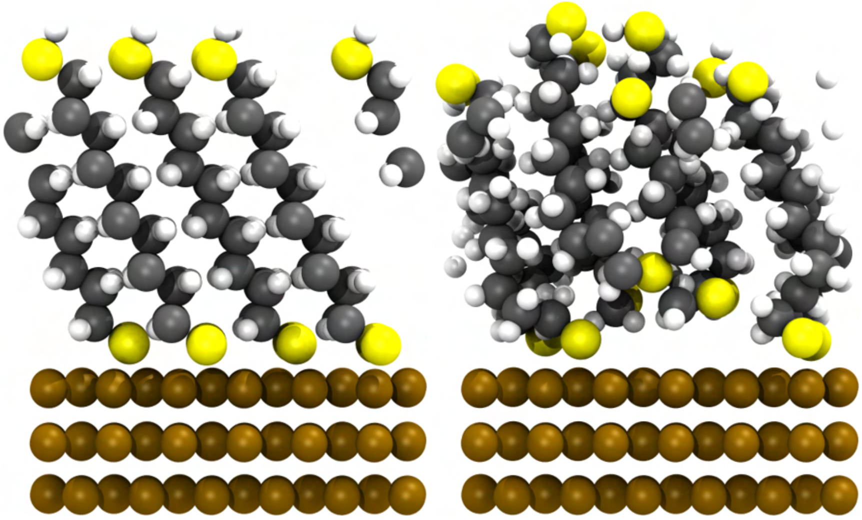

Figure 6.7: Snapshots from MD simulations of 10DT ligands adsorbed on an Au(111) surface, initially tilted in a 30 ° angle (left) with respect to the surface normal. During the simulation, four ligands rapidly dissociated, resulting in a rearrangement where all ligands adopted a less tilted orientation (right). Reprinted with permission from K. Schaefer et al. *J. Phys. Chem. C* 2024, 128, 9, 3994-4008 under an Open Access license.

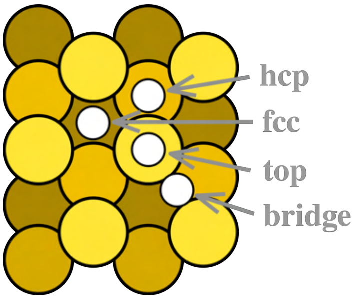

Figure 6.8: Illustration of potential adsorption positions for thiol ligands on Au(111) surfaces. Reprinted with permission from K. Schaefer et al. *J. Phys. Chem. C* 2024, 128, 9, 3994-4008 under an Open Access license.

parameterized for ADT ligands, it is possible that it does not adequately capture the interactions of the tail groups. Further analysis using different methods, such as alternative force fields or DFT, will be necessary to provide more reliable predictions.

6.1.1.5 Adsorption Sites for 10DT Ligands on Au(111) Surfaces

For the eight ligands in the unit cell, various adsorption positions are possible: top, bridge, or hollow sites, with the hollow sites further divided into hexagonal close-packed (hcp) and face-centered cubic (fcc) sites (as shown in Figure 6.8). The average potential energies from MD simulations of 10DT ligands in these adsorption positions are summarized in Table 6.1. Monolayers with ligands adsorbed at fcc hollow sites were slightly more stable than those at hcp hollow sites, with a potential energy difference of $\Delta E_{\text{pot}} = -4.82\,\text{kJ/mol}$. Overall, the following stability trend can be observed: fcc > hcp >> bridge. When all ligands were positioned at the top site, they dissociated from the surface in every simulation, indicating that this adsorption site is the least stable. Ligands initially adsorbed in bridge positions partially moved to the hollow sites, further demonstrating the stability of the hollow site positions.

Table 6.1: Overview of average potential energies for different adsorption sites for eight 10DT ligands on a Au(111) surface.

Position	Number of Simulations	Potential Energy [kJ/mol]
hcp	3	-141053.5 ± 17.9
fcc	5	-141063.1± 52.0
bridge	3	-140983.3 ± 41.8
top	10	all ligands dissociated

These findings align with DFT calculations by Fertitta et al. and Yourdshahyan et al. on methylthiolate adsorbed on Au(111) surfaces, which showed that hollow sites possess the highest adsorption energy, followed by bridge and top sites. In both studies, the fcc hollow site was found to be significantly more stable than the hcp site, with energy differences of $-1.93\,\text{kJ/mol}$ for a single molecule in a (4×4) gold atom unit cell,[141] and $-9.64\,\text{kJ/mol}$ in a (2×2) gold atom unit cell,[142] respectively. The results are also consistent with MD simulations by Luedtke et al., who investigated dodecanethiol on gold nanoclusters. Using a united-atom approach, they demonstrated that ligand molecules predominantly occupy the hollow sites of the Au(111) facets of the clusters, with bridge sites being less frequently used.[90]

In summary, the following insights have been gained onto the structure of ADT monolayers on Au(111) surfaces:

- **Adsorption as Thiolate**: Based on the literature discussion it is likely that ADT are chemisorbed in GNP films. MD simulations, conducted in this work, support this, as ligands only remained adsorbed on the surface in their thiolate form. However, it is important to note that these results may be influenced by the parameterization of the used force field.
- **Ligand Coverage**: With increasing coverage, ADT ligands transition from a laying-down to an upright-standing phase. A fully upright-standing conformation can be obtained with a surface occupation as in the for AMT monolayers commonly reported $(\sqrt{3} \times \sqrt{3})$ R30° structure.
- **Ligand Ordering**: Ligands order (all ligands are upright-standing and tilting in the same direction) only in some MD simulation with 9DT ligands. With a higher chain length (10DT) ordering is more frequently observed. This threshold for forming ordered structures is consistent with literature findings.
- **Tilt Angle**: The observed tilt angle for ADT ligands is lower than the tilt angle observed in AMT monolayers (20° compared to 30°). This may be a result from the polar tail group (SH), but could also result from a faulty description of the tail group interactions by the force field.
- **Preferred Adsorption Site**: The fcc hollow site was found to be the most stable adsorption site. The stability followed the trend: fcc > hcp >> bridge >> top, consistent with findings from the literature.

6.1.2 Model for Dithiol Cross-Linked Particle–Particle Interfaces

With the optimal adsorption sites and monolayer coverages from the SAM simulations, conducted in the previous section, ADT cross-linked surfaces were constructed. Therefore, ligands were initially placed in between the surfaces in a straight, all-trans conformation (see Structure 1 in Figure 6.9). By reducing the distance between to surfaces, as described in Section 8.1, the potential energy of the structures is reduced. The MD snapshots shown below illustrate how the ligands go from the straight, all-trans starting conformation into gauche conformations, until in the lowest-energy structure, no all-trans linkers can be observed.

6.1.2.1 Evaluation of the Model Through Interparticle Distances and Charge Transport Calculations

Pushing simulations were performed with ADTs ranging from 1,6-hexanedithiol (6DT) to 10DT, and average intersurface distances were extracted from the lowest-energy structures of 10 MD simulations for each ligand. The average preferred surface-to-surface distances for the different ADT chain lengths can be found in Figure 6.10. A linear dependence of the distance from the number of carbon units in the ADT ligands was found, consistent with experimental results by Schlicke et al.[18] The increase of 1.2 Å per carbon unit from the simulations is also in good agreement with SAXS measurements on thin films consisting of ~3.2 nm large GNPs, cross-linked with ADTs of different chain lengths (~0.9 Å per carbon unit).[18] Furthermore, the absolute values of the surface-to-surface distances are in reasonable agreement with experimental data (12.0 Å simulated distance for 9DT vs. 10.6 Å measured distance[18]), despite the approximations involved in the model. An even better agreement between the simulated distance and experimental results was observed in 9DT films prepared with larger GNPs (7.44 nm), measured with GISAXS.[117] Interparticle distances of 12.2 Å were obtained, closely resembling our findings. This suggests that the model may better represent the structure of assemblies with larger GNPs compared to smaller ones. These findings can be understood when looking at the faceted structure of the GNPs. Larger GNPs have less curvature or larger facets than smaller GNPs. As a result, large GNPs primarily consist flat surfaces, while the edges play a secondary role. In

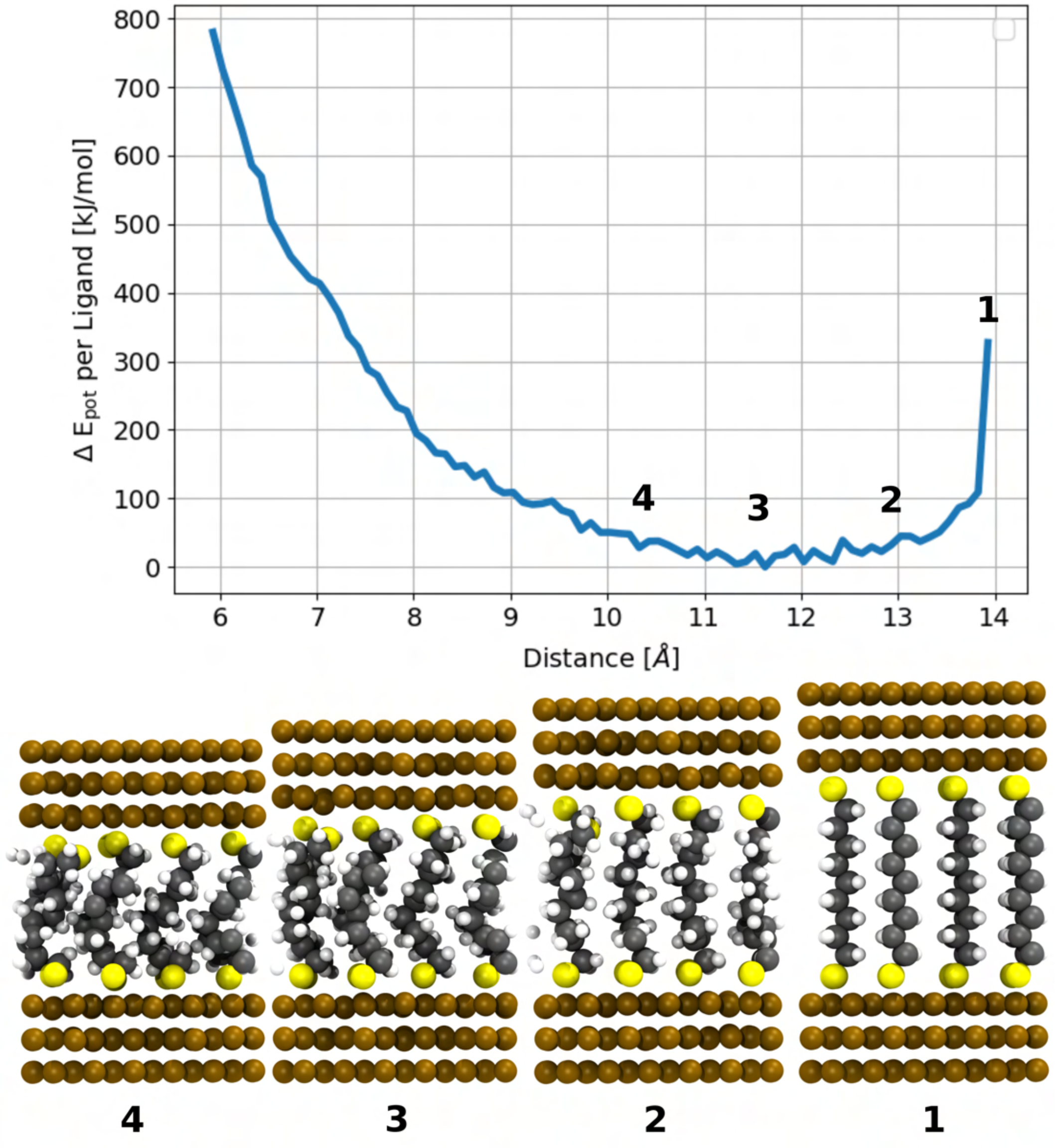

Figure 6.9: Potential energy versus surface-to-surface distance curve from a representative MD simulation of 9DT cross-linked Au(111) surfaces that were pushed together during the simulation. Below the curve, snapshots of the system are presented: the initial structure (1), the configuration shortly before reaching the lowest-energy structure (2), the lowest-energy structure (3), and a configuration shortly after the lowest-energy structure (4). Reprinted with permission from K. Schaefer et al. *J. Phys. Chem. C* 2024, 128, 9, 3994-4008 under an Open Access license.

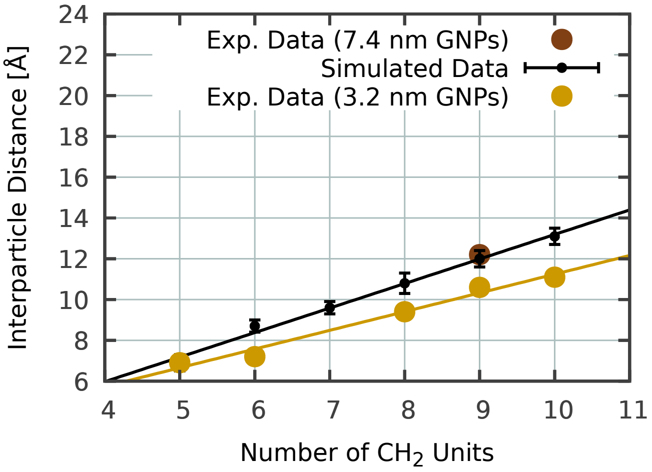

Figure 6.10: Dependence of the surface-to-surface distance between two gold surfaces bridged by ADTs on the number of carbon units in the ligand chains (black). Error bars represent standard deviations derived from 10 MD simulations. The results are compared with interparticle distances obtained from experimental data by Schlicke et al.[18] for approximately 3.2 nm GNPs cross-linked with ADT ligands (orange) and for films composed of 7.4 nm particles (brown).[117] Reprinted in part with permission from K. Schaefer et al. *J. Phys. Chem. C* 2024, 128, 9, 3994-4008 under an Open Access license.

contrast, smaller GNPs have smaller facets, resulting in a greater proportion of their surface being composed of edges. Previous molecular dynamics simulations have demonstrated that the edges significantly contribute to the differences in the GNP structure compared to flat bulk surfaces.[118] Therefore, larger GNPs, which have less edge surface area, are likely to be more accurately represented by a bulk flat surface model.

To further evaluate the accuracy of the flat surface model, charge transport calculations were performed, as described in Section 8.2. A linear dependence of the logarithmic zero-bias conductance on the alkane chain length of the ADT ligands (Figure 6.11) was observed, consistent with the model Equation (3.1). A slope of $-1.4/\mathrm{CH_2}$ was obtained from the linear fit, corresponding to a tunneling decay constant of $1.2\,\text{Å}^{-1}$, assuming an increase of the intersurface distance per carbon unit of 1.2 Å per carbon unit, as obtained from MD simulations. In comparison, experimentally measured tunneling decay constants range from 0.57 to $1.1\,\text{Å}^{-1}$.[16, 18, 21, 25, 143]

Hendrik Schlicke proposed an approach to quantitatively compare the conductances from the single-interface model with those of GNP assemblies by applying a simple geometric model.[117] GNPs with a radius r were assumed to be arranged in a primitive cubic packing configuration, characterized by a lattice constant given by $a = 2r + \delta$, where δ represents the interparticle distance (see Figure 6.12). Internal resistances were assumed to be zero so that the observed resistivity only originates from the interfaces between neighboring particles. As a further approximation, only charge transport between adjacent particles in horizontal direction was considered. For using this model, the number of molecules that cross-link neighboring particles needs to be estimated. For 4 nm large GNP assemblies, around 15 ADT bridging ligands were found in MD simulations by Yeh et al.[44] Assuming that the number of cross-linking ADTs scales linearly with the conductance of an interface, interface conductances $G_{\mathrm{i,exp}}$ can be calculated for each cross-linker. Therefore, the zero-bias conductances $G_{\mathrm{0V,theo}}$ are divided by the number of ADT ligands per unit cell in the single interface model (8) and multiplied by the number of ligands in a 4 nm diameter GNP (15 as found by Yeh et al.). Next, the conductivity σ_{theo} is calculated from the calculated

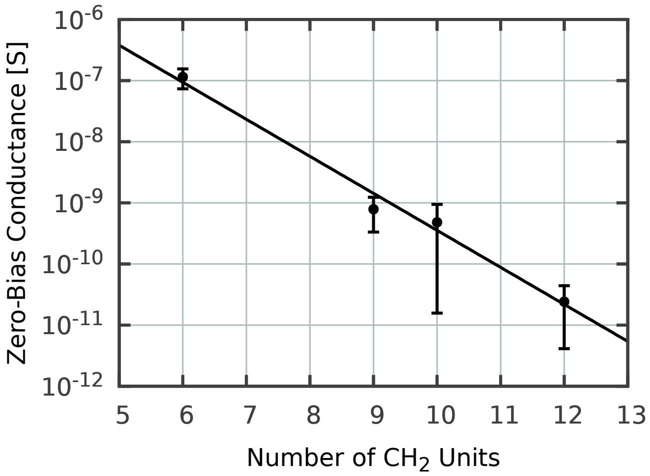

Figure 6.11: Zero-bias conductances averaged over conductances of minimum-energy structures of 8–10 different MD pushing simulations (see Appendix, Figures A.5-A.8 for transmission curves and selection) and their respective standard deviations with ADTs of different alkane chain length. Reprinted in part with permission from K. Schaefer et al. *J. Phys. Chem. C* 2024, 128, 9, 3994-4008 under an Open Access license.

zero-bias conductance $G_{0\mathrm{V,theo}}$

$$\sigma_{\mathrm{theo}} = \frac{G_{0\mathrm{V,theo}} * a}{a^2} = \frac{G_{0\mathrm{V,theo}}}{a} , \tag{6.1}$$

and compared with experimental values for 4 nm sized GNPs (see Table 6.2). Even though this simple geometric model involves several simplifications, a very good agreement for the estimated values with the experimental values were obtained for 9DT (0.0028 and 0.0032 S/cm). The conductivity of 6DT, on the other hand, was overestimated by a factor of 6 (0.44 and 0.071 S/cm).

Table 6.2: To quantitatively compare the conductivity of the single interface model from this work with that of GNP assemblies, a simple geometric model by Hendrik Schlicke was used (see Figure 6.12). First, the zero-bias conductance $G_{0\mathrm{V,theo}}$ from charge transport calculations is divided by the number of ligands in our interfaces (8) and multiplied by the number of ligands in an 4 nm sized particle interface (15, found by Yeh et al.[44]) to obtain the conductance of one GNP interface $G_{\mathrm{i,theo}}$. Next, the theoretical conductivity σ_{theo} is calculated with Equation (6.1), taking into account the lattice constant a received from the particle radius ($r = 4$ nm), and the surface-to-surface distances δ_{theo} from MD simulations. The conductivity for 9DT and 6DT is compared to the experimental conductivity σ_{exp} of assemblies with 3.2 nm large GNPs by Schlicke et al.[18]

Ligand	$G_{0\mathrm{V,theo}}$ [S]	$G_{\mathrm{i,theo}}$ [S]	δ_{theo} [Å]	a [m]	σ_{theo}	σ_{exp}[18]
9DT	$7.86 \cdot 10^{-10}$	$1.47 \cdot 10^{-9}$	12.0	$5.20 \cdot 10^{-9}$	0.0028	0.0032
6DT	$1.15 \cdot 10^{-7}$	$2.15 \cdot 10^{-7}$	8.7	$4.87 \cdot 10^{-9}$	0.44	0.071

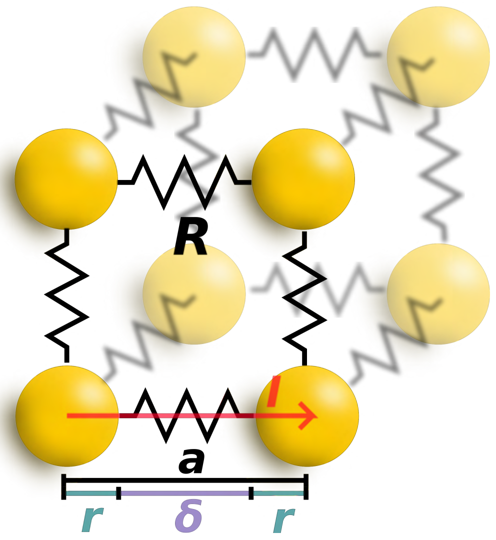

Figure 6.12: Simplified geometric model, proposed by Hendrik Schlicke, used to estimate the conductivity of GNP assemblies based on our calculated zero-bias conductances. In this model, the GNP assemblies are assumed to form a primitive cubic packing, with the assumption that the GNPs exhibit no internal resistance. The lattice constant a can be derived from the nanoparticle radius r and the surface-to-surface distance δ.

6.1.2.2 Structural Insights Derived from the Model

The atomistic structure of the interfaces in GNP assemblies is of great interest, as structural parameters such as the linker configuration or the gold surface were shown to influence the charge transport properties significantly in single molecule junctions.[43] Structural parameters that can be obtained from experiments, are mainly the interparticle distance, the size and morphology of the particles, and the ordering in the assembly. Since the simulations in this work focus on single flat interfaces and do not account for three-dimensional assemblies of particles, they do not provide insights into the GNP's structure or their 3D arrangement. However, they do offer information about the ligand arrangement, which cannot be easily obtained through experimental methods due to limitations in resolution.

From experimental measurements it is known that the interparticle distance in ADT cross-linked GNP assemblies is lower than a fully extended ADT ligand (e.g., 1.0 ± 0.2 nm for 5 nm large GNPs cross-linked with 9DT,[144] compared to 1.3 nm for an extended 9DT molecule). This phenomenon can be explained by two factors: the ADT ligands may adopt an all-trans conformation and tilt, or alternatively, gauche conformations may be present within the structure. In MD simulations of cross-linked GNP assemblies by Yeh et al.,[45] both, all-trans but tilted and gauche conformations, were observed. The authors found that all-trans linkers were preferably located at the edges of a particle–particle interface, where the edge-to-edge distance was slightly increased (e.g., 13.1 Å for 9DT). Gauche bridge linkers, on the other hand, tended to be present at the center of the interfaces, where the edge-to-edge distances were lower (see Figure 6.13). With increasing chain length, the authors observed an increase in gauche relative to all-trans linkers and attribute this to the higher likelihood of gauche conformations occurring as the number of carbon units increases.

In the single interface model, all-trans, tilted ligands were not observed in the lowest-energy structures. Instead, the structures consisted of different gauche conformers (see Figure 6.9(3) or Figure 6.14 for representative 9DT interface structures). At first glance, this may seem contradictory to the findings of Yeh et al., but it can be explained by the absence of interface edges. In the single interface model, the structure is flat and bulk-like, due to the applied

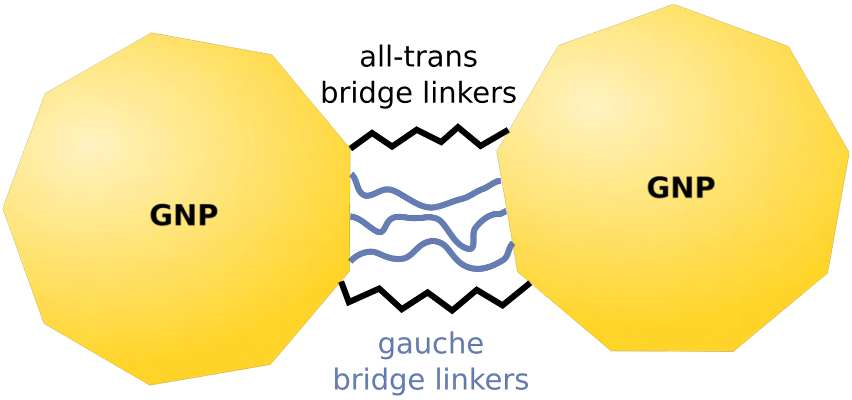

Figure 6.13: Interface between two GNPs, inspired by Yeh et al.[45]. In the central region, gauche linkers (blue) are predominantly observed, while at the edges of the domains, all-trans bridging ligands (black) are more frequent.

periodic boundary conditions. Thus, the model focused purely on the central region of the particle–particle interface. In this region, Yeh et al. also found that gauche linkers were more frequent than all-trans linkers.

Next, we will focus on the cross-linkage in the interfaces. Most of the ADT ligands remained adsorbed at the hollow sites of the gold surfaces. In few simulations, a gold atom moved out of the surface to form a S—Au—S contact between two neighboring ligands, also known as adatom conformation (see Figure 6.14, right). Although all ligands were initially bridging in all starting structures, some of the ligands partially dissociated during the simulation. On average, about 90 % of the ligands were bridging, while the remaining 10 % were bound one-sided (see Table 6.3 for a full summary of the cross-linkage fraction). Free linkers or loop forming linkers were not observed. In contrast, Yeh et al.[45] reported loops formation, especially for shorter chain lengths (5DT to 7DT). For longer chain lengths (from 8DT to 10DT), they found that the number of loop-forming ligands significantly decreased to a small fraction of the total ligands. The ratio of bridging to one-sided ligands was almost 1:1.[45] Experimentally, the cross-linkage of ADT GNP assemblies was studied by Schlicke et al.[18] For 3.2 nm large GNPs, they found a ratio of GNP-bonded to free thiols groups of 0.33. However, the films were prepared by a rapid layer-by-layer spin coating method, where ligands may be trapped and not bound to the GNPs, resulting in a low cross-linking fraction. In another experimental study by Joseph et al.[21] on ADT cross-linked 4 nm large GNPs, a higher proportion of cross-linkers were observed. Films were prepared by a layer-by-layer self-assembly method, resulting in 63 % double-side-bonded and 37 % single-side-bonded 9DT ligands. Overall, the fraction of bridging ligands in the single interface model is larger compared to that obtained from MD simulation studies and experimental measurements of GNP assemblies. This observation can again be attributed to the fact that the model used in this work focuses on the central region of the particle-particle interface. It does not include the edge regions of the interface or interstitial sites between the particles, where a second GNP is not sufficiently close such that the ADT ligands can cross-linkage. As a result, the model artificially enhances the fraction of bridging linkers.

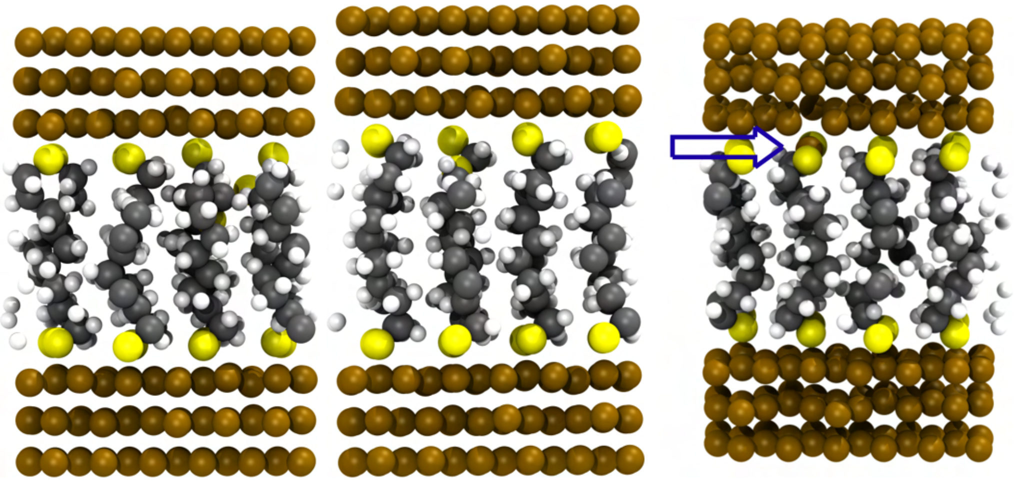

Figure 6.14: Lowest-energy structures from three MD simulations with 9DT cross-linked Au(111) surfaces. Ligands are adsorbed in gauche conformations on the hollow sites. In one simulation (right), one gold atom is pulled out of the surface by a ligand and moves in between two ligands (indicated by the blue arrow). Taken with permission from K. Schaefer et al. *J. Phys. Chem. C* 2024, 128, 9, 3994-4008 under an Open Access license.

Table 6.3: Fraction of cross-linking vs. non cross-linking ligands in interface simulations with different alkane chain lengths.

Ligand	Fraction of Cross-Linkage
5DT	0.89
6DT	0.88
7DT	0.87
8DT	0.91
9DT	0.89
10DT	0.88
12DT	0.99

In summary, the following conclusions can be drawn from the ADT interface simulations:

- **Distances:** Surface-to-surface distances and their dependence on the ADT chain length are accurately described both qualitatively and quantitatively, with particularly good agreement observed for larger GNP particles (∼7 nm).
- **Charge Transport Properties:** The exponential relationship between zero-bias conductance and alkane chain length is well represented. The extracted tunneling decay constant closely resembles experimental values, and conductivity values estimated from a simple geometric model align well with experimental measurements reported in the literature.
- **Ligand Structure:** Ligands adopt gauche conformations, with most ADT molecules effectively cross-linking the surfaces.

6.1.3 Model for Monothiolate Particle–Particle Interfaces

In the previous section, we demonstrated that the properties of GNP assemblies can be accurately replicated using a single-interface model for ADT ligands. In this model, eight ADT ligands occupy the unit cell, effectively cross-linking the gold surfaces. As a result, each surface is connected to eight thiolate groups, reflecting the optimal coverage of Au(111) SAMs.

When we apply the same coverage to AMT interfaces (with eight ligands per surface), a total of 16 ligands is present in the unit cell. An exemplary input structure for the simulation of the 12T configuration is shown in Figure 6.15 (left). During the MD simulation, the gold surfaces were pushed together in an effort to determine the distance corresponding to the lowest energy structure. Although the AMT ligands exhibited some tilting during the simulation, the density of the ligand matrix was so high that the ligands from the two surfaces could not overlap (refer to Figure 6.15, right). This led to an excessive separation distance of 26.3 ± 0.5 Å obtained from the simulations, in stark contrast to the experimental distances, which range from 18 to 23 Å.

Based on these preliminary findings, the surface distances are overestimated for 100 % ligand coverage on each surface. As an alternative approach, we examined intersurface distances of interface structures with lower ligand coverage, specifically using eight ligands per unit cell. This corresponds to the same total number of ligands as in the ADT interface simulations, where the simulated interparticle distances agreed well with experimental findings.

In this setup, each gold surface was occupied with four AMT ligands, allowing the ligands to initially overlap (see Figure 6.16). The preferred surface-to-surface distances for the various AMT ligands, averaged from 10 MD simulations, are presented in Figure 6.17. The dependence of the distance on the length of the AMT carbon chain is well represented. The slope of 1.1 Å per carbon unit is in very good agreement with experimental measurements (1.1 Å increase per carbon unit, measured by Gauvin et al.[17]), as well as with large-scale, coarse-grained MD simulations of assemblies of icosahedral nanoclusters, each consisting of 20 flat Au(111) surfaces, with AMT chain length ranging from 4 to 12 carbon units (1.0 Å increase per carbon unit, found by Liu et al.[145]). However, the distances deviated quantitatively. In experiments, an interparticle distance of 19.0 Å was measured for 12T ligands, which is significantly larger than distances extracted from the single interface model (14.0 Å for 12T ligands). Compared to the coarse-grained simulations by Gauvin et al. (15.7 Å for 12T), the surface-to-surface distance found in this work is similar, but also slightly lower. Consequently, it is likely that the ligand coverage of AMT-stabilized GNP assemblies is between 50 and 100 % with respect to the optimal coverage of flat, bulk Au(111) surfaces.

Numerous studies have demonstrated the significant effect of the GNP surface coverage on the interparticle distances. MD simulations of 12T-stabilized GNPs, using a united-atom model, indicated that the interparticle distance increases by several angstroms with higher

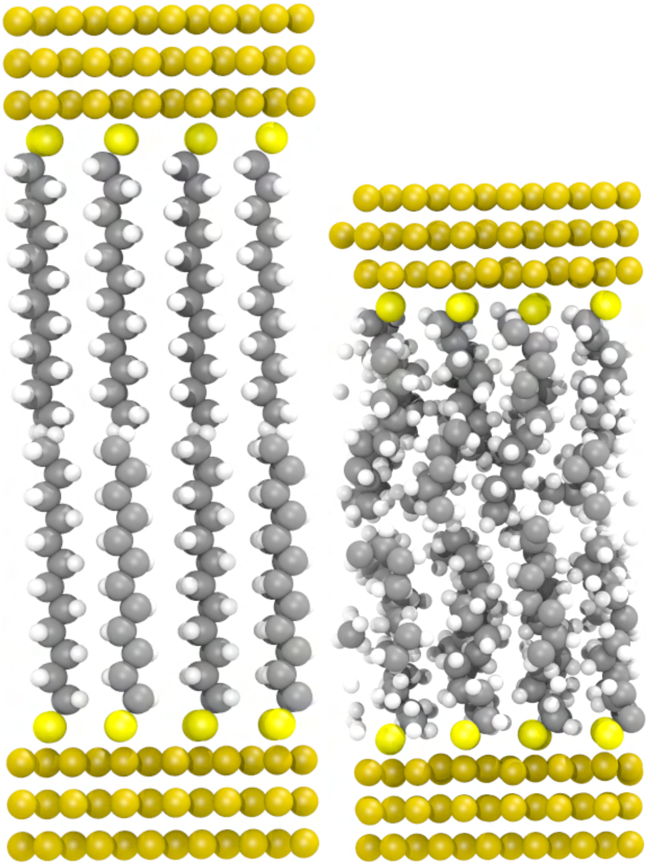

Figure 6.15: Initial (left) and lowest-energy (right) configurations of a 12T interface, where each Au(111) surface is optimally occupied (100 % coverage, 8 ligands per surface).

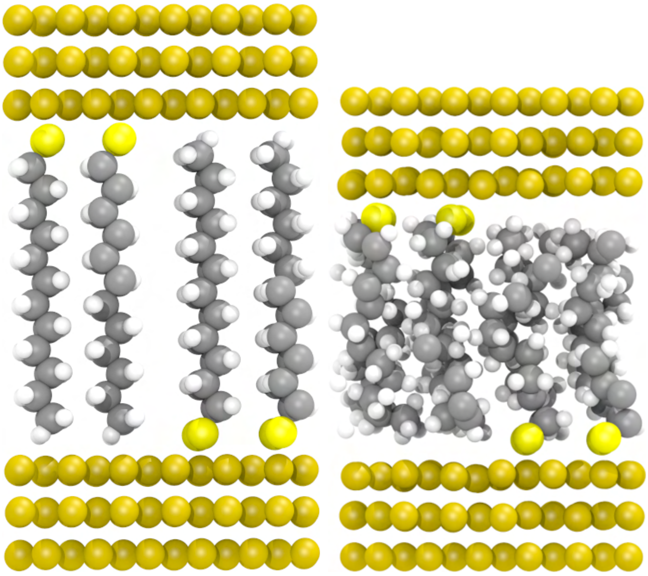

Figure 6.16: Initial (left) and lowest-energy (right) configurations of a 12T interface, where each Au(111) surface is half occupied (50 % coverage, 4 ligands per surface).

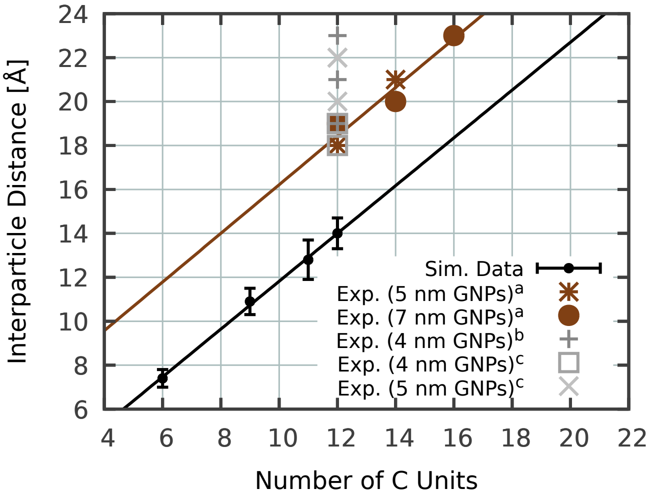

Figure 6.17: Dependence of the surface-to-surface distance between two gold surfaces connected by AMT ligands as a function of the number of carbon units in the ligand chain (black dots). Error bars represent the standard deviations derived from 10 individual MD simulations. A linear fit was applied (black line, with a slope of 1.11 ± 0.18 Å per carbon unit and $r^2 = 0.9275$). The results are compared with interparticle distances obtained from experimental studies of 7 nm GNPs capped with AMTs of varying chain lengths, as reported by Gauvin et al.[17] (shown in brown for both 7 and 5 nm GNPs). Additionally, interparticle distances for 12T-stabilized GNP assemblies with diameters of 4 nm [41, 146] and 5.5 nm [146], measured by Olichwer et al., are included for reference. Note that measurements from Olichwer et al. indicate a variability of several angstroms among individual measurements. Adapted with permission from K. Schaefer et al. *J. Phys. Chem. C* 2024, 128, 9, 3994-4008 under an Open Access license. a: Ref.[17], b: Ref.[41], c: Ref.[146].

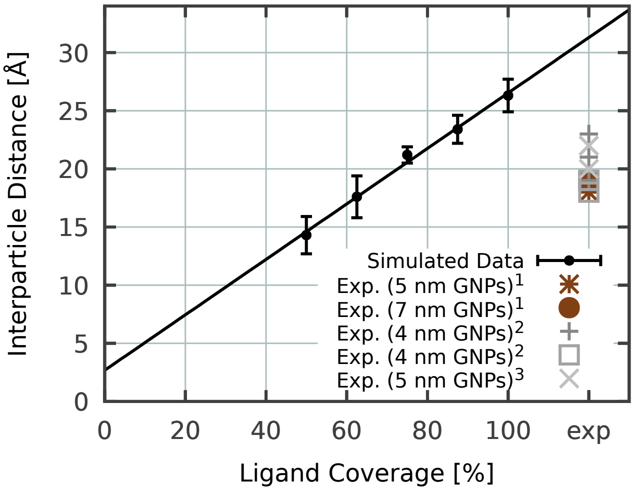

Figure 6.18: Intersurface distances in 12T-stabilized interfaces depending on the 12T coverage. A linear increase of the distance with increasing coverage can be observed (2.4 Å per 10 % increase, $r^2 = 0.9936$).

ligand coverage.[147] Additionally, Reik et al. performed X-ray diffraction measurements to examine how the surface coverage influences the interparticle distance in 12T-stabilized GNP assemblies. Their findings revealed that the interparticle distance increases by 3.2 Å for every 10 % increase in thiol coverage.[148] Compared to the increase in distance measured by Reik et al., atomistic MD simulations conducted by Liu et al. resulted in a smaller distance increase with surface coverage. The authors estimated an increase of 0.5 to 0.6 Å for every 5 % rise in ligand coverage.[97]

To address this issue further, different ligand coverages of the interfaces were investigated. The following discussion will focus mainly on the distances obtained from simulations with different 12T ligand coverages, given that lots of data is available for this ligand. A linear dependence of the preferred surface-to-surface with the ligand coverage was found, where the distance increases by approximately 2.4 Å per 10 % increase in ligand coverage (see Figure 6.18). This value falls between the experimental measurement reported by Reik et al. and the simulated results obtained by Liu et al.

Experimental values for 12T-stabilized GNP films range from 18 to 23 Å. Notably, the distance corresponding to a 75 % coverage in the one-interface model falls right in the middle of this range. Different coverages for 6T and 11T ligands were also investigated regarding their preferred surface-to-surface distance. The data, summarized in the Appendix (Figure A.1), also demonstrates a linear relationship between coverage and surface-to-surface distance. An increase in the distance of 1.0 Å or 2.1 Å for every 10 % rise in ligand coverage was found for 6T and 11T ligands, respectively.

Based on these findings, a ligand coverage of approx. 75 % can be assumed for AMT-stabilized GNP assemblies. With this coverage, the relationship between surface-to-surface distance and the chain length of different AMT ligands (6T, 9T, 11T, and 12T) was analyzed. For each ligand, 10 MD simulations were performed, and the surface-to-surface distances of the lowest-energy configurations were averaged. In Figure 6.19, a linear dependence of the preferred surface-to-surface distance on the length of the AMT ligand can be observed. The slope of the applied linear fit, measuring 1.3 Å per CH_2 unit, aligns with experimental values of 1.1 Å.[17] Additionally, with the optimized ligand coverage, a quantitative agreement of the simulated intersurface distance with experimentally measured interparticle distances is also observed.

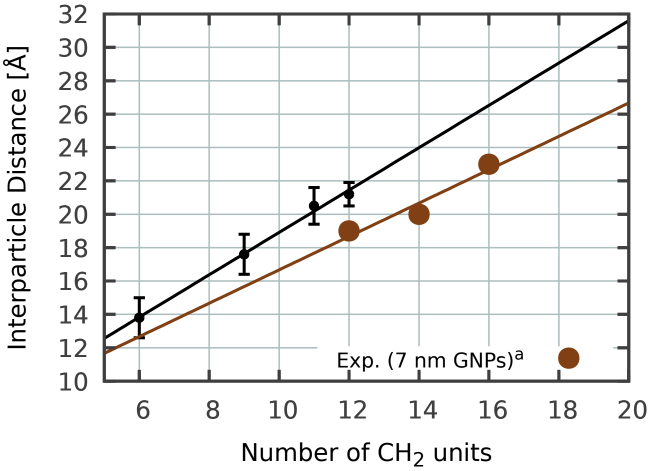

Figure 6.19: Surface-to-surface distance of AMT stabilized surfaces of different carbon chain lengths ranging from 6T to 12T (black). For each ligand, 10 MD simulations were performed and the preferred surface-to-surface distance was averaged. The AMT coverage on each gold surface was 75 %. A linear fit was applied ($r^2 = 0.995$, slope $= 1.27 \pm 0.06$ Å per CH$_2$ unit). The data is compared to experimentally measured distances for 7 nm large GNPs capped with alkanemonothiols of different chain lengths (brown).[17]
a: Ref.[17]

To further validate the AMT interface model, charge transport calculations were performed, as done earlier for the ADT ligands. The zero-bias conductance of AMT ligands with chain lengths ranging from six to twelve carbon units are shown in Figure 6.20. The ligand coverage for all ligands was assumed to be 75 %. A slope of -1.57/CH$_2$ unit was obtained from the linear fit, corresponding to a tunneling decay constant of 1.2 Å^{-1}, assuming an increase in intersurface distance per carbon unit by 1.3 Å per carbon unit, as obtained from MD simulations. This value falls at the upper end of the distances reported in the literature for alkanethiolate-stabilized GNP films, which range from 0.8 to 1.2 Å^{-1}.[16, 25, 149]

In summary, it has been demonstrated that the intersurface distance of AMT-stabilized interfaces is strongly influenced by the AMT surface coverage. Optimal alignment with experimental interparticle distances was achieved at a coverage of 75 %. At this coverage, a linear relationship was observed between intersurface distance and carbon chain length, with an increase of 1.3 Å per additional carbon chain. This finding is in close agreement with experimental values. Additionally, the zero-bias conductance showed a logarithmic dependence on the carbon chain length of the AMT ligands, in accordance with Equation (3.1). By applying a linear fit to the logarithmic data, a tunneling decay of 1.2 Å^{-1} was determined, which is comparable to the upper end of values reported in the literature. Consequently, the single-interface model seems to effectively describes both the structural and charge transport properties of AMT-stabilized films.

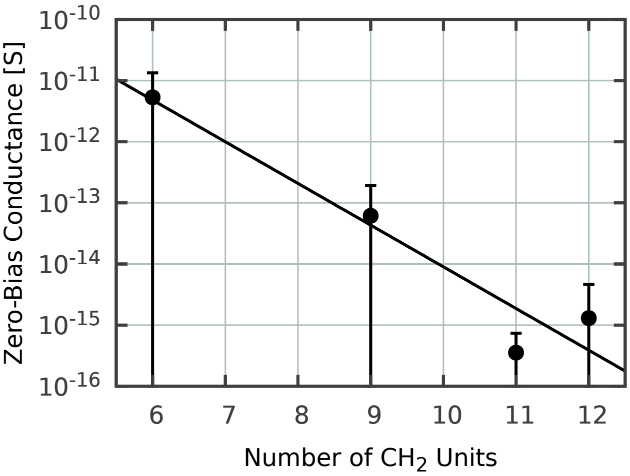

Figure 6.20: Zero-bias conductances averaged over conductances of minimum-energy structures of different MD pushing simulations (see Appendix, Figures A.5-A.8 for transmission curves and selection) and their respective standard deviations with AMTs of different alkane chain length. The large standard deviations, blown out of proportion by the logarithmic scale, suggest that this data may be affected by insufficient structural sampling. It should therefore be considered with caution. A linear fit was applied with a slope of -1.57±0.32 and a coefficient of determination r^2 of 0.92.

6.1.4 Limitation of ReaxFF when Simulating Dithiolates

The ReaxFF parameters developed by Bae and Aikens were initially optimized for AMT ligands adsorbed on gold surfaces. For these systems, bond lengths and angles obtained from simulations with small gold clusters, as well as in gold-thiolate SAMs, agreed well with those obtained from DFT calculations using a PBE functional.[109] The same parameters have also been applied for break-junction simulations of gold with 1,8-bis(methylthio)octane ligands[150] and methylsulfide-functionalized trans-α,ω-diphenyloligoenes.[151]

For singly deprotonated dithiol ligands on an Au(111) surface, good agreement with theoretical calculations and experimental observations were obtained. Furthermore, the distance of cross-linked surfaces could be accurately described by the force field, showing its potential to use the parameters also for dithiol ligands.

However, in some MD simulations involving dithiol ligands, spontaneous chemical reactions of free thiolate groups were observed that were not found with monothiolate ligands. These free thiolate groups (such as those from dissociated ligands) interacted with neighboring ligand molecules, leading to the formation of $R{-}CH_2{-}S{-}CH_2{-}R$ motives and $SCH_2{-}R$, where R represents a part of the alkane chain in the ligands. This suggests that the force field may struggle to accurately interpret the behavior of thiolate groups that are not bound to gold atoms. It is likely that those reactions are artifacts of the ReaxFF and do not represent reality. Therefore, a self-written PYTHON script (see Appendix B, Code Example 1) was used that identifies S—C—S, S—H, C—S—C, and S—S bonds based on estimated bond lengths (1.6 Å for S—H, 2.0 Å for S—C, and 3.0 Å for S—S bonds). Trajectories were excluded when those reactions occurred before reaching the lowest-energy point of the simulation or closely after reaching it. Reactions were observed in about 30 to 50 % of the interface simulations, with the likelihood of such reactions decreasing as the chain length increased (see Table 6.4).

Furthermore, the force field is restricted to n-alkanes and does not accurately reproduce double bonds or aromatic systems. For instance, benzene rings tend to adopt a cyclohexane

Table 6.4: Probability of reactions in interface simulations with alkanedithiolate ligands of different chain lengths.

Ligand	Probability of Reactions
5DT	52 %
6DT	50 %
7DT	41 %
8DT	38 %
9DT	29 %
10DT	33 %
12DT	17 %

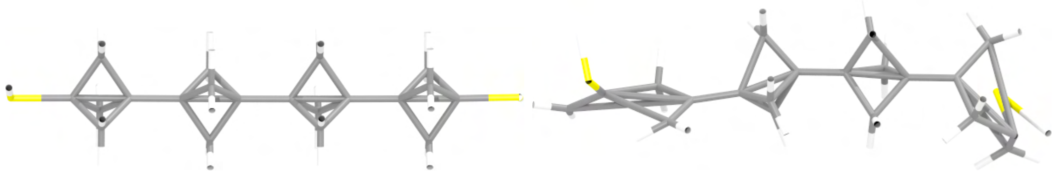

Figure 6.21: The 4-staffane-3,3'-dithiol molecule (left) is inadequately represented by the ReaxFF, resulting in rapid decomposition (right).

configuration or break down into smaller chains or individual atoms. The faulty representation of aromatic systems can be explained by the missing description for aromatic systems in the force field, as described in Section 4.3.Additionally, more complex ligands, such as cycloalkanes like 4-staffane-3,3'-dithiol, cannot be accurately represented by the force field and decompose rapidly (see Figure 6.21).

6.1.5 How Stable are the Results from the Simulations?

In this section, the stability of the simulation results will be examined. We will begin by investigating how the artificial pulling affects the intersurface distance and whether the results can be replicated using slower pushing speeds or alternative MD ensembles. Then, we will analyze the averaging procedure to determine if using a different approach yields different results. Finally, we will discuss the equilibration time and assess whether it is sufficient for the ligands to relax properly.

6.1.5.1 MD Simulation protocol

To make sure that our artificial pushing in the MD simulations does not lead to artifacts, three additional tests were performed on a 9DT cross-linked system: a) simulations were repeated with half the pushing speed, b) simulations were repeated with an isothermal-isobaric (NPT) ensemble without any pushing, and c) an additional simulation was performed, where pushing and pulling steps were alternated.

Too high pushing speeds may not allow sufficient time for the ligand molecules to relax, potentially resulting in increased surface-to-surface distances. Therefore, 10 simulations were performed with the same settings as in the standard simulations, despite the pushing speed that was halved compared to the standard protocol. An average preferred surface-to-surface distance of 12.0 ± 0.7 Å was found, which is not deviating from the 12.0 ± 0.4 Å extracted with the standard pushing speed. This indicates that the time for ligand relaxation in the simulations with the standard protocol is sufficient.

By performing simulations in a NPT ensemble without constraining the movement of the atoms, the system can relax by adapting an optimal surface-to-surface distance without

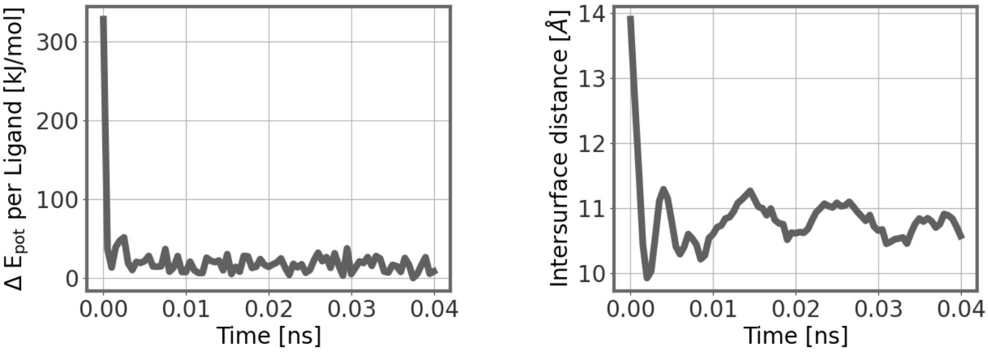

Figure 6.22: Left: Potential energy versus simulation time for the same system. The simulation allows the system to relax and reach an optimal surface-to-surface distance without the application of artificial forces. Right: Surface-to-surface distance as a function of simulation time for a representative MD simulation of 9DT cross-linked surfaces within an NPT ensemble.

artificially pushing the surfaces together. With the 9DT test system, 10 individual MD simulations in a NPT ensemble were performed for 0.04 ns. A distance versus simulation time, and energy versus simulation time plot of a representative simulation are shown in Figure 6.22. During the simulations, the distance between the two surfaces decreased and oscillated around an approximate value of 11.5 Å. The surface-to-surface distance, averaged from the measurements at the energetic minima across all 10 MD simulations, was found to be 11.7 ± 0.4 Å. This distance is also very close to the value obtained by the standard pushing protocol. For this study, the standard pushing protocol was preferred over the NPT protocol because it allows for precise control of the forces, making it suitable for investigating mechanical properties in the future.

Alternating pushing and pulling steps enables the identification of artifacts in the simulation, e.g., unstable configurations, forcing the system into a local minimum. One simulation was performed with the 9DT cross-linked system, during which pushing and pulling steps were alternated. In each alternation, the range of the pushing and pulling steps was increased. No significant changes were observed in the potential energy versus distance curve until a threshold was reached, at which the structure was compressed to such an extent that one 9DT ligand dissociated, releasing the pressure on the system. This dissociation resulted in a noticeable change of the curve's shape (see Figure 6.23).

6.1.5.2 Averaging Procedure

In the standard protocol, the preferred surface-to-surface distances were determined by averaging the distances from the lowest-energy structures across 10 individual simulations, each initialized with different velocity seeds (Approach A, see Figure 6.24a). The associated standard deviations of the determined distances were calculated with the **numpy.std** function via Python. Given that the energy curves, shown in Figure 6.24a, are relatively flat, it is possible that the obtained distances may be imprecise. In addition, individual simulations may land in local minima, shifting the position of the minimum. To investigate the impact of these effects, two additional averaging procedures were tested: First, the 10 MD curves were averaged, and the minimum point of the average curve was extracted directly (Approach B, as indicated in Figure 6.24b). Secondly, the average-curve was fitted around its minimum with a parabola, and the preferred distance was taken from the minimum of the parabola (Approach C, as indicated in Figure 6.24c). Surface-to-surface distances, extracted with the three procedures, are summarized in Table 6.5. No significant differences

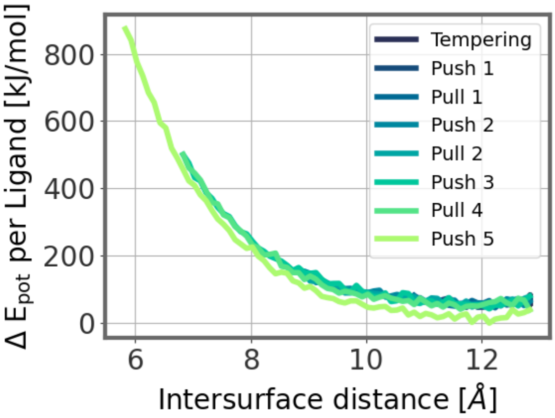

Figure 6.23: Distance vs. potential energy curve from a MD simulation of a 9DT interface structure, where alternating pushing and pulling forces were applied, with the range of these forces being increased step-wise. Initially, the curve exhibited no significant changes during the push-pull alternations. However, upon exceeding a certain compression threshold, the structure experienced a notable change in the shape of the curve as one ligand began to dissociate (Push 4).

were observed when comparing the extracted surface-to-surface distances, showing that the standard procedure is reliable, despite the flat energy curves.

Table 6.5: A comparison of the surface-to-surface distances of sandwich structures with ADTs and AMTs of varying chain lengths was conducted using different averaging approaches. In Approach A, the preferred distance was determined by averaging the minima from all 10 MD curves. In Approach B, an average energy versus distance curve was created from the individual curves, and the preferred surface-to-surface distance was derived from the minimum of this average-curve. Finally, in Approach C, the average-curve was fitted around its minimum with a parabola.

Ligand	Approach A [Å]	Approach B [Å]	Approach C [Å]
5DT	6.9 ± 0.7	7.5	6.9
6DT	8.7 ± 0.5	9.0	8.8
7DT	9.6 ± 0.6	9.7	9.4
8DT	10.8 ± 0.7	11.3	10.7
9DT	12.0 ± 0.4	11.7	11.7
10DT	13.1 ± 0.5	12.9	12.9
6T	7.5 ± 0.5	7.4	7.8
9T	10.9 ± 0.4	11.2	11.0
11T	12.8 ± 0.3	12.2	13.2
12T	14.0 ± 0.4	14.0	14.0

6.1.5.3 Is the Equilibration Period Sufficient?

With simulation lengths of 40 to 50 ps, depending on the ligand length, the pushing simulations are relatively short. Frequent artifacts in the ReaxFF simulations of ADT ligands, which resulted in interligand reactions, made it challenging to sample for longer time periods or to add an equilibration period to the simulation. The comparison of different simulations strategies (simulations with reduced pushing speed, NPT ensemble, or alternated pushing

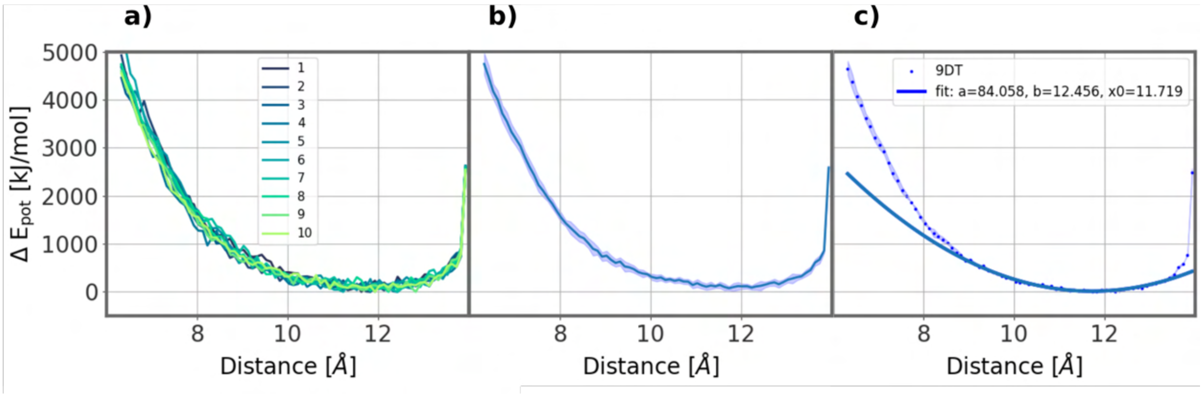

Figure 6.24: a) Standard averaging procedure (Approach A) for determining the preferred surface-to-surface distance, derived by extracting distances from the 10 lowest-energy configurations across 10 MD simulations and calculating their average. b) Potential energy versus distance curves from all ten simulations are averaged to identify a single curve, from which the minimum value is extracted (Approach B). c) The averaged potential energy curve is fitted with a parabola around its minimum, and the preferred surface-to-surface distance is determined from the minimum point of the fitted parabola (Approach C).

steps, as discussed above) already indicated that the system likely has adequate time for relaxation during the pushing process even without a designated equilibration phase. However, to further validate this, a more detailed analysis was conducted on the time required for system equilibration.

First, a longer MD simulation on a 10DT monolayer system was performed. A single Au(111) surface was covered with singly deprotonated 10DT ligands, with the same coverage as in the single interface systems. The structure was allowed to relax for 0.5 ns, without any external pushing, while the outer Au layer remained frozen to maintain its position during the relaxation process. Equilibration was reached after approximately 0.0025 ns (see Figure 6.25a). The lowest-energy point in pushing simulations is reached after approximately 0.01 ns (see Figure 6.25b).

As artifacts in the simulations involving ADT ligands prevented longer structural sampling and longer relaxation of the system, it is possible that equilibration of the system was not reached by the time, the first reactions occurred in the simulation. In MD simulations with AMT ligands, on the other hand, such reactions were not observed. Here, longer equilibration is possible, and changes in the energy are only related to reasonable variations in the ligand structure. Therefore, the simulation was repeated with 10T ligands occupying an Au(111) surface. The potential energy versus simulation time curve for this system (shown in Figure 6.26) indicates that equilibration was achieved after approximately 0.005 ns. This equilibration time is consistent with the equilibration time observed for the 10DT system.

Finally, the stability of the lowest-energy structure obtained from the interface simulation was analyzed. The lowest-energy configurations for both a 9DT and a 12T simulations were extracted from MD pushing simulations. Then NVT simulations were performed at constant intersurface distances, during which the outer gold layers were kept fixed. In the 9DT interface simulation, significant reactions occurred at 0.6 and 4.2 ns leading to significant changes in the potential energy of the system, as shown in Figure 6.27a. During the initial 0.2 ns, as shown in the zoomed-in graph of Figure 6.27b, the potential energy remained relatively stable, indicating that equilibration is not necessary in this system. In contrast, the 12T simulation exhibited no such reactions. Instead, the energy remained

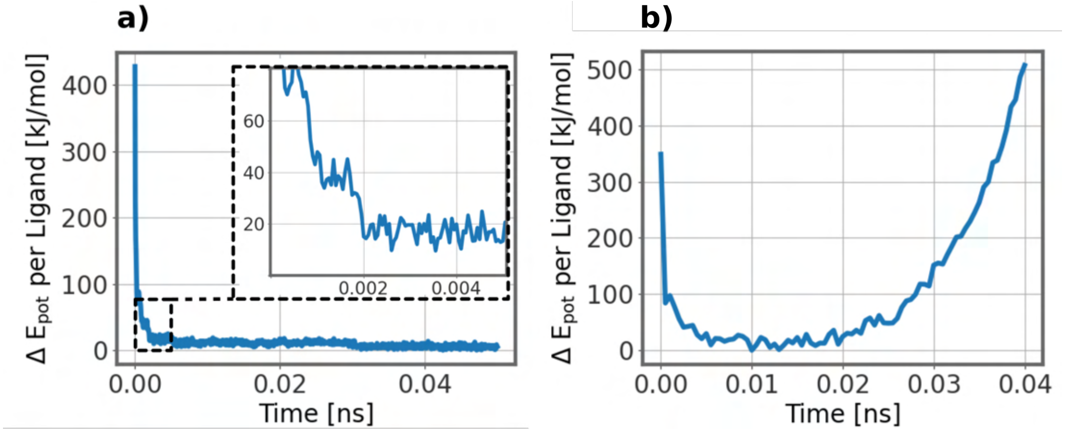

Figure 6.25: a) Plot of potential energy versus simulation time for the 10DT monolayer system. Equilibration is approximately achieved after 0.0025 ns. After that time, the energy exhibits only slight changes at 0.005 ns and 0.06 ns. The latter fluctuation is attributed to interligand reactions involving the tail groups of the 10DT ligands, which occur due to artifacts in the ReaxFF force field. b) Plot of potential energy versus simulation time for the 10DT interface system. The minimum potential energy is observed at about 0.01 ns, which is after the approximate equilibration time identified in the monolayer simulation.

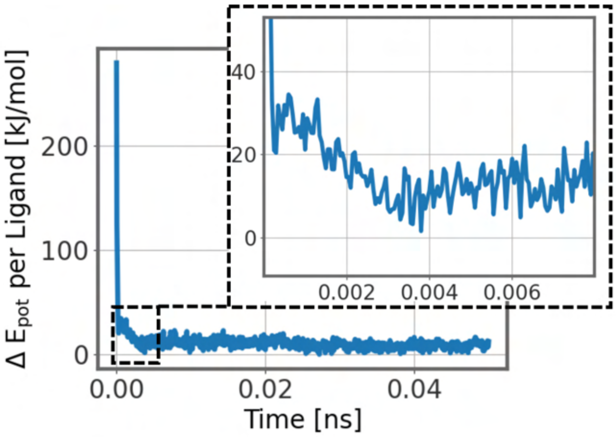

Figure 6.26: Plot of potential energy versus simulation time for the 10T monolayer system. Equilibration is approximately achieved after 0.005 ns, which is consistent with the equilibration period, required for 10DT systems to equilibrate (0.0025 ns) and shorter than the time required to reach the minimum in pushing simulations (0.01 ns for 10DT).

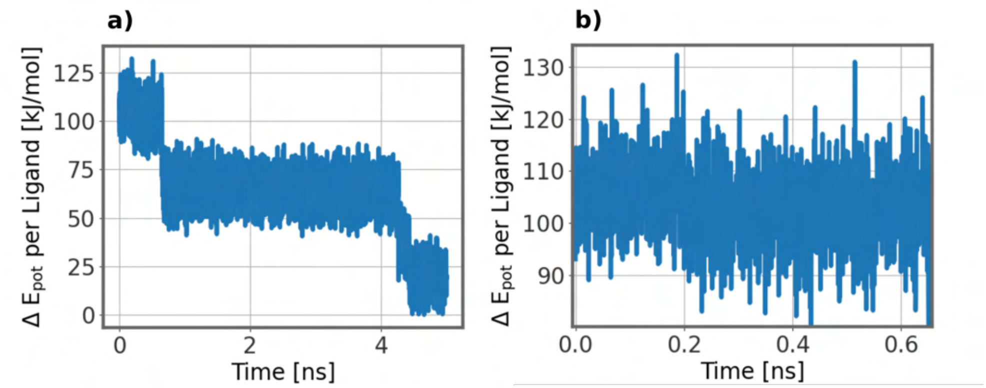

Figure 6.27: a) Potential energy versus simulation time for a constant-distance simulation of a 9DT interface structure, conducted at the lowest-energy surface-to-surface distance. Interligand reactions occur at 0.6 ns and 4.2 ns, resulting in notable decreases in the average potential energy of the system. During the initial 0.2 ns (shown in the zoomed-in graph b)), the average energy remains relatively stable, indicating that equilibration is not a critical factor in this phase of the simulation.

stable throughout the entire duration of the simulation, further confirming the stability of the lowest-energy structure derived from the pushing simulations.

6.1.6 Summary and Outlook

In this section, the potential of a single-interface model for describing molecule-linked GNP assemblies was explored. The model consists of two flat Au(111) surfaces interconnected by ADT or AMT ligands. To achieve a more realistic representation of these systems and their dynamics compared to coarse-grained or classical force fields, a ReaxFF was applied. Since this ReaxFF was parameterized for interactions between AMT and gold, its performance for MD simulations involving singly deprotonated ADTs on individual Au(111) surfaces was investigated. The ligand coverage in these simulations aligned well with experimental data on SAMs of AMTs. A transition from somewhat disordered to ordered monolayers was observed as the number of CH_2 units increased from 9 to 10, in agreement with previous MD simulations on AMTs. Additionally, the tilt angle of the ADT ligands adsorbed on Au(111) surfaces was found to be smaller than that of AMT ligands (approximately 20°), in contrast to about 30° for AMTs. Instead, the tilt angles of ADT ligands are comparable to measured tilt angles for AMTs containing hydroxy tail groups. While these findings appear reasonable, not enough studies on the SAM structure of ADTs exist to exclude that the lower tilt angle is a shortcoming of the ReaxFF, rather than an effect of the polar tail group of the ADT ligands.

A significant shortcoming of the ReaxFF for modeling (singly deprotonated) ADTs on single Au(111) surfaces, in contrast to AMTs, was its tendency to predict unlikely chemical reactions. These reactions involved the free thiol tail groups of dithiol ligands and resulted in the formation of S–C bonds. These artifacts were found less frequently also in sandwich structures involving ADT ligands. To address this problem, a self-written PYTHON script was developed (see Appendix B, Code Example 1) designed to detect the formation of S–C–S, S–H, and C–S–C bonds and to exclude any affected MD trajectories from further analysis. While this ensured that only chemically plausible structures were analyzed, the length of the MD trajectories was restricted and consequently the quality of the structural sampling was limited by these artifacts. In the long run, reparameterizing the ReaxFF or using machine-learned force fields[152–154] could provide a more satisfactory solution to this problem.

Next, the change of the interparticle distance with increasing chain length of the ligands was examined. An increase of 1.2 and 1.3 Å per carbon unit was found for ADT and AMT interfaces, respectively, which aligned with experimental observations. The simulated interparticle distance of the 9DT-cross-linked interface aligned well with the distance measured for assemblies involving larger particles of approximately 7.4 nm. In contrast, the experimental distance of smaller (approximately 3.2 nm large) ADT-linked particles was about 1.5–2 Å lower that in our simulations. Furthermore, the calculated surface-to-surface distances of AMT interface structures with ligand coverage of 75 % also agreed well with experimental findings.

Further insights into the properties of the interfaces were gained through charge transport calculations, which used representative MD snapshots and combined DFTB with a coherent tunneling approach. These calculations revealed an exponential decrease in zero-bias conductance with increasing chain length for both ADT and AMT ligands. This result is in both qualitative and quantitative agreement with theoretical models and experimental observations on GNP assemblies documented in the literature. Moreover, a simplified geometric model indicated that the absolute values of our simulated zero-bias conductances for ADT-linked single interfaces align well with the range of measured conductivities of cross-linked GNP assemblies.

Although we cannot rule out the possibility of error cancellation, we find that our single, flat interface model effectively captures the interparticle distances and charge transport characteristics in GNP assemblies with both qualitative and quantitative accuracy for AMT-capped and ADT-cross-linked systems. By concentrating on a single, flat interface, a level of atomistic detail was achieved that is often unattainable with larger models that describe entire GNPs or their assemblies, which typically use coarse-grained representations of the ligands. This approach makes it possible to explore how factors such as ligand arrangements, coverages, and interlinkages influence interparticle distance and conductance. Furthermore, this model can be adapted to investigate different ligands or ligand mixtures, including combinations with analyte molecules, to evaluate their potential as sensors. This application will be the focus of the subsequent sections.

6.2 Extraction of the Single-Interface Model to Mixed-Ligand Systems

As discussed before, enhancing the chemiresistive and mechanical sensing response can be achieved by tuning structural parameters of the GNP films, such as the size of the GNPs or their interparticle distance. The interparticle distance can be adjusted by varying the length of the ligand chains. With longer chains, not only the distance between particles is increased but also the mechanical flexibility of the film is usually enhanced. Additionally, the type of ligand significantly impacts the device's properties. For instance, ligands like ADTs, which cross-link particles through chemical bonds, tend to be less flexible and, consequently, exhibit lower sensitivity compared to non-cross-linking ligands such as AMTs (compare for example Refs. [21] and [41]). However, ADT ligands generally provide higher overall conductivity than AMT ligands of the same chain length (e.g., room-temperature conductivities in the range of $10^{-4}\,\Omega^{-1}cm^{-1}$,[21] and $10^{-7}\,\Omega^{-1}cm^{-1}$[41] were measured for GNP assemblies with 12DT and 12T ligands, respectively.

Recent studies have explored the benefits of mixing two different types of ligands to combine advantages of both ligands.[38, 39] For instance, Liu et al.[39] combined 9DT ligands with different AMT ligands (6T, 11T and 12T) as well as with mercaptocarboxylic acids. They found that when mixing 9DT with longer AMT ligands (11T and 12T), the conductivity of the resulting films decreased compared to pure 9DT films. The measured conductivities were also significantly influenced by the length of the ligands and the proportion of AMT ligands in the mixtures. As the proportion of AMTs in the mixtures increased, the film's conductivity decreased. This decrease was especially significant in mixed-ligand assemblies with 12T ligands, compared to a smaller decrease in 11T systems. The authors attributed this phenomenon to an increase in interparticle distance when longer AMT ligands were added to the 9DT ligands. At the same time, the incorporation of AMT ligands, particularly those with longer chain lengths than 9DT (11T and 12T), enhanced the sensitivity towards non-polar solvents. Additionally, the authors observed that the incorporation of mercaptocarboxylic acids improved sensor responses in the presence of polar analytes. By assembling an array of films with these ligand mixtures, they successfully demonstrated their ability to discriminate between a range of organic vapors, which would not have been possible with films composed solely of 9DT ligands.[39]

In this study, we aim to investigate the morphology of such mixed-ligand films, particularly those consisting of ADT and AMT ligands, as studied by Liu et al. The structure of ADT/AMT mixed-ligand GNP films has not been explored in depth yet. However, research on the structure of different individual mixed-ligand GNPs has been ongoing for several decades, as mixed ligands have been shown to enhance various properties of individual GNPs, including solubility, cellular penetration, and catalytic activity.[155] The following summary will review some of the research conducted on the mixing behavior of ligands with varying chain lengths or tail groups on gold SAMs. This overview aims to provide a foundational understanding of the morphology of these structures.

In an early study in 1989, Bain et al.[156] investigated the structure of SAMs with mixtures of alkanethiols with different chain lengths, and varying tail groups ($HS(CH_2)_nX$ and $HS(CH_2)_mY$ ligands with X and Y being CH_3 or OH groups and with $n > m$). When combining two AMT ligands with different alkane chain length, they observed that the adsorption of the longer alkane chain length was slightly preferred.[156] When combining ligands with different tail groups, the adsorption of the less polar compound was preferred in polar solvents like ethanol, while the opposite effect was observed in non-polar solvents.[157] The macroscopic structure of the mixed-ligand SAMs with AMTs of different chain lengths showed no separation of the different ligands into islands (small domains), at least no islands larger than a few tens of angstroms, which was the resolution limit of the measurement technique. The authors suggested, however, that the two compounds are probably not randomly dispersed withing the SAM. Instead, there may be some clustering, not visible by X-ray photoelectron spectroscopy, especially when the ligands differ in both chain length and tail group. In a similar study in 1992, Laibinis et al. also observed no phase segregation into macroscopic islands for 12T/18T and 12T/22T mixtures on gold SAMs using polarized infrared external reflectance spectroscopy.[158]

Numerous publications from the Stellaci group, which have generated considerable discussion within the scientific community, suggest the formation of one-molecule-wide stripe-like domains.[155, 159–165] However, researchers have encountered challenges in reproducing these findings experimentally. Cesbron et al., for example, proposed that the observed stripes may actually arise from STM artifacts.[166] Aside from that debate, the formation of domains – though not specifically stripe-like – is generally accepted within the scientific community, particularly when there are significant structural differences between the two compounds.

When mixing long AMT ligands, such as 16T, with 3-mercaptopropionic acid (MPA) ligands, for example, phase separation occurs, caused by the enhanced intermolecular interactions when separating. As 16T ligands have 13 methylene units more than MPA ligands, less van der Waals interactions are possible between 16T and MPA, compared to 16T and 16T.[167] In these MPA/AMT mixtures, the size of the MPA domains was found to increase linearly with the length of the AMT ligand chain.[168] Phase segregation was also observed when mixing monothiols with different terminal functional groups, including $-CH_3$, $-CO_2CH_3$, $-OH$, and $-CN$. With STM, nanometer-scale molecular domains were observed on Au(111) surfaces.[169, 170] In mixed-ligand monolayers consisting of alkanethiols and mercapto-alcohols, the morphology of the GNPs was found to be influenced by the difference in length between the two ligand types. When there was no length difference, Monte Carlo simulations revealed that the two ligands form well-mixed monolayers. However, when the mercapto-alcohol ligand was significantly longer than the alkanethiol ligand, a strong segregation occurred, leading to the formation of Janus-like monolayers. Conversely, when the alkanethiol was shorter, phase segregation still took place, but to a lesser extent.[171]

Mixing AMT ligands with different lengths but no chemical mismatches, resulted in SAMs with separated domains when the difference in chain length was sufficient. Fetisov and Siepmann[172] investigated mixtures of 6T/10T, 6T/14T and 10T/14T on spherical GNPs with diameters ranging from 50 to 90 Å using Monte Carlo simulations. Starting from a random initial distribution, they found Janus-like arrangements and phase separation in the 6T/14T mixtures, where the difference in ligand chain length was significant. In contrast, for mixtures with less pronounced chain length differences (6T/10T and 10T/14T), they noted that the ligands were not homogeneously distributed. However the did not detect ordered domains, such as stripes or complete phase separation.

In another Monte Carlo study, Shevade et al.[173] analyzed the adsorption of aliphatic mixtures with varying chain lengths onto Au(111) surfaces. Their findings revealed a preferential adsorption of longer-chain alkanes over shorter ones, aligning with previous observations by Bain et al. When the chain lengths of the two ligand types differed by two or fewer carbon units, uniformly mixed SAMs were observed. However, when the chain length difference was three units, phase segregation occurred. A clear phase separation was found when the difference exceeded three carbon units.[173] Experimentally, using STM, Bumm et al. also reported the presence of homogeneously distributed mixtures on Au(111) surfaces for ligands with similar lengths (10T/12T mixture).[174] In contrast to the findings of Bain et al. and Shevade et al., Bumm et al. observed no preferential adsorption of the longer AMT ligand; the proportion of 12T remained consistent both in solution and within the SAM. This is further supported by Kim et al. who also observed no preferred adsorption of 8T or 12T, and phase-separation with few nanometer-sized domains in mixed-ligands SAMs using STM and linear-scan voltammetry investigations.[175]

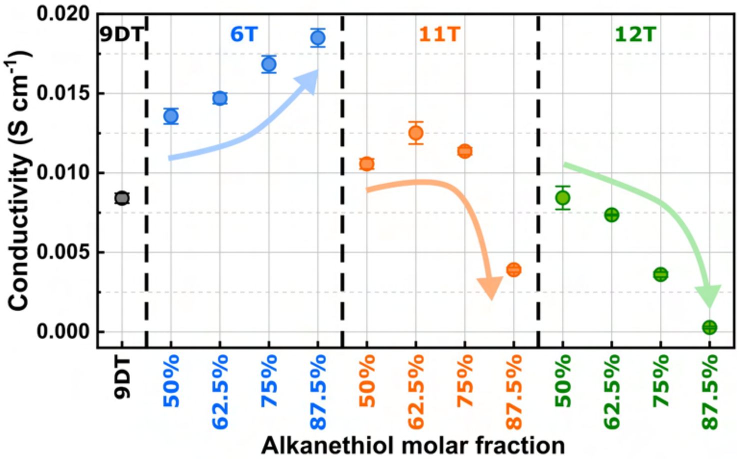

Figure 6.28: Room temperature conductivities of GNP films prepared with pure 9DT cross-linkers and mixtures of AMT/9DT with varying AMT molar fractions. Taken with permission from C.-Y. Liu “From Fabrication to Application: Developing High-Performance Gold Nanoparticle-Based Sensors Using Mixed Ligand/Linker Systems”, University of Hamburg, 2024.

6.2.1 Alkanedithiol/Alkanemonothiol Mixed-Ligand GNP Assemblies – Summary of an Experimental Literature Study

While several studies on mixing AMTs with different lengths and functional tail groups exist, information on the structure of mixtures consisting of ADT and AMT ligands are limited. A detailed experimental investigation has been performed by Chih-Yin Liu as part of her PhD thesis in the group of Tobias Vossmeyer at the University of Hamburg.[176] Parts of this results have also been published in Ref.[39]. Findings on the structure of these mixed-ligand films from C.-Y. Liu’s thesis will be summarized in the following.

GNP mixed-ligand films with 7.5 nm-sized GNPs were prepared,[176] using a layer-by-layer spin-coating (LbL-SC) technique described in Ref.[39]. The examined AMT/9DT mixtures included AMT ligands shorter than 9DT (specifically, 6T) and those longer than 9DT (11T and 12T). Mixing ratios of 7:1, 6:2, 3:5, and 4:4 were investigated, which correspond to AMT molar fractions of 87.5 %, 75 %, 62.5 %, and 50 %, respectively. Additionally, a GNP film with pure 9DT was fabricated to serve as a reference, allowing for a comparison of the structure and performance between the mixed-ligand films and the pure ligand film.

Conductivity measurements of the mixed-ligand films and the pure 9DT film by C.-Y. Liu, shown in Figure 6.28, revealed a decrease in conductivity for the longer-chained AMTs and an increase for the shorter-chained AMTs in comparison to the pure 9DT film. According to Equation (3.1), a decrease in conductivity is typically associated with an increase in interparticle distance, and conversely, an increase in conductivity correlates with a decrease in interparticle distance. Hence, conductivity measurements indicate that the interparticle distance decreased with increasing AMT ratio in the 6T/9DT films, while it increased for the 11T/9DT and the 12T/9DT film.

Furthermore, C.-Y. Liu applied Equation (3.1) to estimate the absolute difference in interparticle distances of mixed-ligand films compared to pure 9DT films from the conductivity measurements. As the GNP films were consisted purely of hydrophobic molecules with similar permittivity, the activation energy term was expected to vary minimally. Consequently, the observed variation in the films’ conductivity was assumed to be predominantly influenced by the tunneling distance between the GNPs, while the influence of the activation energy term was expected to be negligible. A tunneling decay constant β of 1.0 Å^{-1} was chosen, based on the mean values reported in the literature for AMT and ADT cross-linked

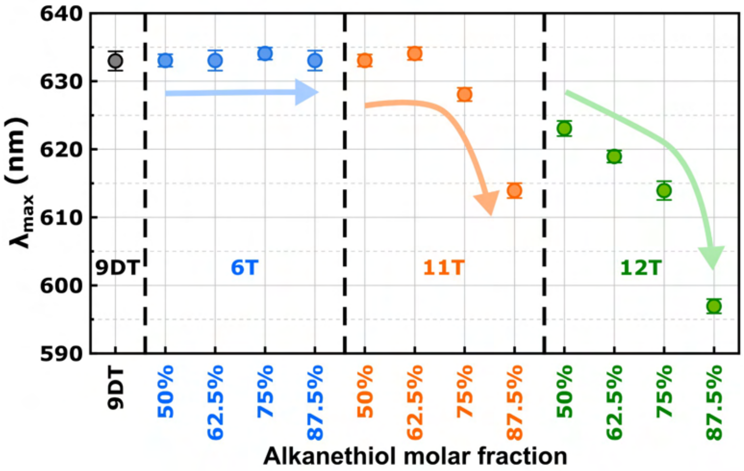

Figure 6.29: Spectral positions of the LSPR bands from UV/Vis measurements from GNP films prepared with pure 9DT cross-linkers and mixtures of AMT/9DT with varying AMT molar fractions. Taken with permission from C.-Y. Liu “From Fabrication to Application: Developing High-Performance Gold Nanoparticle-Based Sensors Using Mixed Ligand/Linker Systems”, University of Hamburg, 2024.

GNP films.[16, 18, 21, 25] Hence, the difference in interparticle distance $\Delta\delta$ relative to the pure 9DT films was estimated as follows:

$$ln\left(\frac{\sigma}{\sigma_{9\mathrm{DT}}}\right) \sim -\beta \cdot \Delta\delta \sim -1 \cdot \Delta\delta \; . \tag{6.2}$$

The resulting distances of the 6T/9DT films changed only slightly. A decrease of approximately 0.8 Å was calculated for the 87.5 %6T-9DT film compared to pure 9DT. The distance change of the 11T/9DT films was also modest. The 87.5 % 11T/9DT film also showed an increase in distance of approximately 0.8 Å. In contrast, the difference in interparticle distance for the 12T/9DT films was more pronounced, with an increase of 3.4 Å at the highest molar fraction of 12T compared to pure 9DT.

For further evaluations, the interparticle distances were also estimated from the position of the localized surface plasmon resonance (LSPR) band in UV/Vis measurements (see Figure 6.29). C.-Y. Liu observed no significant difference in the LSPR band position of the 6T/9DT film, compared to the pure 9DT film, suggesting that the interparticle distances in both films were similar. In contrast, the 11T/9DT and 12T/9DT films exhibited a slight and a more pronounced shift towards shorter wavelengths, respectively, which correlated with a slight and a more substantial increase in interparticle distance as the AMT ratio increased, compared to the pure 9DT film.

Both UV/Vis and electrical conductivity measurements revealed that the interparticle distance increased upon the addition of 12T ligands to the 9DT cross-linker, with a more pronounced increase observed at higher molar fractions of 12T. In the case of the longer AMT ligand, 11T, a rise in both conductivity and UV/Vis LSPR band position was found at the highest molar fraction of 11T. However, for the 75 % 11T fractions, the results from the two measurement techniques diverged. While the conductivity measurements showed no significant increase in interparticle distance compared to pure 9DT, the UV/Vis measurements indicated a substantial increase. Conversely, for the 6T ligand, the conductivity measurements suggested a decrease in interparticle distance, whereas the UV/Vis data showed no change relative to pure 9DT.

Table 6.6: Nearest-neighbor distances (NNDs) and interparticle distances δ of pure 9DT und different AMT/9DT mixed-ligand films. The NNDs were extracted from the GISAXS measurements from C.-Y. Liu, and δ were calculated by subtracting the GNP size of 7.48 nm.

GNP Film	NND [nm]	δ[Å]	$\delta - \delta_{\mathrm{9DT}}$ [Å]
9DT	8.80	13.2	-
87.5% 6T-9DT	8.74	12.6	-0.6
87.5% 11T-9DT	9.33	18.5	5.3
50% 12T-9DT	9.40	19.2	6.0
87.5% 12T-9DT	9.19	17.1	3.9

Several factors may be the reason for the discrepancies in interparticle distances observed between the two measurement techniques employed by C.-Y. Liu. Firstly, the UV/Vis measurements only include a small localized area. Although the LSPR bands depicted in Figure 6.29 were averaged over four different spots, these may not accurately represent the entire film. In mixtures, the two ligands may segregate into distinct domains or may not be uniformly distributed. Consequently, the selected spots may predominantly reflect areas enriched with one ligand. Thus, the interparticle distance obtained from the UV/Vis measurements may be biased. Similarly, the electrical conductivity measurements may not fully capture the average interparticle distances across the entire film. These measurements specifically focused on the tunneling distances along the percolation pathways, which may differ from the distances measured throughout the entire film.

For further insights, GISAXS measurements were performed by C.-Y. Liu on five selected samples. The interparticle distances, calculated from the GISAXS measurements, are summarized in Table 6.6.

The interparticle distance of the 6T/9DT mixture, as calculated by GISAXS, exhibited a slight reduction of 0.6 Å compared to the pure 9DT film. This finding aligned with the trends observed in conductivity measurements, which indicated a difference of 0.8 Å in interparticle distance, as derived from conductivity using Equation (6.3). In the case of the 11T/9DT mixture, where the molar fraction of 11T was 87.5 %, the GISAXS measurements revealed that the interparticle distance was 5.3 Å greater than that of the pure 9DT films. This trend is consistent with both UV/Vis and conductivity measurements. However, the value significantly exceeded the increase predicted by the conductivity data.

For the 87.5% 12T-9DT film, the interparticle distance measured by GISAX corresponds to an increase of 3.9 Å with respect to pure 9DT. This increase is comparable to the estimated increase from conductivity data (3.6 Å). Despite this, both UV/Vis and conductivity measurements suggest that the interparticle distance of the 50% 12T-9DT film should be lower than that of the higher fraction of the 12T/9DT mixture. Contrary to this expectation, the distance from GISAXS measurements of the 50% 12T-9DT film is significantly larger than that of the 87.5% 12T-9DT film. Furthermore, based on these two measurement techniques, the interparticle distance of the 87.5% 12T-9DT should also be larger than that of the 87.5% 11T-9DT film.

While the reliability of UV/Vis and conductivity measurements to predict the interparticle distances of the films have been discussed above, distances calculated from GISAXS measurements may also be inaccurate. The interparticle distance of another GISAXS measurement by C.-Y. Liu of a 9DT film, prepared and measured on a different day, for example, deviated by about 1 Å from the first measurement.[176] This could also explain why the trend of increasing interparticle distance with higher molar fractions of 12T was not observed in the GISAXS measurements, as the films with 87.5% 11T-9DT and 50% 12T-9DT were measured on a different day than the other three samples. Deviations could be attributed to slight differences in sample alignment or assumptions made during the analysis. For example, a uniform GNP size and interparticle distances, and the presence of an FCC superlattice structure are assumed. However, the film's structures are usually not homogeneous (see Figure 6.30).

Moreover, it is important to note that the actual ligand composition on the GNP surfaces was not analyzed further. Instead, it was assumed that the molar ratio of ADT and AMT ligands on the GNPs were the same as that of the solution. However, several studies have indicated a preference for the adsorption of one ligand type.[156, 173] Some studies even found that the molar fraction in the film was almost independent of the solution composition, particularly in cases with attractive electrostatic interactions between ligands.[177] Conversely, the results of C.-Y. Liu clearly demonstrate that the properties of the films depend on the molar fraction in solution, suggesting that the molar fraction on the GNPs resembles that in solution.

Apart from extracting interparticle distances, GISAXS measurements can also be evaluated regarding the ordering in the films. In the five selected films, investigated by C.-Y. Liu, distorted arrangements of the GNPs were observed. The films seemed to consist of numerous small ordered domains. In the films with the highest fractions of longer AMT ligands (87.5% 11T-9DT and 87.5% 12T-9DT) these domains appeared to be larger and well-ordered. These observations were supported by SEM images from C.-Y. Liu (see Figure 6.30 h and j).[176] A similar GNP morphology for mixtures has been predicted by Merz et al. for alkanethiols and mercapto-alcohols. They observed that when shorter AMTs were combined with longer mercapto-alcohols, there was reduced phase separation compared to mixtures consisting of longer AMTs and shorter mercapto-alcohols. In the latter case, the authors reported strong phase separation, leading to the formation of Janus-like monolayers.[171]

The formation of domains in the 11T/9DT and 12T/9DT films is further supported by the following observation made by C.-Y. Liu:[176] attempts to apply the LbL-SC procedure to produce pure AMT-stabilized films were unsuccessful. However, this technique proved effective for pure 9DT films as well as all AMT/9DT mixed-ligand films, even in cases where the interparticle distance exceeded 1.5 Å (the length of an all-trans 9DT molecule), where a cross-linkage should not be possible. The dependence of the success of the technique on the presence of 9DT ligands suggests that cross-linkage is required in this approach. Given that the average interparticle distances in the 11T/9DT and 12T/9DT mixtures are too large for 9DT ligands to facilitate cross-linking, and considering the observed domains in GISAXS and SEM measurements, it is possible that two distinct domains exist within these structures. One domain may have a higher average interparticle distance and be primarily occupied by long AMT ligands, while the other exhibits a smaller average interparticle distance, predominantly composed of 9DT cross-linkers, as shown in Figure 6.31. This distinction may also help explain the discrepancies observed between the interparticle distances derived from conductivity data and those obtained from UV/Vis measurements.

In the following sections, we will discuss MD simulations together with charge transport calculations on mixed-ligand systems to further understand the underlying atomistic structure of the mixed-ligand GNP films and to validate or falsify the proposed formation of domains.

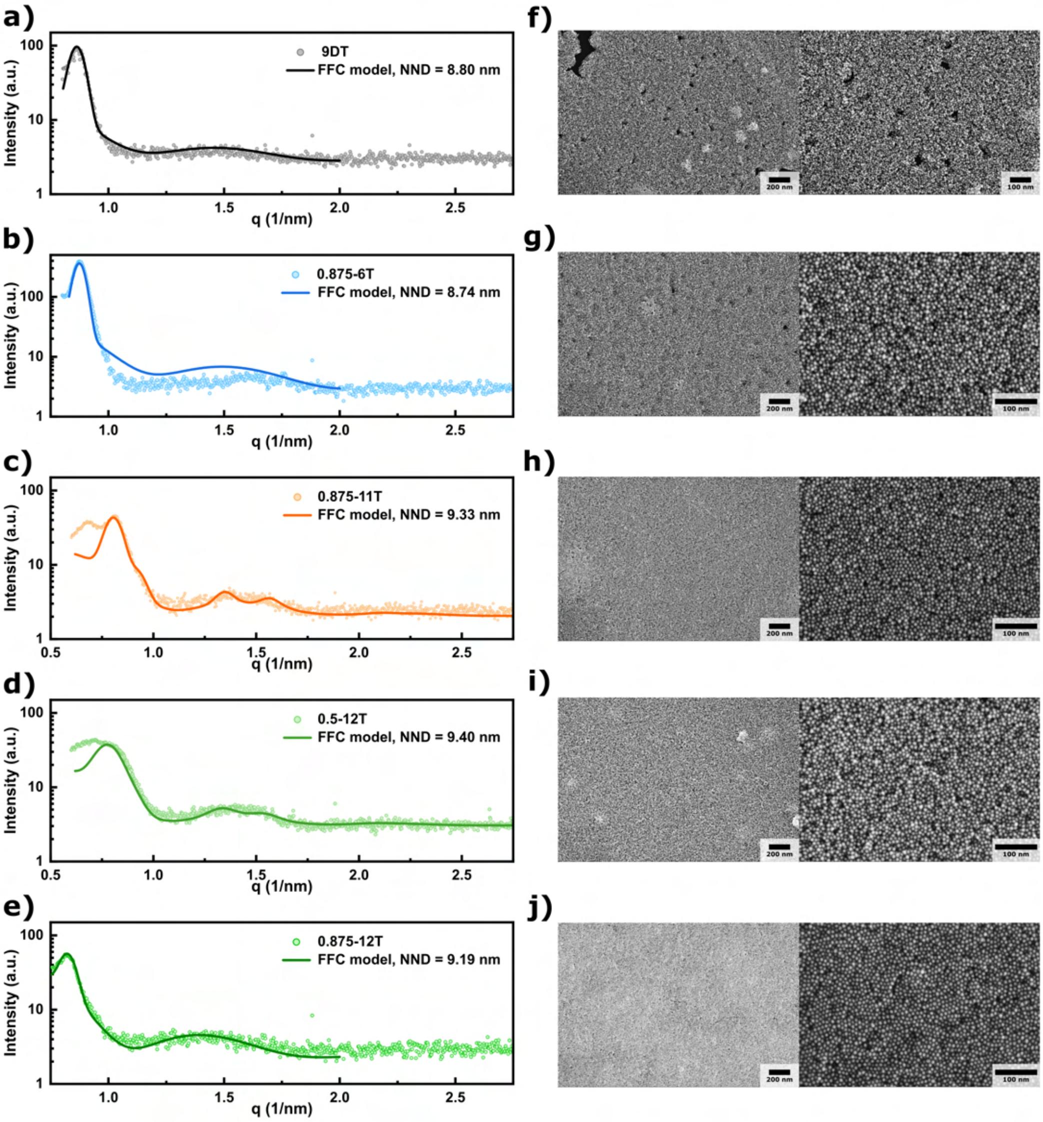

Figure 6.30: Left: GISAXS measurements of thin GNP films, prepared with a) pure 9DT, b) 87.5 % 6T/9DT, c) 87.5 % 11T/9DT, d) 50 % 12T/9DT, and e) 87.5 % 12T/9DT. Average nearest-neighbor distances were computed from fitting a fcc model (solid lines) onto the scattering data points. Right: SEM images of the thin films prepared with f) pure 9DT, g) 87.5 % 6T/9DT, h) 87.5 % 11T/9DT, i) 50 % 12T/9DT, and j) 87.5 % 12T/9DT. Taken with permission from C.-Y. Liu “From Fabrication to Application: Developing High-Performance Gold Nanoparticle-Based Sensors Using Mixed Ligand/Linker Systems”, University of Hamburg, 2024.

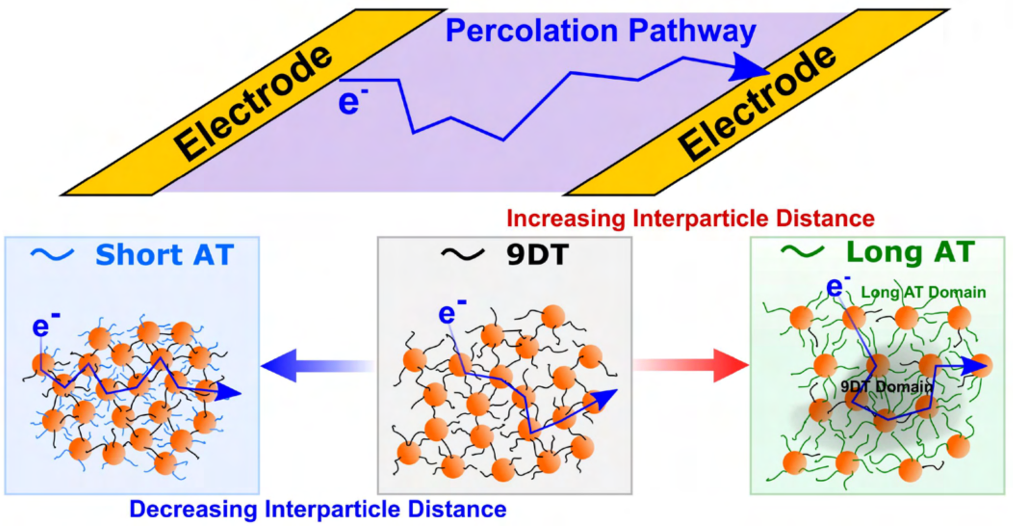

Figure 6.31: Percolation pathways for electron transport in GNP films composed of various AMT/9DT ligand mixtures with AMT ligands shorter (e.g. 6T) and those longer (e.g. 11T and 12T) than 9DT. The blue panel illustrates the effect of incorporating shorter ligands, which results in a slight reduction in average interparticle distances compared to pure 9DT (gray panel). The interparticle distance in these mixtures is small enough for 9DT molecules to cross-link, enhancing connectivity within the film. Conversely, the green panel demonstrates the introduction of longer AMT ligands, such as 11T and 12T, potentially leading to the formation of two distinct domains: one dominated by AMT and the other by 9DT. Electrons can traverse both domains that collectively contribute to the overall conductivity of the film. Taken in parts with permission from C.-Y. Liu et al. *Adv. Mater. Interfaces* 2024, 11, 2301058.

6.2.2 Structure of Mixed-Ligand Self-Assembled Monolayers

To gain first insights into the mixing behavior of ADT and AMT ligands, MD simulations with a ReaxFF of mixed-ligand monolayers were performed. The same ligand coverage and arrangement as in pure ADT or AMT monolayers was estimated (see Section 6.1.1). For a 1:1 12T/9DT mixtures, four 9DT and four 12T ligands were placed onto a Au(111) surface, consisting of 72 gold atoms in three layers. All ligands were initially adsorbed in an all-trans, non-tilted conformation. Semi-periodic boundary conditions were applied to extend the monolayer structure along the surfaces. To account for limitations of the ReaxFF when modeling thiol or thiolate groups that are not directly attached to a gold surface, as discussed in Section 6.1.4, we again used a PYTHON script (see Appendix B, Code Example 1) to filter out trajectories where reactions involving the thiol side groups occurred.

Five different arrangements of the ligands on the gold surface were investigated (see Figure 6.32), based on findings from experiments discussed in the beginning of Section 6.2.1. First, we prepared two structures in which four 12T and four 9DT ligands were placed randomly on the surface, without any ordering (random a and random b in Figure 6.32). Next, we created a configuration in which the four 9DT ligands occupied one-half of the surface while the four 12T ligands occupied the other, simulating the presence of small domains. To investigate the stability of stripe-like domains, we designed a structure with four alternating rows, where each row consisted either of two 12T ligands or two 9DT ligands. As the unit cell only consists of eight total ligands, the formation of large domains with only one unit cell was not possible. Therefore, we constructed a unit cell containing eight 9DT ligands and another with eight 12T ligands. To estimate the energy of the separate-domain configuration, we averaged the energies of both structures by halving each and then summing the results.

Five independent MD simulations were started from the thus-constructed initial structures, and the energies were averaged over the complete simulation time of 50 ps, excluding a tempering phase of 2.5 ps, where the ligands moved into tilted arrangements. The average total energies of the ligand mixtures are summarized in Table 6.7. The energies of these different ligand arrangements are comparable, suggesting that all configurations could be feasible in experimental settings, or that the differences only become pronounced for larger domains. The striped structure may be the least probable configuration, as it exhibits a higher energy compared to the other arrangements.

At the beginning of Section 6.2, we discussed the mixing behavior of various ligand combinations, with a particular focus on different lengths of AMT ligands, which have been extensively studied in experiments. The Stellaci group reported the formation of one-ligand-wide, stripe-like domains, similar to the “striped” structure examined in this work, which were highly discussed within the scientific community. Our preliminary results on SAM structures suggest that this configuration is the least stable among those investigated. In contrast, randomly mixed or separated structures appear to play a more significant role.

The formation of distinct domains has been especially noted in experiments on ligand combinations differing by the length of their carbon chains or by the functional groups at their tails.[169, 170, 172, 173, 175] However, other studies have indicated that mixing AMT ligands of different lengths resulted in no observable separation into domains,[158] particularly when the difference in length was less than three carbon units.[173] In the case of 12T/9DT mixture, investigated in this section, both the difference in carbon chain length – exceeding the previously reported threshold of three carbon units – and the variation in tail groups suggest that the arrangement into separate domains should be favored. Surprisingly, our findings indicate that both randomly mixed and separated structures exhibit similar stability. This may imply that the difference in lengths, along with the stability resulting from intermolecular interactions between the SH tail groups, is not substantial enough to drive domain separation. Alternatively, it is however also possible that these intermolecular interactions are not adequately captured by the ReaxFF employed in our simulations, resulting in the non-favoring of the separated structures.

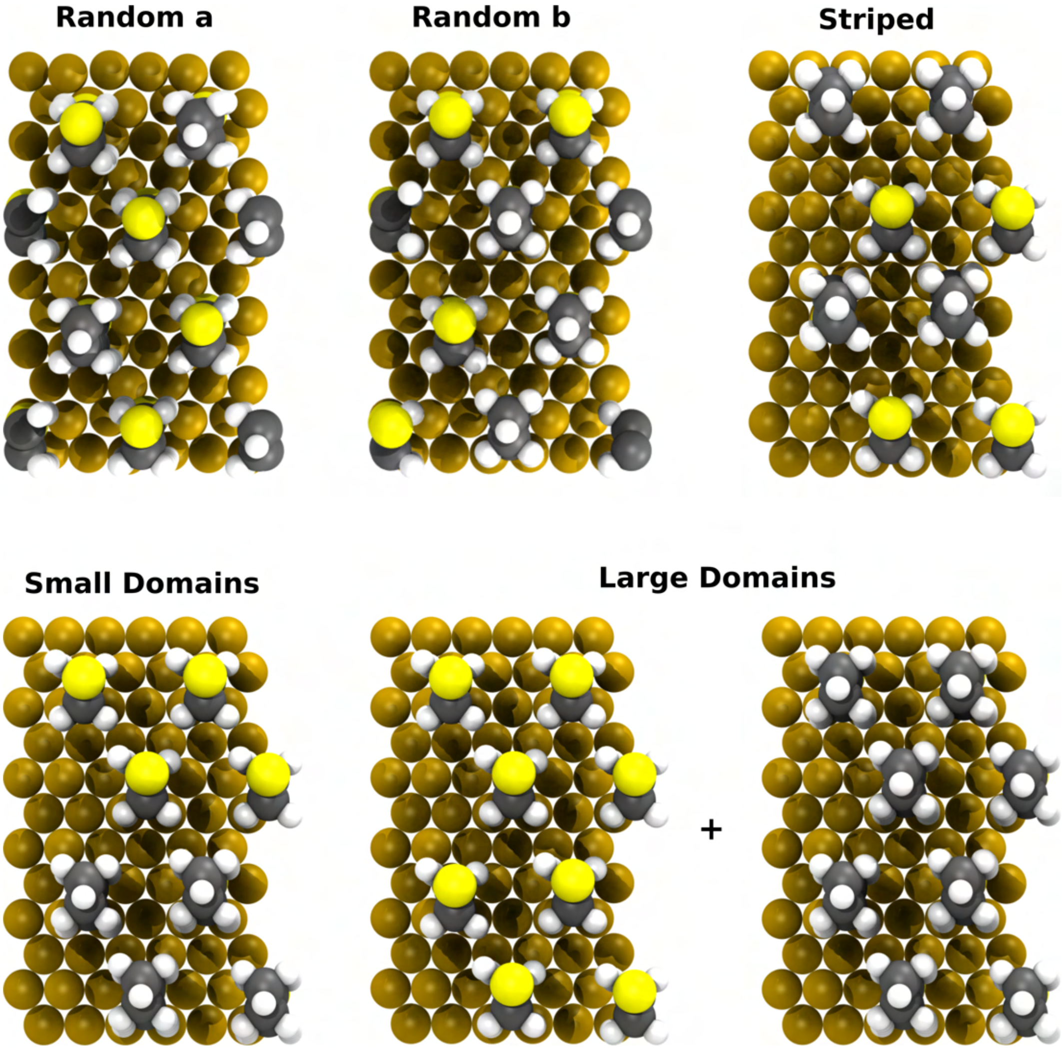

Figure 6.32: Investigated ligand arrangements for 9DT/12T mixtures (1:1). The analysis includes two randomly mixed structures (random a and b), a one-molecule-wide stripe-like domain structure (striped), and two structures featuring domains of different sizes (small and large domains). The large domain structures were modeled by considering two interfaces: one composed purely of 12T ligands and the other of 9DT ligands. The total energy for these configurations is calculated by summing the energies of both interfaces and then halving the result.

Table 6.7: Total energies of different SAM 9DT/12T (1:1) mixture arrangements. Energies were averaged from five independent MD simulations with different velocity seeds over the complete simulation of time of 50 ps, excluding a tempering phase of 2.5 ps.

Ligand arrangement	Average energy [eV]
small domains	-1509.87 ± 0.32
random a	-1509.79 ± 0.80
random b	-1509.51 ± 0.39
striped	-1508.65 ± 0.26
large domains	-1509.74 ± 0.37

Furthermore, it is important to acknowledge that our preliminary results offer only limited insights into the structure of three-dimensional GNP assemblies, where the ligand arrangements may be more complex. For instance, our simulations on domain structures depict a separation of ligands into highly ordered, distinct domains. In contrast, GNP assemblies may exhibit a different phenomenon, where ligands separate into domains that are predominantly composed of one ligand type while still containing a minority of the other ligand type, which is not included in our model. Due to the small size of our simulation cell, we can also not consider potential variations of the ligand composition at the transition phase from one domain to the other.

6.2.3 Comparing Potential Structures of Mixed-Ligand Interfaces

In the next step, the single interface model, as described earlier, was applied to study the properties of mixed-ligand GNP assemblies. Especially the mixtures studied by C.-Y. Liu in her PhD thesis (6T/9DT, 11T/9DT, and 12T/9DT) were investigated. Our preliminary analysis of potential mixed-ligand monolayer structures, combined with insights drawn from experimental results from the literature, has demonstrated that both random distributions of AMT and ADT ligands, as well as the formation of distinct, separated domains, are reasonable. Based on these findings, we proposed three different structural arrangements for AMT/ADT mixed-ligand interfaces, as shown in Figure 6.33. When the two ligand types mix into random distributions, the ADT ligands can either cross-link the gold surfaces (see Figure 6.33, *interlinked* model) or remain attached to just one of the gold surfaces (*intercalated* model in Figure 6.33). The preferred structural model among these two may vary depending on the length of the AMT ligand. For AMT ligands shorter than 9DT, such as 6T, the ligands may be sufficiently short that the 9DT ligands cross-link (as shown in the *interlinked* model). Conversely, when the AMT ligand are larger than 9DT, the *interlinked* model may become unreasonable.

When the two ligand types separate into domains, an interface would consist (almost) exclusively of either ADT or AMT ligands (*domain* model in Figure 6.33). Depending on the property measured and the experimental conditions, the overall GNP behavior may be a mixture of both types of interfaces or be dominated by one of them. From experimental observations, as described in Section 6.2.1, the *domain* model should be preferred for longer AMT ligands, such as 11T or 12T, while mixtures with 6T ligands should rather arrange as shown in the *interlinked* model.

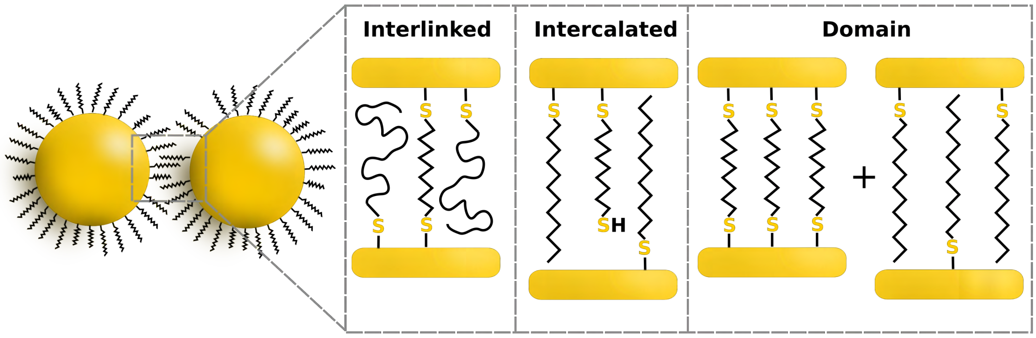

Figure 6.33: Different structural arrangements plausible for AMT/ADT mixed-ligand interfaces. When the ADT and AMT ligands mix, the ADT ligand can either cross-link the surfaces (*interlinked* model), or remain attached to only one surface (*intercalated* model). AMT and ADT ligands could also not mix but form separated domains (*domain* model).

6.2.3.1 Interfaces with Eight Total Ligands per Unit Cell

For pure ADT cross-linked interfaces, as discussed in Section 6.1.2, the interface contains a total of eight ligands per unit cell. As a first approach, we used the same number of total ligands for our mixed-ligand interfaces. At a AMT to 9DT ratio of 1:1, for example, the interface consisted of four AMT and four 9DT ligands (as shown in Figure 6.34, right). Initially, the ligands were adsorbed onto the surfaces in an all-trans, non-tilted arrangement.

We prepared input structures for the three mixtures (6T/9DT, 11T/9DT, and 12T/9DT) in all three structural models (*interlinked*, *intercalated*, and *domain*), each with different AMT to total thiol ratios ranging from 50 to 87.5 %. The only exception was the 6T/9DT mixture, where the *intercalated* model could not be realized as the 6T molecule is much shorter than the 9DT molecule, so the 9DT always cross-linked in the initial, straight structure. To prepare the *domain* structures, simulations with pure 9DT interfaces and pure AMT interfaces were conducted and the individual surface-to-surface distances were each averaged over 10 simulations, separately. This simulates a scenario in GNP assemblies where some interfaces are completely covered with AMT ligands, while others are exclusively cross-linked with ADT ligands. The effective surface-to-surface distances δ_{eff} of the mixtures were derived by a linear combination model with weighting factors A and B, reflecting the relative molar fraction of 9DT and AMT ligands

$$\delta_{\text{eff}} = A \times \delta_{\text{MT}} + B \times \delta_{\text{DT}} \ . \tag{6.3}$$

To prepare the *interlinked* structures, a structure was extracted from a pure AMT interface simulation, where the surface-to-surface distance was around 17 Å (length of an all-trans 9DT ligand plus 4 Å). Then, AMT ligands were randomly deleted according to the desired mixing ratio and were replaced by upright-standing, all-trans 9DT ligands (see Figure 6.34, left).

With each mixed-ligand interface structure, 10 individual MD simulations with different initial velocity seeds were performed using a ReaxFF. In these simulations, the distance between the gold surfaces was reduced by pushing the surfaces together. The preferred surface-to-surface distances were extracted from the minimum-energy structure of each simulation. Details on the simulation method can be found in Section 8.1. The averaged surface-to-surface distances are summarized in Figure 6.35 for all structural models and AMT ratios.

Based the experimental study by C.-Y. Liu, discussed in Section 6.2.1, the interparticle distance in the 6T/9DT structure is expected to be similar to or slightly smaller than that

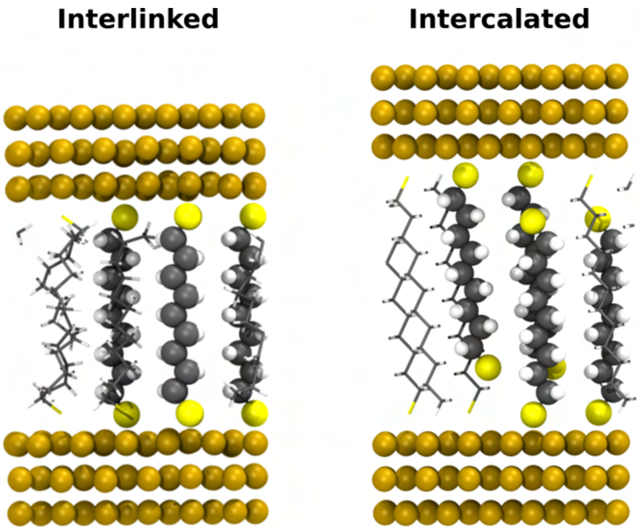

Figure 6.34: Initial structures of 12T/9DT (1:1) mixed-ligand interfaces. The 9DT ligands either cross-link the surfaces (*interlinked* model, left) or are only connected to one surface *intercalated* model, right). In both structures, the 9DT ligands are displayed in a ball-and-stick representation, while the 12T ligands are shown as lines. This way, the difference between both models can be highlighted (9DT ligands cross-link in the left model, and are only connected to one gold surface in the right model.

in the pure 9DT structure, and this distance should remain relatively independent of the 6T ratio. In contrast, for the 11T/9DT and 12T/9DT mixtures, an increase in interparticle distance compared to pure 9DT was observed, where the distance increased as the ratio of the AMT ligand increased.[176] Additionally, the experimental results indicated that the 6T/9DT mixture adopts a randomly distributed structure, where the 9DT ligands most likely cross-link the GNPs, consistent with our *interlinked* model. Conversely, the 11T/9DT and 12T/9DT mixtures likely form distinct domains, as illustrated in our *domain* model.

The trends observed in the MD simulations are partially consistent with experimental trends from UV/Vis and conductance measurements by C.-Y. Liu. As anticipated, the surface-to-surface distance increased with a higher proportion of longer AMT ligands (11T or 12T) and decreased when the proportion of shorter AMT ligand (6T) increased, compared to the distance of pure 9DT interfaces. However, the dependence of the distance on the AMT fraction was less pronounced for the longer AMT ligands than expected from experiments, while it was more pronounced for the shorter AMT ligands than anticipated based on the experimental results. Overall, the interparticle distances of the three investigated structural models (*interlinked*, *intercalated*, and *domain*) do not deviate significantly. Consequently, no prediction on the potential structure of the mixed-ligand systems could be made, based on the interparticle distances.

The lowest-energy structures were extracted from 5 selected MD simulations and used for charge transport calculations. These calculations were performed using DFTB electronic structure calculations using Green's functions, as described in Section 8.2. The resulting transmissions at the Fermi energy (which are related to the zero-bias conductance via Equation (8.1) are shown in Figure 6.36. For the 6T/9DT mixed-ligand system the transmission at the Fermi energy was increased, compared to the pure 9DT system, in both the *interlinked* and the *domain* model. This increase is in agreement with experimental conductivity data from C.-Y. Liu, shown in Figure 6.28. In contrast, the transmission results for the 12T/9DT and 11T/9DT systems showed significant deviations from experimental expectations. While C.-Y. Liu observed a significant decrease in conductivity for the 11T/9DT and 12T/9DT films compared to pure 9DT films, the calculated transmissions at the Fermi

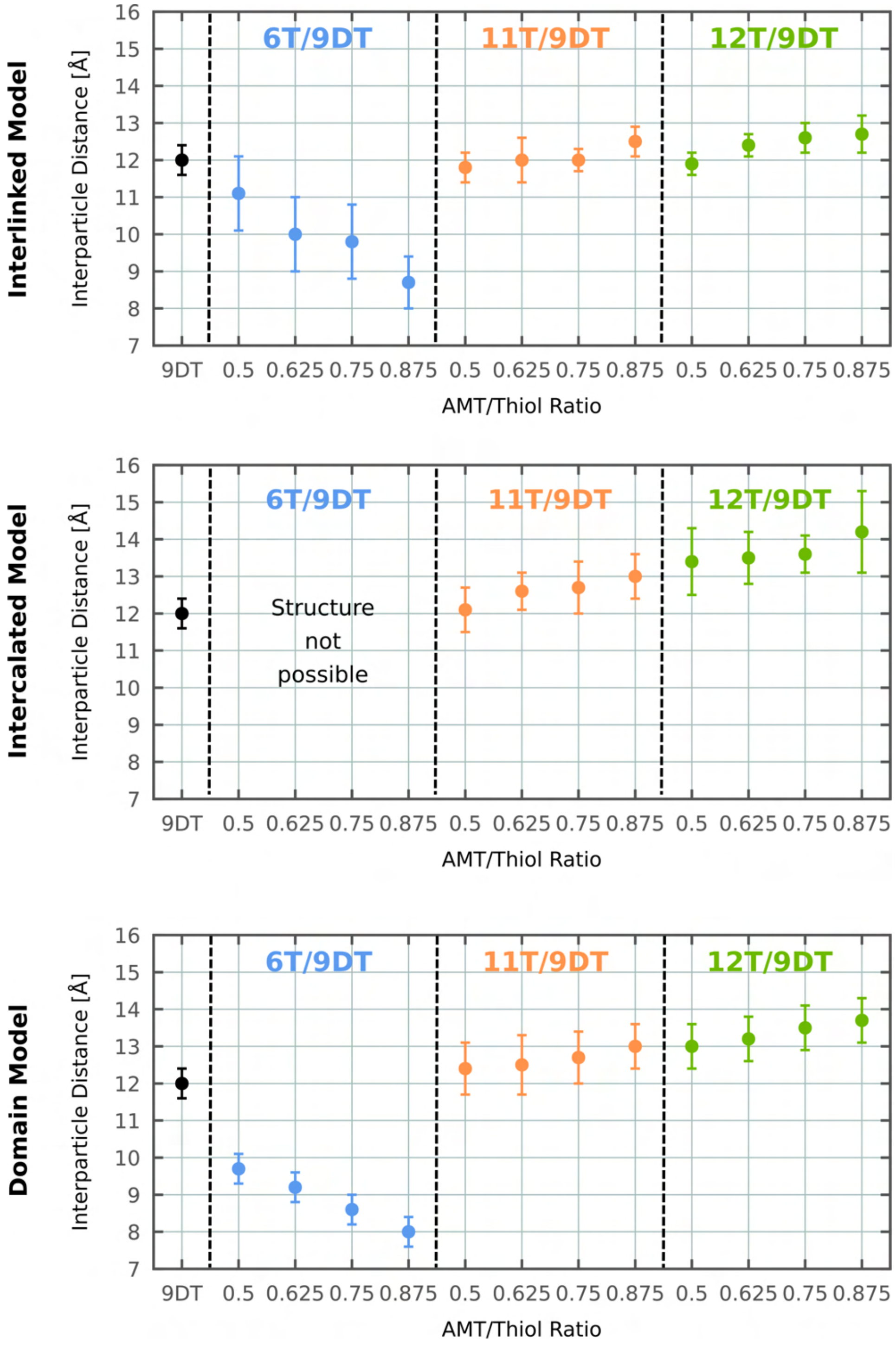

Figure 6.35: Average interparticle distances from 10 MD simulations for pure 9DT interfaces (black), as well as mixtures of 6T/9DT (blue), 11T/9DT (orange), and 12T/9DT (green), with varying monothiol to total thiol (AMT+ADT) ratios. The gold surfaces of the interface structures were covered with ligands such that 50 % of the positions were occupied. Three distinct structural models were examined: the *interlinked* model depicts the scenario where the 9DT ligands cross-link the two surfaces (top), the *intercalated* model illustrates the situation where the 9DT ligands do not engage in cross-linking (center), and *domain* model shows the segregation of 9DT and AMT ligands into two separate domains (bottom). In the case of the 6T/9DT mixture, the *intercalated* model is not feasible due to the sufficiently small intersurface distance, which always results in cross-linking.

energy for these mixtures was comparable to, and in some cases even greater than that of the pure 9DT system. Furthermore, as the simulated interparticle distances also did not align with experimental observations, these results suggested that the interface model may inadequately represent the structure of mixed-ligand films.

To evaluate the accuracy of interface model for describing mixed-ligand systems, we compared the interparticle distances from our simulations with GISAXS measurements, performed by C.-Y. Liu as part of her PhD thesis (see Table 6.6). While the distances of the pure 9DT interface model aligned well with distances measured by GISAXS (~ 12 Å from simulations, and $\sim 12-13$ Å from experiments by Chih-Yin Liu), distances for mixed-ligand systems were significantly underestimated. For the 87.5 % 6T-9DT film, for example, an interparticle distance of 12.6 Å was measured, while a distance of around 8 Å was obtained from the simulations. Similarly, for the 87.5 % 11T-9DT film, a distance of 18.5 Å was measured, while simulations resulted in a distance of around 13 Å.

In Section 6.1.3, we already discussed that a total number of eight ligands per unit cell resulted in a very good description of the interparticle distances compared to experimental results for ADT interfaces, while the distances of AMT interfaces were significantly underestimated at this ligand coverage. When the ligand coverage in the AMT interfaces was increased up to 75 % (corresponding to a total of 12 ligands per unit cell) the alignment of the interparticle distance with experimental values was increased. It is plausible that by increasing the ligand coverage in the mixed-ligand interface structures, the interparticle distances and the charge transport properties of these systems may be described more accurately.

6.2.3.2 Increasing the Ligand Coverage

The simulations from the previous section were repeated with increased ligand coverage, such that 75 % of the adsorption sites were covered. This was chosen, as this was the optimal coverage in AMT interface simulations (see Section 6.1.3). Input structures were again prepared for the three mixtures (6T/9DT, 11T/9DT, and 12T/9DT) in all three structural models (*interlinked*, *intercalated*, and *domain*). For each model and mixtures, different AMT to total thiol ratios ranging from 50 to 87.5 % were investigated. Exemplary structures are shown in Figure 6.37 and in the Appendix, Figure A.13. With the increased total number of ligands in the unit cell, the *intercalated* model was possible also for the 6T/9DT mixture, which was not the case with the lower ligand coverage investigated in the previous section. On the other hand, the *interlinked* structure was only feasible for the 6T/9DT mixture. The preferred surface-to-surface distance of both the 11T and 12T interfaces were too high to replace ligands with 9DT such that the 9DT could act as cross-linker. With 11T, for example, the distance, extracted from MD simulations, was around 20.5 Å, agreeing well with experimental distances of 11T-stabilized GNP assemblies, as described in Section 6.1.3. The size of a fully extended 9DT ligand, on the other hand, is only about 13 Å.

The surface-to-surface distances of each mixture in all possible models, each averaged from 10 individual MD pushing simulations, are summarized in Figure 6.38. Based on experimental results by C.-Y. Liu (discussed in detail in Section 6.2.1), the interparticle distance of the 6T/9DT mixtures should be close to that in pure 9DT films. A minor decrease or no change in interparticle distance, depending on the measurement technique, was observed when the proportion of 6T was increased. GISAXS and SEM images suggested no or only minor formations of domains in these mixtures. In our simulations, intersurface distances in the 6T/9DT systems were close to that of pure 9DT interfaces for all three structural models. In the *intercalated* as well as in the *domain* model, however, the interparticle distances were slightly larger than in the pure 9DT interface, while experiments suggested that they should rather be smaller than the distance in pure 9DT films. This was the case in the *interlinked* model, where the interparticle distance was almost 1 Å smaller than the distance of the pure 9DT interface. Compared to GISAXS data from C.-Y. Liu, a quantitative agreement of the simulated with the experimental interparticle distance was also reached with the *interlinked*

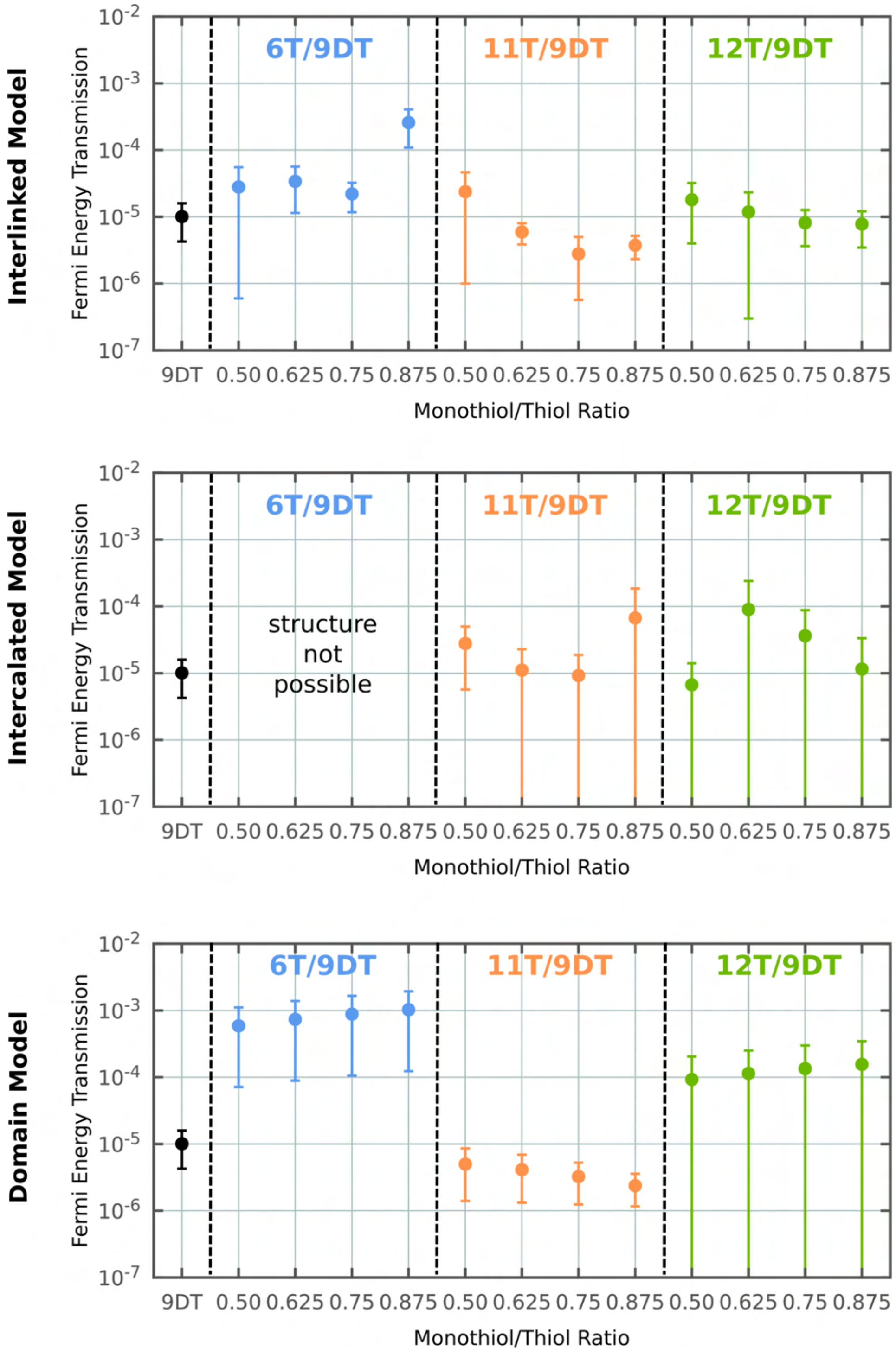

Figure 6.36: Average transmission at the Fermi energies, each averaged from 5 structures, extracted from MD pushing simulations, of 6T/9DT (blue), 11T/9DT (orange), and 12T/9DT (green) mixed-ligand interfaces versus the AMT to total thiol (AMT+ADT) ratio of the mixtures. The gold surfaces of the interface structures were covered with ligands such that 50 % of the positions were occupied. Three distinct structural models were examined: in the *interlinked* model 9DT ligands cross-link the two surfaces (top), in the *intercalated* model 9DT ligands cross-link (center), and in the *domain* model 9DT and AMT ligands segregate into two separate domains (bottom). In the case of the 6T/9DT mixture, the *intercalated* model is not feasible due to the sufficiently small intersurface distance, which always results in cross-linking.

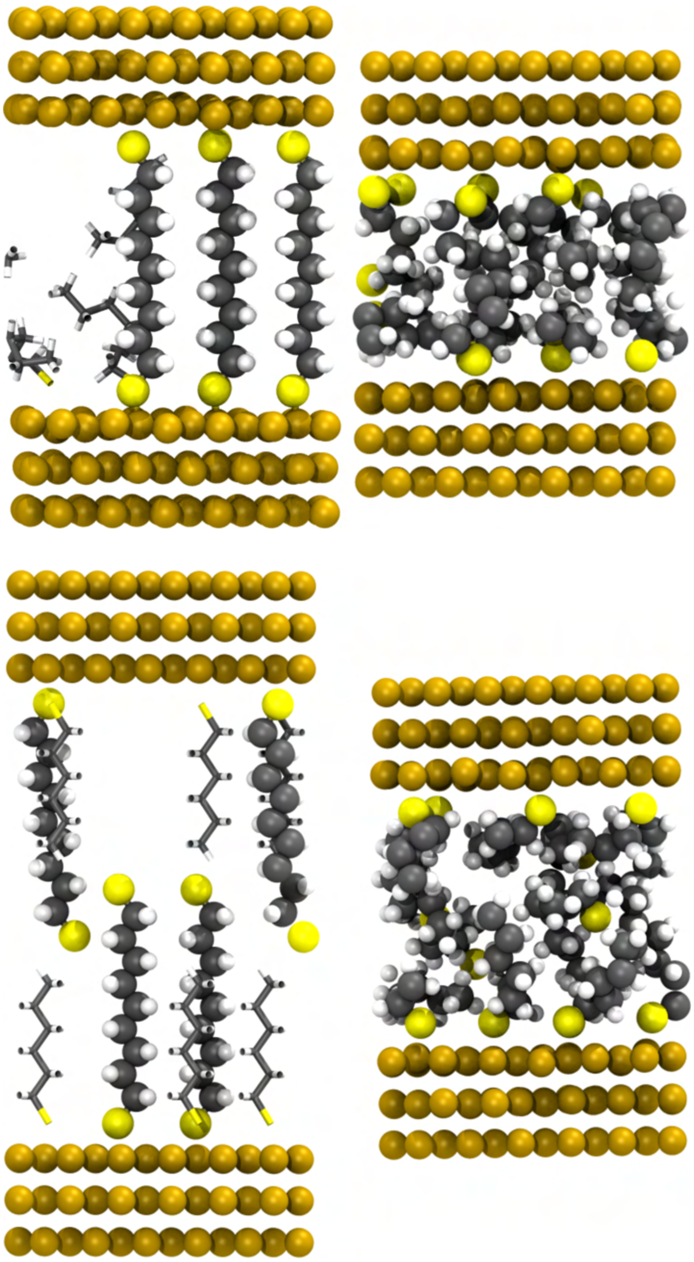

Figure 6.37: Exemplary initial (left) and lowest-energy structures (right) of 6T/9DT mixed-ligand interfaces. The 9DT ligands initially either cross-link the surfaces (*interlinked* model, top) or are connected to only one of the surfaces (*intercalated* model, bottom).

model. For the 6T/9DT mixture, an interparticle distance of 12.6 Å was measured with GISAXS for the mixture with 87.5 % of 6T, close to the distance of 12.2 Å obtained from MD simulations of the mixture containing 90 % 6T. The distances obtained for 6T/9DT interfaces with the *intercalated* and the *domain* model were in the range of 13 to 14 Å, deviating more from the GISAXS distance than the *interlinked* model. On the other hand, GISAXS measurements are not fully reliable, and deviations of around 1 Å have been found for the same film when they were measured on different days (see Section 6.2.1). So a clear answer to the question, which model best describes the structure of the 6T/9DT interfaces can not be made only by comparing the interparticle distances.

For the 11T/9DT and the 12T/9DT film, the experimentally obtained interparticle distances were shown to be significantly larger than the distance in pure 9DT films, increasing with rising ratios of the AMT ligand (see Section 6.2.1). This trend was also obtained from MD simulations of 11T/9DT and 12T/9DT interfaces with the *intercalated* and the *domain* model (see Figure 6.38 center and top, respectively). As described earlier, the *interlinked* model was not possible for these mixtures. Comparing the intersurface distances obtained from the *intercalated* and the *domain* model, the distances from the former model were almost 1 Å larger compared to the domain structures, potentially caused by the reduced ordering in these structures. Interparticle distances from GISAXS measurements by C.-Y. Liu, summarized in Table 6.6, ranged from around 17 to 19 Å for selected 11T/9DT and 12T/9DT mixtures. This interparticle distance range was better represented by the *domain* model in the simulation than by the *intercalated* model, suggesting that this might describe the structure of 11T/9DT and 12T/9DT mixed-ligand GNP assemblies more accurately. However, as discussed before, GISAXS measurements may not always be entirely reliable, making it again difficult to definitively favor one structural model over the other, purely based on the interparticle distance data.

To gain further insights into which of the structural models shown in Figure 6.33 best describes the features of the different mixed-ligand films, we also analyzed the charge transport properties of these systems. Therefore, the lowest-energy structures extracted from the MD pushing simulations were used and prepared for charge transport calculations using self-consistent DFTB electronic structure calculations and the Landauer coherent tunneling approach, as described in Section 8.2. The transmissions at the Fermi energies, are summarized in Figure 6.39 for all three models. As described in the Introduction, charge transport in GNP assemblies occurs through thermally activated tunneling, and it particularly depends on the distance between the GNPs (see Equation (3.1)). Consequently, the dependence of the transmission at the Fermi energy on the AMT ratio was expected to be similar as the dependence of the interparticle distance on the AMT ratio. In case of the 6T/9DT mixture, the transmission was expected to be similar as or slightly larger than the pure 9DT interface transmission. The transmission of the 11T/9DT and the 12T/9DT mixtures, on the other hand, were expected to be lower than the transmission of the pure 9DT system, and the transmission was expected to decrease significantly with rising AMT proportion in the mixture. These trends were also observed in conductivity measurements by C.-Y. Liu, as shown in Figure 6.28.

For the 6T/9DT interfaces, the calculated transmissions at the Fermi energies from the *intercalated* and the *domain* model (see Figure 6.39 center and bottom, respectively) were lower than the transmission of the pure 9DT interface, which is contrary to expectations based on Equation (3.1), and results from conductivity measurements by C.-Y. Liu. Additionally, in both of these models, the transmission at the Fermi energy decreased with increasing ratio of 6T in the mixture, which is also contrary to experimental expectations. The results from the *interlinked* model aligned better with experimental expectations, as the transmission at the Fermi energies of the 6T/9DT mixtures were close to the transmission of the 9DT system. However, the transmission obtained from this model also increased slightly with rising ratio of 6T in the mixture, which is contrary to experimental expectations. It is possible that the contribution of AMT ligands to the charge transport was underestimated in the transport calculations, resulting in transmissions lower than expected based on experimental results.

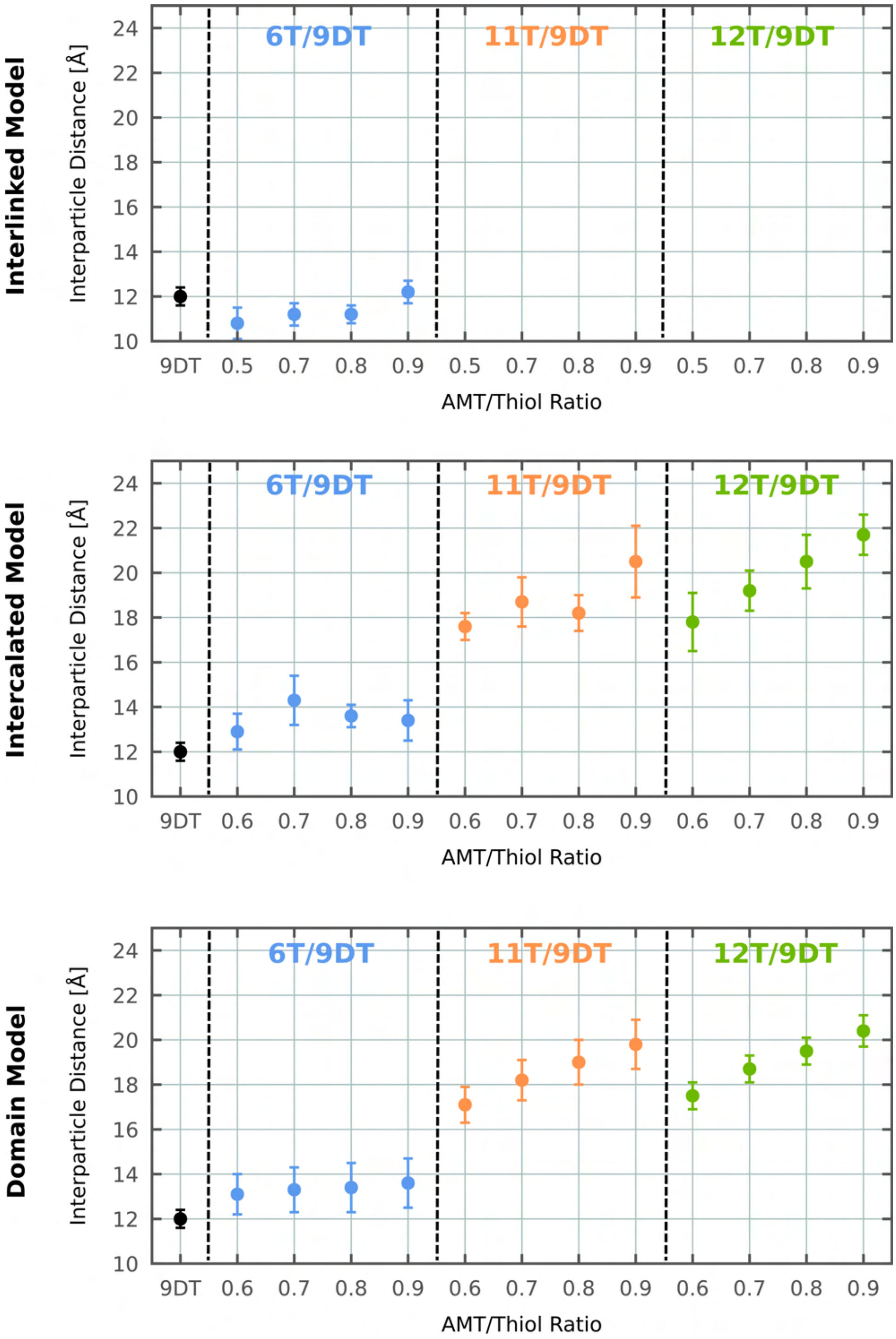

Figure 6.38: Average interparticle distances from 10 individual MD simulations for pure 9DT interfaces (black), as well as mixtures of 6T/9DT (blue), 11T/9DT (orange), and 12T/9DT (green), with varying monothiol to total thiol (AMT+ADT) ratios. The gold surfaces of the interface structures were covered with ligands such that 75 % of the positions were occupied. Three distinct structural models are examined: the *interlinked* model depicts the scenario where the 9DT ligands cross-link the two surfaces (top), the *intercalated* model illustrates the situation where the 9DT ligands do not engage in cross-linking (center), and the *domain* model shows the segregation of 9DT and AMT ligands into two separate domains (bottom). The *interlinked* structure was only possible for the 6T/9DT mixtures, as the interparticle distances of the 11T/9DT and the 12T/9DT structures were too high to facilitate cross-linkage.

On the other hand, it is also possible that our model overestimated the intersurface distance in the 6T/9DT mixtures, causing the lower transmissions in these structures.

Turning our attention to the 11T/9DT and 12T/9DT mixtures, the calculated transmissions at the Fermi energies of the mixtures were lower than that of the pure 9DT interface for the *intercalated* as well as the *domain* model (see Figure 6.39 center and bottom, respectively), qualitatively aligning with experimental expectations. However, the transmission differences between the mixtures and the pure 9DT system in the two models deviate significantly. In the *intercalated* model, the transmission was several orders of magnitude lower than that of the pure 9DT system, whereas in the *domain* model, the difference was just one order of magnitude. A quantitative comparison of the transmission at the Fermi energy with experimental data, as done for pure ADT GNP films in Section 6.1.2.1, is difficult, as this requires in-depth information on the 3D structure of the GNP assembly, which is not available for mixed-ligand GNP assemblies. We can, however, still interpret the results qualitatively. The transmission at the Fermi energies obtained for 11T/9DT and 12T/9DT mixtures from the *intercalated* model was close to the transmissions obtained for pure AMT interfaces (see Figure 6.20). Conversely, in the *domain* model, the transmission appeared to be primarily influenced by the more effective 9DT cross-linker, resulting in only a one-order-of-magnitude decrease, and a transmission close to that of the pure 9DT interface. Experimental results, on the other hand, showed a decrease in conductivity by several orders of magnitude when using large fractions of 11T or 12T in the mixtures, compared to the conductivity of pure 9DT films (see Figure 6.28). This trend is better reflected in the charge transport calculations of the *intercalated* model.

To summarize, we can draw the following conclusions:

- **Stability of Mixed-Ligand SAMs**: Various mixed-ligand structures composed of four 12T and four 9DT ligands were investigated through MD simulations. The examined configurations included random distributions, one-molecule-wide striped domains, and both small and large domains, all of which have been documented in the literature for similar mixtures. Although the energy differences among these structures were minimal, the striped configuration showed the highest average energy, indicating that it may be the least favorable arrangement. Despite the differing tail groups (CH_3 vs. SH) and a carbon chain length difference of over three carbon units (both factors that were shown to cause formation of separate domains in the literature) our preliminary investigations suggest that random distributions and distinct domain formations are both plausible.
- **Interface Models**: Three distinct structural models of the mixed-ligand interfaces were investigated: an *interlinked* model in which 9DT ligands cross-linked the surfaces, an *intercalated* model in which 9DT ligands were only connected to one of the surfaces, and a *domain* model in which AMT and 9DT ligands were separated completely. For the 6T/9DT mixture, both the intersurface distances and transmission at the Fermi energies showed the best agreement with experimental data in the *interlinked* model. In the 11T/9DT and 12T/9DT mixtures, the *intercalated* and the *domain* model produced intersurface distances that aligned with experimental trends. The *intercalated* model yielded slightly higher distances and the *domain* model demonstrated good quantitative agreement of the interparticle distances with experimental results. Conversely, the charge transport characteristics were better represented by the *intercalated* model.

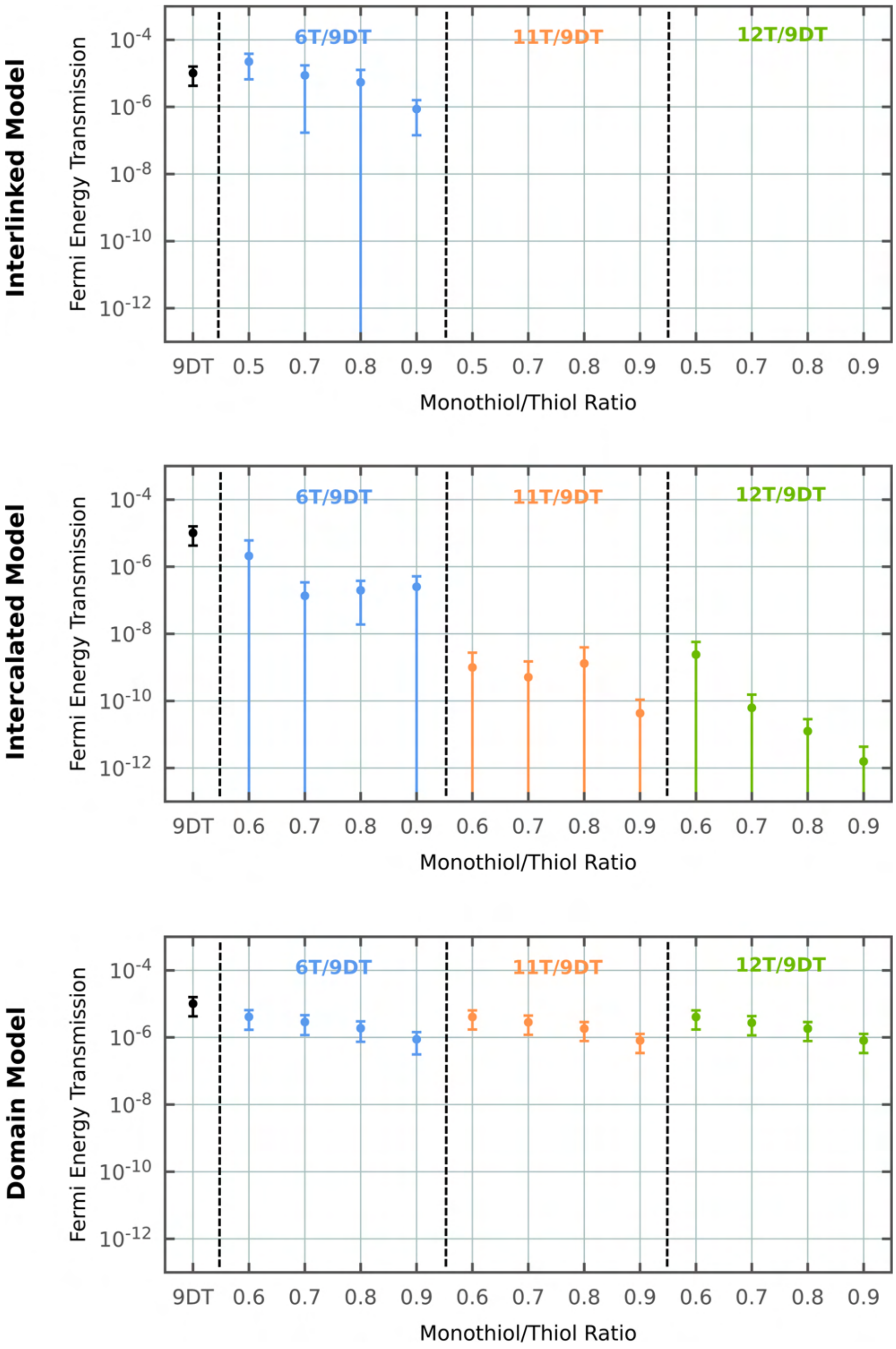

Figure 6.39: Average transmissions at the Fermi energies for mixtures of 6T/9DT (blue), 11T/9DT (orange), and 12T/9DT (green), with varying monothiol to total thiol (AMT+ADT) ratios. Each transmission is averaged from 10 lowest-energy structures, extracted from MD pushing simulations. The gold surfaces of the interface structures were covered with ligands such that 75 % of the positions were occupied. Three distinct structural models are examined: the *interlinked* model depicts the scenario where the 9DT ligands cross-link the two surfaces (top), the *intercalated* model illustrates the situation where the 9DT ligands do not engage in cross-linking (center), and the *domain* model shows the segregation of 9DT and AMT ligands into two separate domains (bottom). In the case of the 11T/9DT and the 12T/9DT mixture, the *interlinked* model is not feasible, as the preferred surface-to-surface distances of these mixtures are too high to facilitate cross-linkage of 9DT.

6.3 Application and Testing of a Single-Interface Model in Analyte Sensing

When analyte molecules are introduced to GNP films, they can diffuse into the ligand matrix. This diffusion can cause the films to swell, resulting in an increased interparticle distance. According to Equation (3.1 this causes a in conductance. Sometimes, however, an increase in conductivity may also be observed. In such cases, it is assumed that the transport is primarily influenced by changes in permittivity rather than swelling. Joseph et al., among others, have demonstrated that the rigidity of the ligand or linker molecule, as well as the compatibility of solubilities between the analyte and ligand, influence which effect dominates. In rigid films (e.g. cross-linked by staffane linkers), it is assumed that the analyte molecules do not diffuse into the ligand matrix but rather diffuse into voids in the GNP films, thus not causing swelling. Conversely, when the ligands are more flexible, as in the case of ADT linkers, the analyte molecules can diffuse into the ligand matrix. The authors suggest that in this cases, the rate of diffusion is determined by the solubility compatibility between the analyte and ligand.[178]

In this study, we aim to confirm whether analyte molecules diffuse into the ligand matrix when their solubilities align. Therefore, we will place alkane molecules in close proximity to AMT ligands on Au(111) surfaces and analyze whether the analyte molecules diffuse into the ligand matrix. Then we will investigate potential diffusion into the ligand matrix at AMT or ADT particle–particle interfaces. Finally, we will incorporate the analyte molecules directly into ligands matrix in the interface structure, assuming that the analyte molecules have diffused into the ligand matrix, and analyze the resulting swelling and changes in the zero-bias conductance. To validate this approach, we will also examine the expected number of analyte molecules per ligand in a GNP assembly.

6.3.1 Diffusion of Ligands into SAMs

Cho et al. focused on sensing toxic cations using striped gold nanoparticle films.[179] Alongside their measurements, the authors conducted MD simulations to investigate the intercalation of cations into the ligand matrix. The films investigated in their study consisted of GNPs stabilized by ligand mixtures of 6T and alkanethiols terminated with ethylene glycol (EG) units. The stripes were four molecules wide. For the MD simulations, the authors modeled the system using Au(111) SAMs featuring a $(\sqrt{3} \times \sqrt{3})$ R30° lattice arrangement. Metal cations were strategically positioned at the edges of the EG stripes on the Au(111) SAMs. Throughout the MD simulations, the authors observed multiple intercalation events in which the EG ligands wrapped around the cations. These events typically occurred at the boundaries between the EG stripes and the 6T stripes, where the conformational space made trapping of the cations possible. With pure EG SAMs, they also observed trapping events, but the residence time of the cations in the ligand matrix was significantly shorter compared to the mixtures.[179]

Instead of toxic cations, this section focuses on the diffusion of alkanes into AMT SAMs. Alkanes are benchmark gases, particularly for sensors designed to detect volatile organic compounds (VOCs), which include alkanes.[34, 39, 180] Alkanes can also be simulated with the ReaxFF parameters applied in the previous sections, as they consist of saturated hydrocarbons and do not contain any heteroatoms. Different alkane (methane and hexane) molecules were placed in close proximity to the ligand matrix on Au(111) surfaces, distributed in a $(\sqrt{3} \times \sqrt{3})$ R30° lattice (as described in Section 6.1.1). As ADT SAMs are prone to artifacts in the ReaxFF, this section focuses on AMT ligand SAMs. Initial simulations, where the analyte molecules were placed into simulation cells with unrelaxed, straight AMT ligands, following the method of Cho et al. described above, rarely resulted in intercalation events. In these systems, the analyte molecules were usually repelled quickly by the ligand matrix, while the ligands relaxed into tilted structures (see Appendix, Figure A.14).

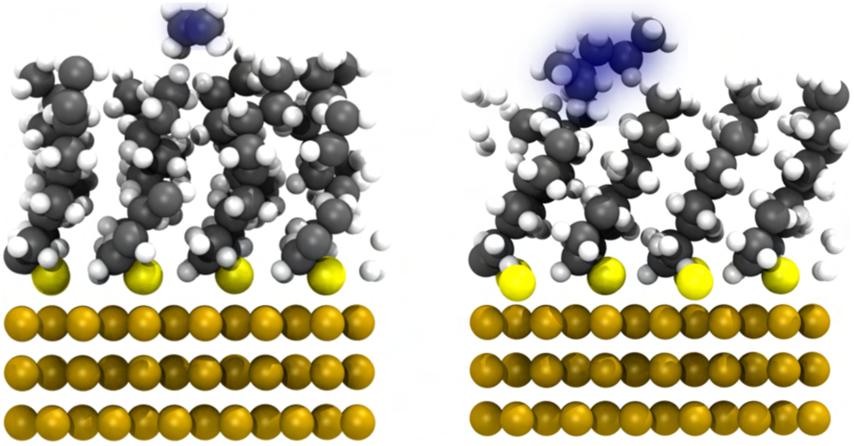

Figure 6.40: 9T SAM with one hexane analyte molecule initially placed close to the ligand matrix (left). During the simulation, the hexane molecule partially enters the ligand matrix (right). For an easier distinction, the hexane analyte molecule is highlighted in blue.

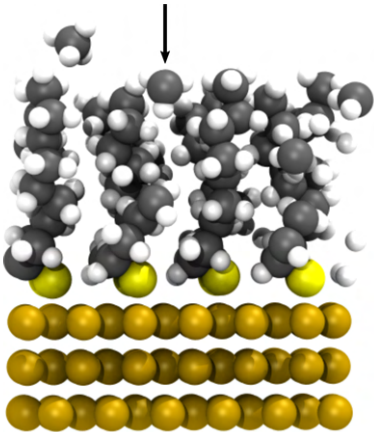

Figure 6.41: One of the methane analyte molecules (highlighted by the black arrow) gets trapped partially inside the 9T ligand matrix.

When the SAM structures were equilibrated before introducing analyte molecules, analyte molecules were usually not repelled instantly. The straight SAM structure was first equilibrated for 50 ps using a NVT ensemble with fixed Au atoms, resulting in tilted ligands. Then analyte molecules were placed in close proximity to the ligand molecules, and a second MD simulation with a NVT ensemble was performed for 500 ps. With one hexane analyte molecule, that was initially placed above the ligand matrix (see Figure 6.40, left), the analyte molecules adsorbed on the surface of the ligand matrix, and in some cases also partially diffused into the ligand matrix (see Figure 6.40, right). With methane molecules, complete trapping of one methane molecule in the ligand matrix was observed (see Figure 6.41). The simulations suggest that diffusion of small alkane analyte molecules into the dense ligand matrix of AMT SAMs is in principle reasonable.

6.3.2 Diffusion of Ligands into Interface Structures

In the next step, we investigated whether alkane analyte molecules can also diffuse into the ligand matrix of an interface structure. In the interface structures the structural flexibility of the ligand matrix is reduced compared to SAM structures, which should make a diffusion of analyte molecules into the matrix more difficult than in SAMs. As the ADT ligands cross-link the surfaces and do not have free thiol tail groups as in the SAM simulations, they can again be considered in this part of the study.

The interface structures that have been simulated so far are periodic, and mimic infinite bulk surfaces. In contrast to GNP assemblies, the interface model does not include the regions of the GNP structure where ligands exhibit greater flexibility, such as at the edges of two facets of a particle or near voids within the assembly. However, these regions of the structure are likely the areas through which analyte molecules can enter the ligand matrix. To still apply the single interface model, the periodicity had to be broken such that ligands could be placed outside of the ligands matrix. Removing periodicity in the simulations in either x or y direction (along the gold surfaces), however, is not possible as severe edge effects can be observed. The ligand molecules partially moved around the surfaces or the gold surface bends (see Appendix, Figure A.15).

To prevent a movement of ligand molecules around the gold surfaces, and to increase the stability of the gold surfaces in the absence of periodicity, the gold surface was extended to the left and to the right (x direction), while not adding any additional ligand molecules. Periodicity is preserved in y direction but not along the x direction. This way, we intended to mimic the edge of the interfaces, where the ligands are less restrained in their movement. Several methane molecules were placed in the resulting voids at the edges of the ligand matrix (see Figure 6.42, left). During the MD simulation, the gold surfaces remained stable, and the 9DT ligand molecules mostly cross-linked the surfaces. A short trapping event of one methane molecule was observed when one of the 9DT ligands disconnected from one of the gold surfaces to make space for the methane molecule. This ligand was located at the edge of the interface. Thus, it can only accommodate the space for the methane to enter the matrix due to the disrupted periodicity of the interface structure. In a densely packed interface, however, the available space for such ligand movement is limited, making this observed trapping event an artifact of the artificial simulation structure. At the edge of the interface, the available space, on the other hand, may be sufficient for such an event.

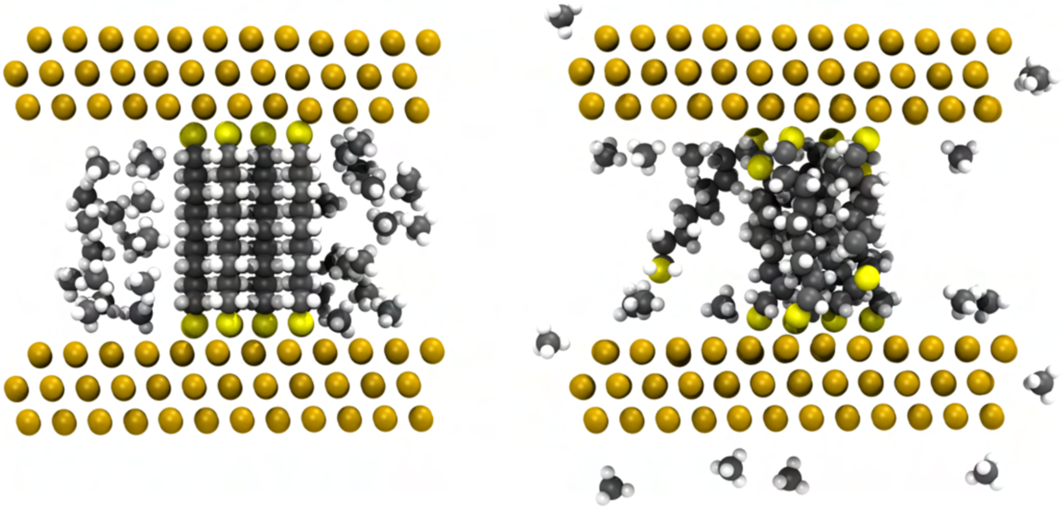

Figure 6.42: Methane analyte molecules were introduced into the voids created by the extension of the gold surfaces (left). During the pushing MD simulation, the cross-linking behavior of the 9DT ligands was mostly preserved. However, one ligand detached from a gold surface (right). The resulting space was occupied by methane molecules, which became confined within the ligand matrix.

6.3.3 Incorporating Analyte Molecules into Interface Structure

Simulating the diffusion of analyte molecules into a ligand matrix can often require long computational time. To address this, a common strategy is to directly position the analyte molecules in suitable locations within the ligand matrix.[181, 182] In his bachelor thesis, which was conducted in the context of this PhD project, Alexander Seiler carried out MD simulations in which alkane analyte molecules were placed in the small voids between the ligands of the interface structures. Analysis of the data from MD simulations, as well as charge transport calculations were conducted by the author of this thesis.

In this Section, first, different strategies for placing analyte molecules into the interface structure will be compared. For these initial studies, methane will be used as benchmark analyte molecule. Then, the interparticle distance change upon incorporation of different amounts of hexane and octane molecules will investigated for 9DT and 12T interfaces. The resulting distances will be compared to experimental distances from the literature. As literature on these experimental distances is limited, additionally, the relative resistance change upon analyte adsorption will be calculated from the interparticle distance change, and compared to literature values. Furthermore, charge transport calculations will be performed as a different technique to calculate the change in conductance and relative resistance upon analyte adsorption. Finally, we will assess whether the analyte-to-ligand ratio in our model is reasonable by comparing it to ratios estimated from experimental measurements from the literature.

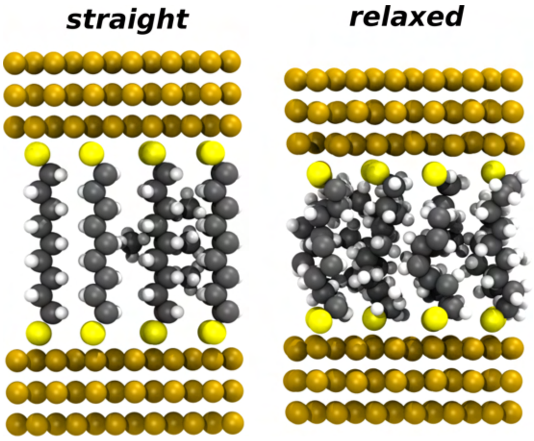

Figure 6.43: Comparison of two initial interface structures occupied by four methane analyte molecules each. Left: The 9DT ligands are initially arranged in a straight configuration, with methane molecules directly positioned within this linear structure. Right: The pure 9DT interface structure was first equilibrated to relax the system before the methane molecules were inserted. The underlying data of this Figure were already published in A. Seiler, "Influences of the presence of analyte molecules on structural and electrical properties in cross-linked gold surfaces", Bachelor thesis, University Hamburg, 2023.

6.3.3.1 Comparing Two Strategies for Introducing Analyte Molecules Into the Interface Structures

9DT cross-linked interfaces were first populated with methane analyte molecules. Two distinct interface structures were examined: a *straight* interface structure, where the ligands were arranged in a linear, all-trans configuration (see Figure 6.43, left), and an *equilibrated* interface structure, extracted from a pushing simulation as described in Section 6.1.2, where the ligands mostly adapted gauche conformations (see Figure 6.43, right). Positioning ligands in the straight structure was more straightforward due to the clearer visibility of voids. On the other hand, the equilibrated structure more accurately reflects the real interface.

We aimed to determine whether the choice of interface structure would impact the results. Therefore, we investigated the average preferred intersurface distance in 10 independent MD simulations with different seed velocities for each configuration, each occupied by four methane molecules. For the straight structure, pushing simulations were performed as described in Section 8.1 (see Figure 6.44a). During the MD simulations involving the equilibrated structure, after an initial tempering phase of 1 ps, the gold surfaces were pulled apart for 0.6 ps, to mimic an increase in interparticle distance due to swelling, followed by a pushing phase for 2.5 ps (see Figure 6.44b). The resulting preferred intersurface distances of the 10 simulations were averaged and found to be 12.3 ± 0.2 Å for the straight structure and 12.2 ± 0.3 Å for the equilibrated structure. The lowest-energy structures of both starting configurations also had similar appearances, showing that both configurations yield very similar outcomes. This suggests that both structures are equally viable for this analysis. The obtained distances were not further analyzed and compared to experimental values, as methane is usually not used as analyte molecule for GNP sensing experiments. Methane was solely used as a benchmark analyte in this paragraph for comparing the two configurations.

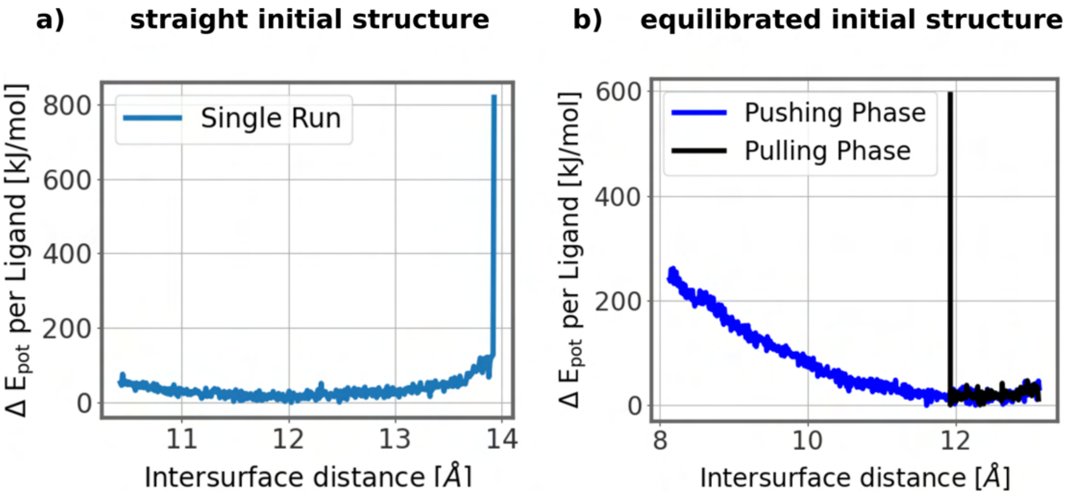

Figure 6.44: Two representative plots showing potential energy as a function of intersurface distance from MD simulations. a) illustrates a configuration with four methane molecules occupying a straight ligand structure, where the gold surfaces are pushed together. b) depicts the scenario with an equilibrated ligand structure, in which the gold surfaces are first pulled apart and then pushed together.

6.3.3.2 Intersurface Distance Change Upon Alkane Analyte Adsorption

Given that positioning the ligands in the straight structure was more straightforward, we decided to use these configurations to investigate the changes in interparticle distance upon introducing hexane or octane analyte molecules into 9DT cross-linked or 12T (50% coverage) stabilized interfaces. Analyte molecules, ranging from one to eight in number, were inserted into the small voids between the eight ligands within the interfaces.

Before discussing the results, the reasonableness of such analyte-to-ligand ratios is discussed. Based on thermogravimetric analysis (TGA), quartz crystal microbalance (QCM) measurements, and TEM measurements, conducted by Olichwer et al,[41] the number of ligands per particle, as well as the number of toluene analyte molecules per ligand can be calculated. Detailed calculations are available in the Appendix, Section A.8. According to these calculations, 268 12T ligands occupy a single 3.8 nm-sized GNP. At a toluene concentration of 10,000 ppm, there are approximately 5 ligand molecules for each toluene analyte molecule. Assuming that the ratio remains the same for alkane analyte molecules, the analyte-to-ligand ratios in the interface structures with one or two incorporated analyte molecules should reflect the analyte concentrations investigated in the experiments.

After incorporating the analyte molecule into the straight interface structures, MD simulations were performed, where the gold surfaces were pushed together, as described in Section 8.1. The preferred surface-to-surface distances were extracted from the lowest-energy structure of the simulations. For each analyte concentration, 10 individual MD simulations were performed with different initial velocity seeds, and the extracted distances of these simulations were averaged.

Experimental studies have demonstrated that the adsorption of analyte vapor typically leads to an increase in interparticle distance, commonly referred to as swelling. One key factor influencing this phenomenon is the rigidity of the ligands, which affects their sensitivity to analyte vapor and, consequently, the extent of film swelling.[178] For instance, when cross-linking GNPs with 6DT, a significant decrease in sensitivity was observed compared to non-cross-linked GNPs.[183] Based on these findings, it can be anticipated that the interparticle distance will undergo a greater change upon analyte incorporation in 12T-capped interfaces compared to those that are cross-linked with 9DT.

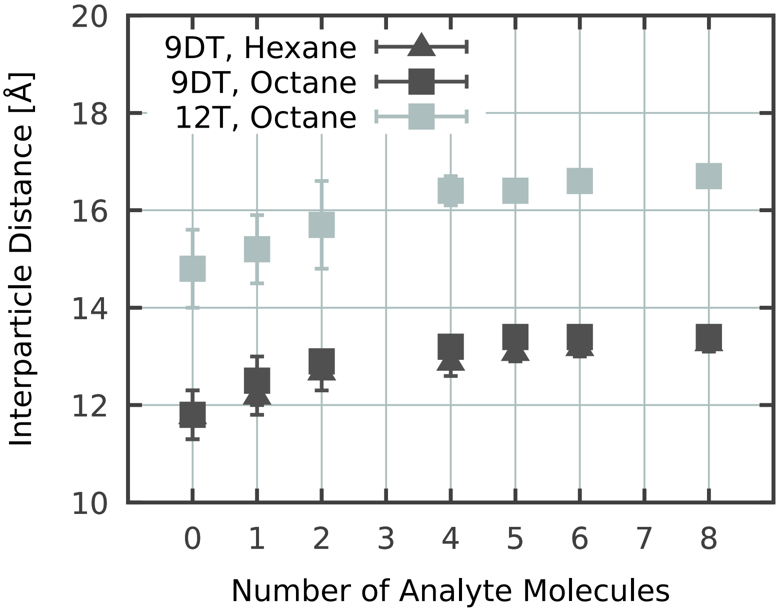

Figure 6.45: Dependence of the intersurface distance on the number of analyte molecules (hexane and octane) in the 9DT cross-linked interface (dark gray) and in the 12T-capped interface (light gray). The intersurface distance increases exponentially with the number of analyte molecules, reaching a plateau at around five analyte molecules.

The relationship between the averaged intersurface distance and the number of analyte molecules in the 9DT-cross-linked and the 12T-capped interfaces is summarized in Figure 6.45. An exponential increase of the intersurface distance with the number of analyte molecules for both types of ligands (9DT and 12T) and both analytes (hexane and octane) can be observed, reaching a plateau around five analyte molecules.

When comparing the hexane and octane analyte molecules within the 9DT system, the change in intersurface distance was slightly larger for octane, which is expected due to its larger molecular size. Furthermore, comparing the 12T and 9DT interfaces, distance increase is slightly stronger in the 12T system than in the 9DT system. This observation aligns with expectations that AMT ligands exhibit more structural flexibility than ADT cross-linkers. Additionally, the longer chain length of 12T further contributes to its increased flexibility compared to 9DT.

As shown above, the MD simulations yield trends that align with our expectations. We now aim to quantitatively compare our results with experimental data. Although experimental data for alkane analyte molecules primarily focuses on changes in relative resistances[34, 39] and does not explore distance changes upon analyte adsorption, studies have demonstrated that the responses to alkanes like octane are comparable to those observed for toluene,[33] for which more extensive experimental data is available. For instance, *in situ* GISAXS measurements of 4 nm large GNP films stabilized with 12T ligands revealed an intersurface distance change of up to 0.12 Å at a concentration of 10,000 ppm toluene vapor.[41] Conversely, *in situ* small-angle X-ray diffraction (SAXRD) measurements of 5 nm large particles, also stabilized with 12T ligands, indicated a distance change from 18 to 25 Å upon exposure to toluene-saturated cotton swabs.[184] In the second publication, no concentration of toluene is specified, making it difficult to compare the results of the experimental studies. Since they use saturated cotton swabs, it is however possible that the toluene concentration in the assembly is very high, causing the large interparticle distance change, compared to 0.12 Å at a concentration of 10,000 ppm, measured by Olichwer et al.

In our simulations, we observed the smallest change in distance for 12T interfaces and octane when one octane molecule was adsorbed (0.37 Å compared to the absence of any analyte in the interface). This increase is three times larger than the 0.12 Å measured for 10,000 ppm toluene vapor by Olichwer et al., yet it is still significantly below the 7 Å change recorded for toluene-saturated cotton swabs.

The larger change in interparticle distance observed in our simulations, compared to the measured changes at 10,000 ppm, may be explained by an overestimation of the analyte concentration. However, calculations of the estimated analyte-to-ligand ratio based on TGA, QCM, and TEM measurements indicate that having one analyte molecule per interface results in a ratio smaller than that observed in the experiments at 10,000 ppm. Here, it is important to note that the ratio calculated for GNP assemblies reflects the analyte distribution across the entire GNP film. The ratio at the particle–-particle interfaces may differ from this value, as small voids within the GNP assembly could potentially accommodate more analyte molecules than the ligand matrix at the interfaces. This is due to the fact that analyte molecules can diffuse more easily into these voids than into the dense ligand matrix present at the interfaces.

6.3.3.3 Estimating the Relative Resistance from the Intersurface Distance

Additionally, we can further evaluate our findings on the interparticle distance change upon ligand adsorption by estimating the relative change in resistance resulting from the change in intersurface distance, denoted as $\Delta\delta$. This approach allows us to obtain a quantity, the relative change in resistance, for which more data is available in the literature than on interparticle distances. The relative change in resistance $\frac{\Delta R}{R_0}$ can be derived from Equation (3.1):

$$\frac{\Delta R}{R_0} = e^{\beta \Delta\delta} \, e^{\Delta E_\mathrm{A}/kT} - 1 \; , \tag{6.4}$$

where β is the tunneling decay constant, ΔE_A is the change in activation energy required for charging the gold cores, k is the Boltzmann constant, and T is the temperature. When the difference in permittivity between the analyte molecule and the ligand matrix is negligible, the second exponential term can be disregarded, simplifying the equation to:

$$\frac{\Delta R}{R_0} = e^{\beta \Delta\delta} - 1 \; . \tag{6.5}$$

Values for the tunneling decay constant β, have been documented in the literature, ranging from 0.57 to 1.1 Å^{-1} (see Table 6.8). Alternatively, values from the MD simulations conducted in this thesis (see Section 6.1.2) yielded values of 1.2 and 1.3 Å^{-1} for AMT and ADT ligands, respectively. Figure 6.46 presents the relative resistance obtained for $\beta = 0.8\,\text{Å}^{-1}$, which in in the middle of the literature values. For further comparison, relative resistance values derived from other plausible values of β can be found in the Appendix, Figures A.16-A.18. The choice of β significantly influences the calculated relative resistance; for instance, using β values of 0.57 Å^{-1} and 1.3 Å^{-1} results in relative resistance values of 19 % and 10 %, respectively, for eight octane molecules in 12T interfaces.

Experimental data for relative resistances are also available for alkanes adsorbed in 9DT cross-linked films. For hexane analytes, relative resistances of approximately 0.75 % and 1.0 % have been reported at concentrations of 4,000 and 6,000 ppm, respectively.[185] Another study indicated that relative resistances for octane in 9DT cross-linked films ranged from 0.3 % at 100 ppm to 2.5 % at 2,000 ppm.[33] The experimental relative resistances are considerably lower than those observed in our simulated data, even at low concentrations of hexane or octane molecules. For instance, with just one octane molecule in the 9DT interface, the relative resistance reached 78 %. Apart from potential errors in Equations

Table 6.8: Overview of tunneling decay constants for ADT cross-linked or AMT-capped GNP assemblies from literature.

Reference	β	Ligand Type	Carbon Units Range
Cui et al.[143]	$0.57\,^{-1}$	ADT	8-12
Joseph et al.[21]	0.61 or $0.71\,^{-1}$	ADT	6-16
Wuelfing et al.[25]	$0.8\,^{-1}$	ADT	4-16
Schlicke et al.[18]	$1.1\,^{-1}$	ADT	4-10
Terrill et al.[16]	$1.2\,^{-1}$	AMT	8-16

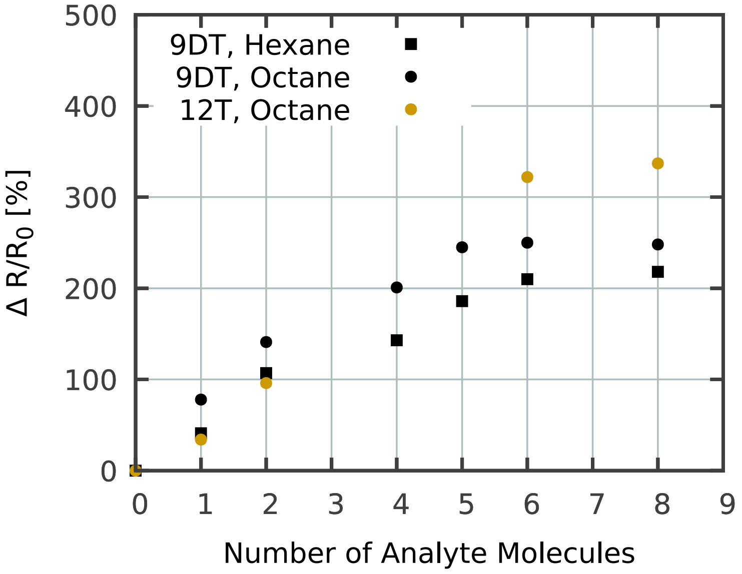

Figure 6.46: Relative resistance changes in percent estimated from Equation (6.5) for 9DT (black) and 12T (orange) interfaces with $\beta = 0.8\,^{-1}$, occupied with varying numbers of hexane or octane analyte molecules.

3.1 and 6.5, as discussed in Section 3, it is likely that the observed overestimation of the relative resistance change was primarily due to a too high change in interparticle distance that resulted from an overestimation of the ligand concentration.

This contrast becomes even more obvious when larger values of β are used. For example, with β set to $1.2\,\text{Å}^{-1}$, the relative resistance increases to 137 % with only one octane molecule present in the 9DT interface (see Appendix, Figure A.18).

6.3.3.4 Relative Resistance Change Upon Analyte Adsorption from Charge Transport Calculations

In addition to estimating the relative resistance from changes in intersurface distance, it can also be derived from charge transport calculations. Therefore, the structures from Alexander Seilers MD simulations were prepared for the charge transport calculations as detailed in Section 8.2. For each analyte concentration, the lowest-energy structures obtained from each of the 10 MD simulations were used for the transport calculations. The resulting zero-bias conductances for these 10 structures were then averaged. The results of these calculations are summarized in Figure 6.47 (left). Notably, no clear trend is evident in the plot. Furthermore, negative relative resistances can be found, a phenomenon not observed in experiments involving these analyte molecules.

A negative relative resistance arises when the zero-bias conductance increases upon the introduction of analyte molecules into the interfaces (see Figure 6.47, right). Typically, one would expect a decrease in zero-bias conductance with an increased tunneling distance. However, in this case, despite the increase in tunneling distance, an increase in conductance is still observed. This suggests the possibility of additional transport pathways involving the analyte molecules within the interfaces, which may contribute to the observed increase in conductance. The contributions of these additional pathways may be either overestimated by the program or may suggest that incorporating analyte molecules into the dense ligand matrix at the interfaces is unlikely.

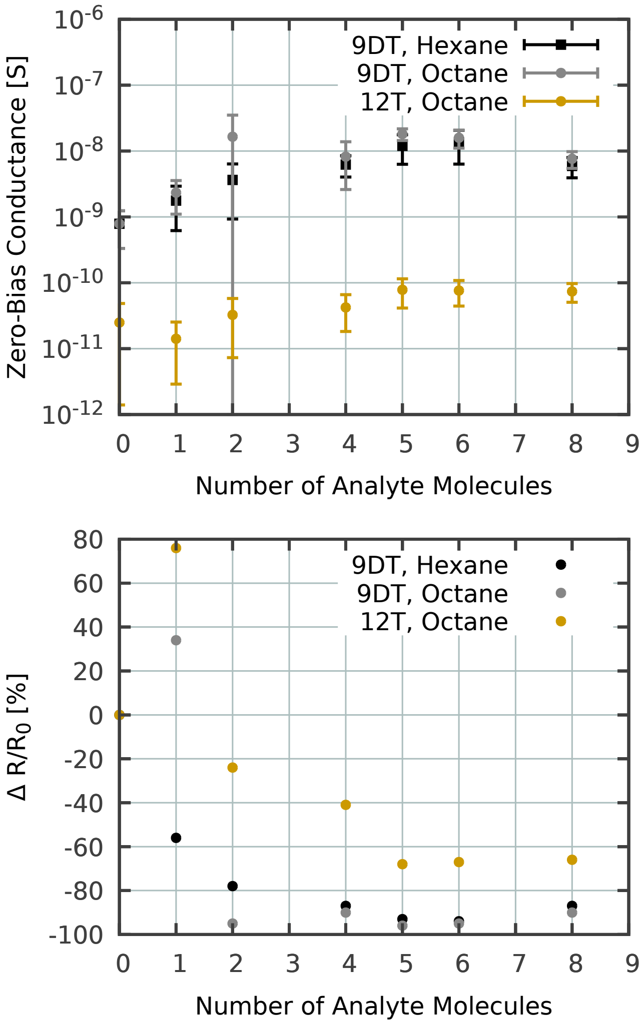

Figure 6.47: Top: Zero-bias conductances obtained from charge transport calculations using a DFTB approach for 9DT cross-linked or 12T-capped interfaces, occupied with different number of octane or hexane analyte molecules. For each analyte concentration, the lowest-energy structures from the 10 MD simulations were extracted and used for the transport calculations. The resulting conductances of the 10 lowest-energy structures were averaged. The underlying transmission functions can be found in the Appendix, Figures A.19-A.36.
Bottom: Relative resistances in percent, calculated from the averaged zero-bias conductances of each structure.

6.3.4 Conclusions

In conclusion, our findings suggest that diffusion of analyte molecules, particularly small ones such as methane, into the dense ligand matrix at the particle–particle interfaces is theoretically possible. Furthermore, they show that the likelihood of such diffusion may be greater at the edges of these interfaces, where ligands exhibit increased structural flexibility.

Artificially introducing analyte molecules into the interface structure led to the anticipated increase in intersurface distance. However, our model overestimated this distance change. Specifically, the increase was three times greater for the lowest number of analyte molecules examined than the distances reported in literature for a 10,000 ppm analyte concentration. As a result, the relative resistances derived from the distances obtained through MD simulations were also higher than those measured experimentally.

One possible explanation for this discrepancy is an overestimated analyte-to-ligand ratio in our model. To address this, we estimated the ratio based on TGA, QCM, and TEM data from an experimental literature study and compared it with the ratio used in our simulations. The estimated analyte-to-ligand ratio from experiments was approximately 1:6 for a 10,000 ppm analyte concentration, while the smallest ratio in our simulations was 1:8. This suggests that our ratio should theoretically be comparable to the experimental values. However, it is possible that the ratio deviates in the real GNP assembly structure, as small voids within the assembly may accommodate more analyte molecules than the densely packed interfaces, where diffusion is more restricted.

Moreover, our charge transport calculations yielded significantly higher relative resistances compared to experimental results. The majority of relative resistances were negative, in contrast to experimental results, where only positive relative resistances have been observed for such ligands. This suggests that the incorporated analyte molecules might create new transport pathways, enhancing conductance through the interfaces.

Overall our results indicate that the actual concentration of analyte molecules at the interfaces of GNP assemblies is likely lower than what our simulations assume. Consequently, our simplified model of particle–particle interfaces may not be sufficient to fully describe sensing mechanisms in GNP assemblies.

6.4 Towards Radical Molecular Ligands: Understanding the Magnetotransport Behavior of Blatter Radical Single-Molecule Junctions

The research presented here is the result of a collaboration with Gautam Mitra, Jueting Zheng, Michael Deffner, Jonathan Z. Low, Luis M. Campos, Carmen Herrmann, Theo A. Costi, and Elke Scheer. The results have already been published.[186] Unless otherwise noted, all calculations, data analysis and writing have been performed by the main author of this thesis.

One of the main challenges associated with thiol-capped GNPs is their vulnerability to oxidation.[187] When exposed to air for extended periods, such as weeks or months, these GNP films can degrade, affecting their properties. For example, particles may aggregate or the film's response towards analyte vapors may change.[188] As an alternative to alkanethiol ligands, organic radicals may offer more stable options for ligands in sensing materials, which can also be easily modified structurally.[46, 189–191] For example, Zheng et al. showed the potential of pyreno-triazinyl radicals in solution as pH sensors that react to pitric acid by a change of the color of the solution.[192] In sensors based on GNP assemblies, such radicals have however not been used yet.

Unlike closed-shell molecules like ADT or AMT, which were discussed in the previous sections, organic radicals contain unpaired electrons. Therefore they also possess spin, making them interesting for potential future applications,[47] e.g. in so-called spintronic devices, which employ spin rather than electric charges to process and store information, differentiating them from conventional electronic devices.[193]

For future applications of such radicals in devices, it is essential to first study their fundamental properties. In particular, to be able to use them in spintronic devices or other technologies that rely on spin, it is crucial that these radicals maintain their spin characteristics. Among the investigated molecules are the 1,2,4-benzotriazin-4-yl type radicals, commonly referred to as Blatter radicals. Thin organic films of these radicals grown on SiO_2/Si(111) surfaces have demonstrated very good stability in both air and vacuum environments, with the paramagnetic nature of the Blatter radical remaining intact over a long period of time (at least five months).[46]

When adsorbed onto Au(111) surfaces, research by Low et al.[194] indicated that the radical characteristics of the Blatter radical were also preserved. However, single-molecule conductance measurements revealed spontaneous oxidation within the junction. This oxidation was attributed to two main factors: first, the singly occupied molecular orbital (SOMO) of the Blatter radical is situated close to the Fermi level of gold, which facilitates charge transfer from the molecule to the metal. Second, the undercoordinated nature of the gold atoms in the break junction enhances the binding to the Blatter radical, thereby promoting the oxidation process.[194]

Incorporating an electron-withdrawing group into the radical was shown to enhance its stability and prevent oxidation.[195] Nonetheless, first-principles quantum chemistry calculations conducted by Jiang et al. suggested that non-functionalized Blatter radicals are also capable of retaining their open-shell character within a junction formed between gold electrodes.[196]

To further investigate the behavior of Blatter radicals in molecular junctions, our collaboration partners conducted a systematic transport study using a mechanically controlled break junction at low temperatures.[186] The Blatter radical in this study contained two methylthioether ($-SCH_3$) units, which allowed for effective coupling to the electrodes (see Figure 6.48a).

In this study, zero-bias anomalies in the current-voltage characteristics were observed for most junctions. These zero-bias anomalies, resulting from the Kondo effect indicate that the radical character was preserved when the radical was coupled to the electrodes. However, some junctions did not exhibit any zero-bias peak and instead displayed significant negative magneto resistance (MR). While the combination of weak MR and Kondo features can be explained by a spin-1/2 Kondo effect, the origin of the pronounced negative MR observed in combination with the absence of a zero-bias peak remains unclear.

A similar phenomenon has been observed in junctions of perchlortrityl radicals with the same ($-\mathrm{SCH_3}$) anchoring group, where junctions that did not show any Kondo features showed pronounced MRs.[197] In contrast to the Blatter junctions, in these junctions the MR was sometimes positive and sometimes negative. Here, the authors attributed the high MR to spin-dependent scattering at the interface between the metal and the molecule and a resulting quantum interference effect.[197] In the Blatter radical junctions, however, our collaborators suggest that there is likely a different mechanism explaining the MR, as they observed only negative MR in the Blatter radicals, compared to negative and positive MRs in the perchlortrityl radical junctions. Additionally, the coupling between the singly occupied/unoccupied molecular orbital (SOMO/SUMO) and the Au electrodes is expected to be strong in case of the perchlortrityl radical,[197] while first-principles quantum transport calculations have suggested a weak coupling in case of Blatter radical junctions.[196]

As an alternative explanation for the observed negative MR and the absence of Kondo features, our collaborators proposed that these junctions might consist of double quantum dot systems. In this scenario, a Blatter radical connected to both electrodes is coupled to a second quantum dot, which could be a gold atom or cluster with an unpaired spin, a molecular fragment, or another Blatter radical (see Figure 6.48b, type D junction). This second quantum dot would also have a spin of $S = 1/2$. Such a system can be modeled using the Anderson impurity model, which is side-coupled to a second $S = 1/2$ quantum dot through an antiferromagnetic exchange interaction characterized by a strength J. The Hamiltonian describing this system is given by[186]

$$H = H_{\mathrm{dot}} + H_{\mathrm{leads}} + H_{\mathrm{tunneling}} + H_{\mathrm{J}} + H_{\mathrm{B}} \ . \tag{6.6}$$

H_{dot} describes the Hamiltonian of the quantum dot which represents the Blatter radical with $S = 1/2$. H_{leads} is the Hamiltonian of the leads/electrodes, and $H_{\mathrm{tunneling}}$ describes the tunneling of electrons from the leads onto the dot and off the dot. H_{J} describes the antiferromagnetic coupling between the Blatter radical and the quantum dot, and H_{B} describes a magnetic field that acts on the combined spins of the quantum dot and the side-coupled quantum dot. With the help of Equation (6.6), the many-body eigenstates and eigenvalues were obtained, allowing the calculation of the magnetic field, the bias voltage and the temperature dependence of the differential conductance $G(V, T, B)$. The latter can then be used to extract the MR value at bias voltage V and temperature T (for more information, see Ref. [186]). The MR values obtained by this model for different voltages exhibited a similar dependence on the magnetic field as in experiments, indicating that the singlet-triplet Kondo model may be a valid explanation for the observed MR.

To further validate this hypothesis, DFT calculations, as well as charge transport calculations were performed in this thesis and compared to experimental results. DFT calculations were performed using the B3LYP functional in combination with Ahlrichs' def2-TZVP basis set, and Grimme's empirical dispersion correction (DFT-D3), as further described in Section 8.3.

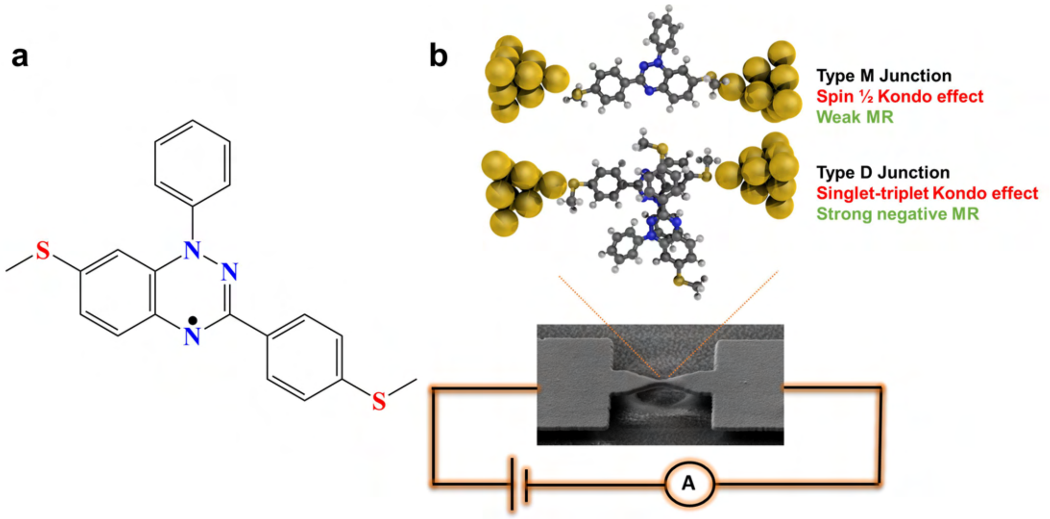

Figure 6.48: Illustration of Blatter radical molecular junctions. a) Chemical structure of the Blatter radical. b) Schematic representation of the types of Blatter radical junctions formed between two Au electrodes in a mechanically controlled break junction device. Type M indicates a monomer junction and Type D indicates a dimer junction. Reprinted with permission from G. Mitra et al. Conventional versus singlet-triplet Kondo effect in Blatter radical molecular junctions: Zero-bias anomalies and magnetoresistance. *Chem* 2025, 102500 under an Open Access license.

6.4.1 How Strongly do Blatter Radicals Bind to Each Other?

To gain a preliminary understanding of the stability of the coupling between two Blatter radicals, we analyzed the binding energies of the resulting dimers. Therefore, four different initial guesses for Blatter dimer structures were proposed (D1-D4, shown in Figure 6.49), each differing in the specific regions of the aromatic systems of the two monomers that were coupled together. The four structures were each optimized in the closed-shell singlet (cs), triplet (t), and the open-shell (os) singlet (s) states, as described in Section 8.3. The energies of the four dimer structures in all spin states are summarized in Table 6.9. The majority of the dimer structures are most stable in the open-shell singlet spin state, but in one of the four dimer configurations, the triplet was the most favorable state. For interpreting the binding energies, a monomer structure (M) was optimized as well. The binding energies E_{bind} of the dimers ranged from about 77 to 108 kJ/mol, showing the strong noncovalent binding between the Blatter radicals.

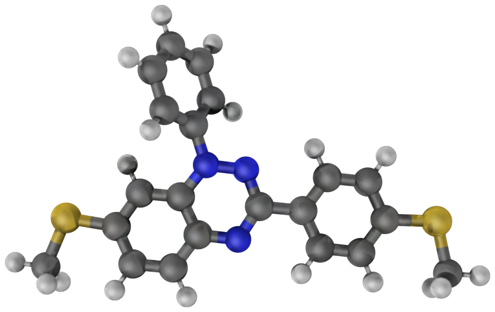

Monomer Structure (M)

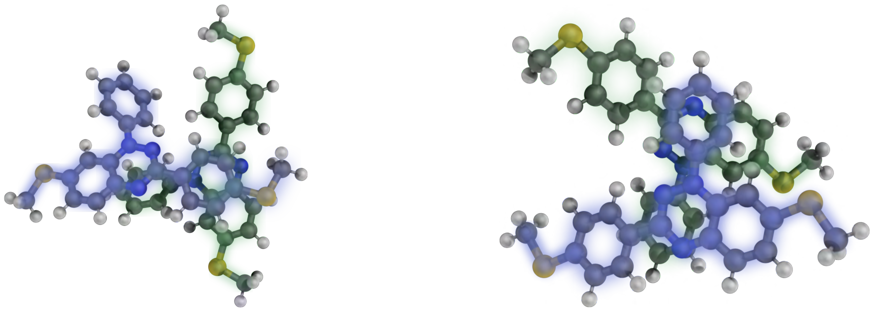

Dimer 1 (D1): triplet
$E_{\text{bind}} = 92.2\,\text{kJ/mol}$
$J = 24.9\,\text{cm}^{-1}$

Dimer 2 (D2): os singlet
$E_{\text{bind}} = 76.9\,\text{kJ/mol}$
$J = -234.3\,\text{cm}^{-1}$

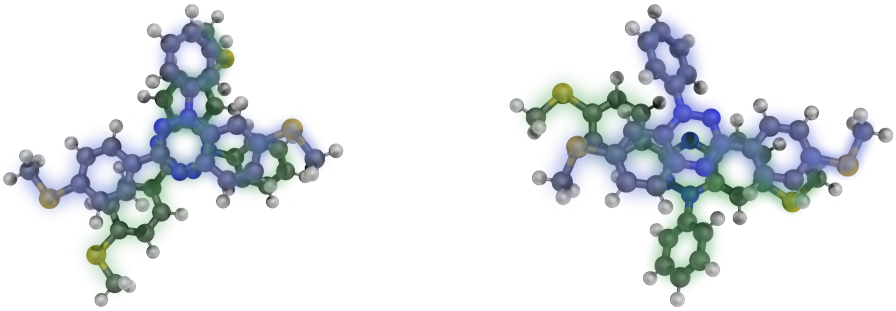

Dimer 3 (D3): os singlet
$E_{\text{bind}} = 95.3\,\text{kJ/mol}$
$J = -142.2\,\text{cm}^{-1}$

Dimer 4 (D4): os singlet
$E_{\text{bind}} = 107.7\,\text{kJ/mol}$
$J = -93.8\,\text{cm}^{-1}$

Figure 6.49: Optimized structures of Blatter radical monomer and dimers (with their respective binding energies E_{bind}) in their respective spin ground states. In each dimer structure, one Blatter radical is marked in blue while the other is indicated in green to enhance clarity and differentiation.

6.4.2 Exchange-Spin-Coupling Constant of Isolated Dimers and Dimer Junctions

The dimer structures remained reasonably similar to one another when optimized in different spin states. The evaluation of the local unpaired-electron densities showed that the distribution of the spins remained the same during the DFT optimization (see Table 6.10). Coupling constants (J) of the four dimers were calculating using Equation (8.2) and are summarized in see Table 6.9 together with the spin expectation values obtained from DFT calculations. In most dimer structures, negative J values were obtained, ranging from -94 to $-234\,\text{cm}^{-1}$, indicating antiferromagnetic coupling. Only in one case, a positive J value of $25\,\text{cm}^{-1}$ was observed, indicating ferromagnetic coupling. These findings are consistent with previous research on Blatter dimers in solid materials,[198] as well as with the favored singlet ground state observed in so-called pancake-bonded radical dimers.[199] The two "extreme" cases – one with a positive J and the other with the most negative J – correspond to the dimer structures with the highest energies. However, since the energy differences among the four dimer structures are not substantial, they may also be experimentally accessible depending on their relative energy.

Table 6.9: Energies E, coupling constants J, and total spin expectations values $\langle \hat{S}^2 \rangle_{\text{os}}^{\text{t or s}}$ for the different isolated dimer configurations, optimized dimer junctions and non-optimized dimer junctions. The lowest-energy spin state of each dimer configuration is written in bold letters. Negative Js indicate antiferromagnetic coupling.

	D1	D2	D3	D4
		Isolated Dimers		
E_{cs} [a.u.]	-3542.9474	-3542.9180	-3542.9599	-3542.9672
E^{t} [a.u.]	**-3542.9727**	-3542.9654	-3542.9733	-3542.9782
E^{s}_{os} [a.u.]	-3542.9726	**-3542.9669**	**-3542.9739**	**-3542.9786**
$\langle \hat{S}^2 \rangle^{\text{t}}$	2.0327	2.0335	2.0340	2.0322
$\langle \hat{S}^2 \rangle^{\text{s}}_{\text{os}}$	1.0326	1.0310	1.0010	1.0044
J [cm^{-1}]	**24.9**	**-234.3**	**-142.2**	**-93.8**
		Optimized Dimer Junctions		
$E^t[a.u.]$	-6258.0757	-6258.0774	-6258.0939	-6258.1232
$E^s_{os}[a.u.]$	-6258.0758	-6258.1046	-6258.0934	-6258.1251
$\langle \hat{S}^2 \rangle^{\text{t}}$	3.9770	3.9432	3.9975	3.8374
$\langle \hat{S}^2 \rangle^{\text{s}}_{\text{os}}$	2.9708	2.9398	3.0203	2.7887
J' [cm^{-1}]	**-27.1**	**-5941.4**	**107.1**	**-411.7**
		Non-Optimized Dimer Junctions		
E^{t} [a.u.]	**-6258.0499**	-6258.0426	-6258.0641	**-6258.0575**
E^{s}_{os} [a.u.]	-6258.0500	**-6258.0427**	**-6258.0655**	-6258.0572
$\langle \hat{S}^2 \rangle^{\text{t}}$	3.9471	3.9771	4.0115	3.9025
$\langle \hat{S}^2 \rangle^{\text{s}}_{\text{os}}$	2.9441	2.9741	3.0391	2.8903
J [cm^{-1}]	**-21.9**	**-19.1**	**-312.3**	**67.6**

As previously demonstrated, the coupling of Blatter radicals to electrodes can significantly affect the properties of these radicals.[194] Therefore, the evaluation of J was repeated with the radicals positioned inside a junction. Therefore, the optimized dimer structures were placed between two 10-atomic gold-clusters with initial sulfur–gold distances of $\text{d}_{Au-S} = 2.40\,\text{Å}$, and with gold–gold distances of $\text{d}_{Au-Au} = 2.88\,\text{Å}$. The positions of the electrodes were fixed during the optimization. The structural optimization of some of the dimer junctions were not fully converged, due to the tight convergence criteria chosen for the energy gradient

Table 6.10: Unpaired-electron density of each Blatter radical in the isolated dimer structures, the optimized dimer junctions, and the non-optimized dimer junctions, evaluated by summing up the Mulliken local unpaired-electron densities.

Spin state	Molecule	D1	D2	D3	D4
Isolated Dimers					
triplet / $\upharpoonleft\downharpoonright$	1	0.9774	1.0054	0.9763	0.996
	2	1.0058	1.0026	0.9756	0.9839
os singlet / $\upharpoonleft\upharpoonright$	1	0.9706	0.9807	0.9763	0.9813
	2	-0.9875	-0.986	-0.9553	-0.965
Optimized Dimer Junctions					
triplet / $\upharpoonleft\downharpoonright$	1	0.9961	0.9709	-0.9499	0.9926
	2	0.9685	1.0	0.9902	0.9718
	electrode	0.0208	0.0174	1.9764	0.0494
os singlet / $\upharpoonleft\upharpoonright$	1	0.9948	0.9269	-0.9716	0.9787
	2	-0.9632	-0.9689	-0.9774	-0.9516
	electrode	-0.0021	0.033	1.9705	-0.0378
Non-Optimized Dimer Junctions					
triplet / $\upharpoonleft\downharpoonright$	1	0.995	1.0105	-0.9614	0.9912
	2	0.9873	0.9951	0.9715	1.0117
	electrode	0.0242	0.0322	1.9804	-0.0177
os singlet / $\upharpoonleft\upharpoonright$	1	-0.9822	-0.9366	-0.9758	-0.9751
	2	0.9675	0.9867	0.9702	1.012
	electrode	0.0227	-0.0002	-0.0027	-0.0173

(10^{-4} a.u. rather than the standard 10^{-3} a.u.) and the somewhat flat potential energy landscape. Nonetheless, gradients of all structures are within, or below, the 10^{-3} a.u. range (see Appendix, Table A.2 for gradients). Initially, the dimers were positioned such that one radical was connected to both electrodes, while the other radical was π-stacked with the first but remained unconnected to the electrodes. However, during the optimization process, the second radical rotated to establish a connection with one of the gold electrodes via the thioether group in approximately half of the optimizations (see Figure 6.50, center). In the other half of the optimizations, the second radical remained π-stacked but unconnected to the electrodes (see Figure 6.50, right). An overview of the final positions of the second dimer is summarized in the Appendix, Table A.2.

An interpretation of which structure is more plausible, and whether the second radical is solely π-stacked or also linked to a gold electrode, is challenging, as it may be influenced by factors such as the shape of the gold electrode, which were not varied here. A relatively flat electrode (more like a flat Au(111) surface rather than a pointed electrode), for example, that could potentially form during break junction experiments, could further enhance the likelihood of the second radical connecting to the electrodes. Overall, our data suggests that the potential energy landscape of these systems is relatively flat, indicating that minor changes, such as a change in spin state (e.g., induced by an external magnetic field) could result in significant structural rearrangements.

Dimer structures, optimized inside a gold junction, showed considerably stronger preference for the open-shell singlet compared to the triplet state in most cases than isolated dimers (see Table 6.10). This is reflected in mainly negative and large J values. However, there is a significant transfer of spin density between the radicals and the gold clusters, as reflected in the $\hat{S}^2$ expectation values, which are considerably larger than the values of 1 and 2 expected for an ideal open-shell singlet and triplet, respectively (see Table 6.10). While we have confidence in the resulting electronic structures for interpreting conductances, we must consider that the spin-state energetics may be influenced by the spin transfer to the gold clusters, which are significantly smaller than the electrodes used in break-junction experiments. Consequently, we do not further analyze these data, except to note that the binding of the gold electrodes may slightly favor open-shell singlet states compared to the optimized isolated dimers.

For interpreting the Kondo effect, independently of these structural rearrangements, the coupling constants were also calculated for the dimer junctions prior to structural optimizations (see Table 6.9). Therefore, the optimized dimer structures were placed inside a junction and a single-point calculation was performed. The resulting J values are in a similar range as the values obtained for the dimers outside of a junction. For most structures, negative J values, corresponding to antiferromagnetic coupling, were obtained, with the values ranging from -19 to $312\,\mathrm{cm}^{-1}$, where the dimer structure with the lowest J value is the most stable structure. As for the isolated dimers, in one case, a positive J value of $67\,\mathrm{cm}^{-1}$ was obtained, indicating ferromagnetic coupling is also possible for some junctions. A significant transfer of the spin density between the radicals and the gold clusters is only found in one of the structures (D3 in the triplet spin state, see Table 6.10), rather that in two as in the optimized junction structures.

6.4.3 Conductance Values for Different Molecular Junction Configurations

The conductances of the optimized dimer and monomer junction structures were evaluated assuming coherent tunneling, as described in Section 8.3. In case of the monomer junction, the majority-spin (spin-up) transmission (Figure 6.50) exhibited peaks on either side of a reasonable range of Fermi energies (-4 to $-5\,\mathrm{eV}$), with a minimum in between going down to about 10^{-3}. The minority spin (spin-down) transmission displayed a Fano-resonance-like feature, featuring a pronounced negative peak near the range of reasonable Fermi energies. As a result, the contribution of minority spins to the overall transmission was significantly lower than that of the majority spins. The calculated monomer transmission functions aligned closely with the transmissions reported by Jiang et al. [196] when appropriately shifted according to their Fermi energy and adjusted to account for the wider HOMO-LUMO gap. This shift was necessary as hybrid functionals were used in our calculations, while Jiang et al. employed an exchange-correlation functional at the level of GGA within the PBE formulation. The adjustment was made by scaling our transmission function (see Figure 6.52).

For the dimer junctions and the isolated dimers, the closed-shell singlet spin states were energetically significantly less stable than the open-shell singlet and the triplet spin state. Therefore, the closed-shell singlet state transmission was not interpreted further. The open-shell singlet and triplet dimer transmissions were reasonably close to each other, and overall, the different optimized structures did not result in vastly different values for the transmissions around E_F (see Table 6.11). Even if the second radical was also connected on one side to the electrode, the transmission did not increase or decrease significantly (see Table 6.11, D3 (triplet and os singlet) and D4 (cs, triplet, and os singlet)).

The overall transmission shapes for open-shell triplet and open-shell singlet dimers closely resembled that of the monomer transmission, but shifted towards somewhat larger values. Notably, the zero-bias conductances span a range that is approximately half to an order of magnitude larger than that observed in the monomer junction (see Table 6.12). The only exception was for a Fermi energy level of $E_F = -4\,\mathrm{eV}$, where the conductance values of the monomer and the D4 dimer were comparable. The range of zero-bias conductances, approximately 10^{-3} to 10^{-2} G_0, interestingly aligned with the range of conductance peaks found in the experiment. While this suggests strong agreement, it should be noted that the computational methods used typically overestimate conductance values by up to an order of magnitude [200]. This suggests that out of the different analyzed junction configurations, the ones with the highest conductances were the ones that corresponded best to experimental data. Consequently, our simulations imply that dimers, rather than monomers, are more consistent with the experimentally observed conductance peaks. This observation is further supported by the significant binding energies between Blatter radicals and aligned with the finding that spin coupling between adjacent radicals corresponds with the observed Kondo properties according to the singlet-triplet model developed by our collaborators.

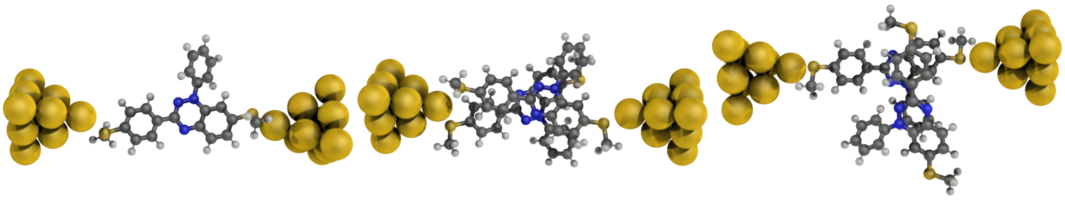

Figure 6.50: Left: Structure of the optimized monomer junction. Middle: An example of a dimer junction (derived from D3) in which one Blatter radical bridges the electrodes, while the second Blatter radical connects to one electrode through one of its thioether groups after optimization. Right: Another example of a dimer junction (based on D1), where one Blatter radical bridges the electrodes, and the second radical π-stacks with the first but does not connect to the electrodes. An overview of the types of structures achieved in each case is provided in the Appendix, Table A.2. An overview of all dimer junction structures can be found in the Appendix, Figures A.37. Reprinted with permission from G. Mitra et al. Conventional versus singlet-triplet Kondo effect in Blatter radical molecular junctions: Zero-bias anomalies and magnetoresistance. *Chem* 2025, 102500 under an Open Access license.

Table 6.11: Spin-up and spin-down transmissions of monomer (M) and dimer (D) junctions for different values of the Fermi energy. The energetically most stable spin states for each case are highlighted in bold-face.

Struct.	Spin State	T(−5.0 eV)		T(−4.54 eV)		T(−4.0 eV)	
		↑	↓	↑	↓	↑	↓
M	**os doublet**	**0.001007**	**0.000111**	**0.001311**	**0.000248**	**0.004124**	**0.000529**
D1	cs	0.001949	0.001949	0.007564	0.007564	0.002918	0.002918
D1	tripl.	0.000115	0.006299	0.000682	0.006648	0.001732	0.013063
D1	**os singl.**	**0.008419**	**0.000171**	**0.008474**	**0.000963**	**0.015307**	**0.002282**
D2	cs	0.009656	0.009656	0.019957	0.019957	0.014034	0.014034
D2	tripl.	0.000348	0.011456	0.001094	0.011187	0.002405	0.019342
D2	**os singl.**	**0.000364**	**0.011838**	**0.001166**	**0.011423**	**0.002539**	**0.018954**
D3	cs	0.025099	0.025099	0.004431	0.004431	0.001949	0.001949
D3	**tripl.**	**0.005091**	**0.000493**	**0.004675**	**0.001009**	**0.006784**	**0.001510**
D3	os singl.	0.005703	0.001709	0.004649	0.000933	0.006954	0.001396
D4	cs	0.005387	0.005387	0.000941	0.000940	0.000975	0.000975
D4	tripl.	0.000621	0.002022	0.000464	0.002003	0.000711	0.003557
D4	**os singl.**	**0.002282**	**0.000422**	**0.002122**	**0.000505**	**0.003576**	**0.000787**

Table 6.12: Zero-bias conductances of monomer and dimer junctions. The lowest-energy spin state (see Appendix, Table A.2) of each dimer structure is marked as bold.

Structure	Spin State	$G_{0V}(-5.0\ \text{eV})/G_0$	$G_{0V}(-4.54\ \text{eV})/G_0$	$G_{0V}(-4.0\ \text{eV})/G_0$
M		1.12×10^{-3}	1.56×10^{-3}	4.65×10^{-3}
D1	cs	3.90×10^{-3}	1.51×10^{-2}	5.84×10^{-3}
D1	triplet	6.41×10^{-3}	7.33×10^{-3}	1.48×10^{-2}
D1	**os singlet**	8.59×10^{-3}	9.44×10^{-3}	1.76×10^{-2}
D2	cs	1.93×10^{-2}	3.99×10^{-2}	2.81×10^{-2}
D2	triplet	1.18×10^{-2}	1.23×10^{-2}	2.17×10^{-2}
D2	**os singlet**	1.22×10^{-2}	1.26×10^{-2}	2.15×10^{-2}
D3	cs	5.05×10^{-2}	8.86×10^{-3}	3.90×10^{-3}
D3	**triplet**	5.59×10^{-3}	5.68×10^{-3}	8.29×10^{-3}
D3	os singlet	7.41×10^{-3}	5.58×10^{-3}	8.35×10^{-3}
D4	cs	1.08×10^{-2}	1.88×10^{-3}	1.95×10^{-3}
D4	triplet	2.64×10^{-3}	2.47×10^{-3}	4.27×10^{-3}
D4	**os singlet**	2.70×10^{-3}	2.63×10^{-3}	4.36×10^{-3}

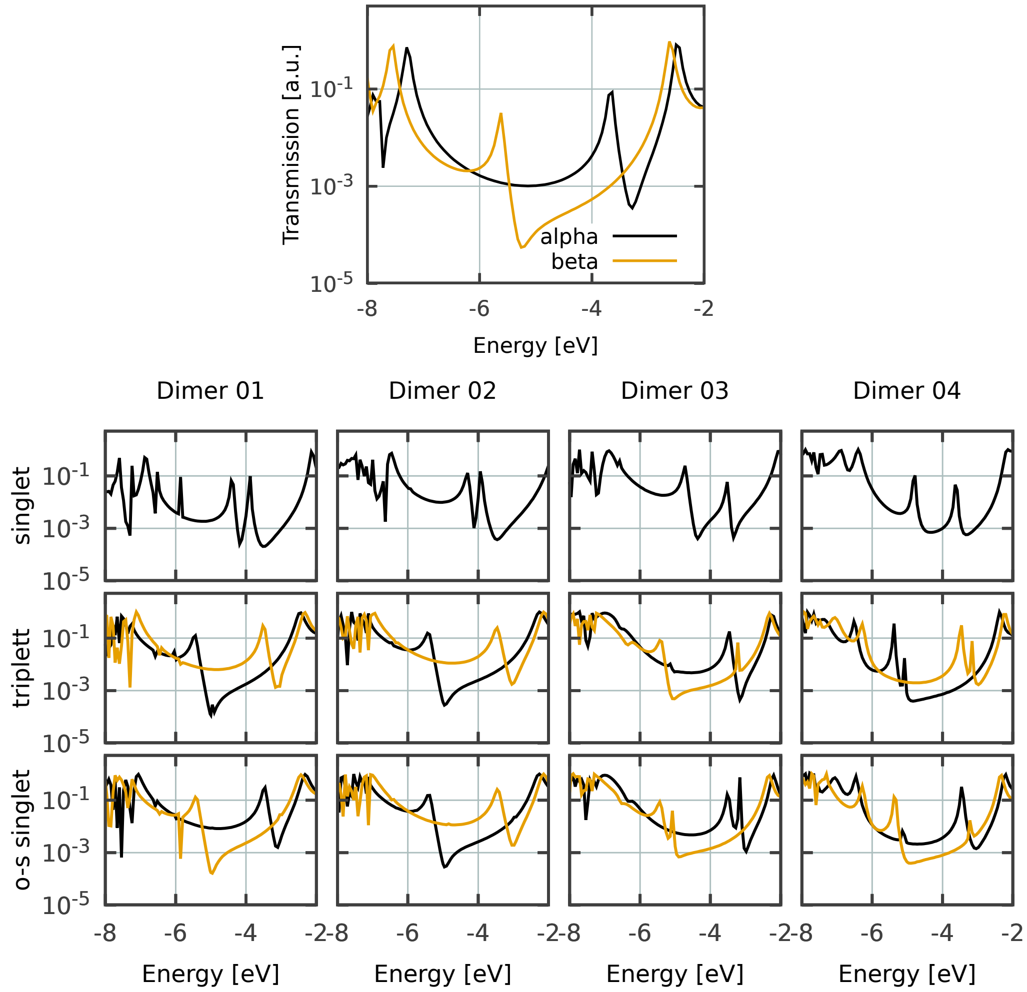

Figure 6.51: Top: Spin-up/majority (black) and spin-down/minority (orange) transmissions of a monomer junction. Bottom: Spin-up/majority (black) and spin-down/minority (orange) transmissions of dimer junctions. Note that due to spin transfer between the radicals and the gold clusters modeling the electrodes, spin-down electrons can become majority *on the radicals*. This explains why in some transmission plots, the color codes appear to be switched. Reprinted with permission from G. Mitra et al. Conventional versus singlet-triplet Kondo effect in Blatter radical molecular junctions: Zero-bias anomalies and magnetoresistance. *Chem* 2025, 102500 under an Open Access license.

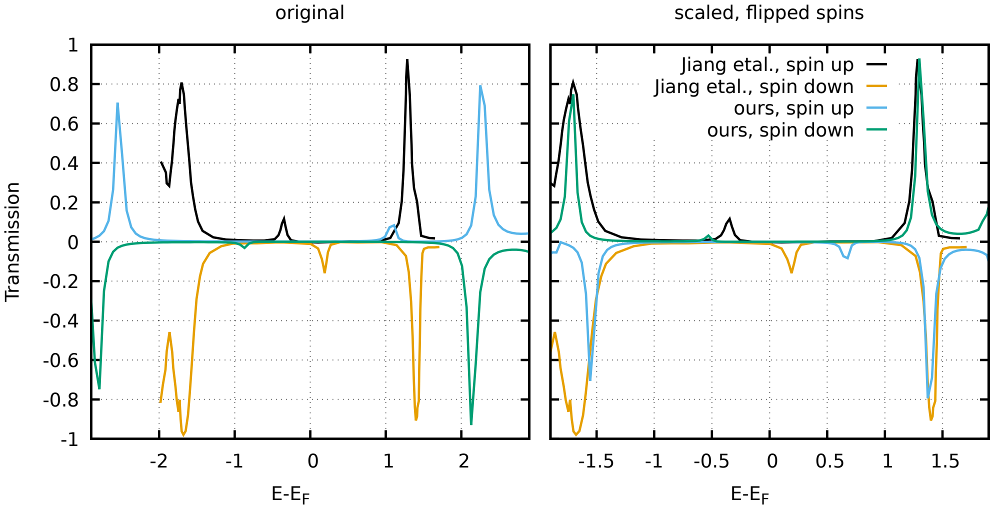

Figure 6.52: Transmission function calculated by Jiang et al. [196] compared to our monomer junction calculations. To align our transmission function with that of Jiang et al., in both graphs, our transmission function was shifted by 4.75 eV. Our calculations, which employed hybrid functionals, also exhibit a wider HOMO-LUMO gap, as reflected in the transmission function. To address this discrepancy, we scaled our transmission function by a factor of 0.61 (right). Although the positions of the SOMOs remain slightly shifted, the main features are effectively reproduced. It is noteworthy that the majority spin in our calculations is inverted compared to that reported in Ref. [196]. Reprinted with permission from G. Mitra et al. Conventional versus singlet-triplet Kondo effect in Blatter radical molecular junctions: Zero-bias anomalies and magnetoresistance. *Chem* 2025, 102500 under an Open Access license.

7 Conclusions & Outlook

This thesis has focused on the potential of single-interface models composed of Au(111) surfaces interconnected by alkanedithiol (ADT) or alkanemonothiol (AMT) ligands to accurately represent properties of cross-linked gold nanoparticle (GNP) assemblies, such as interparticle distances and zero-bias conductances. To achieve a more realistic description of these systems and their dynamic behaviors than what is provided by coarse-grained or classical force fields, a reactive force field (ReaxFF) approach was used. The validity of the single-interface model was assessed by analyzing how interparticle distances varied with increased chain lengths of the ligands. The interparticle distance was found to increase by 1.2 and 1.3 Å per carbon unit for ADT (see Section 6.1.2) and AMT (see Section 6.1.3) ligands, respectively, closely aligning with experimental results. The simulated interparticle distance for (1,9-nonanedithiol) 9DT also corresponded well with values measured for assemblies build from larger particles (approximately 7.4 nm). However, the measured distances for smaller ADT-linked particles (around 3.2 nm) were found to be 1.5 to 2 Å lower than simulated values. In the case of AMT interfaces, the selection of ligand coverage and thereby a reasonable amount of interlacing of the AMT ligands played a critical role in achieving good agreement with experimentally determined distances; the optimal alignment with experimental data was observed when 75 % of the Au(111) surface was covered with AMT ligands.

Further evaluation of the model included an examination of charge transport properties derived from representative MD snapshots, using a density functional tight-binding (DFTB) approach combined with a coherent tunneling approach. An exponential decrease in zero-bias conductance was obtained as the chain length increased for both ADT and AMT ligands, a finding that matched both qualitatively and quantitatively with predictions from theoretical models and experimental data found in the literature on GNP assemblies. Additionally, a highly simplified geometric model was employed, in which the GNPs are assumed to be arranged in a primitive cubic packing and exhibit no internal resistance. This approach allows for a quantitative comparison of the calculated zero-bias conductances with the measured conductivities. Notably, the conductivities calculated from the model were within the range of the measured conductivities of cross-linked GNP assemblies.

While the analysis of interparticle distances and zero-bias conductances indicated that the single-interface model, using ReaxFF, serves as a reasonable approximation for GNP assemblies, certain limitations were observed in simulations involving ADT ligands (see Section 6.1.4). Specifically, these simulations resulted in unrealistic chemical reactions, such as the formation of S—C bonds, due to the presence of free thiol tail groups. To mitigate this issue, a Python script was implemented to automatically detect and exclude trajectories with problematic S—C—S, S—H, and C—S—C bond formations from further analysis (see Appendix B). Although this approach ensured chemically valid structures, it restricted the length of MD trajectories and thereby limited the quality of structural sampling. Future work should focus on reparameterizing the ReaxFF or exploring machine-learning-based force fields[152–154] to create a more flexible and robust modeling framework.

The single-interface model was also applied to examine the structures of mixed-ligand GNP assemblies incorporating AMT and ADT ligands (see Section 6.2). Comparative analyses of different structural models revealed that mixtures of (1-hexanethiol) 6T and 9DT ligands are likely to assemble in a manner characterized by random distribution, wherein 9DT ligands effectively cross-link the surfaces. In contrast, results obtained for mixtures of 1-undecanethiol

(11T) or (1-dodecanethiol (12T) with 9DT were contradictory: while experimental intersurface distances aligned with those from MD simulations featuring randomly distributed ligands without cross-linking, charge transport calculations indicated that the ligands separate into distinct domains, complicating predictions regarding ligand distributions in these structures.

Furthermore, the introduction of alkane molecules as analyte gases into the interface structures resulted in increased preferred intersurface distances, simulating the swelling effect observed in GNP assemblies upon gas adsorption (see Section 6.3.3). The calculated change in interparticle distance upon incorporating a single analyte molecules was, however, three times larger than the experimentally reported values for 10,000 ppm analyte concentrations. Additionally, the calculated relative resistance from charge transport measurements was predominantly negative, which contradicted experimental observations. The analyte-to-ligand ratio used in the simulations (1:8) was comparable to that estimated in the literature (approximately 1:6 for an analyte concentration of 10,000 ppm). This indicates that the analyte distribution in GNP assemblies varies significantly, and the concentration of analytes in the interface regions where the ligands are densely packed may be significantly lower than in the remaining parts of the assemblies. Therefore, the single-interface model may not adequately capture the properties of GNP assemblies during analyte adsorption, highlighting the need for larger models that incorporate regions beyond the interface.

Overall, thesis has contributed to the development of a simplified structural model for GNP assemblies, outlining both its capabilities and limitations in describing these systems and uncovering atomistic insights into their sensing mechanisms. By concentrating on single, flat interfaces, a level of atomistic detail was reached that would have been challenging to achieve with larger models that encompass entire GNP assemblies,[44, 45, 89, 93, 97, 145] which typically rely on coarse-grained or united-atom representations of the ligands. Additionally, the relatively small scale of the model facilitates charge transport calculations employing a DFTB approach within the framework of Landauer transport theory. While the current application of ReaxFF is limited to ADT and AMT ligands, future advancements could include generalizing the model[53, 201] or applying techniques such as machine-learned force fields[152–154] or DFTB-MD[137], which may offer greater adaptability and prevent the occurrence of artifacts. Coupled with machine-learning methodologies for conductance,[150, 202–204] a focus on single interfaces could eventually facilitate the rapid screening of ligands or ligand combinations for various sensing applications.

In the final section of this thesis (Section 6.4), Blatter radical junctions were explored to determine whether the experimentally reported anomalous behavior – characterized by high negative magnetoresistance in some junctions with Kondo features – could be attributed to the formation of Blatter radical dimers within these junctions. Density functional theory (DFT) calculations demonstrated a strong noncovalent interaction between pairs of Blatter radicals. The exchange coupling constants for both isolated dimers and those embedded in junctions predominantly exhibited antiferromagnetic properties. Furthermore, the zero-bias conductances calculated for dimer junctions using a Green's function approach combined with DFT more closely matched experimental conductances than those calculated for monomer junctions. These results support the hypothesis that the anomalous magnetoresistive behavior observed in certain junctions can be explained by the formation of Blatter radical dimers. Thereby, this thesis has contributed to a better understanding of fundamental properties of Blatter radicals, which could be interesting building blocks for future spintronic devices, but also potential ligands for GNP assemblies, due to their relatively high conductance and stability compared to ADT and AMT ligands.

8 Computational Methods

8.1 Molecular Dynamics Simulations of Particle–Particle Interfaces

MD simulations were performed using the LAMMPS[205] MD simulator. A ReaxFF was used with parameters from Bae and Aikens,[109] inspired by simulations of molecular break-junction experiments with similar ligands by Deffner et al.[150] In contrast to classical force fields, using a ReaxFF enables the simulation of bond formations (e.g., ligand associations), as well as bond breaks (e.g. ligand dissociation, or rupture of bonds under mechanical stress). Simulations were performed using a canonical (NVT) ensemble with timesteps of 0.5 fs. The temperature was kept fix at 300 K by a Berendsen thermostat. Semi-periodic boundary conditions, along the gold surface, were used to prevent edge effects (e.g., ligands at the edge of the gold surface moving around it to its bottom side). If not stated otherwise, the simulation cell was $10.0 \times 17.3 \times z$, where the height z was adjusted according to the length of the organic ligand.

The three-layered Au(111) surface consisted of 72 atoms. Ligand molecules were placed onto the gold surface such that they occupied the fcc hollow sites. A 100 % coverage corresponds to that of a $(\sqrt{3} \times \sqrt{3})$ R30° structure, reported in the literature for gold surfaces with alkanethiol ligands.[127] Figure 6.4 highlights the adsorption positions of the ligand molecules on the gold surface. Singly deprotonated alkanethiols were placed onto the surface in all-trans conformation with a distance of 2 Å toward the center of the gold atoms in the top layer. An exemplary interface starting structure can be found in Figure 6.9, Structure 1. To relax the structures, and to identify the lowest-energy surface-to-surface distance, the two gold surfaces were pushed together. Therefore, the structure was divided into three regions: the *handle*, the *mobile*, and the *fixed* region (see Figure 5.1 center). Forces on atoms in both the handle and fixed region were set to zero in all directions. To freeze the atoms in the fixed region, the velocities of these atoms was additionally set to zero. Atoms in the handle region, on the other hand, were moved toward the other gold surface with a constant velocity of 2×10^{-4} Å/fs (where 1 Å/fs= 10^5 m/s). The remaining atoms in the mobile region were allowed to move freely, with respect to the laws of motion. In the course of the MD simulations, the total energy for each step was determined, along with the respective contributions from potential and kinetic energy. The potential energy was evaluated to identify the lowest-energy structures, as the kinetic energy was primarily affected by minor changes in the simulation temperature, and was therefore less meaningful for determining the most stable structure. Simulations were repeated 10 times from the same starting structure but with different initial seed velocities, to receive a statistical analysis of the lowest-energy surface-to-surface distance of each structure. The average preferred surface-to-surface distance was then calculated from the minima of the potential energy vs distance curve of the 10 simulations. A different approach for calculating the average preferred surface-to-surface distance, involving a parabola fit of the average potential energy vs. the distance, resulted in similar distances (see Figure 6.24 and discussions in Section 6.1.5.2), showing that the extracted average distance is robust with respect to the averaging procedure.

The lowest-energy structure and thereby the preferred surface-to-surface distance may also be affected by the artificial decrease of the surface-to-surface distance. Therefore, simulations were also performed with half the pushing speed, and without fixing atoms movement or pushing, using an isothermal–isobaric (*NPT*) ensemble, both resulting in distances very close to the standard pushing simulation (see Section 6.1.5.1). For the NPT simulations, full periodic boundary conditions were applied. The height of the simulation cell was adjusted by adding approx. 25 Å, resulting in pseudo semi-periodic boundary conditions. The temperature was set to 300 K, and the pressure to 1.0 atmospheres. With timesteps of 0.5 fs, the structures were usually relaxed for 250,000 steps.

In around 40 % of all simulations involving alkanedithiol ligands, dissociation of ligands, followed by reactions of the free thiol group with neighboring ligands occurred. These reactions resulted in the formation of R—S—R, R—S—S—R, or S—H motives, where R is an organic rest. To identify those trajectories, a PYTHON script was written that detected those structural motives, and automatically removed the complete trajectory, when the reaction occurred before reaching the lowest-energy point, or shortly after reaching it. Such artifacts were almost never observed in structures consisting solely of alkanemonothiol ligands.

8.2 Charge Transport Calculations of Particle–Particle Interfaces

The lowest-energy structures from the MD simulations were extracted, and six additional gold layers were added to each 3-layered gold surface to form the contact regions. In structures with dissociated ligands (S—Au distance > 3 Å), hydrogen atoms were added to the free thiolate groups prior to the transport calculations, since free thiolate groups caused artifacts in some of the calculations, where the transmissions varied by several orders of magnitude compared to those of structures without free thiolate groups (see Appendix, Section A.2.3). Periodic boundary conditions were again applied in all directions, and a vacuum gap of 30 Å was added in *z*-direction (transport direction). Thereby, pseudo semi-periodic conditions were established, allowing for expansion of the gold surfaces in the *x* and y directions while maintaining pseudo non-periodicity along the transport direction due to the presence of the vacuum gap.

Charge transport calculations were performed using self-consistent DFTB electronic structure calculations using Green's functions, and the Landauer coherent tunneling approach, as implemented in the DFTB+[206] code. Auorg[72, 77, 78] Slater-Koster files were used. Monkhorst-Pack sets of $6 \times 6 \times 10$ for the contact region, and $4 \times 4 \times 1$ for the device regions gave best performances according to the K-point sampling (see Appendix, Section A.2.2). Note that only one K-point in *z*-direction was required for the device region, as the system is quasi non-periodic in this direction. Shell-resolved self-consistent charge (SCC) was turned on, and a tolerance of $10^{\circ}{-6}$ was used with 200 maximal SCC iterations for the contact calculations, and 1000 iterations for the device calculation. A Fermi energy of −4.6848 eV was calculated when applying shell-resolved SCC (see Section A.2.1 for a discussion on the best choice of approximations in the electronic structure description for the Fermi energy of periodic gold-ligand systems). Although this value aligns reasonably well with the experimentally determined work function of bulk gold (approximately −5.5 eV) and the observed shift caused by hydrocarbon thiolate ligands to more positive values, [207, 208] it is important to consider that the position of the Fermi energy may be influenced not only by the selection of approximations but also by the simplified atomistic model used.

Transmissions were computed in an energy range around the calculated Fermi energy between −5 and −4 eV with energy steps of 0.01 eV, to cover the most probable Fermi energy values. Zero-bias conductances $G_{0\mathrm{V}}$ were calculated by

$$G_{0V} = \frac{2e^2}{h} T(E_F) \ , \tag{8.1}$$

where e is the elemental charge, h is Planck's constant, and $T(E_F)$ is the Fermi energy.

8.3 First-Principles Calculations on Blatter Radical Junctions

Structure optimizations were performed using Kohn–Sham density functional theory (KS-DFT) as implemented in the program package Turbomole 6.6.[209] The exchange–correlation functional B3LYP [69, 70, 210, 211] with m4 integration grids was used, along with Ahlrichs' def2-TZVP [212] single-particle atom-centered basis set. In addition, Grimme's empirical dispersion corrections (DFT-D3) [213] with Becke–Johnson damping [214] was used. Convergence criteria for the energy in the self-consistent-field (SCF) algorithm of 10^{-7} a.u. and for the gradient in the molecular structure optimizations of 10^{-4} were set. Molecular structures of the Blatter dimers were each optimized in the closed-shell singlet (cs), the triplet (t), and the open-shell singlet (s) states, the latter modeled by a broken-symmetry determinant.[215] The coupling constants were obtained based on the Heisenberg–Dirac–van Vleck Hamiltonian $H = -2JS_AS_B$, with S_A and S_B being the radicals local spin vectors, and the Yamaguchi formula,[216, 217]

$$J = \frac{E^{\mathrm{s}}_{\mathrm{os}} - E^{\mathrm{t}}}{\langle \hat{S}^2 \rangle^{\mathrm{t}} - \langle \hat{S}^2 \rangle^{\mathrm{s}}_{\mathrm{os}}} \ , \tag{8.2}$$

where E refers to the total energies of the different spin states and $\langle \hat{S}^2 \rangle$ to their total spin expectation values.

The conductance of the Blatter radical junctions was evaluated assuming coherent tunneling as the dominant transport mechanism (Landauer regime). The zero-bias conductance G_{0V} was calculated from the transmission at the Fermi energy E_F,

$$G_{0V} = \frac{e^2}{h}(T_{\uparrow}(E_F) + T_{\downarrow}(E_F)) \tag{8.3}$$

with the unit charge e, the Planck's constant h, the spin-up/majority-spin transmission $T_{\uparrow}$, and the spin-down/minority-spin transmission $T_{\downarrow}$. The transmissions were modeled via a Green's function approach combined with DFT calculations for zero-bias electronic structures. A wide-band limit for the self-energies of the electrodes was employed, as described earlier.[218–221], and a local density of states (LDOS) of $0.036\,\mathrm{eV}^{-1}$ was applied. Transmission functions were evaluated using Artaios [222], based on the Fock and overlap matrices from the KS-DFT electronic structure calculations of the molecular junctions. As the value of the Fermi energy can not be predicted straightforwardly in first-principles calculations on molecular junctions, as it can be influenced by factors such as the irregular atomistic shapes of the electrodes and the adsorption of nonbridging molecules on the electrodes, the zero-bias conductances were evaluated for a range of reasonable Fermi energies ($-5\,\mathrm{eV}$, $-4.5\,\mathrm{eV}$, $-4\,\mathrm{eV}$).

Bibliography

1. Kramp, T., van Kranenburg, R. & Lange, S. in *Enabling Things to Talk: Designing IoT solutions with the IoT Architectural Reference Model* (eds Bassi, A. *et al.*) 1–10 (Springer Berlin Heidelberg, Berlin, Heidelberg, 2013). ISBN: 978-3-642-40403-0.
2. Franke, M. E., Koplin, T. J. & Simon, U. Metal and Metal Oxide Nanoparticles in Chemiresistors: Does the Nanoscale Matter? *Small* **2,** 36–50. eprint: `https://onlinelibrary.wiley.com/doi/pdf/10.1002/smll.200500261` (2006).
3. Ou, L.-X., Liu, M.-Y., Zhu, L.-Y., Zhang, D. W. & Lu, H.-L. Recent Progress on Flexible Room-Temperature Gas Sensors Based on Metal Oxide Semiconductor. en. *Nanomicro Lett.* **14,** 206. ISSN: 2311-6706, 2150-5551 (Dec. 2022).
4. Montes-García, V. *et al.* Chemical sensing with Au and Ag nanoparticles. *Chem. Soc. Rev.* **50,** 1269–1304 (2 2021).
5. Verma, A., Gupta, R., Verma, A. S. & Kumar, T. A review of composite conducting polymer-based sensors for detection of industrial waste gases. *Sens. Actuators Rep.* **5,** 100143. ISSN: 2666-0539 (2023).
6. Kauffman, D. R. & Star, A. Carbon Nanotube Gas and Vapor Sensors. *Angew. Chem., Int. Ed.* **47,** 6550–6570. eprint: `https://onlinelibrary.wiley.com/doi/pdf/10.1002/anie.200704488` (2008).
7. Goldoni, A., Petaccia, L., Lizzit, S. & Larciprete, R. Sensing gases with carbon nanotubes: a review of the actual situation. *J. Phys. Condens. Matter.* **22,** 013001 (Dec. 2009).
8. Meyyappan, M. Carbon Nanotube-Based Chemical Sensors. *Small* **12,** 2118–2129. eprint: `https://onlinelibrary.wiley.com/doi/pdf/10.1002/smll.201502555` (2016).
9. Zhou, X. *et al.* Silicon nanowires as chemical sensors. *Chem. Phys. Lett.* **369,** 220–224. ISSN: 0009-2614 (2003).
10. Tonezzer, M. Selective gas sensor based on one single SnO2 nanowire. *Sens. Actuators B Chem.* **288,** 53–59. ISSN: 0925-4005 (2019).
11. Alwarappan, S., Nesakumar, N., Sun, D., Hu, T. Y. & Li, C.-Z. 2D metal carbides and nitrides (MXenes) for sensors and biosensors. *Biosens. Bioelectron.* **205,** 113943. ISSN: 0956-5663 (2022).
12. Goel, N., Kushwaha, A. & Kumar, M. Two-dimensional MXenes: recent emerging applications. *RSC Adv.* **12,** 25172–25193. ISSN: 2046-2069 (2022).
13. Daniel, M.-C. & Astruc, D. Gold Nanoparticles: Assembly, Supramolecular Chemistry, Quantum-Size-Related Properties, and Applications toward Biology, Catalysis, and Nanotechnology. *Chemical Reviews* **104,** 293–346. eprint: `https://doi.org/10.1021/cr030698+` (2004).
14. Potyrailo, R. A. Toward high value sensing: monolayer-protected metal nanoparticles in multivariable gas and vapor sensors. *Chem. Soc. Rev.* **46,** 5311–5346 (17 2017).
15. Ibañez, F. J. & Zamborini, F. P. Chemiresistive Sensing with Chemically Modified Metal and Alloy Nanoparticles. *Small* **8,** 174–202 (Nov. 2011).
16. Terrill, R. H. *et al.* Monolayers in Three Dimensions: NMR, SAXS, Thermal, and Electron Hopping Studies of Alkanethiol Stabilized Gold Clusters. *J. Am. Chem. Soc.* **117,** 12537–12548 (Dec. 1995).

17. Gauvin, M., Wan, Y., Arfaoui, I. & Pileni, M.-P. Mechanical Properties of Au Supracrystals Tuned by Flexible Ligand Interactions. *J. Phys. Chem. C* **118,** 5005–5012 (Feb. 2014).
18. Schlicke, H. *et al.* Tuning the Elasticity of Cross-Linked Gold Nanoparticle Assemblies. *J. Phys. Chem. C* **123,** 19165–19174. eprint: `https://doi.org/10.1021/acs.jpcc.9b03553` (2019).
19. Sangeetha, N. M., Decorde, N., Viallet, B., Viau, G. & Ressier, L. Nanoparticle-Based Strain Gauges Fabricated by Convective Self Assembly: Strain Sensitivity and Hysteresis with Respect to Nanoparticle Sizes. *J. Phys. Chem. C* **117,** 1935–1940. eprint: `https://doi.org/10.1021/jp310077r` (2013).
20. García-Berríos, E. *et al.* Response versus Chain Length of Alkanethiol-Capped Au Nanoparticle Chemiresistive Chemical Vapor Sensors. *J. Phys. Chem. C* **114,** 21914–21920 (Aug. 2010).
21. Joseph, Y. *et al.* Self-Assembled Gold Nanoparticle/Alkanedithiol Films: Preparation, Electron Microscopy, XPS-Analysis, Charge Transport, and Vapor-Sensing Properties. *J. Phys. Chem. B* **107,** 7406–7413. eprint: `https://doi.org/10.1021/jp030439o` (2003).
22. Vossmeyer, T. *et al. Gold-nanoparticle/dithiol films as chemical sensors and first steps toward their integration on chip* in *Physical Chemistry of Interfaces and Nanomaterials III* (eds Hartland, G. V. & Zhu, X.-Y.) **5513** (SPIE, 2004), 202–212.
23. Liao, J. *et al.* Ordered nanoparticle arrays interconnected by molecular linkers: electronic and optoelectronic properties. *Chem. Soc. Rev.* **44,** 999–1014 (4 2015).
24. Wessels, J. M. *et al.* Optical and Electrical Properties of Three-Dimensional Interlinked Gold Nanoparticle Assemblies. *J. Am. Chem. Soc.* **126,** 3349–3356. eprint: `https://doi.org/10.1021/ja0377605` (2004).
25. Wuelfing, W. P., Green, S. J., Pietron, J. J., Cliffel, D. E. & Murray, R. W. Electronic Conductivity of Solid-State, Mixed-Valent, Monolayer-Protected Au Clusters. *J. Am. Chem. Soc.* **122,** 11465–11472. eprint: `https://doi.org/10.1021/ja002367+` (2000).
26. Joseph, Y., Guse, B., Vossmeyer, T. & Yasuda, A. Gold Nanoparticle/Organic Networks as Chemiresistor Coatings: The Effect of Film Morphology on Vapor Sensitivity. *J. Phys. Chem. C* **112,** 12507–12514. eprint: `https://doi.org/10.1021/jp8013546` (2008).
27. B. Abeles Ping Sheng, M. C. & Arie, Y. Structural and electrical properties of granular metal films. *Adv. Phys.* **24,** 407–461. eprint: `https://doi.org/10.1080/00018737500101431` (1975).
28. Brust, M., Fink, J., Bethell, D., Schiffrin, D. J. & Kiely, C. Synthesis and reactions of functionalised gold nanoparticles. *J. Chem. Soc., Chem. Commun.,* 1655–1656 (16 1995).
29. Vossmeyer, T., Stolte, C., Ijeh, M., Kornowski, A. & Weller, H. Networked Gold-Nanoparticle Coatings on Polyethylene: Charge Transport and Strain Sensitivity. *Adv. Funct. Mater.* **18,** 1611–1616. eprint: `https://onlinelibrary.wiley.com/doi/pdf/10.1002/adfm.200701509` (2008).
30. Parthasarathy, R., Lin, X.-M. & Jaeger, H. M. Electronic Transport in Metal Nanocrystal Arrays: The Effect of Structural Disorder on Scaling Behavior. *Phys. Rev. Lett.* **87,** 186807 (18 Oct. 2001).
31. Griesemer, S. D. *et al.* The role of ligands in the mechanical properties of Langmuir nanoparticle films. *Soft Matter* **13,** 3125–3133 (2017).
32. Ketelsen, B. *et al.* Fabrication of Strain Gauges via Contact Printing: A Simple Route to Healthcare Sensors Based on Cross-Linked Gold Nanoparticles. *Appl. Mat. & Interf.* **10,** 37374–37385 (Oct. 2018).

33. Ketelsen, B., Tjarks, P. P., Schlicke, H., Liao, Y.-C. & Vossmeyer, T. Fully Printed Flexible Chemiresistors with Tunable Selectivity Based on Gold Nanoparticles. *Chemosensors* **8,** 116 (Nov. 2020).
34. Schlicke, H., Bittinger, S. C., Noei, H. & Vossmeyer, T. Gold Nanoparticle-Based Chemiresistors: Recognition of Volatile Organic Compounds Using Tunable Response Kinetics. *Appl. Nano Mat.* **4,** 10399–10408 (Sept. 2021).
35. Cheng, H.-W., Yan, S., Shang, G., Wang, S. & Zhong, C.-J. Strain sensors fabricated by surface assembly of nanoparticles. *Biosens. Bioelectron.* **186,** 113268. ISSN: 0956-5663 (2021).
36. Ketelsen, B. *et al.* Nanoparticle-Based Strain Gauges: Anisotropic Response Characteristics, Multidirectional Strain Sensing, and Novel Approaches to Healthcare Applications. *Adv. Funct. Mat.* **33,** 2210065. eprint: `https://onlinelibrary.wiley.com/doi/pdf/10.1002/adfm.202210065` (2023).
37. Wu, S.-D. *et al.* Fabrication of Eco-Friendly Wearable Strain Sensor Arrays via Facile Contact Printing for Healthcare Applications. *Small Methods* **7,** 2300170. eprint: `https://onlinelibrary.wiley.com/doi/pdf/10.1002/smtd.202300170` (2023).
38. Nadav, L., Tsion, O.-R. & Offer, Z. Improving the properties of a gold nanoparticle barium sensor through mixed-ligand shells. *Talanta* **208,** 120370. ISSN: 0039-9140 (2020).
39. Liu, C.-Y. *et al.* Tuning the Interfacial Chemistry of Nanoparticle Assemblies via Spin-Coating: From Single Sensors to Monolithic Sensor Arrays. *Adv. Mater. Interfaces* **11,** 2301058. eprint: `https://onlinelibrary.wiley.com/doi/pdf/10.1002/admi.202301058` (2024).
40. Zeiri, O. Metallic-Nanoparticle-Based Sensing: Utilization of Mixed-Ligand Monolayers. *ACS Sens.* **5,** 3806–3820. eprint: `https://doi.org/10.1021/acssensors.0c02124` (2020).
41. Olichwer, N., Meyer, A., Yesilmen, M. & Vossmeyer, T. Gold nanoparticle superlattices: correlating chemiresistive responses with analyte sorption and swelling. *J. Mat. Chem. C* **4,** 8214–8225 (2016).
42. Steinecker, W. H., Rowe, M. P. & Zellers, E. T. Model of Vapor-Induced Resistivity Changes in Gold-Thiolate Monolayer-Protected Nanoparticle Sensor Films. *Anal. Chem.* **79,** 4977–4986 (May 2007).
43. Li, Z. *et al.* Understanding the Conductance Dispersion of Single-Molecule Junctions. *J. Phys. Chem. C* **125,** 3406–3414. eprint: `https://doi.org/10.1021/acs.jpcc.0c08428` (2021).
44. Yeh, K.-C., Chiang, Y. & Chang, S.-W. Full Atomistic Simulation of Cross-Linked Gold Nanoparticle Assemblies. *Multiscale Sci. Eng.* **2,** 242–251 (Oct. 2020).
45. Yeh, K.-C., Tsai, Y.-Y. & Chang, S.-W. The Role of Cross-Linkers in the Mechanical Responses of Gold Nanoparticle Assemblies. *J. Phys. Chem. C* **126,** 6456–6464. eprint: `https://doi.org/10.1021/acs.jpcc.2c00630` (2022).
46. Ciccullo, F. *et al.* A Derivative of the Blatter Radical as a Potential Metal-Free Magnet for Stable Thin Films and Interfaces. *ACS Appl. Mater. Interfaces* **8,** 1805–1812. eprint: `https://doi.org/10.1021/acsami.5b09693` (2016).
47. Ji, Y., Long, L. & Zheng, Y. Recent advances of stable Blatter radicals: synthesis, properties and applications. *Mater. Chem. Front.* **4,** 3433–3443 (12 2020).
48. Spiegelman, F. *et al.* Density-functional tight-binding: basic concepts and applications to molecules and clusters. *ADV PHYS-X* **5,** 1710252 (Jan. 2020).
49. Szabo, A. 1. *Modern quantum chemistry introduction to advanced electronic structure theory* (ed Ostlund, N. S.) (Dover Publications, Inc., 1996).
50. Püschner, D. *Quantitative Rechenverfahren der Theoretischen Chemie* 43–51 (Springer Spektrum Wiesbaden, 2017).

51. Van Duin, A. C. T., Dasgupta, S., Lorant, F. & Goddard, W. A. ReaxFF: A Reactive Force Field for Hydrocarbons. *J. Phys. Chem. A* **105,** 9396–9409. eprint: `https://doi.org/10.1021/jp004368u` (2001).
52. Järvi, T. T., van Duin, A. C. T., Nordlund, K. & Goddard, W. A. Development of Interatomic ReaxFF Potentials for Au–S–C–H Systems. *J. Phys. Chem. A* **115,** 10315–10322 (2011).
53. Furman, D. & Wales, D. J. A well-behaved theoretical framework for ReaxFF reactive force fields. *J. Chem. Phys.* **153,** 021102 (2020).
54. Senftle, T. P. *et al.* The ReaxFF reactive force-field: development, applications and future directions. en. *NPJ Comput. Mater.* **2,** 15011. ISSN: 2057-3960 (Mar. 2016).
55. Chan, H. & Král, P. Self-standing nanoparticle membranes and capsules. *Nanoscale* **3,** 1881–1886 (4 2011).
56. Niklasson, A. M. N. Extended Born-Oppenheimer Molecular Dynamics. *Phys. Rev. Lett.* **100,** 123004 (12 Mar. 2008).
57. Warshel, A. & Levitt, M. Theoretical studies of enzymic reactions: Dielectric, electrostatic and steric stabilization of the carbonium ion in the reaction of lysozyme. *J. Mol. Biol.* **103,** 227–249. ISSN: 0022-2836 (1976).
58. Wesolowski, T. A. & Warshel, A. Frozen density functional approach for ab initio calculations of solvated molecules. *J. Phys. Chem.* **97,** 8050–8053. eprint: `https://doi.org/10.1021/j100132a040` (1993).
59. Behler, J. & Parrinello, M. Generalized Neural-Network Representation of High-Dimensional Potential-Energy Surfaces. *Phys. Rev. Lett.* **98,** 146401 (14 Apr. 2007).
60. Gastegger, M., Behler, J. & Marquetand, P. Machine learning molecular dynamics for the simulation of infrared spectra. *Chem. Sci.* **8,** 6924–6935 (10 2017).
61. Hohenberg, P. & Kohn, W. Inhomogeneous Electron Gas. *Phys. Rev.* **136,** B864–B871 (3B Nov. 1964).
62. Born, M. & Oppenheimer, R. Zur Quantentheorie der Molekeln. *Ann. Phys.* **389,** 457–484. eprint: `https://onlinelibrary.wiley.com/doi/pdf/10.1002/andp.19273892002` (1927).
63. Kohn, W. & Sham, L. J. Self-Consistent Equations Including Exchange and Correlation Effects. *Phys. Rev.* **140,** A1133–A1138 (4A Nov. 1965).
64. Perdew, J. P. & Schmidt, K. Jacob's ladder of density functional approximations for the exchange-correlation energy. *AIP Conf. Proc.* **577,** 1–20. ISSN: 0094-243X. eprint: `https://pubs.aip.org/aip/acp/article-pdf/577/1/1/12108089/1\_1\_online.pdf` (July 2001).
65. Mardirossian, N. & Head-Gordon, M. Thirty years of density functional theory in computational chemistry: an overview and extensive assessment of 200 density functionals. *Mol. Phys.* **115,** 2315–2372. eprint: `https://doi.org/10.1080/00268976.2017.1333644` (2017).
66. Perdew, J. P., Burke, K. & Ernzerhof, M. Generalized Gradient Approximation Made Simple. *Phys. Rev. Lett.* **77,** 3865–3868 (18 Oct. 1996).
67. Becke, A. D. Density-functional exchange-energy approximation with correct asymptotic behavior. *Phys. Rev. A* **38,** 3098–3100 (6 Sept. 1988).
68. Perdew, J. P. Density-functional approximation for the correlation energy of the inhomogeneous electron gas. *Phys. Rev. B* **33,** 8822–8824 (12 June 1986).
69. Lee, C., Yang, W. & Parr, R. G. Development of the Colle-Salvetti correlation-energy formula into a functional of the electron density. *Phys. Rev. B* **37,** 785–789 (2 Jan. 1988).
70. Becke, A. D. Density-functional thermochemistry. III. The role of exact exchange. *J. Chem. Phys.* **98,** 5648–5652. ISSN: 0021-9606. eprint: `https://pubs.aip.org/aip/jcp/article-pdf/98/7/5648/19277469/5648\_1\_online.pdf` (Apr. 1993).

71. Koskinen, P. & Mäkinen, V. Density-functional tight-binding for beginners. *Comput. Mater. Sci.* **47,** 237–253. ISSN: 0927-0256 (2009).

72. Elstner, M. *et al.* Self-consistent-charge density-functional tight-binding method for simulations of complex materials properties. *Phys. Rev. B* **58,** 7260–7268 (11 Sept. 1998).

73. Frenzel, J., Oliveira, A., Jardillier, N., Heine, T. & Seifert, G. Semi-relativistic, self-consistent charge Slater-Koster tables for density-functional based tight-binding (DFTB) for materials science simulations. *TU-Dresden* (2004-2009).

74. Gaus, M., Goez, A. & Elstner, M. Parametrization and Benchmark of DFTB3 for Organic Molecules. *J. Chem. Theory Comput.* **9,** 338–354. eprint: `https://doi.org/10.1021/ct300849w` (2013).

75. Gaus, M., Cui, Q. & Elstner, M. DFTB3: Extension of the Self-Consistent-Charge Density-Functional Tight-Binding Method (SCC-DFTB). *J. Chem. Theory Comput.* **7,** 931–948. eprint: `https://doi.org/10.1021/ct100684s` (2011).

76. Rauls, E., Elsner, J., Gutierrez, R. & Frauenheim, T. Stoichiometric and non-stoichiometric $(10\bar{1}0)$ and $(11\bar{2}0)$ surfaces in 2H–SiC: a theoretical study. *Solid State Commun.* **111,** 459–464. ISSN: 0038-1098 (1999).

77. Niehaus, T., Elstner, M., Frauenheim, T. & Suhai, S. Application of an approximate density-functional method to sulfur containing compounds. *J. Mol. Struc.: THEOCHEM* **541,** 185–194. ISSN: 0166-1280 (2001).

78. Fihey, A. *et al.* SCC-DFTB parameters for simulating hybrid gold-thiolates compounds. *J. Comput. Chem.* **36,** 2075–2087. eprint: `https://onlinelibrary.wiley.com/doi/pdf/10.1002/jcc.24046` (2015).

79. Marx, D. & Parrinello, M. Ab initio path-integral molecular dynamics. en. *Z. Phys. B Con. Mat.* **95,** 143–144. ISSN: 0722-3277, 1434-6036 (1994).

80. Alder, B. J. & Wainwright, T. E. Phase Transition for a Hard Sphere System. *J. Chem. Phys.* **27,** 1208–1209. eprint: `https://doi.org/10.1063/1.1743957` (1957).

81. Hollingsworth, S. A. & Dror, R. O. Molecular Dynamics Simulation for All. *Neuron* **99,** 1129–1143. ISSN: 0896-6273 (2018).

82. Durrant, J. D. & McCammon, J. A. Molecular dynamics simulations and drug discovery. *BMC Biol.* **9,** 1741–7007 (2011).

83. Gelpí, J., Hospital, A., Goñi, R. & Orozco, M. Molecular dynamics simulations: Advances and applications. *Adv. Appl. Bioinforma. Chem.* **10,** 37 (Nov. 2015).

84. Karplus, M. & McCammoon, J. A. Molecular dynamics simulations of biomolecules. *Nat. Struct. Biol.* **9,** 646–652 (Sept. 2002).

85. Xu, J., Kjelstrup, S. & Bedeaux, D. Molecular dynamics simulations of a chemical reaction; conditions for local equilibrium in a temperature gradient. *Phys. Chem. Chem. Phys.* **8,** 2017–2027 (17 2006).

86. Gissinger, J. R., Jensen, B. D. & Wise, K. E. Modeling chemical reactions in classical molecular dynamics simulations. *Polymer* **128,** 211–217. ISSN: 0032-3861 (2017).

87. Gao, Q., Han, Y., Liang, P. & Meng, J. Influence of an external electric field on the deprotonation reactions of an Fe3+-solvated molecule: a reactive molecular dynamics study. *Phys. Chem. Chem. Phys.* **22,** 6291–6299 (2020).

88. Sami, S. & Marrink, S. J. Reactive Martini: Chemical Reactions in Coarse-Grained Molecular Dynamics Simulations. *J. Chem. Theory Comput.* **19,** 4040–4046. eprint: `https://doi.org/10.1021/acs.jctc.2c01186` (2023).

89. Luedtke, W. D. & Landman, U. Structure, Dynamics, and Thermodynamics of Passivated Gold Nanocrystallites and Their Assemblies. *J. Phys. Chem.* **100,** 13323–13329. eprint: `https://doi.org/10.1021/jp961721g` (1996).

90. Luedtke, W. D. & Landman, U. Structure and Thermodynamics of Self-Assembled Monolayers on Gold Nanocrystallites. *J. Phys. Chem. B* **102,** 6566–6572 (Aug. 1998).
91. Ghorai, P. K. & Glotzer, S. C. Molecular Dynamics Simulation Study of Self-Assembled Monolayers of Alkanethiol Surfactants on Spherical Gold Nanoparticles. *J. Phys. Chem. C* **111,** 15857–15862. eprint: `https://doi.org/10.1021/jp0746289` (2007).
92. Ghorai, P. K. & Glotzer, S. C. Atomistic Simulation Study of Striped Phase Separation in Mixed-Ligand Self-Assembled Monolayer Coated Nanoparticles. *J. Phys. Chem. C* **114,** 19182–19187 (Oct. 2010).
93. Landman, U. & Luedtke, W. D. Small is different: energetic, structural, thermal, and mechanical properties of passivated nanocluster assemblies. *Faraday Discuss.* **125,** 1–22 (0 2004).
94. Salerno, K. M., Bolintineanu, D. S., Lane, J. M. D. & Grest, G. S. High Strength, Molecularly Thin Nanoparticle Membranes. *Phys. Rev. Lett.* **113,** 258301 (25 Dec. 2014).
95. Salerno, K. M., Bolintineanu, D. S., Lane, J. M. D. & Grest, G. S. Ligand structure and mechanical properties of single-nanoparticle-thick membranes. *Phys. Rev. E* **91,** 062403 (6 June 2015).
96. Salerno, K. M. & Grest, G. S. Temperature effects on nanostructure and mechanical properties of single-nanoparticle thick membranes. *Faraday Discuss.* **181,** 339–354 (0 2015).
97. Liu, X., Lu, P. & Zhai, H. Ligand coverage dependence of structural stability and interparticle spacing of gold supracrystals. *J. Appl. Phys.* **123,** 045101. ISSN: 0021-8979. eprint: `https://pubs.aip.org/aip/jap/article-pdf/doi/10.1063/1.5005094/15206410/045101\_1\_online.pdf` (Jan. 2018).
98. Srivastava, I. *et al.* Mechanics of Gold Nanoparticle Superlattices at High Hydrostatic Pressures. *J. Phys. Chem. C* **123** (June 2019).
99. Zhao, Y.-P., Wang, F.-C. & Chi, M. in *Handbook of Adhesion Technology* (eds da Silva, L. F. M., Öchsner, A. & Adams, R. D.) 1559–1595 (Springer International Publishing, Cham, 2018). ISBN: 978-3-319-55411-2.
100. Car, R. & Parrinello, M. Unified Approach for Molecular Dynamics and Density-Functional Theory. *Phys. Rev. Lett.* **55,** 2471–2474 (22 Nov. 1985).
101. Groenhof, G. Solving Chemical Problems with a Mixture of Quantum-Mechanical and Molecular Mechanics Calculations: Nobel Prize in Chemistry 2013. *Angew. Chem. Int. Ed.* **52,** 12489–12491. eprint: `https://onlinelibrary.wiley.com/doi/pdf/10.1002/anie.201309174` (2013).
102. Rappe, A. K., Casewit, C. J., Colwell, K. S., Goddard, W. A. I. & Skiff, W. M. UFF, a full periodic table force field for molecular mechanics and molecular dynamics simulations. *J. Am. Chem. Soc.* **114,** 10024–10035. eprint: `https://doi.org/10.1021/ja00051a040` (1992).
103. Allinger, N. L., Yuh, Y. H. & Lii, J. H. Molecular mechanics. The MM3 force field for hydrocarbons. 1. *J. Am. Chem. Soc.* **111,** 8551–8566. eprint: `https://doi.org/10.1021/ja00205a001` (1989).
104. McCammon, J. A., Gelin, B. R. & Karplus, M. Dynamics of folded proteins. *Nature* **267,** 585–590 (June 1977).
105. Weiner, S. J. *et al.* A new force field for molecular mechanical simulation of nucleic acids and proteins. *J. Am. Chem. Soc.* **106,** 765–784. eprint: `https://doi.org/10.1021/ja00315a051` (1984).
106. Jones, J. E. & Chapman, S. On the determination of molecular fields. —II. From the equation of state of a gas. *Proc. R. soc. Lond. Ser. A-Contain. Pap. Math. Phys. Character* **106,** 463–477. eprint: `https://royalsocietypublishing.org/doi/pdf/10.1098/rspa.1924.0082` (1924).

107. Morse, P. M. Diatomic Molecules According to the Wave Mechanics. II. Vibrational Levels. *Phys. Rev.* **34,** 57–64 (1 July 1929).

108. Gorbunov, S., Volkov, A. & Voronkov, R. Periodic boundary conditions effects on atomic dynamics analysis. *Comput. Phys. Commun.* **279,** 108454. ISSN: 0010-4655 (2022).

109. Bae, G.-T. & Aikens, C. M. Improved ReaxFF Force Field Parameters for Au–S–C–H Systems. *J. Phys. Chem. A* **117,** 10438–10446 (Sept. 2013).

110. Cuevas, J. C. & Scheer, E. *Molecular Electronics* 2nd. eprint: `https://www.worldscientific.com/doi/pdf/10.1142/10598` (WORLD SCIENTIFIC, 2017).

111. Nitzan, A. *Chemical dynamics in condensed phases: relaxation, transfer and reactions in condensed molecular systems* OCLC: ocm62118341. ISBN: 9780198529798 (Oxford University Press, Oxford ; New York, 2006).

112. Parthasarathy, R., Lin, X.-M., Elteto, K., Rosenbaum, T. F. & Jaeger, H. M. Percolating through Networks of Random Thresholds: Finite Temperature Electron Tunneling in Metal Nanocrystal Arrays. *Phys. Rev. Lett.* **92,** 076801 (7 Feb. 2004).

113. Landauer, R. Spatial Variation of Currents and Fields Due to Localized Scatterers in Metallic Conduction. *IBM Journal of Research and Development* **1,** 223–231 (1957).

114. Heikkilä, T. T. *The Physics of Nanoelectronics: Transport and Fluctuation Phenomena at Low Temperatures* ISBN: 9780199592449 (Oxford University Press, Jan. 2013).

115. Ryndyk, D. *Theory of Quantum Transport at Nanoscale: An Introduction* en. ISBN: 9783319240862 9783319240886 (Springer International Publishing, Cham, 2016).

116. Paulsson, M. *Non Equilibrium Green's Functions for Dummies: Introduction to the One Particle NEGF equations* 2002.

117. Schaefer, K. *et al.* Cross-Linked Gold Nanoparticle Assemblies: What Can We Learn from Single Flat Interfaces? *J. Phys. Chem. C* **128,** 3994–4008. eprint: `https://doi.org/10.1021/acs.jpcc.3c07646` (2024).

118. Djebaili, T., Richardi, J., Abel, S. & Marchi, M. Atomistic Simulations of the Surface Coverage of Large Gold Nanocrystals. *J. Phys. Chem. C* **117,** 17791–17800. eprint: `https://doi.org/10.1021/jp403442s` (2013).

119. Sellers, H. On the chemisorption and dissociation of HSCH3 on the Au(111) surface. *Surf. Sci.* **294,** 99–107 (Sept. 1993).

120. Hasan, M., Bethell, D. & Brust, M. The Fate of Sulfur-Bound Hydrogen on Formation of Self-Assembled Thiol Monolayers on Gold: 1H NMR Spectroscopic Evidence from Solutions of Gold Clusters. *J. Am. Chem. Soc.* **124,** 1132–1133 (Jan. 2002).

121. Matthiesen, J. E., Jose, D., Sorensen, C. M. & Klabunde, K. J. Loss of Hydrogen upon Exposure of Thiol to Gold Clusters at Low Temperature. *J. Am. Chem. Soc.* **134,** 9376–9379 (May 2012).

122. Widrig, C. A., Chung, C. & Porter, M. D. The electrochemical desorption of n-alkanethiol monolayers from polycrystalline Au and Ag electrodes. *J. Electroanal. Chem. and Interfacial Electrochem.* **310,** 335–359 (July 1991).

123. Love, J. C., Estroff, L. A., Kriebel, J. K., Nuzzo, R. G. & Whitesides, G. M. Self-Assembled Monolayers of Thiolates on Metals as a Form of Nanotechnology. *Chem. Rev.* **105,** 1103–1170 (Mar. 2005).

124. Inkpen, M. S. *et al.* Non-chemisorbed gold–sulfur binding prevails in self-assembled monolayers. *Nat. Chem.* **11,** 351–358 (Mar. 2019).

125. Pacchioni, G. A not-so-strong bond. *Nat. Rev. Mater.* **4,** 226–226 (Mar. 2019).

126. Camillone N., I. *et al.* New monolayer phases of n-alkane thiols self-assembled on Au(111): Preparation, surface characterization, and imaging. *J. Chem. Phys.* **101,** 11031–11036. ISSN: 0021-9606. eprint: `https://pubs.aip.org/aip/jcp/article-pdf/101/12/11031/19323412/11031\_1\_online.pdf` (Dec. 1994).

127. Schreiber, F. Structure and growth of self-assembling monolayers. *Prog. Surf. Sci.* **65,** 151–257. ISSN: 0079-6816 (2000).

128. Poirier, G. E. Coverage-Dependent Phases and Phase Stability of Decanethiol on Au(111). *Langmuir* **15,** 1167–1175 (1999).

129. Nuzzo, R. G., Dubois, L. H. & Allara, D. L. Fundamental studies of microscopic wetting on organic surfaces. 1. Formation and structural characterization of a self-consistent series of polyfunctional organic monolayers. *J. Am. Chem. Soc.* **112,** 558–569. eprint: `https://doi.org/10.1021/ja00158a012` (1990).

130. Tour, J. M. *et al.* Self-Assembled Monolayers and Multilayers of Conjugated Thiols, a,w-Dithiols, and Thioacetyl-Containing Adsorbates. Understanding Attachments Between Potential Molecular Wires and Gold Surfaces. *J. Am. Chem. Soc.* **117.** 463, 9529–9534 (1995).

131. Brust, M., Blass, P. M. & Bard, A. J. Self-Assembly of Photoluminescent Copper(I)—Dithiol Multilayer Thin Films and Bulk Materials. *Langmuir* **13,** 5602–5607. eprint: `https://doi.org/10.1021/la970493u` (1997).

132. Rieley, H., Kendall, G. K., Zemicael, F. W., Smith, T. L. & Yang, S. X-ray Studies of Self-Assembled Monolayers on Coinage Metals. 1. Alignment and Photooxidation in 1,8-Octanedithiol and 1-Octanethiol on Au. *Langmuir* **14,** 5147–5153 (1998).

133. Joo, S. W., Han, S. W. & Kim, K. Adsorption of 1,4-Benzenedithiol on Gold and Silver Surfaces: Surface-Enhanced Raman Scattering Study. *J. Colloid Interface Sci.* **240,** 391–399. ISSN: 0021-9797 (2001).

134. Leung, T. Y. B. *et al.* 1,6-Hexanedithiol Monolayers on Au(111): A Multitechnique Structural Study. *Langmuir* **16,** 549–561. eprint: `https://doi.org/10.1021/la9906222` (2000).

135. Yu, J.-J., Ngunjiri, J. N., Kelley, A. T. & Garno, J. C. Nanografting versus Solution Self-Assembly of , -Alkanedithiols on Au(111) Investigated by AFM. *Langmuir* **24,** 11661–11668. eprint: `https://doi.org/10.1021/la802235c` (2008).

136. Jiang, W. *et al.* Structure and Bonding Issues at the Interface between Gold and Self-Assembled Conjugated Dithiol Monolayers. *Langmuir* **21,** 8751–8757. eprint: `https://doi.org/10.1021/la0474316` (2005).

137. Ulman, A., Ioffe, M., Patolsky, F., Haas, E. & Reuvenov, D. Highly active engineered-enzyme oriented monolayers: formation, characterization and sensing applications. en. *J. Nanobiotechnol.* **9,** 26 (2011).

138. Li, C. *et al.* Charge Transport in Single Au | Alkanedithiol | Au Junctions: Coordination Geometries and Conformational Degrees of Freedom. *J. Am. Chem. Soc.* **130,** 318–326. eprint: `https://doi.org/10.1021/ja0762386` (2008).

139. Zhang, L., Goddard, W. A. & Jiang, S. Molecular simulation study of the c(4×2) superlattice structure of alkanethiol self-assembled monolayers on Au(111). *J. Chem. Phys.* **117,** 7342–7349. eprint: `https://doi.org/10.1063/1.1507777` (2002).

140. Porter, M. D., Bright, T. B., Allara, D. L. & Chidsey, C. E. D. Spontaneously organized molecular assemblies. 4. Structural characterization of n-alkyl thiol monolayers on gold by optical ellipsometry, infrared spectroscopy, and electrochemistry. *J. Am. Chem. Soc.* **109,** 3559–3568. eprint: `https://doi.org/10.1021/ja00246a011` (1987).

141. Fertitta, E., Voloshina, E. & Paulus, B. Adsorption of multivalent alkylthiols on Au(111) surface: Insights from DFT. *J. Comput. Chem.* **35,** 204–213 (Nov. 2013).

142. Yourdshahyan, Y., Zhang, H. K. & Rappe, A. M. *n*-alkyl thiol head-group interactions with the Au(111) surface. *Phys. Rev. B* **63,** 081405 (Feb. 2001).

143. Cui, X. D. *et al.* Changes in the Electronic Properties of a Molecule When It Is Wired into a Circuit. *J. Phys. Chem. B* **106,** 8609–8614. eprint: `https://doi.org/10.1021/jp0206065` (2002).

144. Leibowitz, F. L., Zheng, W., Maye, M. M. & Zhong, C.-J. Structures and Properties of Nanoparticle Thin Films Formed via a One-Step Exchange—Cross-Linking—Precipitation Route. *Anal. Chem.* **71,** 5076–5083. eprint: `https://doi.org/10.1021/ac990752f` (1999).

145. Liu, X. P., Ni, Y. & He, L. H. Molecular dynamics simulation of interparticle spacing and many-body effect in gold supracrystals. *Nanotechnology* **27,** 135707 (Feb. 2016).

146. Olichwer, N. *et al.* Gold nanoparticle superlattices: structure and cavities studied by GISAXS and PALS. *RSC Adv.* **6,** 113163–113172 (114 2016).

147. Liepold, E. R., Smith, A., Lin, B., de Pablo, J. & Rice, S. A. Pair and many-body interactions between ligated Au nanoparticles. *J. Chem. Phys.* **150,** 044904. ISSN: 0021-9606. eprint: `https://pubs.aip.org/aip/jcp/article-pdf/doi/10.1063/1.5064545/16772804/044904\_1\_online.pdf` (Jan. 2019).

148. Reik, M. *et al.* The influence of fractional surface coverage on the core–core separation in ordered monolayers of thiol-ligated Au nanoparticles. *Soft Matter* **15,** 8800–8807 (43 2019).

149. Zamborini, F. P., Smart, L. E., Leopold, M. C. & Murray, R. W. Distance-dependent electron hopping conductivity and nanoscale lithography of chemically-linked gold monolayer protected cluster films. *Anal. Chim. Acta* **496,** 3–16. ISSN: 0003-2670 (2003).

150. Deffner, M. *et al.* Learning Conductance: Gaussian Process Regression for Molecular Electronics. *J. Chem. Theory Comput.* **19,** 992–1002. eprint: `https://doi.org/10.1021/acs.jctc.2c00648` (2023).

151. Berritta, M., Manrique, D. Z. & Lambert, C. J. Interplay between quantum interference and conformational fluctuations in single-molecule break junctions. *Nanoscale* **7,** 1096–1101 (3 2015).

152. Sauceda, H. E. *et al.* BIGDML—Towards accurate quantum machine learning force fields for materials. *Nat. Commun.* **13,** 3733 (2022).

153. Kocer, E., Ko, T. W. & Behler, J. Neural Network Potentials: A Concise Overview of Methods. *Annu. Rev. Phys. Chem.* **73,** 163–186 (2022).

154. Unke, O. T. *et al.* Machine Learning Force Fields. *Chem. Rev.* **121,** 10142–10186 (2021).

155. Ong, Q., Luo, Z. & Stellacci, F. Characterization of Ligand Shell for Mixed-Ligand Coated Gold Nanoparticles. *Acc. Chem. Res.* **50,** 1911–1919 (Aug. 2017).

156. Bain, C. D. & Whitesides, G. M. Formation of monolayers by the coadsorption of thiols on gold: variation in the length of the alkyl chain. *J. Am. Chem. Soc.* **111,** 7164–7175 (Aug. 1989).

157. Bain, C. D., Evall, J. & Whitesides, G. M. Formation of monolayers by the coadsorption of thiols on gold: variation in the head group, tail group, and solvent. *J. Am. Chem. Soc.* **111,** 7155–7164 (Aug. 1989).

158. Laibinis, P. E., Nuzzo, R. G. & Whitesides, G. M. Structure of monolayers formed by coadsorption of two n-alkanethiols of different chain lengths on gold and its relation to wetting. *J. Phys. Chem.* **96,** 5097–5105 (June 1992).

159. Jackson, A. M., Myerson, J. W. & Stellacci, F. Spontaneous assembly of subnanometre-ordered domains in the ligand shell of monolayer-protected nanoparticles. *Nat. Mat.* **3,** 330–336 (Apr. 2004).

160. Jackson, A. M., Hu, Y., Silva, P. J. & Stellacci, F. From Homoligand- to Mixed-Ligand- Monolayer-Protected Metal Nanoparticles: A Scanning Tunneling Microscopy Investigation. *J. Am. Chem. Soc.* **128,** 11135–11149 (Aug. 2006).

161. Centrone, A. *et al.* The role of nanostructure in the wetting behavior of mixed-monolayer-protected metal nanoparticles. *Proc. Natl. Acad. Sci.* **105,** 9886–9891 (July 2008).

162. Ghosh, A., Basak, S., Wunsch, B. H., Kumar, R. & Stellacci, F. Effect of Composition on the Catalytic Properties of Mixed-Ligand-Coated Gold Nanoparticles. *Angew. Chem. Int. Ed.* **50,** 7900–7905 (July 2011).
163. Huang, R., Carney, R. P., Stellacci, F. & Lau, B. L. T. Colloidal Stability of Self-Assembled Monolayer-Coated Gold Nanoparticles: The Effects of Surface Compositional and Structural Heterogeneity. *Langmuir* **29,** 11560–11566 (Aug. 2013).
164. Ong, Q. K., Zhao, S., Reguera, J., Biscarini, F. & Stellacci, F. Comparative STM studies of mixed ligand monolayers on gold nanoparticles in air and in 1-phenyloctane. *Chem. Commun.* **50,** 10456–10459 (2014).
165. Ong, Q., Nianias, N. & Stellacci, F. A review of molecular phase separation in binary self-assembled monolayers of thiols on gold surfaces. *Europhys. Lett.* **119,** 66001 (Sept. 2017).
166. Cesbron, Y., Shaw, C. P., Birchall, J. P., Free, P. & Lévy, R. Stripy Nanoparticles Revisited. *Small* **8,** 3714–3719 (Nov. 2012).
167. Aoki, K. Theory of phase separation of binary self-assembled films. *J. Electroanal. Chem.* **513,** 1–7 (Oct. 2001).
168. Munakata, H., Kuwabata, S., Ohko, Y. & Yoneyama, H. Spatial distribution of domains in binary self-assembled monolayers of thiols having different lengths. *J. Electroanal. Chem.* **496,** 29–36 (Jan. 2001).
169. Stranick, S. J., Parikh, A. N., Tao, Y.-T., Allara, D. L. & Weiss, P. S. Phase Separation of Mixed-Composition Self-Assembled Monolayers into Nanometer Scale Molecular Domains. *J. Phys. Chem.* **98,** 7636–7646 (Aug. 1994).
170. Stranick, S. J. *et al.* Nanometer-scale phase separation in mixed composition self-assembled monolayers. *Nanotechnol.* **7,** 438–442 (Dec. 1996).
171. Merz, S. N., Hoover, E., Egorov, S. A., DuBay, K. H. & Green, D. L. Predicting the effect of chain-length mismatch on phase separation in noble metal nanoparticle monolayers with chemically mismatched ligands. *Soft Matter* **15,** 4498–4507 (22 2019).
172. Fetisov, E. O. & Siepmann, J. I. Structure and Phase Behavior of Mixed Self-Assembled Alkanethiolate Monolayers on Gold Nanoparticles: A Monte Carlo Study. *J. Phys. Chem. B* **120,** 1972–1978 (Jan. 2016).
173. Shevade, A. V., Zhou, J., Zin, M. T. & Jiang, S. Phase Behavior of Mixed Self-Assembled Monolayers of Alkanethiols on Au(111): A Configurational-Bias Monte Carlo Simulation Study. *Langmuir* **17,** 7566–7572 (Oct. 2001).
174. Bumm, L. A. *et al.* Directed Self-Assembly to Create Molecular Terraces with Molecularly Sharp Boundaries in Organic Monolayers. *J. Am. Chem. Soc.* **121,** 8017–8021 (Aug. 1999).
175. Kim, Y.-K. *et al.* Adsorption behavior of binary mixed alkanethiol molecules on Au: Scanning tunneling microscope and linear-scan voltammetry investigation. *Appl. Surf. Sci.* **252,** 4951–4956 (May 2006).
176. Liu, C.-Y. *From Fabrication to Application: Developing High-Performance Gold Nanoparticle-Based Sensors Using Mixed Ligand/Linker Systems* PhD thesis (University of Hamburg, 2024).
177. Chu, Z., Han, Y., Král, P. & Klajn, R. “Precipitation on Nanoparticles”: Attractive Intermolecular Interactions Stabilize Specific Ligand Ratios on the Surfaces of Nanoparticles. *Angew. Chem. Int. Ed.* **57,** 7023–7027. eprint: `https://onlinelibrary.wiley.com/doi/pdf/10.1002/anie.201800673` (2018).
178. Joseph, Y. *et al.* Vapor Sensitivity of Networked Gold Nanoparticle Chemiresistors: Importance of Flexibility and Resistivity of the Interlinkage. *J. Phys. Chem. C* **111,** 12855–12859. eprint: `https://doi.org/10.1021/jp072053+` (2007).

179. Cho, E. S. *et al.* Ultrasensitive detection of toxic cations through changes in the tunnelling current across films of striped nanoparticles. *Nat. Mat.* **11,** 978–985 (Sept. 2012).

180. McGinn, C. K., Lamport, Z. A. & Kymissis, I. Review of Gravimetric Sensing of Volatile Organic Compounds. *ACS Sens.* **5,** 1514–1534. eprint: `https://doi.org/10.1021/acssensors.0c00333` (2020).

181. Zalake, P., Ghosh, S., Narasimhan, S. & Thomas, K. G. Descriptor-Based Rational Design of Two-Dimensional Self-Assembled Nanoarchitectures Stabilized by Hydrogen Bonds. *Chem. Mater.* **29,** 7170–7182. eprint: `https://doi.org/10.1021/acs.chemmater.7b01183` (2017).

182. Halder, S., Mondal, J., Ortega-Castro, J., Frontera, A. & Roy, P. A Ni-based MOF for selective detection and removal of Hg2+ in aqueous medium: a facile strategy. *Dalton Trans.* **46,** 1943–1950 (6 2017).

183. Ibañez, F. J., Gowrishetty, U., Crain, M. M., Walsh, K. M. & Zamborini, F. P. Chemiresistive Vapor Sensing with Microscale Films of Gold Monolayer Protected Clusters. *Anal. Chem.* **78,** 753–761. eprint: `https://doi.org/10.1021/ac051347t` (2006).

184. Wan, Y., Goubet, N., Albouy, P.-A., Schaeffer, N. & Pileni, M.-P. Hierarchy in Au Nanocrystal Ordering in a Supracrystal: II. Control of Interparticle Distances. *Langmuir* **29,** 13576–13581. eprint: `https://doi.org/10.1021/la403583q` (2013).

185. Schlicke, H., Bittinger, S. C. & Vossmeyer, T. Lithographic Patterning and Selective Functionalization of Metal Nanoparticle Composite Films. *ACS Appl. Electron. Mater.* **2,** 3741–3748. eprint: `https://doi.org/10.1021/acsaelm.0c00770` (2020).

186. Mitra, G. *et al.* Conventional versus singlet-triplet Kondo effect in Blatter radical molecular junctions: Zero-bias anomalies and magnetoresistance. *Chem,* 102500. ISSN: 2451-9294 (2025).

187. Srisombat, L., Jamison, A. C. & Lee, T. R. Stability: A key issue for self-assembled monolayers on gold as thin-film coatings and nanoparticle protectants. *Colloids Surf. A* **390,** 1–19. ISSN: 0927-7757 (2011).

188. Joseph, Y., Guse, B. & Nelles, G. Aging of 1, -Alkyldithiol Interlinked Au Nanoparticle Networks. *Chem. Mat.* **21,** 1670–1676. eprint: `https://doi.org/10.1021/cm803407n` (2009).

189. Ratera, I. & Veciana, J. Playing with organic radicals as building blocks for functional molecular materials. *Chem. Soc. Rev.* **41,** 303–349 (1 2012).

190. Rodriguez-Méndez, M. L., Gay, M. & de Saja, J. A. New insights into sensors based on radical bisphthalocyanines. *J. Porphyr. Phthalocya.* **13,** 1159–1167. eprint: `https://doi.org/10.1142/S1088424609001509` (2009).

191. Nguyen, D. C. T. *et al.* Conjugated Radical Polymer-Based Organic Electrochemical Transistors for Biosensing Devices. *Chem. Mat.* **36,** 7897–7908. eprint: `https://doi.org/10.1021/acs.chemmater.4c01321` (2024).

192. Zheng, Y., Miao, M.-s., Kemei, M. C., Seshadri, R. & Wudl, F. The Pyreno-Triazinyl Radical – Magnetic and Sensor Properties. *Isr. J. Chem.* **54,** 774–778. eprint: `https://onlinelibrary.wiley.com/doi/pdf/10.1002/ijch.201400034` (2014).

193. Dieny, B. *et al.* Opportunities and challenges for spintronics in the microelectronics industry. *Nat. Electron.* **3,** 446–459 (Aug. 2020).

194. Low, J. Z. *et al.* The Environment-Dependent Behavior of the Blatter Radical at the Metal–Molecule Interface. *Nano Lett.* **19,** 2543–2548. eprint: `https://doi.org/10.1021/acs.nanolett.9b00275` (2019).

195. Hurtado-Gallego, J. *et al.* Thermoelectric Enhancement in Single Organic Radical Molecules. *Nano Lett.* **22,** 948–953. eprint: `https://doi.org/10.1021/acs.nanolett.1c03698` (2022).

196. Jiang, Y. *et al.* Does a Blatter Radical Retain Its Open-Shell Character When Incorporated into Gold–Molecule–Gold Junctions? *J. Phys. Chem. C* **127,** 9268–9277. eprint: `https://doi.org/10.1021/acs.jpcc.3c00224` (2023).

197. Mitra, G. *et al.* Interplay between Magnetoresistance and Kondo Resonance in Radical Single-Molecule Junctions. *Nano Lett.* **22,** 5773–5779. eprint: `https://doi.org/10.1021/acs.nanolett.2c01199` (2022).

198. Deumal, M., Vela, S., Fumanal, M., Ribas-Arino, J. & Novoa, J. J. Insights into the magnetism and phase transitions of organic radical-based materials. *J. Mater. Chem. C* **9,** 10624–10646 (33 2021).

199. Kertesz, M. Pancake Bonding: An Unusual Pi-Stacking Interaction. *Chem. Eur. J.* **25,** 400–416. eprint: `https://chemistry-europe.onlinelibrary.wiley.com/doi/pdf/10.1002/chem.201802385` (2019).

200. Lindsay, S. M. & Ratner, M. A. Molecular Transport Junctions: Clearing Mists. *Adv. Mater.* **19,** 23–31. eprint: `https://onlinelibrary.wiley.com/doi/pdf/10.1002/adma.200601140` (2007).

201. Leven, I. *et al.* Recent Advances for Improving the Accuracy, Transferability, and Efficiency of Reactive Force Fields. *J. Chem. Theory Comput.* **17,** 3237–3251 (2021).

202. Lopez-Bezanilla, A. & von Lilienfeld, O. A. Modeling electronic quantum transport with machine learning. *Phys. Rev. B* **89,** 235411 (23 June 2014).

203. Bürkle, M. *et al.* Deep-Learning Approach to First-Principles Transport Simulations. *Phys. Rev. Lett.* **126,** 177701 (17 Apr. 2021).

204. Topolnicki, R., Kucharczyk, R. & Kamiński, W. Combining Multiscale MD Simulations and Machine Learning Methods to Study Electronic Transport in Molecular Junctions at Finite Temperatures. *J. Phys. Chem. C* **125,** 19961–19968. eprint: `https://doi.org/10.1021/acs.jpcc.1c03210` (2021).

205. Thompson, A. P. *et al.* LAMMPS - a flexible simulation tool for particle-based materials modeling at the atomic, meso, and continuum scales. *Comp. Phys. Comm.* **271,** 108171 (2022).

206. Hourahine, B. *et al.* DFTB+, a software package for efficient approximate density functional theory based atomistic simulations. *J. Chem. Phys.* **152.** 124101. ISSN: 0021-9606. eprint: `https://pubs.aip.org/aip/jcp/article-pdf/doi/10.1063/1.5143190/16711771/124101\_1\_online.pdf` (Mar. 2020).

207. Alloway, D. M. *et al.* Tuning the Effective Work Function of Gold and Silver Using ω-Functionalized Alkanethiols: Varying Surface Composition through Dilution and Choice of Terminal Groups. *J. Phys. Chem. C* **113,** 20328–20334 (2009).

208. Osella, S., Cornil, D. & Cornil, J. Work function modification of the (111) gold surface covered by long alkanethiol-based self-assembled monolayers. *Phys. Chem. Chem. Phys.* **16,** 2866 (2014).

209. Balasubramani, S. G. *et al.* TURBOMOLE: Modular program suite for ab initio quantum-chemical and condensed-matter simulations. *J. Chem. Phys.* **152,** 184107 (2020).

210. Vosko, S. H., Wilk, L. & Nusair, M. Accurate spin-dependent electron liquid correlation energies for local spin density calculations: a critical analysis. *Can. J. Phys.* **58,** 1200–1211 (1980).

211. Stephens, P. J., Devlin, F. J., Chabalowski, C. F. & Frisch, M. J. Ab initio calculation of vibrational absorption and circular dichroism spectra using density functional force fields. *J. Phys. Chem.* **98,** 11623–11627 (1994).

212. Weigend, F. & Ahlrichs, R. Balanced basis sets of split valence, triple zeta valence and quadruple zeta valence quality for H to Rn: Design and assessment of accuracy. *Phys. Chem. Chem. Phys.* **7,** 3297–3305 (2005).

213. Grimme, S., Antony, J., Ehrlich, S. & Krieg, H. A consistent and accurate ab initio parametrization of density functional dispersion correction (DFT-D) for the 94 elements H-Pu. *J. Chem. Phys.* **132,** 154104 (2010).

214. Grimme, S., Ehrlich, S. & Goerigk, L. Effect of the damping function in dispersion corrected density functional theory. *J. Comput. Chem.* **32,** 1456–1465 (2011).

215. Noodleman, L. Valence bond description of antiferromagnetic coupling in transition metal dimers. *J. Chem. Phys.* **74,** 5737–5743 (1981).

216. Kitagawa, Y., Saito, T. & Yamaguchi, K. in *Symmetry (Group Theory) and Mathematical Treatment in Chemistry* (ed Akitsu, T.) chap. 7 (IntechOpen, Rijeka, 2018).

217. Yamanaka, S. *et al.* Quantum spin correction scheme for ab initio spin-unrestricted solutions: Multiple bonds case. *Int. J. Quantum Chem.* **2005,** 605–614.

218. Caroli, C., Combescot, R., Nozieres, P. & Saint-James, D. Direct calculation of the tunneling current. *Phys. C: Solid State Phys.* **4,** 916 (June 1971).

219. Herrmann, C., Solomon, G. C., Subotnik, J. E., Mujica, V. & Ratner, M. A. Ghost transmission: How large basis sets can make electron transport calculations worse. *J. Chem. Phys.* **132,** 024103. ISSN: 0021-9606. eprint: `https://pubs.aip.org/aip/jcp/article-pdf/doi/10.1063/1.3283062/14746897/024103\_1\_online.pdf` (Jan. 2010).

220. Herrmann, C., Solomon, G. C. & Ratner, M. A. Organic Radicals As Spin Filters. *Journal of the American Chemical Society* **132,** 3682–3684. eprint: `https://doi.org/10.1021/ja910483b` (2010).

221. Herrmann, C., Solomon, G. C. & Ratner, M. A. Designing organic spin filters in the coherent tunneling regime. *J. Chem. Phys.* **134,** 224306. ISSN: 0021-9606. eprint: `https://pubs.aip.org/aip/jcp/article-pdf/doi/10.1063/1.3598519/15436765/224306\_1\_online.pdf` (June 2011).

222. Deffner, M. *et al.* ARTAIOS — a postprocessing framework for electronic structure calculations, https://www.chemie.uni-hamburg.de/institute/ac/arbeitsgruppen/herrmann/software/artaios.html. 2008–2024.

223. Berger, L. I. in *CRC Handbook of Chemistry and Physics* (ed Haynes, W. M.) 97th edition (CRC Press, 2017).

Appendix

A Supplementary Data

This section contains supplementary information and data that are not included in the main sections of the thesis.

A.1 Intersurface Distance Dependence on the Coverage for Different Alkanemonothiols

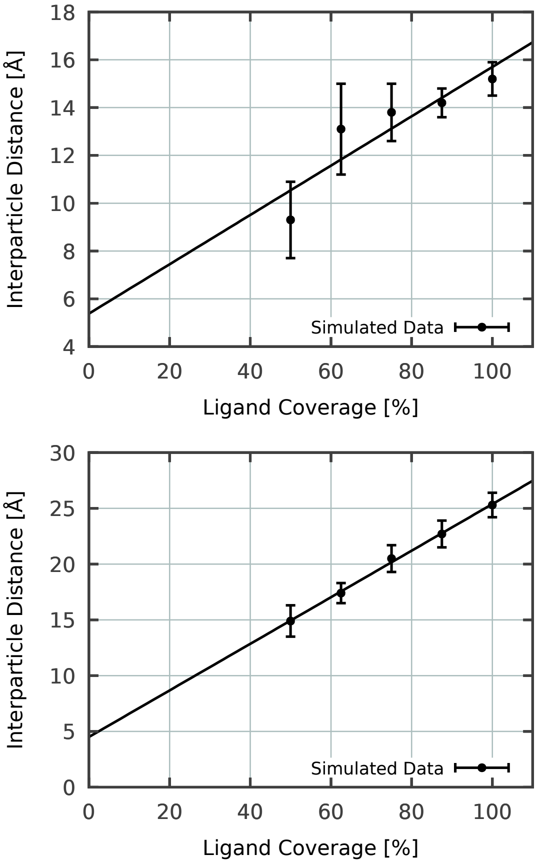

Figure A.1: Averaged intersurface distances, extracted from the lowest-energy structures of 10 individual MD simulations, of 6T- (top) and 11T-capped (bottom) interfaces with different AMT coverages. From the linear fit, a slope of 0.10 ± 0.03 Å can be obtained with $r^2 = 0.8098$ for 6T-capped interfaces and 0.21 ± 0.01 Å with $r^2 = 0.9978$ for 11T-capped interfaces.

A.2 Additional Information for Charge Transport Calculations

In this section, additional information and data regarding the charge transport calculations performed with the single interface structures are provided. This section of the thesis was already published in the Supporting Information in Ref.[117]. All simulations, calculations, data analysis and writing have been performed by the main author of this thesis.

A.2.1 Describing the Fermi Energy Correctly with Periodic Boundary Conditions

DFTB, in combination with a nonequilibrium Green's function formalism as implemented in DFTB+, has previously been used to analyze charge transport in single-molecule break junction events, among other applications.[150] In contrast to these calculations, our system requires the use of periodic boundary conditions (PBCs). To evaluate whether DFTB+ can accurately capture the electronic features of periodic systems, we conducted charge transport calculations under PBCs and compared the results to those obtained from single clusters (non-periodic). For this analysis, a representative structure from individual MD simulations was selected and modified to allow the transformation into cluster-like structures. Specifically, all ligands except for the one at the center of the unit cell were manually removed (see Figure A.2).

Charge transport calculations were conducted in the contact regions (source and drain). With self-consistent charge (SCC) conditions, Fermi energies of approximately −4 eV were obtained for the cluster depicted in Figure A.2, whereas under PBCs, the Fermi energies were around −2.6 eV. For comparison, experimental values for bulk gold are expected to be approximately −5.5 eV.[223] These discrepancies in Fermi energy resulted in a corresponding shift in the transmission function (see Figure A.3).

One approach to adjust the Fermi energy to a more realistic value is to apply a potential to the contacts, as shown in Figure A.3 for a potential of −2.5 eV. Alternatively, as a less arbitrary method shell-resolved SCC can be activated, which yielded Fermi energies of −5.3 eV and −4.7 eV for cluster and periodic conditions, respectively. Enabling shell-resolved SCC allows for the application of distinct Hubbard U values for different atomic angular momentum shells, rather than uniformly applying the value from the s-shell across all angular momenta.

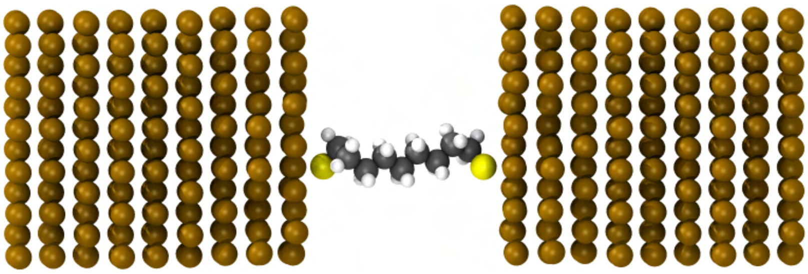

Figure A.2: Simplified 9DT interface structure with only one 9DT ligand used as a model system for comparing charge transport calculations with different parameters. Reprinted with permission from K. Schaefer et al. *J. Phys. Chem. C* 2024, 128, 9, 3994-4008 under an Open Access license.

While the work function of bulk gold is experimentally known to be around −5.5 eV, the Fermi energy relevant for electron transport is much harder to predict, as molecular adsorbates can strongly influence the Fermi level of the electrodes. There is both theoretical and experimental evidence that the work function of gold is shifted to more positive values by hydrocarbon thiolate self-assembled monolayers [207, 208], with a range of −5 to −4 eV covering the most typical values. Accordingly, while the value of −4.6848 eV we have settled on here appears reasonable, it should be kept in mind that it may be affected not only by the approximations in the electronic structure description, but also by the (reduced) atomistic model employed.

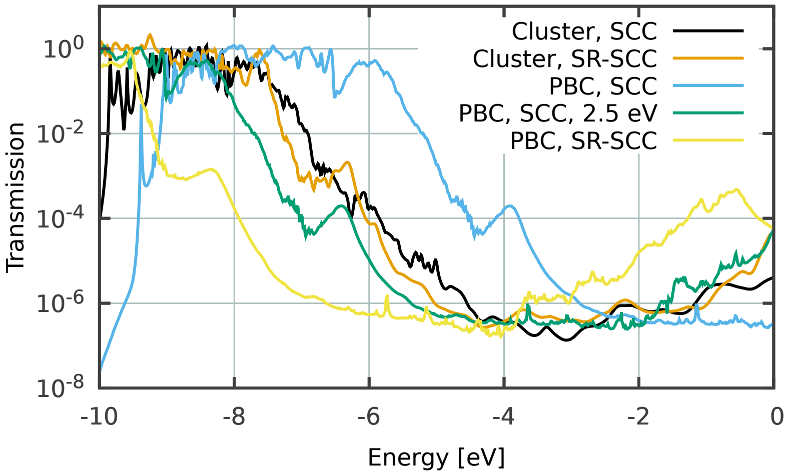

Figure A.3: Transmission functions calculated with different parameters: cluster with standard SCC and wide-band approximation (black), cluster with orbital-resolved SCC and wide-band approximation (orange), periodic boundary conditions with standard SCC (blue), with standard SCC and an additional potential for shifting the Fermi energy by −2.5 eV (green), and periodic boundary conditions with orbital-resolved SCC (yellow). Reprinted with permission from K. Schaefer et al. *J. Phys. Chem. C* 2024, 128, 9, 3994-4008 under an Open Access license.

A.2.2 K-point Grid Selection

Prior to conducting shell-resolved SCC calculations for the various ligand systems, K-point sampling was carried out on a representative 9DT lowest-energy structure using Monkhorst-Pack sets of the form $i \times i \times 10$ for the contacts, where i was incrementally increased. Convergence of the calculated Fermi energies was observed at $i = 6$ (see Figure A.4, left). Similarly, optimal K-point grids for the device region were identified, with a Monkhorst-Pack set of $4 \times 4 \times 1$ proving to be the most effective in balancing accuracy and computational efficiency (see Figure A.4, right). In the transport region, only one K-point was selected in the z-direction (transport direction), as the system is non-periodic in that direction.

A.2.3 Artifacts in Charge Transport Calculations of Structures with Free Thiolate Groups

We performed charge transport calculations on three different 9DT sandwich structures to study the influence of free thiolate groups on the Fermi-energy transmission. In the first structure (a), no free thiolate groups were present (all 8 dithiolate ligands were cross-linkers, Au—S—R—S—Au). In the second structure (b), two of eighth ligands were bound one-sided so two free thiolate groups were present in the structure (Au—S—R—S). To the 2 free thiolate groups, hydrogen atoms were added (Au—S—R—SH) to form the third structure (c). For all three structures, transmissions were calculated using SCC. The Fermi-energy transmissions of the three structure are summarized in Table A.1. The Fermi-energy transmission of the structure with free thiolate groups (c) deviates from the transmissions of the other two

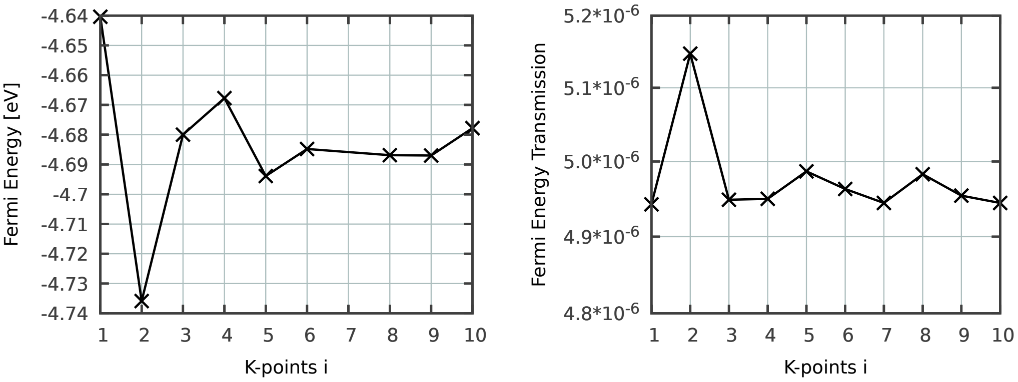

Figure A.4: K-point sampling performed on a 9DT test structure, shown in Figure A.2, with Monkhorst-Pack sets of the form $i \times i \times 10$ for the contact region (left) and $i \times i \times 1$ for the transport region (right). Convergence can be observed at $i = 6$ for the contacts and at $i = 4$ for the transport region. Reprinted with permission from K. Schaefer et al. *J. Phys. Chem. C* 2024, 128, 9, 3994-4008 under an Open Access license.

structures by 3 orders of magnitude, indicating that free thiolate groups may cause artifacts in the charge transport calculations.

We conducted charge transport calculations on three distinct 9DT interface structures to examine the impact of free thiolate groups on Fermi-energy transmission. In the first structure (a), no free thiolate groups were present, as all eight dithiolate ligands functioned as cross-linkers (Au—S—R—S—Au). The second structure (b) incorporated two out of the eight ligands bound on one side, resulting in the presence of two free thiolate groups (Au—S—R—S). For the third structure (c), hydrogen atoms were added to the two free thiolate groups (Au—S—R—SH). Charge transport calculations using SCC were performed for all three structures. A summary of the Fermi-energy transmissions for each structure is provided in Table A.1. Notably, the Fermi-energy transmission of the structure with free thiolate groups (c) differed by three orders of magnitude from the transmissions of the other two structures, suggesting that free thiolate groups may introduce artifacts in the charge transport calculations.

Table A.1: Transmission at the Fermi energy of a 9DT interface structure with no free thiolate groups (a), with two free thiolate groups (b), with two free thiol groups (c). The transmission of the structure with free thiolate groups deviates from that of the other two structures by three orders of magnitudes, indicating that free thiolate groups may cause artifacts in the charge transport calculations.

Structure	Transmission at the Fermi energy (at -2.60 eV)
a	3.35E-6
b	4.08E-3
c	3.27E-6

A.3 Transmission Functions of Alkanemonothiolate and Alkanedithiolate Interface Structures with Different Alkane Chain Lengths

A.3.1 Transmission Functions of Alkanedithiolate-Cross-Linked Interface Structures

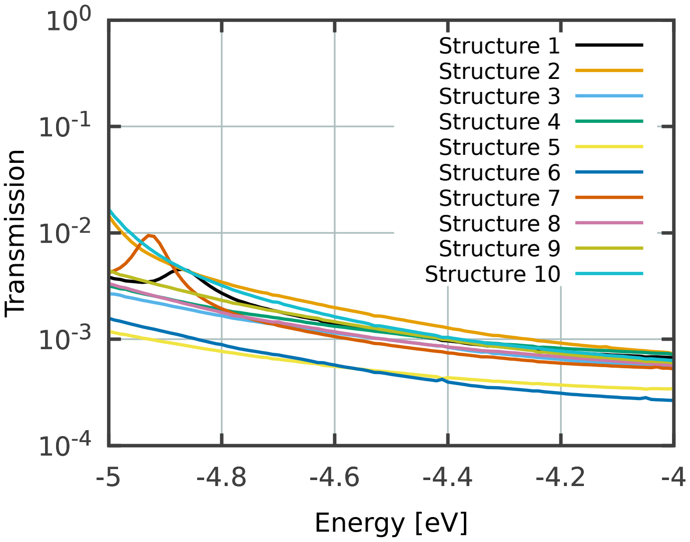

Figure A.5: Transmission functions of 10 lowest-energy 6DT sandwich structures extracted from 10 individual MD simulations with different seeds. No structures were excluded when calculating the average transmission.

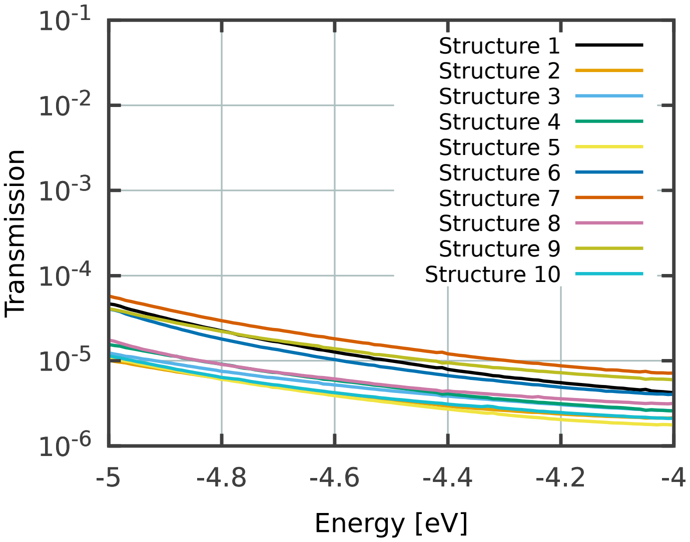

Figure A.6: Transmission functions of 10 lowest-energy 9DT sandwich structures extracted from 10 individual MD simulations with different seeds. No structures were excluded when calculating the average transmission.

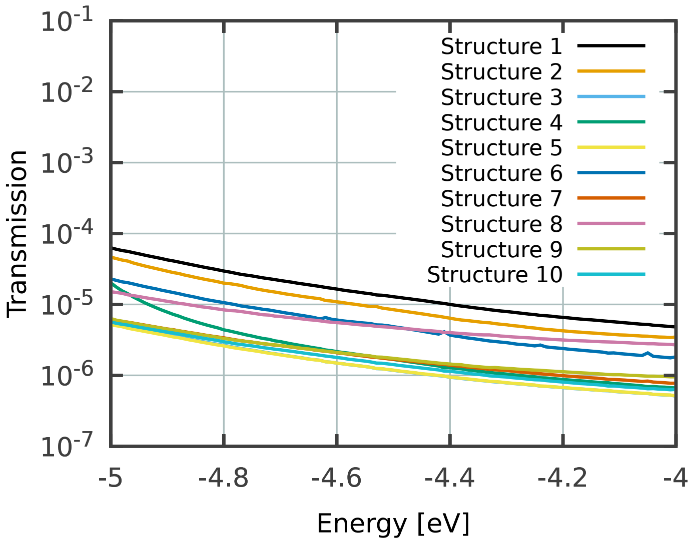

Figure A.7: Transmission functions of 10 lowest-energy 10DT sandwich structures extracted from 10 individual MD simulations with different seeds. No structures were excluded when calculating the average transmission.

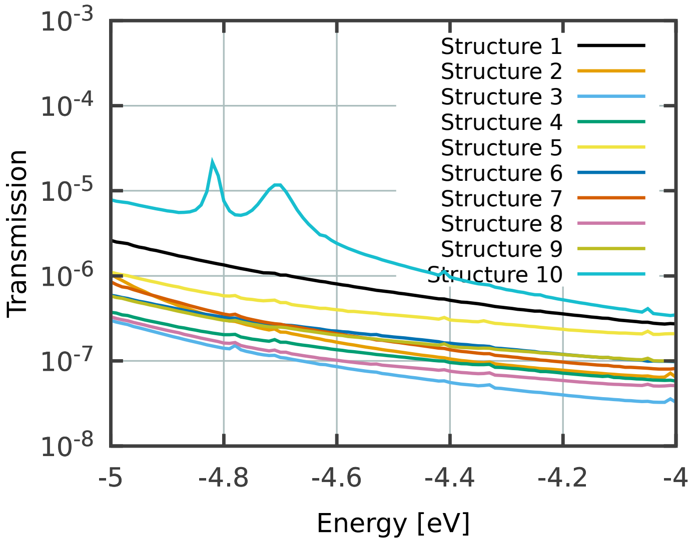

Figure A.8: Transmission functions of 10 lowest-energy 12DT sandwich structures extracted from 10 individual MD simulations with different seeds. Structure 10 was excluded when calculating the average transmission.

A.3.2 Transmission Functions of Alkanemonothiolate-Capped Interface Structures with a Surface Coverage of 75 %

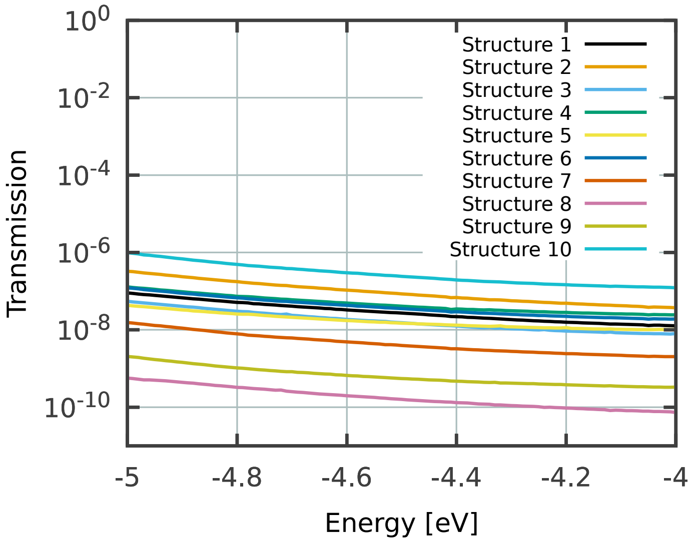

Figure A.9: Transmission functions of 10 lowest-energy 6T sandwich structures extracted from 10 individual MD simulations with different seeds. No structures were excluded when calculating the average transmission.

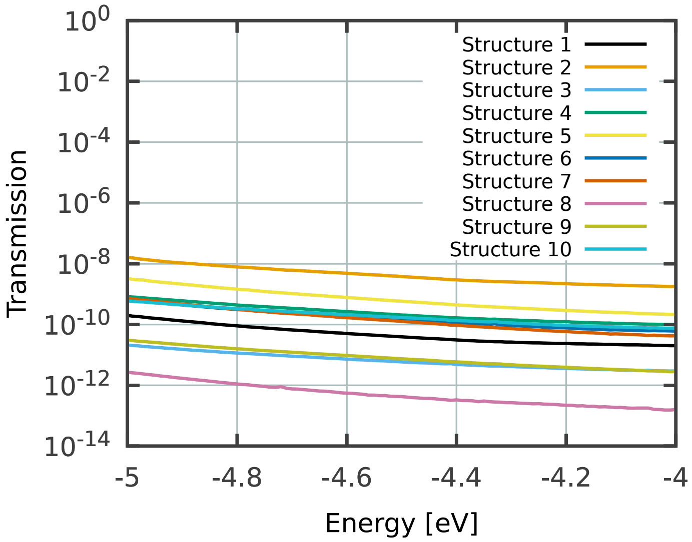

Figure A.10: Transmission functions of 10 lowest-energy 9T sandwich structures extracted from 10 individual MD simulations with different seeds. No structures were excluded when calculating the average transmission.

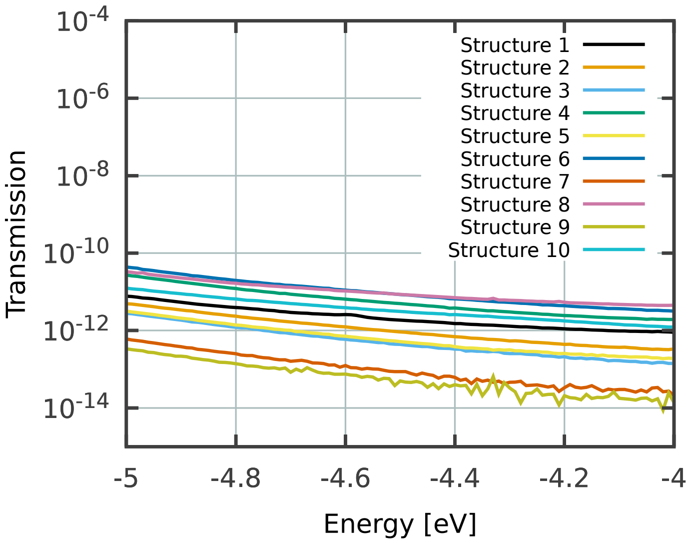

Figure A.11: Transmission functions of 10 lowest-energy 11T sandwich structures extracted from 10 individual MD simulations with different seeds. No structures were excluded when calculating the average transmission.

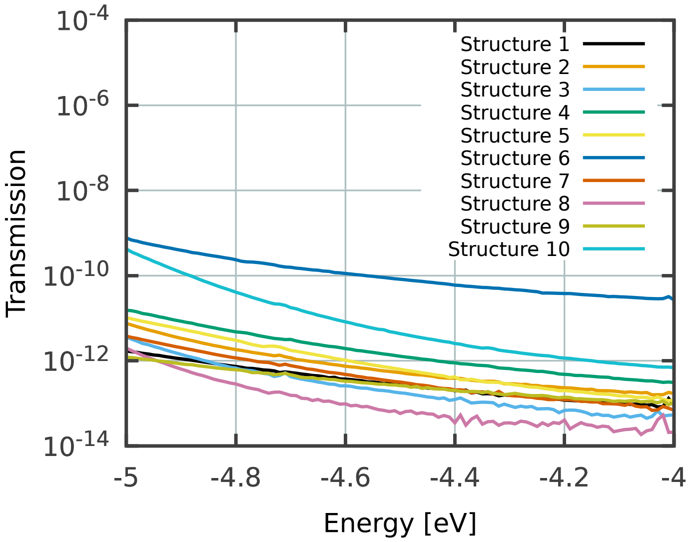

Figure A.12: Transmission functions of 10 lowest-energy 12T sandwich structures extracted from 10 individual MD simulations with different seeds. No structures were excluded when calculating the average transmission.

A.4 Additional Snapshots from Molecular Dynamics Simulations of Mixed-Ligand Interfaces

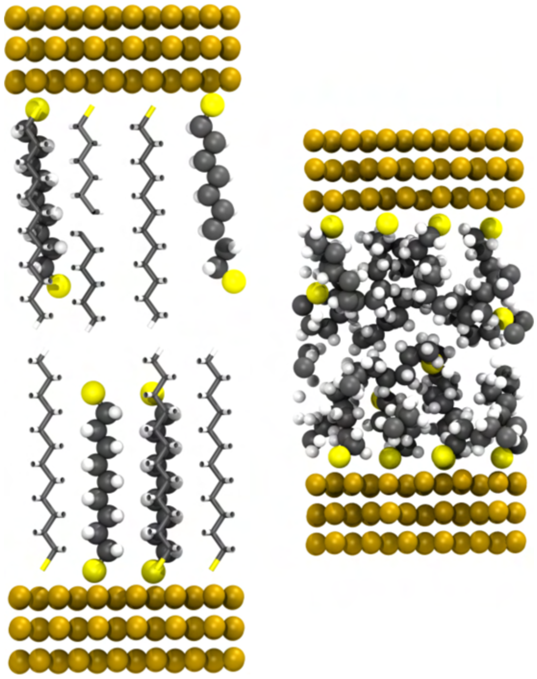

Figure A.13: Exemplary initial (left) and lowest-energy structures (right) of 12T/9DT mixed-ligand interfaces. The 9DT ligands are initially connected to only one of the surfaces (*intercalated* model). For a better distinguished of 12T and 9T ligands, 9DT ligands are represented by a balls and sticks, while the 6T ligands are drawn as lines in the left MD snapshot.

A.5 Additional Snapshots from Molecular Dynamics Simulations of Analyte Diffusion Processes

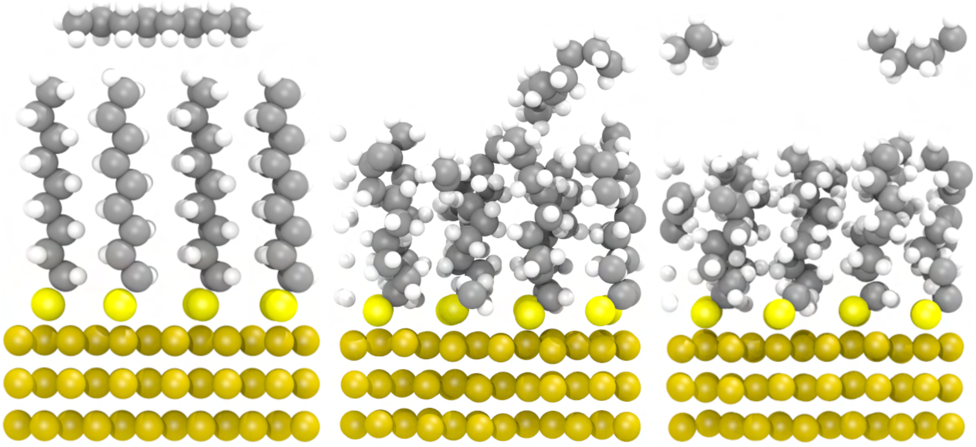

Figure A.14: Snapshots from an MD simulation where the analyte molecule (octane) was placed in closely above the initially straight and all-trans arranged ligand matrix (left). The octane molecule did not enter the ligand matrix during the simulation (center). Instead, it was repelled by the ligand matrix, while the ligands relaxed into tilted structures (right).

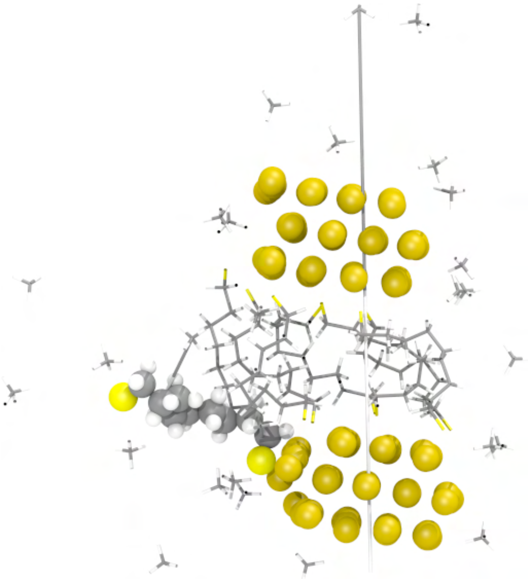

Figure A.15: NPT ensemble MD simulation, where the periodicity along the gold surfaces is broken in y direction by inserting a vacuum gap. In this gap, methane analyte molecules were placed. During the simulation, due to the loss of periodicity, ligand molecules moved around the surface (see highlighted ligand), causing a collapse of the interface structure.

A.6 Relative Resistances upon Analyte Adsorption estimated from Interparticle Distance Changes using Different Values for the Tunneling Decay Constant

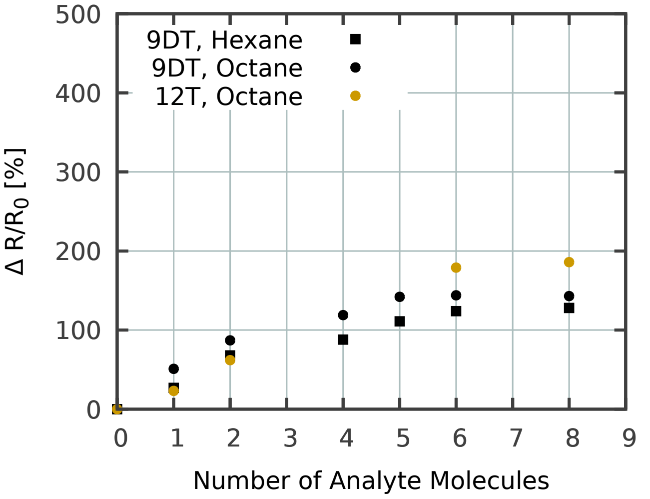

Figure A.16: Relative resistance changes in percent estimated from Equation 6.5 for 9DT (black) and 12T (orange) interfaces with $\beta = 0.75\,^{-1}$, occupied with varying numbers of hexane or octane analyte molecules.

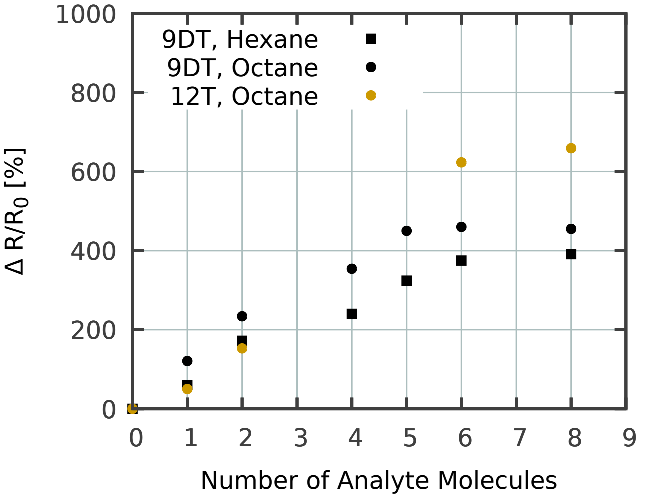

Figure A.17: Relative resistance changes in percent estimated from Equation 6.5 for 9DT (black) and 12T (orange) interfaces with $\beta = 1.1\,^{-1}$, occupied with varying numbers of hexane or octane analyte molecules.

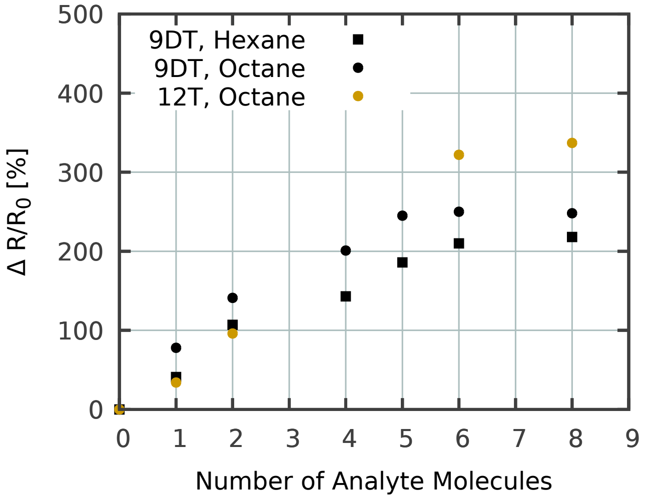

Figure A.18: Relative resistance changes in percent estimated from Equation 6.5 for 9DT (black) and 12T (orange) interfaces occupied with varying numbers of hexane or octane analyte molecules. Values for the tunneling decay constant of $\beta = 1.2^{-1}$ for 9DT systems and $\beta = 1.3^{-1}$ for 12T systems were used, as derived from the single-interface model in Sections 6.1.2 and 6.1.3.

A.7 Transmission Functions used for Calculating the Relative Resistance Change Upon Analyte Adsorption

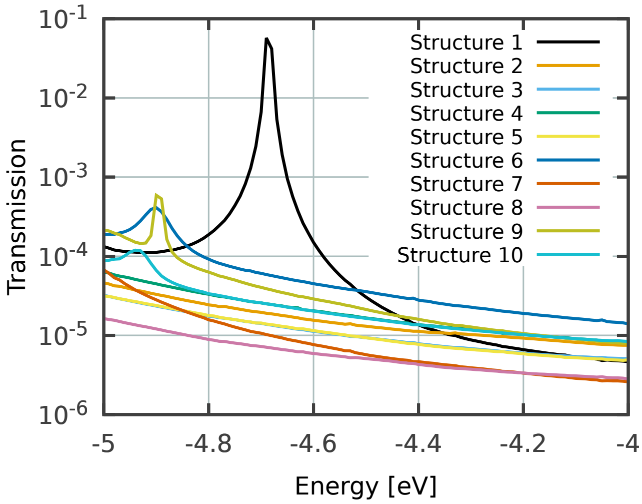

Figure A.19: Transmission functions of 10 lowest-energy 9DT sandwich structures with one incorporated hexane analyte molecules. The structures were extracted from 10 individual MD simulations with different seeds. Structure 2 was excluded when calculating the average transmission.

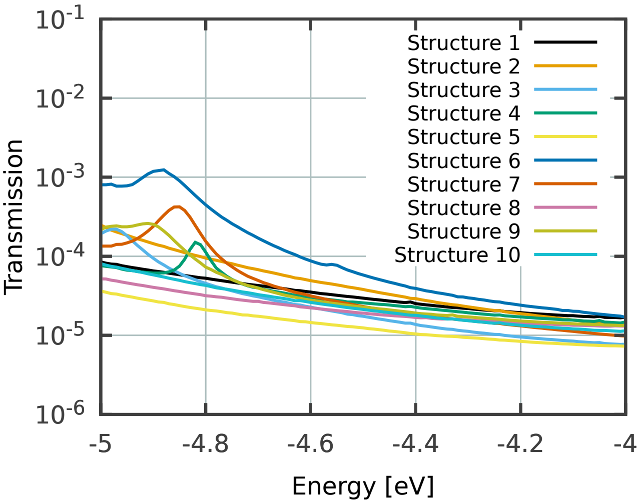

Figure A.20: Transmission functions of 10 lowest-energy 9DT sandwich structures with two incorporated hexane analyte molecules. The structures were extracted from 10 individual 10 individual MD simulations with different seeds. No structures were excluded when calculating the average transmission.

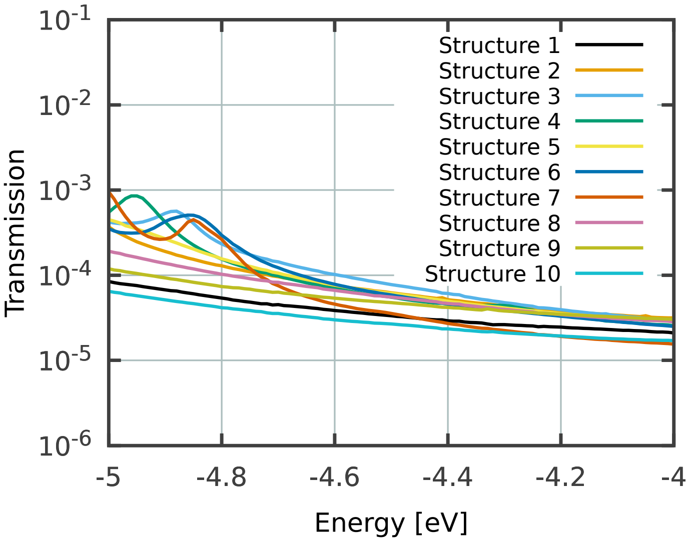

Figure A.21: Transmission functions of 10 lowest-energy 9DT sandwich structures with four incorporated hexane analyte molecules. The structures were extracted from 10 individual 10 individual MD simulations with different seeds. No structures were excluded when calculating the average transmission.

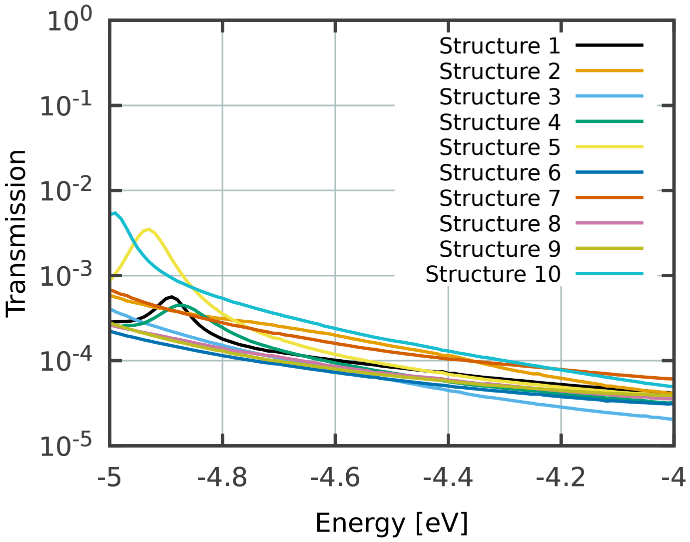

Figure A.22: Transmission functions of 10 lowest-energy 9DT sandwich structures with five incorporated hexane analyte molecules. The structures were extracted from 10 individual 10 individual MD simulations with different seeds. No structures were excluded when calculating the average transmission.

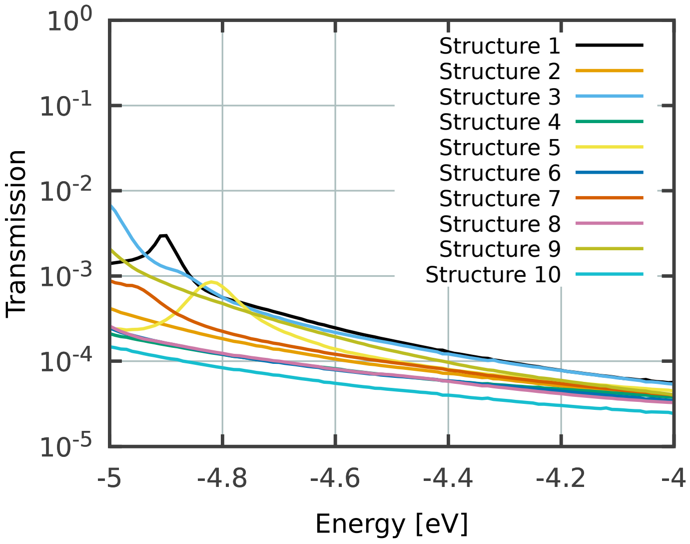

Figure A.23: Transmission functions of 10 lowest-energy 9DT sandwich structures with six incorporated hexane analyte molecules. The structures were extracted from 10 individual 10 individual MD simulations with different seeds. No structures were excluded when calculating the average transmission.

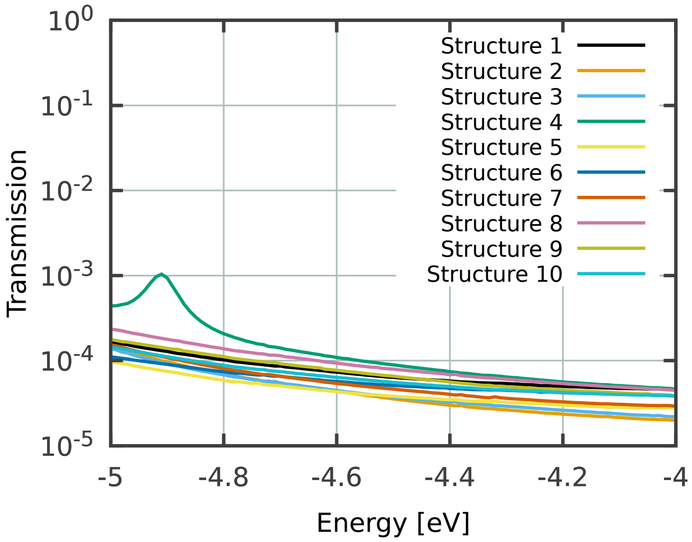

Figure A.24: Transmission functions of 10 lowest-energy 9DT sandwich structures with eight incorporated hexane analyte molecules. The structures were extracted from 10 individual 10 individual MD simulations with different seeds. No structures were excluded when calculating the average transmission.

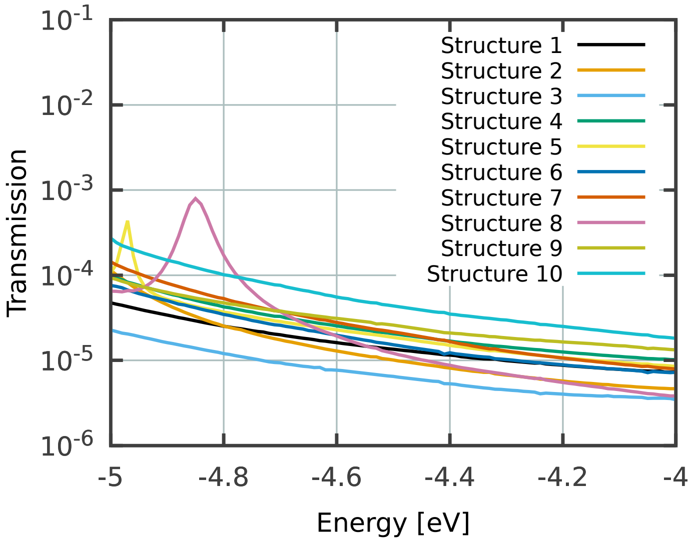

Figure A.25: Transmission functions of 10 lowest-energy 9DT sandwich structures with one incorporated octane analyte molecule. The structures were extracted from 10 individual 10 individual MD simulations with different seeds. No structures were excluded when calculating the average transmission.

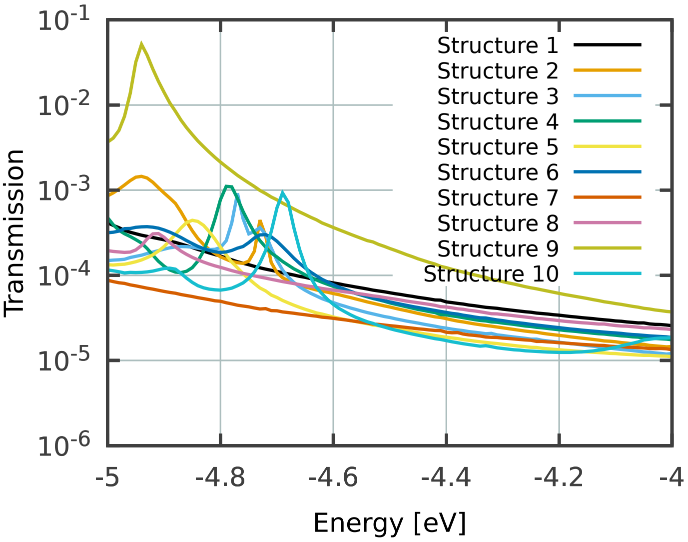

Figure A.26: Transmission functions of 10 lowest-energy 9DT sandwich structures with two incorporated octane analyte molecules. The structures were extracted from 10 individual 10 individual MD simulations with different seeds. No structures were excluded when calculating the average transmission.

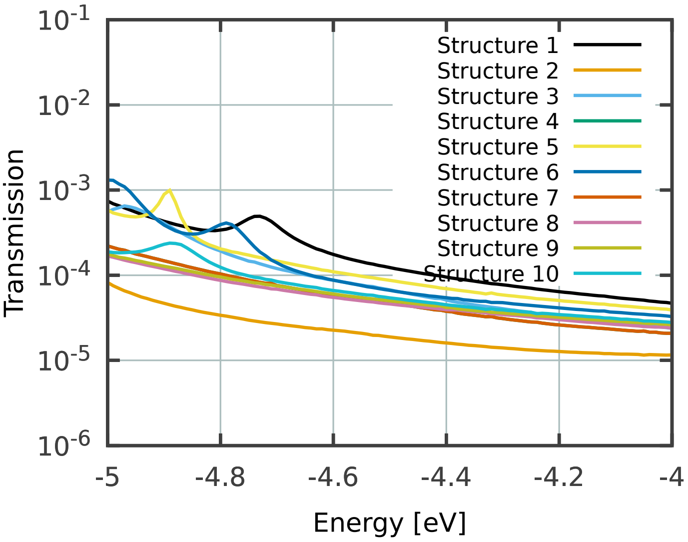

Figure A.27: Transmission functions of 10 lowest-energy 9DT sandwich structures with four incorporated octane analyte molecules. The structures were extracted from 10 individual 10 individual MD simulations with different seeds. No structures were excluded when calculating the average transmission.

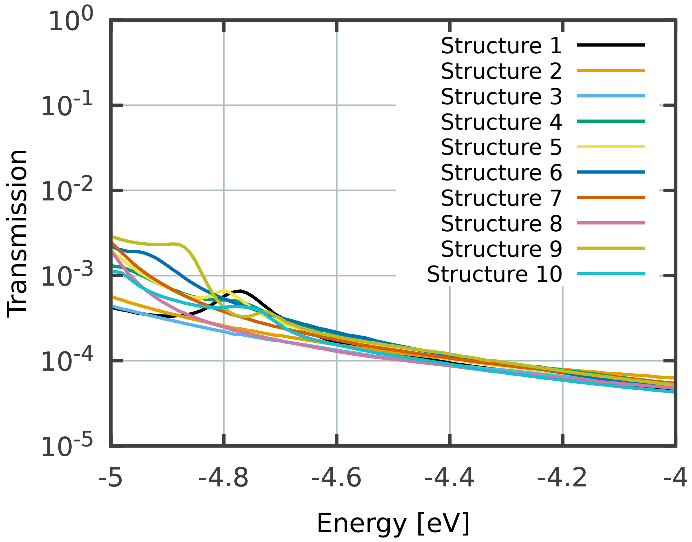

Figure A.28: Transmission functions of 10 lowest-energy 9DT sandwich structures with five incorporated octane analyte molecules. The structures were extracted from 10 individual 10 individual MD simulations with different seeds. No structures were excluded when calculating the average transmission.

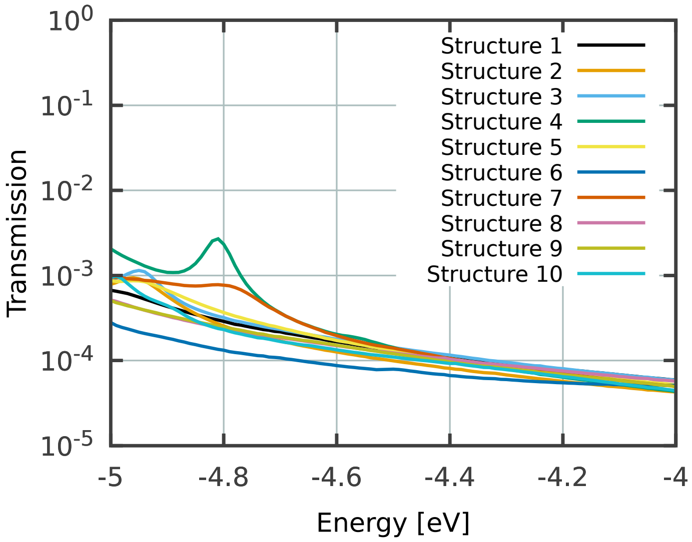

Figure A.29: Transmission functions of 10 lowest-energy 9DT sandwich structures with six incorporated octane analyte molecules. The structures were extracted from 10 individual 10 individual MD simulations with different seeds. No structures were excluded when calculating the average transmission.

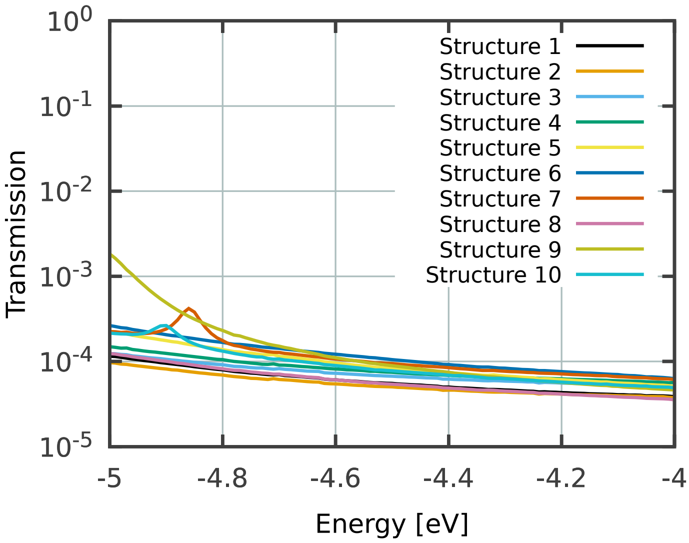

Figure A.30: Transmission functions of 10 lowest-energy 9DT sandwich structures with eight incorporated octane analyte molecules. The structures were extracted from 10 individual 10 individual MD simulations with different seeds. No structures were excluded when calculating the average transmission.

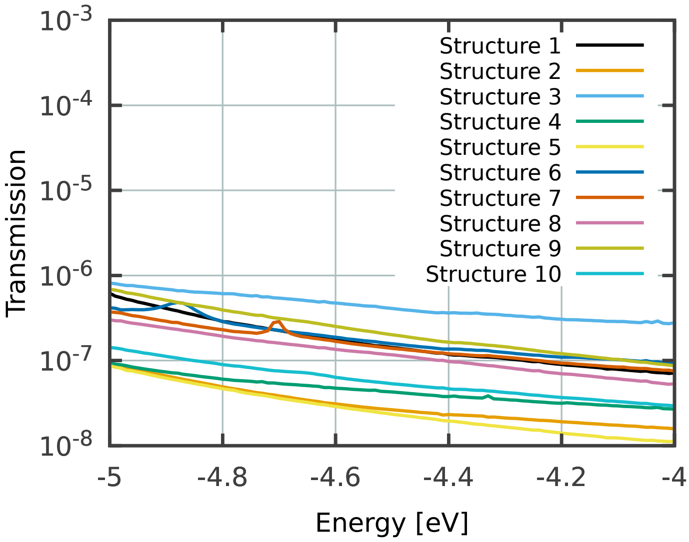

Figure A.31: Transmission functions of 10 lowest-energy 12T sandwich structures with one incorporated octane analyte molecule. The structures were extracted from 10 individual 10 individual MD simulations with different seeds. No structures were excluded when calculating the average transmission.

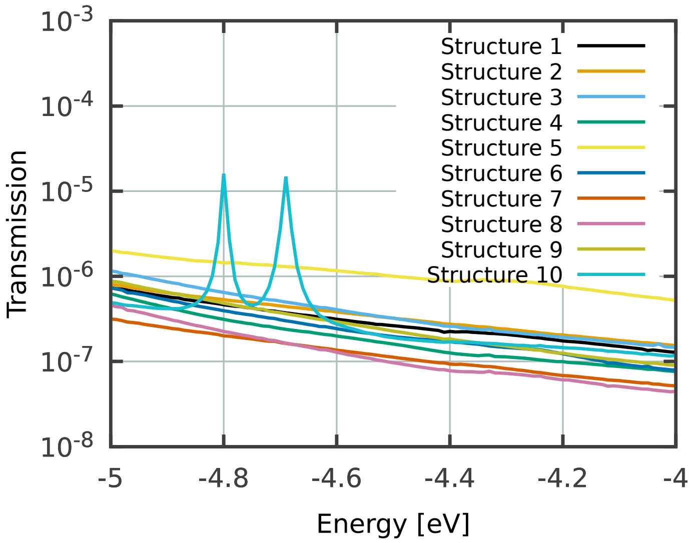

Figure A.32: Transmission functions of 10 lowest-energy 12T sandwich structures with two incorporated octane analyte molecules. The structures were extracted from 10 individual 10 individual MD simulations with different seeds. Structure 2 was excluded when calculating the average transmission.

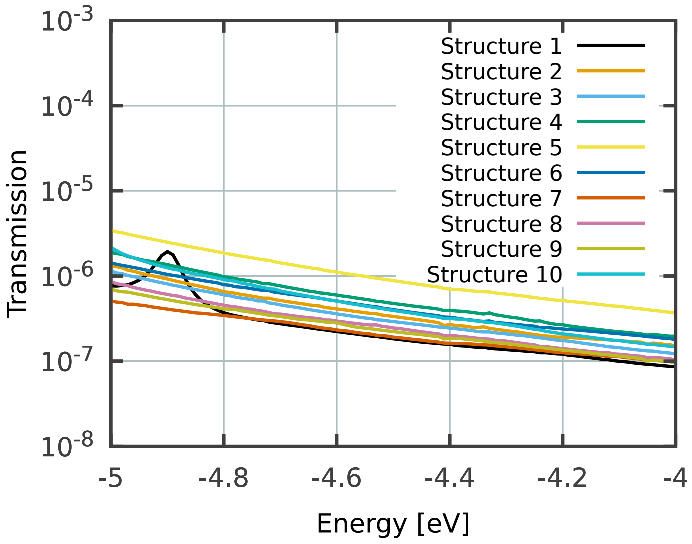

Figure A.33: Transmission functions of 10 lowest-energy 12T sandwich structures with four incorporated octane analyte molecules. The structures were extracted from 10 individual 10 individual MD simulations with different seeds. No structures were excluded when calculating the average transmission.

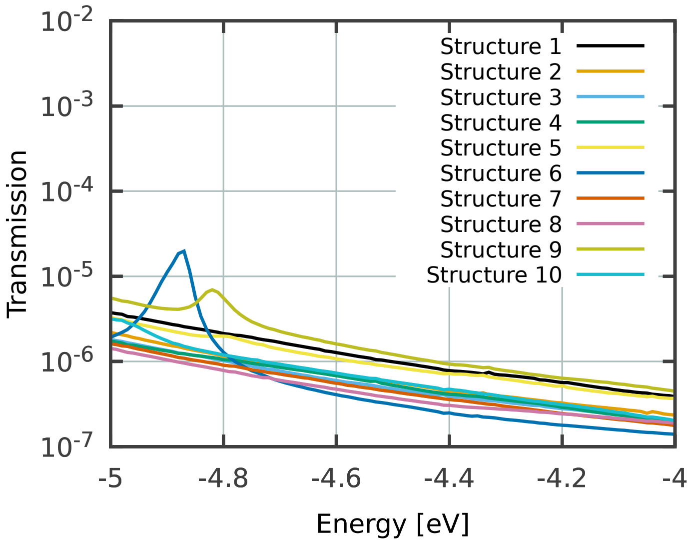

Figure A.34: Transmission functions of 10 lowest-energy 12T sandwich structures with five incorporated octane analyte molecules. The structures were extracted from 10 individual 10 individual MD simulations with different seeds. No structures were excluded when calculating the average transmission.

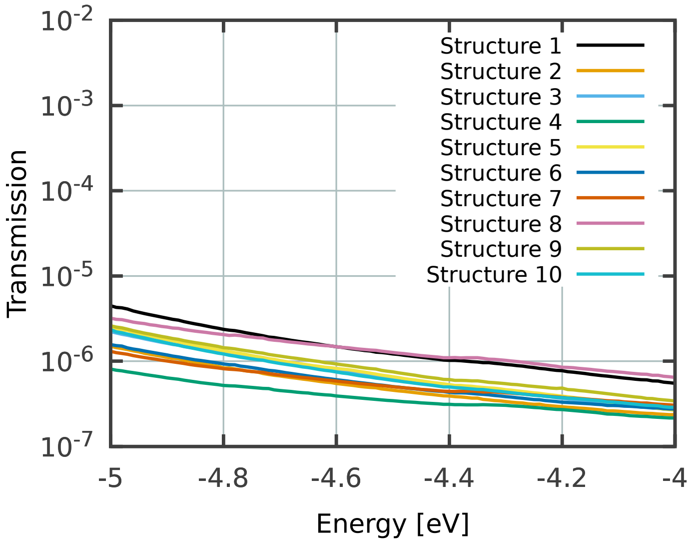

Figure A.35: Transmission functions of 10 lowest-energy 12T sandwich structures with six incorporated octane analyte molecules. The structures were extracted from 10 individual 10 individual MD simulations with different seeds. No structures were excluded when calculating the average transmission.

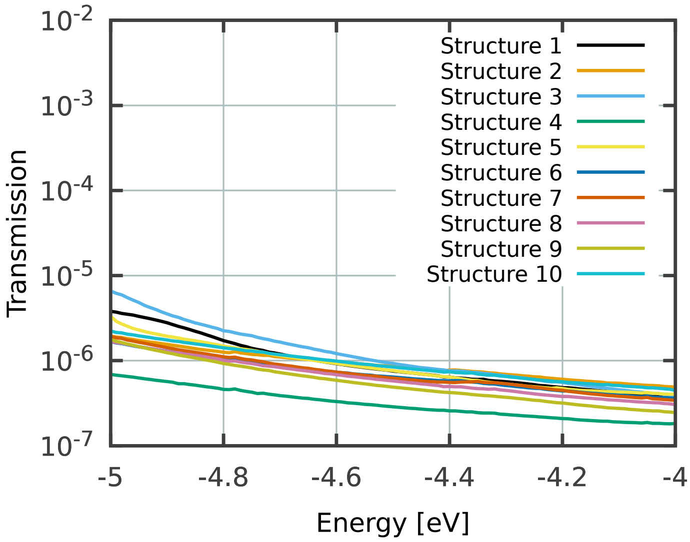

Figure A.36: Transmission functions of 10 lowest-energy 12T sandwich structures with eight incorporated octane analyte molecules. The structures were extracted from 10 individual 10 individual MD simulations with different seeds. No structures were excluded when calculating the average transmission.

A.8 Detailed Calculation of the Experimental Analyte-to-Ligand Ratio

Experimental data used for the following calculations were obtained from Olichwer et al. [41] for 12T-stabilized GNP assemblies.

TGA analysis revealed that the mass of a single GNP accounts for 86 % of the total mass of the particle stabilized by ligands. The mass of a single GNP m_{Au} without any ligands can be calculated from the particle radius $R_{\mathrm{GNP}} = 1.9 \cdot 10^{-7}$cm and the density of gold $\rho_{\mathrm{Au}} = 19.3\,\mathrm{g/cm}$

$$m_{\mathrm{Au}} = \rho_{\mathrm{Au}}\,\frac{4}{3}\,\pi R_{\mathrm{GNP}}^3 = 1.77 \cdot 10^{-19}\ \mathrm{g}\ . \tag{1}$$

Next, the mass of the ligand matrix m_{LM} can be calculated as

$$m_{\mathrm{LH}} = \frac{14 * m_{\mathrm{Au}}}{86} = 9.03 \cdot 10^{-20}\ \mathrm{g}\ , \tag{2}$$

The mass of a single 12T ligand $m_{12\mathrm{T}}$ can be calculated from its molar mass $M_{12\mathrm{T}} = 202.4\,\mathrm{g/mol}$ and the Avogadro number N_{A}

$$m_{12\mathrm{T}} = \frac{M_{12\mathrm{T}}}{N_{\mathrm{A}}} = 3.36 \cdot 10^{-22}\ \mathrm{g}\ . \tag{3}$$

Using the mass of a single 12T ligand, we can calculate the number of ligands in the ligand matrix of one particle n_{LM}

$$n_{\mathrm{LM}} = \frac{m_{\mathrm{LM}}}{m_{12\mathrm{T}}} = 268.58\ . \tag{4}$$

The mass of a GNP occupied with 12T ligands is

$$m_{\mathrm{GNP,12T}} = m_{\mathrm{Au}} + m_{\mathrm{LM}} = 6.45 \cdot 10^{-19} \text{ g} \; . \tag{5}$$

When the GNP film was exposed to toluene vapor in a concentration of 10,000 ppm, an increase in mass of 1.1 % was observed by Olichwer et al. ($\Delta M = 0.011$). The mass of a single toluene molecule can be calculated from its molar mass 92.14 g/mol, giving $m_{\mathrm{tol}} = 1.53 \cdot 10^{-22}$ g. Now, the ratio R of ligand molecules to toluene molecules at a toluene concentration of 10,000 ppm can be calculated

$$\mathrm{R} = \frac{n_{\mathrm{LM}}}{M_{\mathrm{GNP,12T}} \Delta M / m_{\mathrm{tol}}} = 5.79 \; . \tag{6}$$

Hence, there are about 6 ligand molecules per absorbed toluene molecule for a toluene concentration of 10,000 ppm.

A.9 Supporting Data for Blatter Radical Junctions

Table A.2: Total energies E and energy gradients $|dE/d\mathbf{r}|$ from DFT calculations of Blatter radical dimer junctions. The lowest-energy spin state of each dimer structure is marked as bold. At the current state of the calculations, all dimer junctions are the most stable in their singlet / ↿⇂ state. In some junctions, the second radical also formed a connection to one of the electrodes during the optimization. Information on the fate of the second radical is summarized below.

Dimer	Spin State	E [a.u.]	$\lvert dE/d\mathbf{r}\rvert$ [a.u.]	2nd Radical after Opt.
D1	cs	-6258.0441	0.000937	no interaction
D1	triplet / ↿↾	-6258.0757	0.001229	no interaction
D1	**os singlet / ↿⇂**	**-6258.0758**	**converged**	no interaction
D2	cs	-6258.0267	0.002415	no interaction
D2	triplet / ↿↾	-6258.0774	0.006348	no interaction
D2	**os singlet / ↿⇂**	**-6258.1046**	**0.000651**	no interaction
D3	cs	-6258.0618	0.000812	no interaction
D3	**triplet / ↿↾**	**-6258.0939**	**0.000571**	bound to one gold surface
D3	os singlet / ↿⇂	-6258.0934	converged	bound to one gold surface
D4	cs	-6258.0993	0.000226	bound to one gold surface
D4	triplet / ↿↾	-6258.1231	0.004760	bound to one gold surface
D4	**os singlet / ↿⇂**	**-6258.1251**	**converged**	bound to one gold surface

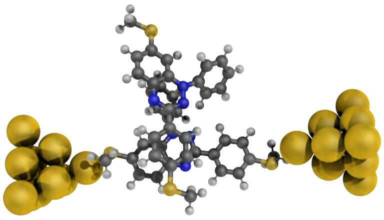

D1: closed-shell

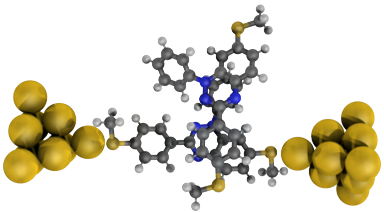

D1: triplet

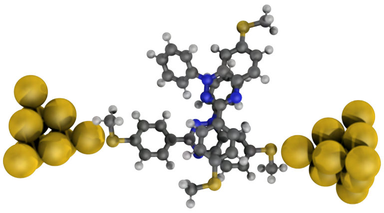

D1: open-shell singlet

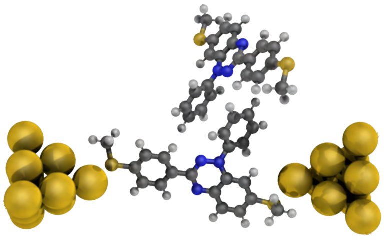

D2: closed-shell

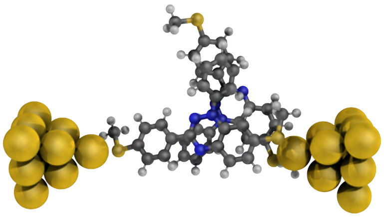

D2: triplet

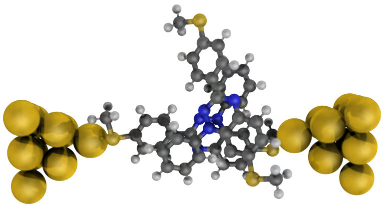

D2: open-shell singlet

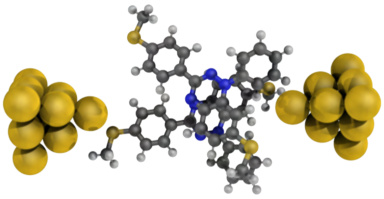

D3: closed-shell

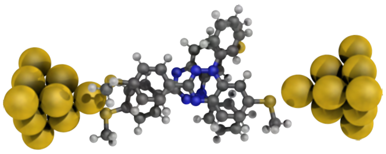

D3: triplet

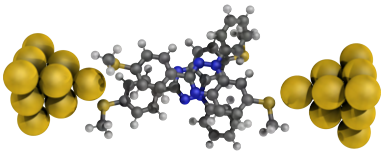

D3: open-shell singlet

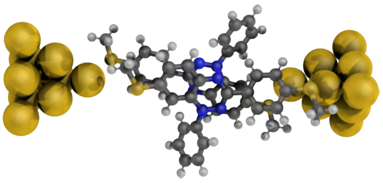

D4: closed-shell

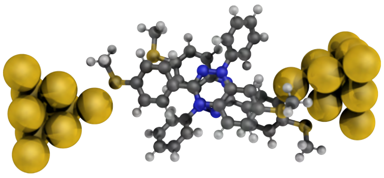

D4: triplet

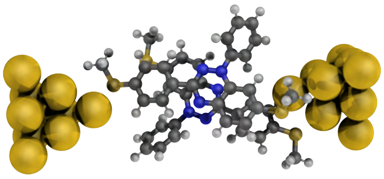

D4: open-shell singlet

Figure A.37: Optimized structures of Blatter radical dimers in junctions in their respective spin ground states.

B Python Scripts

Code example 1: Python script for detecting and removing trajectories with unlikely reactions

```python
#script by Karen Schaefer, Uni Hamburg, 2023
#written for Python 3.7

import sys, re, os, shutil
import numpy as np
from functions import *
from rdkit import Chem
from functions_analysis import *

'''
analyses all lammps simulations subfolders in one folder regarding S-Au distances and adsorbed thiol groups (average over all steps)
moves folders with simulations, where reactions occured before half the simulation time has passed into a new directory called "reactions"
'''

n_runs = 0
avg_dists = []
adsorbed_proportions = []


#redirect printed output to file
old_stdout = sys.stdout
log_file = open("analyse_all.log","w")
sys.stdout = log_file

#scan all directories for log file
current_dir = os.getcwd()
for it in os.scandir(current_dir):
    if it.is_dir():
        subdir_path = it.path
        os.chdir(it.path)
        if os.path.isfile('./out.lammpstrj'):
           print(it)
           movie = traj2xyz('out.lammpstrj', 'trajectory.xyz') #transfers lammps output file format into .xyz format
           xyzs = read_xyzs('trajectory.xyz') #uses read_xyzs function
           step = 0
           steps_with_reactions = []
           for xyz in xyzs:
               atoms = []
               coords = []
               n_atoms = len(xyz)
               for i in range(n_atoms): #append atoms and their coords to a list
                  atoms.append(xyz[i][0])
                  coords.append([float(xyz[i][1]), float(xyz[i][2]), float(xyz[i][3])])
               #check how many sulfur atoms are adsorbed on a gold surface
               try:
                  n_adsorbed, avg_dist, n_S = adsorbed_S(atoms, coords)
                  adsorbed_proportion = n_adsorbed/n_S
                  adsorbed_proportions.append(adsorbed_proportion)
                  avg_dists.append(avg_dist) #calculate average S-Au distance
                  #check for reactions with check_for_reactions function
                  reaction_step = check_for_reactions(atoms, coords, step)
                  if reaction_step != None:
                     steps_with_reactions.append(reaction_step)
               except ZeroDivisionError:
                  print('Error in simulation, possibly nan coordinates')
               step += 1
           total_steps = step * 1000

           # usually the lowest-energy point of a pushing simulation is reached before half of the simulation time had passed
           # trajectories are only excluded if the reactions occured after
```

```
    reaching the lowest-energy point
            if len(steps_with_reactions) != 0 and steps_with_reactions[0] <= (0.5*total_steps):
                print('Reactions occured before half of the simulation time passed --> move this run into subfolder "reactions"')
                if not os.path.exists('../reactions'):
                    os.makedirs('../reactions')
                print(subdir_path)
                shutil.move(it.path, '../reactions')
            if os.path.exists('trajectory.xyz'):
                os.remove('trajectory.xyz')
            n_runs+=1
        else:
            continue


#calculate S-Au distance
avg_dist = np.mean(avg_dists)
dev_dist = np.std(avg_dists)
avg_adsorbed = np.mean(adsorbed_proportions)

print('____________________________________________________')
print('average S-Au distance over ' + str(n_runs) + ' runs: ' + str(avg_dist) + ' +- ' + str(dev_dist))
print('average proportion of adsorbed thiol groups: ' + str(avg_adsorbed))


sys.stdout = old_stdout
log_file.close()
```

Code example 2: Functions Imported in the Python Script (from functions import *)

```
import sys, re, os
import numpy as np

#average
def average(lst):
    return sum(lst)/len(lst)

#read structure output file from lammps simulation and convert it into .xyz file format
def traj2xyz(input, output):
    # open file
    with open(input, 'r') as file:
        lines = file.readlines()

    # get number of atoms
    try:
        natoms = int(lines[3])
    except:
        print('error reading number of atoms')

    # get starting indices for each frame
    start_ids = []
    for i in range(len(lines)):
        if 'ITEM: ATOMS' in lines[i]:
            start_ids.append(i)

    # get atom symbols
    atoms = ['X' for i in range(natoms)]
    for i in range(natoms):
        index = int(lines[start_ids[0]+1+i].split()[0])-1
        atoms[index] = (lines[start_ids[0]+1+i].split()[-1])


    # get structures
    movie = []

    for snaps in start_ids:
        temp = np.zeros([natoms, 3])
        for atom in range(natoms):
```

```python
            index = int(lines[snaps+1+atom].split()[0])-1
            temp[index, 0] = float(lines[snaps+1+atom].split()[2])
            temp[index, 1] = float(lines[snaps+1+atom].split()[3])
            temp[index, 2] = float(lines[snaps+1+atom].split()[4])

        movie.append(temp)

    # write xyz
    with open(output, 'w') as file:
        for i in range(len(movie)):
            file.write(str(natoms)+'\n\n')
            for j in range(natoms):
                string = '{0:^2s} {1: 2.6f} {2: 2.6f} {3: 2.6f}\n'.format(atoms[j], *movie[i][j, :])
                file.write(string)
    return

#read .xyz structure file and write atoms and coordinates to an array
def read_xyzs(filename):
   with open(filename, 'r') as xyzs:
    structures = xyzs.read()
    temp = structures.split()

   #split file into the different xyz files
   n_atoms = int(temp[0])
   chunked_list = list()
   len_structure = (n_atoms * 4) + 1
   #print(temp[0])
   for i in range(0, len(temp), len_structure):
      chunked_list.append(temp[i:i+len_structure])

   structured_list = list()
   final_list = list()
   for l in chunked_list:
      for i in range(1, len(l), 4):
         structured_list.append(l[i:i+4])
   for i in range(0, len(structured_list), n_atoms):
      final_list.append(structured_list[i:i+n_atoms])

   return(final_list)
```

Code example 3: Functions Imported in the Python script for detecting and removing reactions (from functions_analysis import *)

```python
import sys, re, os, math
import numpy as np

#calculate distance between two coordinates
def distance(coord1, coord2):
    dist = math.sqrt(((coord2[0]-coord1[0])**2) + ((coord2[1]-coord1[1])**2) + ((coord2[2]-coord1[2])**2))
    return dist

#calculate average value of a list
def average(lst):
    return sum(lst)/len(lst)

#check how many thiol groups are adsorbed on a gold surface
#thresholds for bonds: {'S-Au':3.0, 'S-C':2.0 , 'S-H': 1.5}
def adsorbed_S(atoms, coords):
    S_coords = []
    Au_coords = []
    S_adsorbed = []
    Au_S_dists = []
    ind_S = np.where(np.array(atoms) == 'S')[0]
    for S in ind_S:
       S_coords.append(coords[S])
    n_S = len(S_coords)
    ind_Au = np.where(np.array(atoms) == 'Au')[0]
    for Au in ind_Au:
```

```
       Au_coords.append(coords[Au])
    for S_coord in S_coords:
       for Au_coord in Au_coords:
          dist = distance(S_coord, Au_coord)
          if dist < 3.0:
              if S_coord not in S_adsorbed:
                 S_adsorbed.append(S_coord)
              Au_S_dists.append(dist)
    avg_dist = average(Au_S_dists)
    n_adsorbed = len(S_adsorbed)
    n_S = len(S_coords)
    return n_adsorbed, avg_dist, n_S

#find reactions in MD simulation
def check_for_reactions(atoms, coords, step):
    step = step * 1000
    S_coords = []
    C_coords = []
    H_coords = []
    ind_S = np.where(np.array(atoms) == 'S')[0]
    for S in ind_S:
       S_coords.append(coords[S])
    ind_C = np.where(np.array(atoms) == 'C')[0]
    for C in ind_C:
       C_coords.append(coords[C])
    ind_H = np.where(np.array(atoms) == 'H')[0]
    for H in ind_H:
       H_coords.append(coords[H])
    for S_coord in S_coords:
       for H_coord in H_coords:
          dist = distance(S_coord, H_coord)
          if dist < 1.6:
              print('Attention! S-H in step ' + str(step))
              return step
    #for S_coord in S_coords:
       n=0
       for C_coord in C_coords:
          dist = distance(S_coord, C_coord)
          #print(dist)
          if dist < 2.0:
              n+=1
              if n > 1:
                 print('Attention! S-C in step ' + str(step))
                 return step
    #for S_coord1 in S_coords:
       for S_coord2 in S_coords:
          dist = distance(S_coord, S_coord2)
          if dist < 2.0 and dist != 0.0:
              print('Attention! S-S in step ' + str(step))
              return step
```

C Data availability

The computational raw data was uploaded to the “Zentrum für nachhaltiges Forschungsdatenmanagement” (ZFDM) of the University of Hamburg, and can be accessed by the community upon request (`DOI: 10.25592/uhhfdm.17668`). Raw data from DFT calculations (from Section 6.4) can be found at `https://nomad-lab.eu` (`https://doi.org/10.17172/NOMAD/2024.12.18-1`). In this dataset, the following calculations are included: isolated monomer structure optimization (entry id: 4s6DBVjmeqvVL8pCfeW2dk2gbA_Q), monomer junction structure optimization and charge transport calculation (entry id: 6F6F8qZxeFT6etC7p3oHcZY6y7A3), dimer junctions structure optimization and charge transport (Tables S5, S7, and S8—dataset “dimer-junction-optimized-transport”), isolated dimer structure optimizations (Figure S12; Table S3—dataset “dimer-isolated-optimizations”), and dimer junctions single point calculations (dataset “dimer-junction-single-point”). Raw data from the publication in Ref.[117] can be accessed openly at the ZFDM of the University of Hamburg (`DOI: 10.25592/uhhfdm.14051`).

D List of Chemicals

No hazardous chemicals according to the Globally Harmonized System of Classification and Labeling Chemicals (GHS) regulation have been used within the scope of this thesis.

E Acknowledgements

The work presented in this thesis would not have been possible without the continuous support of various people throughout the last three years. First and foremost I want to thank Carmen Herrmann for welcoming me in the group and giving me the opportunity to work on this project as part of the Graduate School “Nanohybrid”. Her scientific guidance and support have been very valuable to me. Thank you for always taking time for discussions and for proofreading manuscripts and this thesis. I benefited a lot from her experience and knowledge during the time I spend in the group.

I also would like to thank my second supervisor Tobias Vossmeyer for always taking time for discussions and for giving me insights into his broad knowledge of the field. Furthermore, I want to thank my third supervisor Wolfgang Parak for giving me additional insights into the topic from the perspective of a biophysicist. Additionally, I want to thank all three of my supervisors for being my committee members and for their interest in my work. In this context, I also want to thank Gabriel Bester for taking the time and agreeing to be the co-examiner of this thesis.

Next, I would like to express my gratitude to the group members who helped with accomplishing my research. Especially, I want to thank Michael Deffner and Haitao Zhang for sharing their advice on molecular dynamics simulations, to Sumit Naskar and Michael Deffner for assisting me with DFTB calculations, as well as Ursula Rastetter and Michael Deffner for helping me setting up my first DFT calculations. I also want to thank Michael Deffner and Nathalie Smith for proofreading parts of this thesis. A big thanks goes again to Michael Deffner for always being my “rubber duck” for debugging code or other issues. Furthermore, I want to thank my co-workers Michaela Schneeberger, Ulrich Pototschnig, Eduard Hahn, Lawrence Rybakowski, Aida Saghatchi, Philipp Baltruschat, Ömer Sahin, and Johannes Strauch for their insights and the great time.

To evaluate theoretical models, experimental data is crucial. Therefore, a special thanks goes to Chih-Yin Liu for the close collaboration. Thanks for providing experimental data to the different systems I have studies within this work, and for our valuable discussions. I also really enjoyed the insights into the experimental side I gained when visiting her lab for a few days. Additionally, I want to thank my experimental and theoretical collaborators Andreas Meyer for performing GISAXS calculations, Hendrik Schlicke for scientific discussions, as well as Gautam Mitra, Jueting Zheng, Jonathan Z. Low, Luis M. Campos, Theo A. Costi, and Elke Scheer for providing the experimental and theoretical background for my work on Blatter radical junctions. In this context, I also thank Michael Deffner for providing the structures for the isolated Blatter radical dimers.

Furthermore, I want to acknowledge Alexander Seiler’s work on analyte molecule incorporation into the model as part of his bachelor thesis, as well as Aileen Ripp for testing out different MD software that did not prove to be suitable for the simulations, sparing me time and resources in that regard.

Additionally, I would like to thank the DFTB+ community, especially Balínt Aradi, Alessandro Pecchia, and Thomas Niehaus, for helpful insights into charge transport calculations under periodic boundary conditions.

I would like to thank Svenja Kunze for sparking my interest in gold nanoparticle assemblies while supervising my lab internships during my bachelor’s and master’s studies.

I am grateful for the opportunity to conduct my thesis as part of the graduate school 2536 “Nanohybrid”, which gave me the opportunity to share collaborations with experimental researchers, exchange with students and PIs from different fields, and participate in highly enjoyable but also very fruitful workshops and conferences with fellow graduate school members. I also appreciate the chance to be a part of the planning committee for several RTG workshops and conferences. For funding this graduate school, I thank the Deutsche Forschungsgemeinschaft (DFG, funding ID 408076438).

Moreover, I thank the people in the background, without whom this thesis would not have been possible. Thank you to the IT-service of the chemistry department for their technical support, especially to Christian Schmidt for always helping with solving hardware and software problems. I thank the high performance computing center (RRZ) for providing computational resources, for maintaining the facilities, and for offering excellent technical support. Furthermore, I want to thank Corinna Flügge and Angelina Siemon for assisting with administrative tasks.

Finally, I would like to thank my family and friends for their persistent support and encouragement, which allowed me to follow my interests in science without any restrictions. A special thanks goes to my wife, Ann-Kathrin Schaefer, for always believing in me, for her constant support and patience, and for being a source of strength and motivation throughout this journey.

F Use of Artificial Intelligence Based Tools

The author acknowledges that an artificial intelligence (AI) language model (*ChatGPT4 omni mini* as implemented in UHHGPT) was used to improve readability and language of the work presented in this thesis, for example, by correcting grammatical and language errors. After using this tool, the author reviewed and edited the content as needed and takes full responsibility for the content of the publication. The AI language model was not used to produce scientific insights, to draw scientific conclusions, to restructure whole paragraphs or to generate figures, images or artwork.

G Eidesstaatliche Versicherung

Hiermit versichere ich an Eides statt, die vorliegende Dissertationsschrift selbst verfasst und keine anderen als die angegebenen Quellen und Hilfsmittel benutzt zu haben. Sofern im Zuge der Erstellung der vorliegenden Dissertationsschrift generative Künstliche Intelligenz (gKI) basierte elektronische Hilfsmittel verwendet wurden, versichere ich, dass meine eigene Leistung im Vordergrund stand und dass eine vollständige Dokumentation aller verwendeten Hilfsmittel gemäß der Guten wissenschaftlichen Praxis vorliegt. Ich trage die Verantwortung für eventuell durch die gKI generierte fehlerhafte oder verzerrte Inhalte, fehlerhafte Referenzen, Verstöße gegen das Datenschutz- und Urheberrecht oder Plagiate.

Datum

Karen Schaefer